Université du Québec
Institut National de la Recherche Scientifique
Énergie, MatériauxetTélécommunications

Controlled Synthesis of Nanomaterials for Electrochemical Energy Conversion

Nathanael Rainald Komba

A thesis submitted in partial fulfillment of the requirements for the *degree of Doctor of Philosophy* in Science of Energy and Materials

Evaluation Jury

Research supervisor	Shuhui Sun Professor, INRS-EMT
Research co-supervisor	Federico Rosei Professor, INRS-EMT
Internal examiner and the president of the Jury	Fiorenzo Vetrone Professor, INRS-EMT
External examiner	Zhibin Ye Professor, Concordia University
External examiner	Pablo Bianucci Professor, Concordia University

Acknowledgement

I want to express my sincere gratitude to my supervisor Prof. Shuhui Sun, for accepting me as a student and directing my Ph.D. research program. His guidance, encouragement, and support helped me a lot in the pursuit of my Ph.D. study. I also want to thank Prof. Federico Rosei, my co-supervisor, for his care, guidance, and support throughout my Ph.D. study.

I want to thank Dr. Gaixia Zhang for the scientific discussions, the valuable suggestions on this thesis organization, as well as her help and support during my Ph.D. study. I am grateful to Drs. Régis Chenitz and Michel Lefèvre for their technical assistance and guidance. I thank my colleagues in Profs. Sun and Rosei research groups for their collaborations and supports. Special thanks to Yanqing Fu, Qiliang Wei, Xin Tong, Xiaohua Yang, Amir Hasanpour, Zonghua Pu, Mingjie Wu, Zhangsen Chen, Yufeng Zhou, Daling Cui, Joy Prakash, and Daniel Benetti. I am also indebted to many of my colleagues and friends whom I received friendship and unconditional support over the years. Specifically, I want to thank Ivy Asuo, Charlotte Boukandou, Mohamed Cherif, Ali Almesrati, Ibrahima Ka, Ifeanyichukwu Amaechi, Xin Jin, Fan Yang, and Qingzhe Zhang. I would also like to thank all members of staff at INRS-EMT for their direct and indirect supports.

I am grateful to the UNESCO Chair in Materials and Technologies for Energy Conversion, Saving and Storage (MATECSS) for the Ph.D. Excellence Scholarship for supporting my Ph.D. program at INRS. I also want to thank my employer, the University of Dar es Salaam in Tanzania, for granting me a study leave to undertake this Ph.D. program. Finally, yet importantly, I am indebted to Paul Kortenaar my former teachers’ college tutor, and my family, the Mwalihalalis, for their love and unwavering support during this program, especially in the final year.

Résumé

Les réactions de réduction de l'oxygène et de production de l’hydrogène sont des processus critiques dans l'utilisation efficace des dispositifs de conversion d'énergie électrochimique et d’électrolyse de l'eau. Les principaux obstacles au développement et à l’application à grande échelle de ces dispositifs sont leur coût élevé et leur durabilité à long terme qui est inadéquate. Au cœur de ces barrières, il y a l'utilisation de matériaux à base de métaux précieux qui jouent le rôle d’électrocatalyseurs, facilitant la réaction de réduction de l'oxygène (ORR) et la réaction de dégagement d'hydrogène (RDH). L'exploration de catalyseurs (ORR)/(RDH) non précieux, efficaces, peu coûteux et hautement durables, destinés à remplacer les catalyseurs rares et coûteux à base de platine est cruciale. Par conséquent, le but de cette thèse est de développer par des approches simples des électrocatalyseurs efficaces, peu coûteux et durables, sans métaux ni métaux précieux qu’on appelle ici électrolyseurs sans métal. Pour se faire, nous avons utilisé des méthodes de synthèse électrochimiques, hydrothermales et de dépôt par évaporation lente pour fabriquer et assembler des matériaux. Nous avons réussi à produire du graphène de haute qualité dopée à l'azote, qui a été évalué dans les ORR à la fois comme électrocatalyseur sans métal et comme matériau de support pour les électrocatalyseurs de métaux non précieux (NPMCs) de phtalocyanine de fer (II) (FePc). Nous avons également fabriqué des nanotubes de hautement ordonnés avec des morphologies contrôlées. Ces nanotubes de TiO_2 sont utilisés comme potentielle électrode et comme matériau de support pour MoS_2 pour dans les RDH. En effet, nous avons étudié les approches simples de fabrication d'électrocatalyseurs en utilisant des matériaux abondants et peu coûteux, ainsi que leur application potentielle en tant qu'électrodes actives pour les ORR et les RDH.

Dans cette thèse, nous avons d'abord étudié l'application du graphène en tant qu'électrocatalyseur sans métal pour les ORR. Nous avons réussi à fabriquer du graphène (GP) de haute qualité avec des couches contrôlées, en utilisant une méthode d'exfoliation électrochimique simple, polyvalente et économique. Nos études systématiques ont révélé que le précurseur (graphite), la température de l'électrolyte et les conditions de pyrolyse affectent principalement le nombre de couches, la qualité et la composition chimique du graphène. Par conséquent, tous ces paramètres de synthèse du graphène ont un effet significatif sur les ORR. L'échantillon de graphène optimisé a ensuite été traité thermiquement dans une atmosphère de NH_3 pour obtenir du graphène dopé à l'azote (N-GP). En tant qu'électrocatalyseur sans métal, le N-GP950 optimisé présente une activité ORR efficace et une excellente durabilité avec des performances ORR comparables au catalyseur Pt/C de pointe dans un environnement alcalin.

Par ailleurs, nous avons utilisé le N-GP950 fabriqué dans la section précédente pour l'utiliser comme support pour la phtalocyanine de fer (FePc) dans l'assemblage de FePc/N-GP950 en tant que ECSM. Pendant des décennies, le macrocycle métallique, FePc, a fait l'objet de nombreuses recherches en tant que précurseur de la préparation des électrocatalyseurs ORR. À ce jour, toutefois, son utilisation a été limitée par une faible activité électrocatalytique et une durabilité insuffisante s'il n'est pas incorporé dans le support de carbone par pyrolyse à haute température. Inspirés par sa surface large, uniforme et de haute qualité, ainsi que par ses performances ORR élevées, nous avons utilisé le support N-GP950 pour améliorer les performances ORR de FePc en tant que NPMCs. Les méthodes traditionnelles de synthèse des NPMCs impliquent des produits chimiques dangereux ou une pyrolyse à haute température, ce qui entraîne des problèmes d'environnement et de sécurité, en particulier lors de la production à grande échelle. De ce fait, il est impératif d'explorer des stratégies simples, sûres et peu onéreuses de fabrication de catalyseurs

ORR de hautes performances. Ici, nous avons également étudié le dépôt par évaporation lente, une approche rentable non pyrolyse, d'assembler le catalyseur Fe-N-C en tant que NPMCs en immobilisant FePc sur la surface de N-GP950. Les unités FePc se dispersent uniformément à la surface du N-GP950 et de fortes interactions électroniques-π apparaissent entre FePc et N-GP950. Notre catalyseur composite optimisé (FePc-33/N-GP950), avec une charge de 33% en poids de FePc, présente une performance ORR extrêmement efficace. De façon remarquable, le FePc-33/N-GP950 affiche la densité de courant la plus significative à 0.8 V (5.0 mA.cm^{-2}), ce qui est comparable à 4.0 mA.cm^{-2} du Pt/C commercial. Le FePc-33/N-GP950 affiche également une excellente stabilité à long terme sans perte d'activité significative après des tests de durabilité accélérés pour 5000 cycles de potentiel. La présente étude propose une stratégie simple et peu coûteuse pour concevoir des catalyseurs ORR efficaces et durables destinés aux applications pratiques des piles à combustible alcalines et des batteries métal-air.

Enfin, nous avons exploré la production électrochimique d'hydrogène, qui présente une flexibilité et une compatibilité pour l'utilisation de sources d'énergie renouvelables. La production d'hydrogène par méthode électrochimique offre la promesse d'un vecteur d'énergie propre et durable. Toutefois, la réalisation de cette promesse exigera des électrocatalyseurs durables, à faible coût, extrêmement efficaces. Dans cette étude, nous avons fabriqué des matrices de nanotubes de TiO_2 hautement ordonnées et autonomes (TiO_2-NTs) en anodisant des feuilles de Ti. Nous avons utilisé TiO_2 comme catalyseur et également comme matériau de support de MoS_2 pour RDH en milieu acide et alcalin. La morphologie des TiO_2-NTs a été contrôlée en ajustant les conditions d'anodisation. Des propriétés telles que la longueur du tube, le diamètre, l'épaisseur de la paroi et la surface se sont avérées fortement dépendantes des conditions d'anodisation. Par la suite, nous avons synthétisé les couches de MoS_2 qui ont été déposés sur des nanotubes de TiO_2-NTs en tant

que couche active pour les RDH en utilisant une méthode d'évaporation lente. Les cristallites de MoS_2 se sont uniformément dispersées sur toute la surface des TiO_2-NTs. Les couches de TiO_2-NTs, de MoS_2 et de MoS_2/TiO_2-NTs sont tous actifs vis-à-vis de RDH dans un environnement acide et alcalin. Les couches de MoS_2/TiO_2-NTs présentent des performances RDH particulièrement excellentes dans une solution acide à faible surpotentiel (170 mV) à 10 mA cm^{-2} ainsi que sur une petite pente de Tafel (70 mV/décennie). Plus important encore, les MoS_2/TiO_2-NTs affichent une durabilité supérieure pour les RDH après 5000 cycles de potentiel continu entre -0.4 et - 0.2 (V vs. RHE). Le composite MoS_2/TiO_2-NTs démontre le potentiel d'une électrode rentable pour la production électrochimique d'hydrogène.

Abstract

The oxygen reduction and hydrogen evolution reactions are critical processes in the effective utilization of electrochemical energy conversion devices and water electrolyzers. The main barriers to the widespread development and application of these devices are their high cost and inadequate long-term durability. At the heart of these barriers is the use of precious metal-based materials that are the benchmark electrocatalysts to facilitate the oxygen reduction reaction (ORR) and hydrogen evolution reaction (HER) processes. The exploration of efficient, low cost and highly durable non-precious ORR/HER catalysts to replace the rare and expensive Pt-based catalysts is critical. Therefore, the purpose of this thesis is to develop efficient, low-cost, and durable metal-free and non-precious metal electrocatalysts (NPMCs) via straightforward approaches. We employed electrochemical, hydrothermal, and slow evaporation methods to fabricate and assemble materials. We successfully synthesized N-doped graphene, which was employed as both a support material for FePc catalyst and a metal-free electrocatalyst for ORR. We also fabricated highly ordered TiO_2-nanotubes with controlled morphologies as a potential HER electrode, and as support material for MoS_2 for HER electrocatalysis. Accordingly, in this thesis, we investigated the straightforward approaches to fabricate electrocatalysts by using earth-abundant and low-cost materials and their potential application as active electrodes for the ORR and HER.

In this thesis, we first investigated the application of graphene as a metal-free electrocatalyst for the ORR. We successfully fabricated high-quality graphene (GP) with controlled layers, using a straightforward, versatile, and cost-effective electrochemical exfoliation method. Our systematic studies revealed that the graphite precursors, electrolyte temperatures, and conditions of pyrolysis primarily affect the number of layers, quality, and chemical composition of the graphene. Consequently, all these parameters of graphene have a significant effect on the ORR performance.

The optimized graphene samples were subsequently heat-treated in an NH_3 atmosphere to obtain nitrogen-doped graphene (N-GP). As a metal-free electrocatalyst, the optimized N-GP950 exhibits efficient ORR activity and excellent durability with ORR performance comparable to the state-of-the-art Pt/C catalyst in the alkaline environment.

Furthermore, we employed the N-GP950 as the support for iron phthalocyanine (FePc) in the assembly of FePc/N-GP950 as NPMCs. For decades, the metal macrocycle (FePc) has been widely investigated as a precursor to prepare the ORR electrocatalysts. To date, however, the use of FePc has been limited by its weak electrocatalytic activity and insufficient durability when not embedded in carbon support via high temperature pyrolysis. Inspired by the high-quality and high surface area as well as the high ORR performance, we employed the N-GP950 as the support of FePc, forming FePc/N-GP950 composites with improved ORR performance as NPMCs. Traditional methods to synthesize NPMCs involve hazardous chemicals or high-temperature pyrolysis, leading to environmental and safety issues, particularly when scaling up. As such, exploration of low cost, straightforward and safe strategies to fabricate high-performance ORR catalysts is imperative. Herein, we report on slow evaporation, a cost-effective non-pyrolyzed approach, to assemble Fe-N-C catalyst as NPMCs by immobilizing FePc onto the surface of N-GP950. The FePc units disperse uniformly on the surface of N-GP950, and strong π-π electronic interactions emerge between FePc and N-GP950. Our optimized composite catalyst (FePc-33/N-GP950), with a loading of 33 wt% FePc, exhibits highly efficient ORR performance. Markedly, the FePc-33/N-GP950 displays the most significant current density at 0.8 V (5.0 mA cm^{-2}), which is comparable to 4.0 mA cm^{-2} of commercial Pt/C. The FePc-33/N-GP950 also displays excellent long-term durability with no obvious loss of activity after accelerated durability tests for 5000 potential

cycles. The present study offers a low-cost and straightforward strategy to design efficient and durable ORR catalysts for practical alkaline fuel cell applications and metal-air batteries.

Finally, we explored the electrochemical production of hydrogen, which is a promising and flexible approach towards the conversion of intermittent renewable energy sources into clean chemical fuel. However, low-cost, efficient, and durable electrocatalysts are yet to be developed to attain economies of scale in hydrogen generation. In this study, we fabricated highly ordered free-standing TiO_2 nanotube arrays (TiO_2-NTs), by simply anodizing Ti foils. The tube length, diameter, wall thickness, and surface structure of the TiO_2-NTs can be controlled by adjusting the anodization conditions. Subsequently, we synthesized and supported MoS_2 layers on free-standing TiO_2-NTs as an active material for the hydrogen evolution reaction (HER) using a slow evaporation method. The layers of MoS_2 uniformly disperse on the entire surface of the TiO_2-NTs composite. The electrochemical test shows that the MoS_2-supported free-standing (MoS_2/TiO_2-NTs) system exhibits excellent HER performance in acidic media with a low overpotential at 10 mA cm^{-2} (170 mV), as well as small Tafel slope (70 mV $decade^{-1}$). Also, the MoS_2/TiO_2-NTs displays superior durability for HER after 5000 continuous potential cycles between -0.4 and +0.2 (V vs. RHE). Our results demonstrate the potential of MoS_2/TiO_2-NTs composite for cost-effective electrochemical production of hydrogen.

Keywords

π-π interaction

Anodization

Dispersion

Electrochemical exfoliation

Free-standing

Graphene

Highly ordered

Pyridinic-N

Slow evaporation

TiO_2-nanotubes

Table of Contents

Acknowledgement ii
Résumé iii
Abstract vii
Keywords x
List of Figures xv
List of Tables xxi
List of Acronyms, Abbreviations, and Chemical Compounds xxii
List of Publications xxiv

Chapter 1 Introduction 1
1.1 General introduction 1
1.2 Abridged history of fuel cells 6
1.3 Fundamentals of Fuel cells 8
1.4 Types of fuel cells 10
1.5 Alkaline fuel cells 11
1.6 Oxygen reduction reaction 13
1.7 Electrocatalysts for the oxygen reduction reaction 14
  1.7.1 Precious metal-based electrocatalysts 14
  1.7.2 Non-precious metal-based electrocatalysts 18
  1.7.3 Metal-free carbon-based electrocatalysts 21
1.8 Hydrogen evolution reaction 22
  1.8.1 Steam-methane gas reformation 23
  1.8.2 Photoelectrochemical hydrogen evolution 24
  1.8.3 Electrochemical hydrogen evolution 25
1.9 Thesis objectives and organization 29
  1.9.1 Thesis objectives 29
  1.9.2 Thesis organization 29

Chapter 2 Experimental Methods 32
2.1 Synthesis techniques 32
  2.1.1 Electrochemical exfoliation of graphite 32
  2.1.2 Electrochemical fabrication of Titanium dioxide 34

2.1.3 Slow evaporation method 35
2.1.4 Solvothermal synthesis 36
2.2 Physical characterization methods 37
2.2.1 X-ray photoelectron spectroscopy 37
2.2.2 Transmission electron microscopy 38
2.2.3 Scanning electron microscopy 40
2.2.4 UV-visible electronic absorption spectroscopy 41
2.2.5 X-ray diffraction 43
2.3 Electrochemical characterizations 43
2.3.1 Rotating disk electrode 43
2.3.2 Rotating ring-disk electrode 45
2.3.3 Electrochemical cell setup 46
2.3.4 Linear sweep and cyclic voltammetry 47
2.3.5 Accelerated durability test 52
2.3.6 Chronoamperometry 52
2.4 Presentation of results 53

Chapter 3 Graphene-Based Metal Free Electrocatalyst for Oxygen Reduction 54
3.1 Introduction 54
3.2 Experimental 56
3.2.1 Materials. 56
3.2.2 Electrochemical exfoliation of graphite 57
3.3 Characterization of graphene 58
3.3.1 Physical characterization 58
3.3.2 Electrochemical characterization 59
3.4 Results and discussion 60
3.4.1 The electrochemical exfoliation of graphite 60
3.4.2 The structural morphology of graphene samples 62
3.4.3 The degree of oxidation in graphene 64
3.4.4 The surface chemical composition of graphene 65
3.4.5 The electrochemical properties graphene 67
3.5 Conclusions and perspectives 76

Chapter 4 Graphene-based Metal-Macrocycle Electrocatalyst for Oxygen Reduction 78
4.1 Introduction 78
4.2 Experimental 81
4.2.1Chemicals and materials 81
4.2.2 Preparation of graphene and N-doped graphene 81
4.2.3 Preparation of iron (II) phthalocyanine/N-doped graphene 82
4.3 Characterization of FePc/N-doped graphene 83
4.3.1 Physical characterization 83
4.3.2 Electrochemical characterization 83
4.4 Results and discussion 85
4.4.1 Preparation of FePc/N-doped graphene 85
4.4.2 Surface and structural morphology of FePc/N-doped graphene 85
4.4.3 The surface chemical composition of FePc/N-doped graphene 88
4.4.4 Electrochemical performance of FePc/N-doped graphene 90
4.5 Conclusions and perspectives 101

Chapter 5 Fabrication of MoS_2/TiO_2-Nanotubes for Hydrogen Evolution 103
5.1 Introduction 103
5.2 Experimental 106
5.2.1 Chemicals and Materials 106
5.2.2 Preparation TiO_2-nanotubes 106
5.2.3 Preparation of MoS_2 layers 107
5.2.4 Preparation of MoS_2-supported free-standing TiO_2-NTs 107
5.2.5 Preparation of hydrogen evolution electrodes 108
5.3 Characterization TiO_2 NTs and MoS_2/TiO_2-NTs 108
5.3.1 Physical characterization 108
5.3.2 Electrochemical characterization 109
5.4 Results and discussion 109
5.4.1 Electrochemical anodization of titanium 109
5.4.2 The structural morphology of TiO_2-nanotubes 112
5.4.3 Surface elemental composition of TiO_2-nanotubes 119
5.4.4 Synthesis of MoS_2-supported free-standing TiO_2-nanotubes 120

5.4.5 Hydrogen evolution reaction electrocatalytic activities 122
5.5 Conclusions and perspective 126

Chapter 6 Conclusions and recommendations 127
6.1 Conclusions 127
6.2 Recommendations 130
References 133
Appendix A Synopsis 157

List of Figures

Figure 1-1 The historical development of fuel cells. 6

Figure 1-2 Schematic presentation of energy conversion differences between fuel cells and combustion engines. 9

Figure 1-3 Schematic presentation of the PEMFC and AEMFC 12

Figure 1-4 Trends in oxygen reduction activity plotted as a function of the oxygen binding energy for different metal atoms 16

Figure 1-5 Schematic illustration of Pt-metal nanostructures (a) alloy and (b) core-shell 17

Figure 1-6 General structure of (a) metalloporphyrin and (b) metallopthalocyanine, where M is the central metal atom. 20

Figure 1-7 A sustainable pathway for the production and utilization of hydrogen energy 23

Figure 1-8 Schematic presentation of water electrolytic cells (a) photoelectrochemical based on n-type semiconductor, and (b) electrochemical process. 25

Figure 1-9 Volcano plot of exchange current density (j_o) as a function of DFT-calculated Gibbs free energy (ΔG_{H*}) of adsorbed atomic hydrogen on pure metals 27

Figure 1-10 Conceptual flow chart of the thesis. 31

Figure 2-1 Schematic view of steps in preparation of graphene and FePc/N-graphene composite, (A) an electrochemical cell setup for exfoliation of graphite and subsequent procedures, (B) the steps to obtain N-graphene (N-GP). 33

Figure 2-2 A scheme of fabrication of highly ordered TiO_2-nanotubes arrays by anodic oxidation of Ti substrate (a) anodization experimental setup, and (b) a typical SEM image of the as-anodized TiO_2-NTs. 34

Figure 2-3 schematic illustration of the immobilization of FePc on the N-doped graphene. 35

Figure 2-4 A schematic cross-section view of a Teflon-lined, stainless autoclave. 36

Figure 2-5 Principle of X-ray photoelectron spectroscopy (a) photoelectron generation caused by absorption of incoming light by a core electron, (b) a typical XPS survey spectrum of FePc/N-graphene. 38

Figure 2-6 Block diagram of a typical transmission electron microscopy. 39

Figure 2-7 Block diagram of key components of a typical UV-vis spectrometer. 41

Figure 2-8 Schematic presentation of the working electrode, (a) rotating disk electrode and (b) rotating ring-disk electrode. 44

Figure 2-9 Three-electrode electrochemical cell system. (a) A cell setup, and (b) block diagram of RRDE apparatus for a bipotentiostat. 46

Figure 2-10 Line sweep voltammetry measurement. (a) Excitation of linear sweep voltammetry, (b) typical linear sweep voltammogram of reduction of electroactive species for stationary electrode. (c) Characteristic ORR polarization curve of Pt/C recorded by RDE system with the electrode rotation rate of 2000 rpm.......................................47

Figure 2-11 Schematic presentation of the oxygen reduction reaction processes on a rotating ring-disk electrode. 49

Figure 2-12 Cyclic voltammetry measurement. (a) Cyclic potential scan, (b) a resulting cyclic voltammogram of electroactive species for stationary electrode, (c) a typical cyclic voltammogram of Pt/C in 0.1 M KOH recorded at a scan rate of 50 mV s^{-1}. 51

Figure 3-1 Schematic illustration of the setup for the electrochemical exfoliation production of graphene, and the exfoliation mechanism in aqueous $(NH_4)_2SO_4$ solution. 58

Figure 3-2 Digital image of the experimental setup and foil substrates before and after the electrochemical exfoliation experiment in 1.0 M $(NH_4)_2SO_4$ solution. (a) Before an exfoliation begins, (b) after exfoliation using bias of -10 V and (c) after exfoliation of a graphite foil using +10 V bias potential. Complete exfoliation of graphite foils was observed only when the positive static biased potential applied or alternation to the bias potentials (±10 V). 61

Figure 3-3 TEM images and selected area electron diffraction (SAED) of typical graphene samples exfoliated from graphite foils and plates. (a-c) Graphene of graphite foil (GPf). (d-e) Graphene of graphite plate (GP). (c-d) TEM images of N-doped graphene. (a-b) SEM images of GP at low magnification. Few-layers characterize the graphene from both graphite substrate, uniform, have a well-defined crystalline structure, and large sized. 63

Figure 3-4 UV-vis absorption spectra are showing absorption peaks of the graphene samples prepared in 0.1 M $(NH_4)_2SO_4$ electrolyte containing different doses of organic reducing agent 2,2,6,6-Tetramethylpiperidine-1-oxyl (TEMPO). The reducing agent was added to reduce part of the functional groups introduced during exfoliation....64

Figure 3-5 XPS spectra of graphene exfoliated from a graphite plate (GP) (a) survey of as-exfoliated GP and N-doped graphene (N-GP950) and high-resolution C 1s spectrum (b) as-exfoliated GP and (c) N-GP950, and (d) high-resolution N 1s spectrum of the N-GP950. 66

Figure 3-6 ORR polarization curves of (a) as-exfoliated graphene from graphite foil (GPf, black line) and graphite plate (GP, red line), and N-doped graphene (N-GP950, blue line), (b) The calculated electron transfer number, and peroxide production in the three catalysts. The measurements were carried out in N_2, or O_2 saturated 0.1 M KOH, scan rate: 10 mV/s at 1600 rpm. Showing the electrocatalytic activities towards ORR...68

Figure 3-7 Influence of exfoliation electrolyte temperature on the ORR activity of graphene. (a) Digital images of as-exfoliated graphene products (in the beakers) and their corresponding graphite substrates after 5 minutes of exfoliation at 22, 40, 60 and 80 ºC, respectively. (b) ORR polarization curves ranging from 0 - 1.0 V of the graphene exfoliated at different electrolyte temperature, followed by pyrolysis in Ar at 1050 ºC for 1 hour and NH_3 at 950 ºC for 15 minutes. The corresponding calculated (c) electron transfer number and (d) peroxide produced for the catalysts. Electrolytes: 0.1 M KOH, scan rate: 10 mV/s and rotation: 1600 rpm. 71

Figure 3-8 Tafel plots for ORR of N-doped graphene samples exfoliated at four different electrolyte temperatures; 22, 40, 60 and 80 ºC, respectively. 72

Figure 3-9 The ORR polarization curves of N-GP catalysts. (a) With different layers, (b) after different temperatures of pyrolysis in NH_3, (c) sonication for a different duration. (d) Exfoliated in 0.1 M and 1.0 M $(NH_4)_2SO_4$ electrolytes. All LSVs measurements were carried out in 0.1 M KOH media, scan rate: 10 mV/s, rotation speed: 1600 rpm. 74

Figure 3-10 Long-term performance of the catalysts (before and after ADT test, 5000 cycles). LSVs (a) few layer N-GP950 and (b) 20% Pt/C recorded at 10 mV s^{-1} and1600 rpm in O_2-saturated 0.1 M KOH at room temperature. Showing the stability of electrocatalysts toward ORR...76

Figure 4-1 Schematic view of preparation of FePc/N-GP950 catalyst. The setup of electrochemical exfoliation of graphite (part A) and immobilization of iron (II) phthalocyanine (FePc) into the graphene and nitrogen-doped graphene (part B). ...82

Figure 4-2 TEM images of (a, b) as-exfoliated graphene (GP) and (c, d) N-doped graphene (N-GP950). The as-exfoliated graphene and N-GP950 are very thin and have a uniform morphology with a well-defined crystalline structure. 86

Figure 4-3 TEM images of (a) N-doped graphene (N-GP950), (b) the aggregation of FePc of size ca. 165 nm, (c) FePc-16/N-GP950, (d) FePc-33/N-GP950, (e) FePc-50/N-GP950, and (f) energy dispersive spectroscopy of the N-GP950 and FePc-33/N-GP950. The FePc successfully loaded and homogeneously distributed on the surface of N-GP950. ...87

Figure 4-4 XPS analysis to elucidate the electronic properties of N-doped graphene (N-GP950), FePc, and FePc-33/N-GP950. (a) Survey spectra. High-resolution spectra of (b) Fe 2p and (c) N 1s, and (d) the nominal composition of N-species in the catalysts. (e) A high-resolution C 1s spectra of the N-GP950, FePc, and FePc-33/N-GP950, indicating various forms of carbons. 90

Figure 4-5 Electrochemical performance of FePc, N-GP950, FePc-33/N-GP950, and 20% Pt/C catalysts. (a) CV curves of the catalysts in N_2 (dot lines) and O_2 (solid lines) recorded using a scan rate of 50 mV s^{-1}, (b) ORR polarization curves of the catalysts, (c) corresponding electron transfer number and H_2O_2 yield, and (d) the Tafel plots of the catalysts. The RRDE measurements recorded with scan rate: 10 mV s^{-1}, and the disk rotation rate of 1600 rpm. 91

Figure 4-6 ORR performance of prepared catalysts. The LSVs of catalysts (a) FePc-33/N-GP950 catalysts prepared with different FePc loading 16, 33, 50, and 100 wt%, (b) correlation between content of FePc (wt %) and ORR activity at 0.8 V, (c) the LSVs of as-exfoliated GP and a composite of 33 wt% FePc and as-exfoliated GP (FePc-33/GP), and (d) composite of 33 wt% FePc, and N-doped Hummer’s method exfoliated graphene (FePc-33/N-rGO) and the FePc-33/N-GP950. Electrolyte: 0.1 M KOH, scan rate: 10 mV s^{-1}, RRDE rotation: 1600 rpm. 95

Figure 4-7 The linear sweep voltammograms of N-GP950, N-rGO, FePc-33/GP950, and Pc-33/N-GP950. (a) N-rGO and N-GP950, (b) GP950, FePc-33/GP950 and FePc-33/N-GP950, and (c) 33 wt% phthalocyanine (Pc-33)/N-GP950 and FePc-33/N-GP950. The LSVs recorded using 10 mV s^{-1} and working electrode rotation of 1600 rpm in the O_2-saturated 0.1 M KOH at room temperature. The Pc-33/N-GP950 displayed the lowest activity towards ORR, indicating the Fe in FePc plays a key role in the ORR process...98

Figure 4-8 ORR electrochemical performance of the pyrolyzed FePc-33/N-GP950 (a) the LSVs (b) the corresponding electron transfer number, and H_2O_2 yield. Electrolyte: 0.1 KOH, the scan rate of 10 mV s^{-1}, the electrode rotation speed of 1600 rpm. The activity of the FePc-33/N-GP950 significantly lost after pyrolysis in argon...........99

Figure 4-9 LSVs recorded before and after 5000 cycles ADT test between 0.6 to 1.0 V using scan rate 10 mV s^{-1} and working electrode rotation of 1600 rpm in O_2-saturated 0.1 M KOH for (a) FePc-33/N-GP950 and (b) 20% Pt/C, (c) CV curves of FePc-33/N-GP950 before and after ADT test recorded in N_2-saturated 0.1 M KOH. (d) Chronoamperometric responses (at 0.8 V vs. RHE) of FePc-33/N-GP950 and 20 wt% Pt/C catalysts in O_2-saturated 0.1 M KOH. 100

Figure 5-1 A scheme of fabrication of highly ordered TiO_2 nanotubes arrays (a) anodization experimental setup, (b) *I-t* response during anodization process, and (c) the appearance of anodized Ti substrate after drying and annealing. 110

Figure 5-2 Structural morphology of as-anodized TiO_2-NTs, (a) SEM images of a longitudinal section of free-standing TiO_2-NTs with a closed bottom up, (b) a top view of bottom morphology of the nanotubes, (c) top view morphology. TEM images (d) interspacing between the individual nanotubes, anodized under ice bath, (e) cross-section and its selected area electron diffraction (SAED) pattern as an inset, and (f) high-resolution image of the nanotube prepared at room temperature. 112

Figure 5-3 SEM images of TiO_2 nanostructures formed during anodization of electropolished Ti substrate in EG containing 0.3 wt% NH4F and 2 wt% deionized water, (a) cross-section view of spindle bundles, and (b) top view. 114

Figure 5-4 SEM images of TiO_2 nanotubes, showing the evolution of morphologies with different anodization conditions. (a-d) effect of length of anodization period, and (e-f) effect of the substrate etching on the nanotube surface textures. 115

Figure 5-5 TEM images of the TiO_2-NTs prepared by anodization of Ti substrate, in EG containing 0.3% NH_4F and 2 wt% water, for 7 hours at (a-b) 0 °C, (c) 22 °C, and (d) 50 °C. 117

Figure 5-6 The structure of the annealed TiO_2-NTs. (a) The TEM image of annealed at 450 °C for 2 hours, (b) selected area electron diffraction (SAED), (c) HRTEM image of anatase phase TiO_2-NTs. (d XRD spectra of crystalline TiO_2-NTs array obtained by subjecting the as-anodized sample in hot water steam, and annealed at 450 °C for 2 hours in an air oven, with their corresponding characteristic powder diffraction pattern, for anatase TiO_2 JCPDS: 21-1272. The XPS spectra of the annealed TiO_2-NTs, (e) Survey spectrum, (f) high-resolution Ti 2p, and (g) high-resolution O 1s. 119

Figure 5-7 Fabrication scheme, structure, and chemical composition of the MoS_2 and $MosS_2/TiO_2$-NTs catalysts. (a) Scheme of fabrication of MoS_2/TiO_2-NTs. TEM images of (b) MoS_2, (c) MoS_2/TiO_2-NTs, (d) High resolution TEM of MoS_2/TiO_2-NTs. (e) High-resolution TEM of MoS_2/TiO_2-NTs with a marked area of reduced fast Fourier transform (FFT), (f) FFT image MoS_2/TiO_2-NTs showing the diffraction spots from anatase MoS_2 and TiO_2-NTs, (g) The XRD pattern of MoS_2 and MoS_2/TiO_2-NTs. 121

Figure 5-8 Morphology and elemental composition of catalysts. (a) The electron diffraction spectra of the MoS_2 and MoS_2/TiO_2-NTs showing the elemental composition. (b) High-resolution TEM of MoS_2/TiO_2-NTs indicating respective areas of the energy dispersive X-ray. No adventitious impurity detected from the sample..................122

Figure 5-9 The hydrogen evolution reaction activity of TiO_2-NTs, MoS_2, MoS_2/TiO_2-NTs, and 20 wt% Pt/C (a) The polarisation curves obtained with catalysts, and (b) corresponding Tafel plot recorded on glassy carbon with catalysts loading 0.8 mg cm^{-2} at a scan rate of 10 mV s^{-1} in the 0.5 M H_2SO_4. (c) The polarisation curves recorded on carbon fiber paper (CP) with a similar scan rate and loading for the MoS_2/TiO_2-NTs. (d) The polarisation curves of MoS_2 and MoS_2/TiO_2-NTs on CP recorded in a 1.0 M KOH solution with a similar scan rate. (e) The polarisation curves of MoS_2/TiO_2-NTs composite on CP recorded before and after durability test. Negligible HER current lost after 5000 potential cycles between -0.4 and +0.2 (V vs. RHE) at 100 mV s^{-1}..123

List of Tables

Table 1-1 Comparison of different types of fuel cells 11

Table 1-2 Thermodynamic electrode potentials of oxygen reduction reactions 14

Table 3-1 The ORR performance of recent metal-free electrocatalysts. The electrochemical evaluation was carried out in O_2-saturated 0.1 M KOH, scan rate: 10 mV s^{-1} and disk rotation rate: 1600 rpm. 69

Table 3-2 The ORR performance of N-doped graphene exfoliated from graphite plate at different temperatures. The electrochemical evaluation was carried out in O_2-saturated 0.1 M KOH, scan rate: 10 mV s^{-1} and disk rotation rate: 1600 rpm...72

Table 4-1 The ORR performance of N-doped graphene and recent FePc-based electrocatalysts. The electrochemical evaluation was carried out in O_2-saturated 0.1 M KOH, scan rate: 10 mV s^{-1} and disk rotation rate: 1600 rpm. 92

Table 4-2 The correlation of ORR performance and the percentage of FePc loading in the FePc/N-GP950. The electrochemical evaluation was carried out in O_2-saturated 0.1 M KOH, scan rate: 10 mV s^{-1} and disk rotation rate: 1600 rpm...96

List of Acronyms, Abbreviations, and Chemical Compounds

$(NH_4)_2SO_4$	Ammonium sulfate
1D	One-dimensional
ADT	Accelerated durability test
BE	Binding energy
CV	Cyclic voltammetry
$E_{1/2}$	Half-wave potential
EDS	Energy dispersive spectroscopy
EG	Ethylene glycol
E_{onset}	Onset potential
FePc	Iron phthalocyanine
FePc/N-GP950	A composite of iron phthalocyanine and N-doped graphene
FePc-33/N-GP950	33 wt% iron phthalocyanine in the FePc/N-GP950
GC	Glassy carbon
GP	Graphene exfoliated from graphite plates
GPf	Graphene exfoliated from graphite foils
HER	Hydrogen evolution reaction
HRTEM	High-resolution transmission electron microscope
j_{L}	Diffusion-limited current density
LSV	Linear sweeping voltammetry
M-N-C	Metal-nitrogen-carbon
MoS_2/TiO_2-NTs	Molybdenum sulfide/titanium dioxide nanotubes composite
N-GP	N-doped graphene exfoliated from graphite plate

N-GP950	N-doped graphene obtained by pyrolysis in NH_3 at 950 ºC
NH_4F	Ammonium fluoride
NPMCs	Non-precious-metal electrocatalysts
ORR	Oxygen reduction reaction
Pc	Phthalocyanine
PEMFC	Polymer electrolyte membrane/proton exchange membrane fuel cell
RDE	Rotating ring-disk electrode
RHE	Reversible hydrogen electrode
rpm	Revolutions per minute
RRDE	Rotating ring-disk electrode
SAED	Selected area electron diffraction
SCE	Saturated calomel electrode
SEM	Scanning electron microscopy
TEM	Transmission electron microscopy
TEMPO	2,2,6,6-Tetramethyl-1-piperidinyloxy
TiO_2-NTs	Titanium dioxide nanotubes
Uv-vis	Ultraviolet–visible spectroscopy
XPS	X-ray photoelectron spectroscopy
XRD	X-ray diffraction

List of Publications

1. **N. Komba**, Q. Wei, G. Zhang, F. Rosei, S. Sun, Controlled Synthesis of Graphene Via Electrochemical Route and Its Use as An Efficient Metal-free Catalyst for Oxygen Reduction. *Applied Catalysis B: Environmental* 243 (2019) 373–380.

2. **N. Komba**, G. Zhang, Q. Wei, J. Prakash, R. Chenitz, F. Rosei, S. Sun, Iron (II) Phthalocyanine/N-doped Graphene: A Highly Efficient Non-Precious Catalyst for Oxygen Reduction. *Accepted to International Journal of Hydrogen* Energy 44 (2019) 18103-18114.

3. **N. Komba**, G. Zhang, Z. Pu, M. Wu, F. Rosei, S. Sun, MoS_2-Supported Free-Standing TiO_2-Nanotubes for Efficient Hydrogen Evolution Reaction. *Manuscript in preparation*.

Chapter 1 Introduction

1.1 General introduction

The impact of human activities on the environment is deeply rooted in the current combustion dominated energy generation technologies. These technologies of combustion of high gravimetric energy density fossil fuels are harmful to the environment and raise rise many global concerns, such as climate change, and acidic rains. The energy reliance on finite and diminishing world supplies of fossil fuels for energy is also is a threat to energy security and other global vulnerabilities [1, 2]. On account of ever-increasing energy consumption and demands, exploration for a new, clean, and sustainable energy conversion sources as a replacement of combustion-based energy sources attract significant attention. This search includes options for clean and sustainable energy conversion and storage processes, where electrochemical process is one of the most promising and exciting.

Electrochemical reactions in devices such as fuel cells (FCs) and batteries provide an efficient and clean mechanism for energy conversion and storage. In particular, FCs attract significant attention in sustainable development and energy security because of their compatibility with renewable sources of energy carriers such as hydrogen and lower hydrocarbon alcohols. The advantages of FCs as future power generator include high efficiency and high energy density, and quiet operation, inherent stack modularity, and zero or low emissions [3]. As a result, FCs have a diverse range of applications covering small, stationary, and backup power, portable electronics, transportation, and power grid-scale systems [2-4]. Small, stationary power generators can provide 0.5 kW to 10 kW uninterrupted power supply to households, shopping malls, and data centers. Portable electronics include an auxiliary power units (APU), mobile devices, computers, and smart-phones, etc.

Moreover, the use of low-temperature FCs in transportation represents the future for the automotive industry. Indeed, buses, light vehicles (cars), and trains will soon be running on FCs [1].

In low temperature FCs, at the anode hydrogen is oxidized on the surface of the catalyst to produce electrons and protons. Electrons are then transferred to the cathode through an external circuit while protons are crossing the electrolyte medium. At the cathode, oxygen is reduced upon receiving electrons and promptly reacts with protons to produce water. Both of the half-reactions, at the anode and cathode, require active catalysts to promote the reaction rates of the hydrogen oxidation reaction (HOR) at anode and the oxygen reduction reaction (ORR) at the anode. The known active catalyst layers consist of platinum (Pt) nanoparticles dispersed on the carbon black (Pt/C). The Pt-surfaces exhibit fast HOR electrode kinetics; thus, the anode Pt-loading can be scaled-down as low as 0.05 $\mathrm{mg_{Pt}\ cm^{-2}}$ without compromising the performance [5-7].

Conversely, the ORR at the cathode is particularly challenging as they involve complex 4 electrons transfer mechanism. As a result, the ORR kinetics are very slow and highly irreversible [8, 9]. Thus, highly efficient ORR electrocatalysts are needed to drive the FCs. Pt-based materials have been widely used as ORR electrocatalysts for decades. For example, Pt/C as ORR electrocatalyst were used in alkaline FCs in the early 1960s for the Apollo lunar mission [10, 11]. However, owing to the sluggish kinetics, ORR needs much higher Pt loading (~0.4 mg $\mathrm{cm^{-2}}$) to achieve desirable performance in FCs.

However, the high cost and limited supply of Pt hamper the large-scale commercial application of FCs. Also, Pt-based materials suffer from time-dependent activity [12, 13] and CO poisoning effects [14, 15]. Therefore, considerable efforts have been directed towards (i) development of highly active and durable Pt-based materials with decreased Pt content by engineering Pt nanostructures with exposed high surface area [16], using alloys of Pt and low-cost metals [6, 17] or novel Pt support materials [18-20]; and (ii) replacing Pt-based catalysts with high-performance and low-cost, metal-free catalysts [21] and non-precious metal catalysts (NPMCs) [22, 23]. In the latter group, carbon-based nanomaterials have attracted worldwide attention. The use of these materials as alternative ORR catalysts, could significantly reduce the cost and increase the efficiency of fuel cells [20-25]. In particular, N-doped carbon materials and transition metal-nitrogen-carbon (Me-N-C, Me = Fe, Co, Cu, Ni, Mn, etc.) are widely studied as metal-free and NPMCs, respectively in acidic and alkaline media. These materials exhibit high activity and excellent durability in addition to good alcohol and CO tolerance [25-30].

Recently, graphene, an emerging class of material has attracted significant attention for ORR electrocatalysis as metal-free electrocatalysts [31], NPMCs [32] or support material [33-35] owing to their unique physicochemical properties, such as large surface area, high electronic conductivity, and excellent chemical stability [26]. These unique properties are observed when the quality of the graphene is high having few layers and low degree of oxidation. However, methods to fabricate high-quality graphene on a large scale are limited. Nevertheless, among the many methods reported for the production of graphene, the electrochemical approach is appealing because it is not only environmentally friendly, simple, and straightforward, but also avoids the adventitious contamination of graphene from metallic atoms. Furthermore, this method allows control over the degree of oxidation and thus allows the tuning of the surface functional groups while conserving the majority of the intrinsic properties of graphene. Moreover, the as-exfoliated graphene can be doped with a heteroatom(s) to further enhance ORR electrocatalytic activity further. As such, the electrochemical is the most versatile approach to produce graphene in the quest for the developments of new ORR electrocatalysts.

On the other hand, the realization of meaningful utilization of FCs and energy relies on the supply of hydrogen or other fuels from renewable conversion processes. Hydrogen, with the highest gravimetric energy density chemical fuels (142 MJ kg^{-1}, upper heating value), is considered as the ultimate clean energy carrier, which would significantly mitigate the environmental concerns due to zero emission of carbonaceous species in its use [36]. At present the primary source of hydrogen production is the steam reforming of fossil fuels, which is both energy intensive and emits greenhouse gases in the process [36, 37]. It remains a challenge to produce hydrogen sustainably and achieve economies of scale. Among the other hydrogen-producing means, electrochemical water splitting through hydrogen evolution reaction (HER) presents the most promising option. The HER process is a straightforward and clean route to produce H_2. Nevertheless, the high-performance catalyst for the HER is needed to overcome the overpotential of water reduction and consequently boost the efficiency of this critical electrochemical process.

Currently, the most effective HER electrocatalysts are the precious metals Pt-based material. Unfortunately, rarity, high-cost, and instability of Pt-based materials seriously impede large-scale utilization of the technology [38]. Thus, the search for alternative electrocatalysts from low-cost earthly-abundant elements to replace the precious Pt-group metals is a central research topic for energy conversion. Several classes of transition metals-based materials are currently widely investigated as HER electrodes due to their high catalytic activity. The most promising transition metal-based HER electrodes include alloy ($MoNi_4$) [39, 40], chalcogenides (MoS_2, CoS_2, $CoSe_2$) [41-43], carbides (WC, Mo_2C, Ni_2C) [44, 45], phosphides (Ni_2P, CoP) [46], and oxides (TiO_2, $SrTiO_3$, WO_3, Fe_2O_3, ZnO) [47-50]. Even though most of these materials are active towards the HER, the synthesis methods involving complicated steps impede the scaling-up. However, despite progress made, further studies are highly desirable to develop a scalable and simple route for low-cost HER electrodes. In this section, we devote our effort to fabricate TiO_2-NTs arrays by electrochemical method and use as a support to prepare MoS_2/TiO_2-NTs robust HER electrodes. Our research is driven by TiO_2-NTs unique physical-chemical properties higher surface-to-volume ratio, low-cost and abundance.

Specifically, in this thesis, we first focus on the development of low-cost graphene-based new materials as metal-free and non-precious metal electrocatalysts for ORR by using scalable, and simple, straightforward, and environmentally friendly approaches. The development and use of such materials in a quest to reduce the prohibitive price of FCs. Firstly, we prepared thin and large sheets of high-quality graphene by electrochemical exfoliation of graphite foil and plates. As metal-free electrocatalysts, the graphene (GP) samples exfoliated from the graphite plate exhibited higher activity towards ORR than those of graphene samples (GPf) from graphite foil. Our results show that the ORR activity of the catalysts varied significantly with the exfoliating and post-exfoliation conditions. The optimal N-doped graphene (N-GP950) exhibits comparable ORR performance to commercial Pt/C catalysts. The current density of the N-GP950 at 0.8 V was six times higher than the as-prepared GP with excellent durability for about 5000 potential cycles between 0.6 and 1.0 (V vs. RHE) [51]. For the graphene-based NPMCs, we supported iron II phthalocyanine (FePc) on an optimized sample of N-doped graphene (N-GP950). The transmission electron microscopy characterization of the FePc/N-GP950 revealed that the FePc molecules are highly dispersed on the surface of N-GP950. We also demonstrated that the high dispersion of FePc is the fate of the electronic interaction between the FePc molecules and the support material, the N-GP950.

Consequently, the FePc/N-GP950 exhibited high ORR performance better than state of the art, commercial catalysts Pt/C. Secondly, we focused on the zero-emission spectrum for running the FCs from the standpoint of the production of the fuels. Without sustainable approaches to producing hydrogen, all advantages of FCs to the environment would dwindle. Equally, we consider that it is urgent to develop a cost-effective and scalable HER electrodes. Therefore, our second focus is to prepare and study the physical and chemical properties of MoS_2/TiO_2 nanotubes as one kind of NPMCs for electrochemical hydrogen evolution.

1.2 Abridged history of fuel cells

The concept of FC has been around for about 200 years. Figure 1-1 shows some historical development of the FCs in the past two centuries. The principles of what is known today as FC was demonstrated for the first time by Humphry Davy as early as the 1800s. This was then followed by pioneering work of Christian Friedrich Schönbein in ca.1838 on what were to become FCs [52-54]. In 1839 British chemist, physicist, and lawyer, Sir William R. Grove demonstrated the generation of electricity from an electrochemical reaction for the first time by reversing the electrolysis of water from what he termed a gaseous voltaic battery [2, 4].

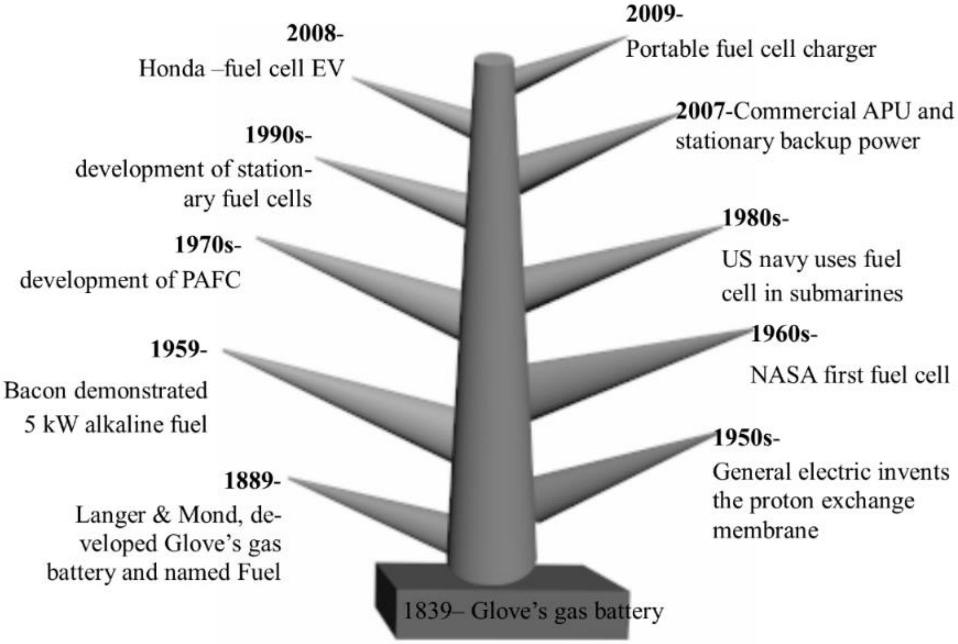

Figure 1-1 The historical development of fuel cells.

The gaseous voltaic battery proved that the chemical energy stored in hydrogen and oxygen bonds could directly convert into electricity at the surface of Pt catalysts in a sulphuric acid electrolyte. Glove is considered as the “father of the FCs” for this invention. Late in the 1880s, Ludwig Mond and Charles Langer further developed Glove’s device and named it fuel cell in their attempt to engineer the first practical FC using air and coal gas [10, 52, 53]. In their design, a porous non-conducting diaphragm impregnated with dilute sulphuric acid acted as the electrolyte. The perforated leaves of Pt was coated with a thin film of Pt black electrodes [54]. With this cell, a current density of 6.5 mA cm^{-2} at the potential of 0.73 V was obtained. In the 1900s, FCs became a subject of intensive research and development but the invention of the combustion engines caused further development of FCs to be stagnant.

In the 1930s Francis Bacon at Cambridge University adopted Mond and Langer’s 1889 concept of the FC to design a system which uses potassium hydroxide solution of as the electrolyte and nickel gauze as electrodes [52]. By the end of the 1950s, Bacon developed a 40-cell stack FC capable of generating 5 kW. The stack was able to power a welding machine, circular saw, and forklift [55]. Bacon's FCs attracted much attention during this time.

In the early 1960s, Pratt & Whitney acquired the license of Bacon work to construct alkaline FCs to power the Apollo spacecraft [10, 55]. Following on, the National Aeronautics and Space Administration (NASA) developed FCs powered spacecraft to ideally supply both electricity and drinking water for the astronauts. Additionally, when the FCs devices was used in the electrolysis mode, it produced breathable oxygen and rocket fuel, hydrogen. The development of FCs in the 1960s is marked by the invention of the polymer as solid electrolytes at General Electric through the work of Thomas Grubb and Leonard Niedrach. Initially, sulfonated polystyrene membranes were used as solid electrolytes in the frontrunner of polymer electrolyte membrane fuel cells (PEMFCs) and soon later replaced by Nafion® membranes in 1966 [52]. These Nafion® membranes remain popular and are in use until today owing to their proven superiority performance and durability.

The oil crisis and increasing environmental awareness in the 1970s further boosted the development of the FCs. The goal for zero emission and energy efficiency became the primary driving forces for FCs adoption in the subsequent decades, in addition to the concurrent calls in climate change and energy security [52]. Many automobile manufacturers and their partners in German, Japanese USA, and Canada began developing FCs powered vehicles by increasing the power density of PEMFC stacks and developing hydrogen fuel storage systems. During the 1980s and 1990s, most automobile manufacturers had demonstration models of hydrogen fuel cell powered vehicles. The world's first demonstration of FC vehicle was a 10-meter transit bus developed in 1993 by the Canadian company Ballard Power Systems [52]. Taken together, these significant developments revolutionized FCs and placed hydrogen in an excellent position as the next energy carrier or fuel for the economy of the world.

1.3 Fundamentals of Fuel cells

FCs are electrochemical energy devices, which can convert the chemical energy stored in chemical bonds (fuels) directly into electrical energy without combustion process. The electrochemical reaction takes place at the two separated electrodes, electrochemical oxidation of fuel at the anode and electrochemical reduction of the oxidant at the cathode. The electrons pass through the external circuit to provide electricity. Conventionally, most FCs consume hydrogen (or hydrogen-rich fuels) and oxygen (or air) to generate electricity, as depicted in the chemical reaction Equation 1-1.

$$2H_2 + O_2 \longrightarrow E + H_2O \tag{1-1}$$

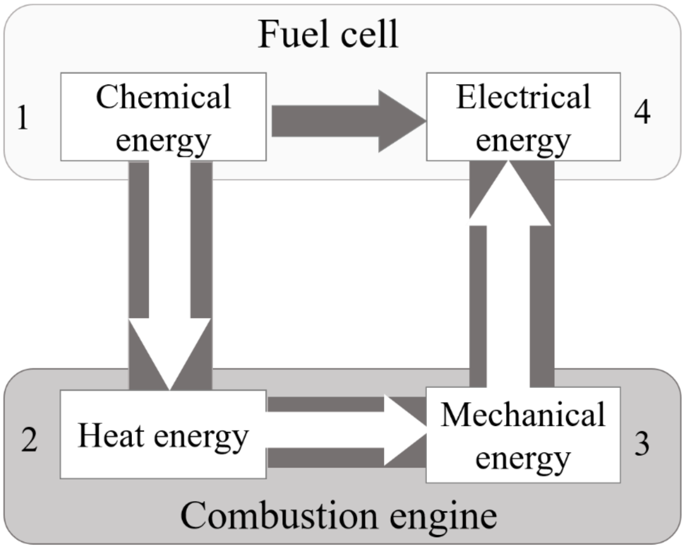

Figure 1-2 Schematic presentation of energy conversion differences between fuel cells and combustion engines.

As FCs generate electricity directly from chemical energy (Figure 1-2), rather than heat or mechanical energy, they are not limited by the Carnot cycle and can theoretically reach higher efficiencies. Accordingly, the FCs are more efficient in extracting energy from a fuel. Under the reasonable operating condition, the efficiency of the fuel cell can be up to 60 % or higher, which is 2-5 times to that of internal combustion engines [2, 56, 57]. Furthermore, as the only by-product in operation is water, and no greenhouse gases, FCs present very clean and environmentally friendly energy conversion technology. Another great appeal of the FCs is that the waste heat is produced, it can also be harnessed, boosting system efficiency even further. Unlike batteries which need to be recharged and have a limited operating time, FCs will run as long as fuel is provided, making these devices particularly attractive for long-range transportation. However, FCs and batteries can be complementary technologies in transportation, where the former serves long-distance and heavy-duty vehicles, and the latter works for short-range and light-duty utility vehicles or urban transport. Also, utilization of FCs and batteries as hybrid system are more attractive to boosting the power.

1.4 Types of fuel cells

Primarily, FCs are classified according to the kind of electrolyte employed. This classification determines the characteristics and applications of these cells. Currently, there are a number of FCs; each with its advantages, limitations, and potential applications. These types are PEMFCs, phosphoric acid fuel cells (PAFCs), molten carbonate fuel cells (MCFCs), solid oxide fuel cell (SOFCs) and alkaline Fuel Cells (AFCs) [56, 57]. Table 1-1 lists the types of FCs. The FCs listed in Table 1-1, can also be divided into two broad groups: low-temperature, PEMFCs (50 – 100 ºC), AFCs (90 – 100 ºC), PAFCs (150 – 200 ºC) and high-temperature, MCFCs (600 °C) and SOFCs (1000 °C). These high-temperature ones can supply enough heat for internal reforming process, thus utilizing the waste heat. The PEMFC and AFC and which operates at rather low temperatures are best suited for transportation or domestic applications. AFCs are one of the first FC technologies to be developed, and they were the first type to be widely used in the U.S. space program to produce spacecraft electrical energy and onboard water [11, 52].

Table 1-1 Comparison of different types of fuel cells [57]

Types of fuel cells	Fuel(s)	Mobile phase	Working Temperature (°C)	Power level (kW)	Electrical efficiency (%)	Start-up	Area of application
Alkaline (AFCs)	H_2	OH^-	90 – 100	10 - 100	>60	Fast	• Backup • Space • Mobile • military
PEMFCs	H_2	H^+	50 - 100	0.01 - 1000	53 - 58	Fast	• Transport • Mobile portable
Phosphoric acid (PAFCs)	H_2	H^+	150 -200	100 - 5000	>40	Moderate	• Distributed generation
Molten carbonates (MCFCs)	H_2	CO_3^{2-}	600 - 700	1000 - 100,000	45 - 47	Slow	• Power station
Solid oxides (SOFCs)	H_2/CO	O^{2-}	600 - 1000	100 -100,000	35 - 43	Slow	• Auxiliary power • Power station

1.5. Alkaline fuel cells

Traditionally, AFCs used an aqueous solution of potassium hydroxide (30 - 45 wt. %) as the electrolyte. The oxygen reduction kinetics are much faster in alkaline electrolyte than in acid, making the AFC a desirable system for future energy conversion devices. However, the use of concentrated hydroxide as an electrolyte restricts the application of AFCs to CO_2-free condition in the fuel and oxidant. Thus, in the more extended operation of AFCs requires the use of high purity of feeds, which adds the cost. The higher open circuit potential of the cell can induce oxidation of CO_2 to carbonates. The formation and accumulation of carbonates can destroy the electrolyte, which is one of the most challenging issues in AFCs. As a part of the solution in the recent advancement of AFCs, a polymer electrolyte has been under development as an anion exchange membrane (AEM) [58]. On the other hand, much of the interest in the anion-exchange membrane fuel cells (AEMFCs) comes from the expectation that can overcome the existing cost barrier inherent to the PEMFCs [59, 60]. In principle, alkaline electrolyte allows for the use of non-precious metal catalysts, which in turn dramatically reduces the cost per kilowatt of power in fuel cell devices [60, 61]. The construction of AEMFCs is similar to conventional PEMFCs except that they use an alkaline-based membrane instead of an acid-based membrane. The scheme shown in Figure 1-3 indicates that both FCs consists of anode, cathode, electrolyte membrane, and an external circuit. In both cells, the central component is the membrane electrode assembly (MEA), in which the electrolyte membrane is sandwiched between the two electrodes, anode, and cathode. The electrolyte membranes separate the gas reactants at either side and conduct protons (in PEMFCs) or OH$^-$ and water (in AEMFCs). However, in AEMFC technology, hydroxyl anions diffuse continuously across the electrolyte from the cathode to the anode while water diffuses the opposite direction [60]. On the other hand, water, which is estimated to be much higher than in PEMFCs per electron transfer, is both produced at the anode and as a reactant at the cathode.

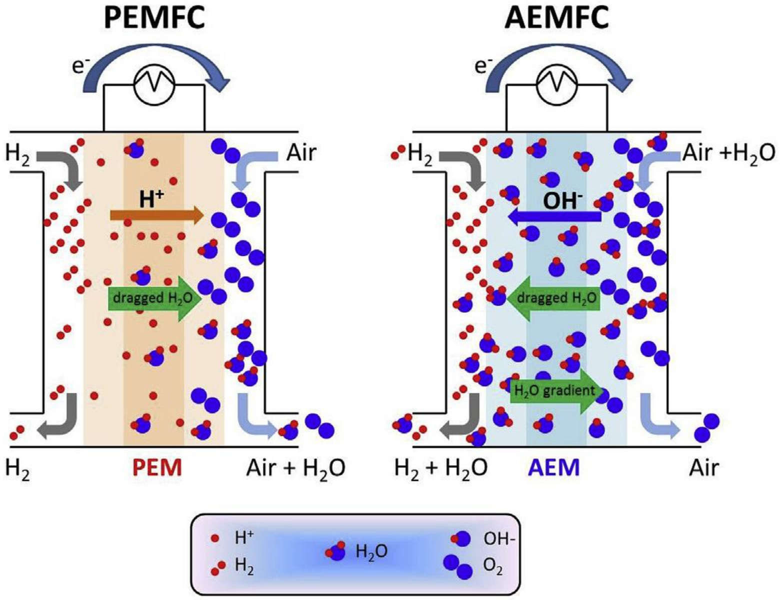

Figure 1-3 Schematic presentation of the PEMFCs and AEMFCs [60].

Apart from allowing the use of low-cost non-precious metals catalysts at the anode and cathode, equally, the AFCs demonstrated high performance and efficiency above 60% (Table 1-1) for the practical applications [10]. However, despite advantages, in development AFCs faced stiff competition from other types of fuel cells since their inception. This is because AFCs demand high purity hydrogen gas and still rely on the expensive Pt catalysts. Other barriers to the development of AFCs technology related to poor chemical stability and low ion conductivity of the hydroxide-conducting polymer [59, 60]. However, with the availability of AEMs, notwithstanding not as satisfactory as commercial PEMs and still in development stages, the investigation on metal-free and NPMCs becomes meaningful.

1.6 Oxygen reduction reaction

The ORR is a fundamental process in FCs and other energy converting systems such as metal-air batteries. The ORR is a cathodic process that plays a critical role in the overall performance of the FCs. Table 1-2 summarizes the ORR mechanism in aqueous solution. The ORR is a multi-electron reaction, depending on the effectiveness of electrocatalysts, the mechanism may include several elementary steps involving different reaction intermediates. It can involve either indirect two-electron (2*e*-) or direct four-electron (4*e*-) pathways. Generally, the 4*e*- direct pathway is highly desirable in FCs. The difference between the direct and indirect pathways is whether free H_2O_2 molecules are released to the electrolyte or not. The ORR in alkaline electrolytes is most favorable, and the potential drop is low. As a result, AFCs yield the highest voltage at a comparable current density, leading to higher efficiency. As a consequence, the fast ORR kinetics in alkaline electrolyte presents AFCs a gained advantage over the other kinds of FCs. For example, FCs can run with the decreased loading of noble metal electrocatalysts and also use the NPMCs.

Table 1-2 Thermodynamic electrode potentials of oxygen reduction reactions [5]

Aqueous electrolyte solution	ORR reactions	E° (V vs. RHE)
Acidic	$O_2 + 4H^+ + 4e^- \rightarrow 2H_2O$	1.229
	$O_2 + 2H^+ + 2e^- \rightarrow H_2O_2$	0.70
	$H_2O_2 + 2H^+ + 2e^- \rightarrow 2H_2O$	1.76
Alkaline	$O_2 + 2H_2O + 4e^- \rightarrow 4OH^-$	0.401
	$O_2 + H_2O + 2e^- \rightarrow HO_2^- + OH^-$	-0.065
	$HO_2^- + H_2O + 2e^- \rightarrow 3OH^-$	0.867

1.7 Electrocatalysts for the oxygen reduction reaction

1.7.1 Precious metal-based electrocatalysts

In the group of precious metal-based ORR electrocatalysts, Pt regarded as the best one. As a result, pure Pt metal-based ORR electrocatalyst has been widely developed and used for decades. The ORR process is susceptible to surface electronic properties. From single crystal studies, it is known that different surface facets of pure Pt exhibit various ORR activities depending on the particular electrolyte [62]. For example, in weakly adsorbing acid electrolyte like $HClO_4$, the order of ORR activity is Pt (100) < Pt (111) < Pt (110). Whilst, in the strongly adsorbing electrolytes of sulfuric the ORR activity increases in the order Pt (111) < Pt (110) < Pt(100) due to the stronger adsorption of sulfate anion (SO_4^{2-}) on Pt (111) vs. on Pt (100) surfaces which limits accessibility of Pt sites, and hence, prevent O_2 adsorption [62, 63]. Thus, it is possible to idealize, hypothesize, and engineer the surface of Pt with altered electronic properties. Accordingly, modified surface electronic properties induce a change in the adsorption behavior, specifically a shift to lower oxygen binding energy. This adsorption behaviour of intermediate species such as O, OH, might be the crucial step of ORR on metal catalysts, as suggested by Nørskov *et al*. [63, 64]. In their work, they show that for Pt (111) as an electrode, at high potentials, adsorbed oxygen tends to be so stable that the proton and electron transfer becomes impossible. By lowering the potential, the stability of the adsorbed oxygen decreases, and the reaction may proceed. Nørskov et al. also pioneered calculations of binding energies of oxygen and hydroxyl for several exciting metal atoms and plotted against ORR activity to obtain an excellent volcano plot [64] as shown in Figure 1-4. In which, the metal sitting at the top of the volcano plot, e.g., Pt and Pd are the best catalysts for ORR. For metal atoms that bind oxygen too strongly, the rate is limited by the removal of adsorbed O and OH species. For a metal surface that binds oxygen too weakly, the rate is limited by the dissociation of O_2, or more likely, the transfer of electrons and proton to adsorbed O_2. Thus, the volcano plot provides a room for improvement.

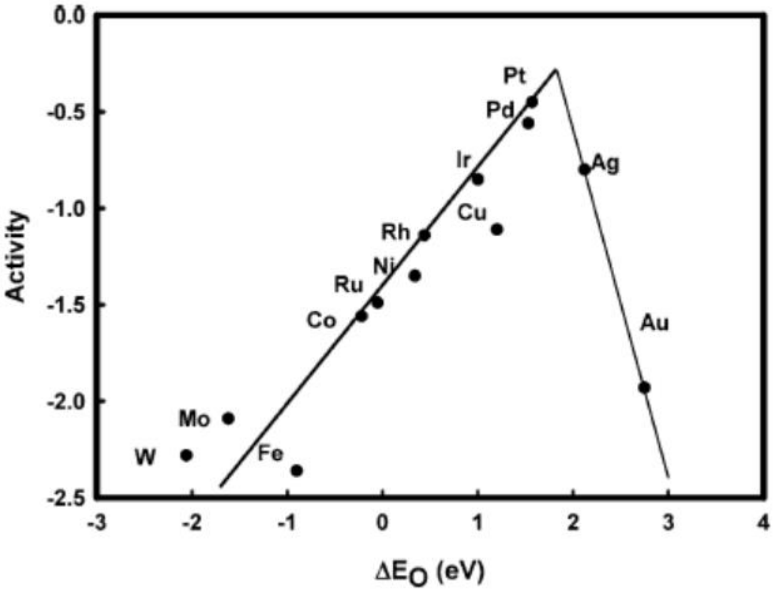

Figure 1-4 Trends in oxygen reduction activity plotted as a function of the oxygen binding energy for different metal atoms [64].

Another strategy used to optimize the activity of Pt-based catalyst is to increase the active exposed surface of the utilized Pt by preparation of nanostructured particles on support [63]. The effect of particle size and shape on the specific activity of Pt is still debatable [65]. However, in practice, it is difficult to reduce the Pt content with this approach because decreased loading increases the sensitivity of the catalyst to poisoning from contaminant even at trace amounts. The other approach is to engineer the specific structure of Pt-metal (Pt-M) as alloys nanoparticles, and core-shell nanostructures [66]. Figure 1-5 displays the schemes of Pt-M nanoparticles. Theoretical studies have shown that metals with lower binding energy than Pt are expected to have a higher rate of ORR. The alloys of Pt with Co, Fe, Ni, and Cr demonstrated to have smaller binding energies than Pt. Indeed, the experimental observation shows the Pt alloys of these metals have a higher ORR activity [64].

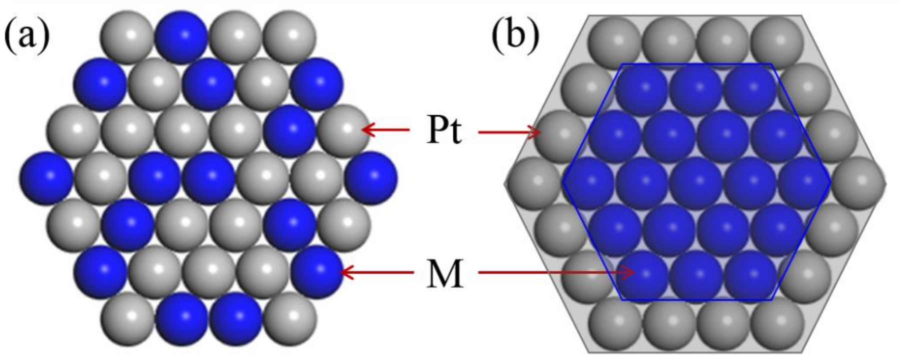

Figure 1-5 Schematic illustration of Pt-metal nanostructures (a) alloy and (b) core-shell [66].

For example, the synthesized Pt-M materials containing core-shell structure with Pt as shell and M as a core (M = Co, Ni, Fe, Cr, etc.) demonstrated higher ORR activity than Pt/C. In this approach, a monolayer of Pt can be deposited onto nanoparticles of transition metals or less expensive precious metals. As a result, the amount of Pt utilization is significantly decreased for about ~70 wt% Pt in the bulk of pure particles used. It has been shown that the core can influence the properties of the Pt shell beneficially by modulating the d-band center. As a consequence, higher activity was reported for the Pt_3Ni (111), Pt-AuNi, Pt-Cu and Pt-Pd, Pt-Co core-shell than that of current state-of-the-art Pt/C catalyst [63, 66]. The high performance of these alloys is attributed to the synergy of the surface geometry, electronic structure, and surface adsorption. The major challenge with this approach is the scalability and instability of the non-noble cores. Unfortunately, this approach still relies on the rare and the high-cost of Pt, which has been a subject to the primary barrier of the commercial mass market of fuel cells. Furthermore, the Pt-based electrode also suffers from susceptibility to time-dependent drift and CO deactivation. Thus, efforts are needed to identify alternative catalysts that are highly reliable, readily available, cost-effective, and show comparable or even better catalytic effects than Pt for cathodic ORR in FCs.

1.7.2 Non-precious metal-based electrocatalysts

Transition-metal-based materials have been the focal point of non-precious metal electrocatalysts (NPMCs) investigations, due to their partially filled d-orbitals, low-cost and relatively high abundance on the earth's crust. Research on NPMCs with Co as the central metal ion started in 1964 with Jasinski's discovery that a cobalt-phthalocyanine with M-N_4 configuration is active towards the ORR [27]. Inspired by the heme-copper complexes present in cytochrome *c* oxidase (an enzyme catalyzing oxygen reduction in the prokaryotes and eukaryotes), Fe-based catalysts with Fe as the central metal ion later emerged [25, 67, 68]. Another kind of NPMCs for ORR was then developed by Yeager *et al.* based on the pyrolysis of macrocycles precursors without M-N_4-coordination [69]. Subsequently, numerous types of NMPCs widely developed and studied for ORR catalysis. These materials include transition metal chalcogenides, oxides, pyrolyzed M/N/C, (M = Fe, Co, Ni, etc.) compounds, and macrocycles (M-N_4-macrocycles). Metal chalcogenides, such as transition metal compounds with S, Se or Te, have been studied and showed significant ORR activity. One of the most promising materials, $Ru_2Mo_4Se_8$, exhibited only 100 - 150 mV lower half-wave potential than Pt in H_2SO_4 [70, 71]. The chalcogenide can lower the stable oxygen binding energy and thus increase the catalytic activity of Ru, Rh, and Co. However, the main concern with these materials is the cycle stability and high risk of toxicity [71, 72].

Transition metal oxides also have been explored in ORR as NPMCs [70]. Due to their oxidizedstate, these materials exhibit high stability in acid. Various combinations of oxides have been synthesized, and their electrochemical activities were evaluated, including ZrO_{2-x}, Co_3O_{4-x}, and TaO_x [70]. It is believed that oxygen vacancies in these materials might be the source of the catalytic activity. Some of these nanoparticles exhibited onset potentials as high as 0.94V *vs.* RHE [73]. Nevertheless, the low reliability of the synthesis approach and poor conductivity are significant challenges to overcome for these materials [74]. Several methods to improve the performance of metal oxides catalysis have been deployed including the doping with nitrogen to reduce the band-gap and produce oxynitrides and supporting the metal oxides on conductive materials such as carbon nanotubes (CNTs).

A breakthrough in NPMCs exploration for ORR came in 2009, when the Dodelet group reported the synthesis of highly active catalysts which reached high cell potential in a single cell PEMFCs [24]. In this work, they introduced pore filler and iron precursor into micropores of carbon black and pyrolyzed the precursor at high-temperature to obtain the Fe/N/C. In the later works, they extended the pore filler invention to other carbon sources, metal-organic framework (Basolite Z1200) [26] and porphyrin (chloroirontetramethoxyporphyrin) [75]. The prepared catalysts exhibited a high-power density of 0.75 W cm^{-2} at 0.6 V, which is comparable to a state-of-the-art Pt-based cathode with a loading of 0.3 mg_{Pt} cm^{-2} [25]. Concurrently, the Zelenay group reported on polyaniline-derived heat-treated Fe/N/C, which combined the high ORR activity with unique performance durability at 0.4 V [76]. However, the high-temperature pyrolysis of these materials results in the formation of complex structural composition and rises potential safety issues.

On the other hand, transition metals macrocycles, porphyrins, and phthalocyanine, shown in Figure 1-6 are the only ones reported to have relatively high ORR performance without the high-temperature pyrolysis process. For instance, in 1964, it was demonstrated that cobalt phthalocyanine is exhibiting high activity towards ORR [27]. The catalytic activities of the macrocycles have a strong dependence on the center metal ion and the pH of the solution. For example, iron-based macrocycles exhibit a predominant 4-electron pathway in alkaline and the 2-electron pathway under acidic electrolyte. The activity and stability of these complexes are compromised by the dissolution of the central metal species or the degradation of the macrocycle, poor conductivity, and aggregation. The strategies employed to address these challenges include; i) attaching the electron-donating group to the FePc structure as an additional electron source to preventing issues arising from slow electron transfer, and (ii) supporting the FePc on a variety of carbon materials, such as carbon black, CNTs, and reduced graphene oxide. In spite of effort made in preparation and usage of FePc as ORR electrocatalyst, the level of performance cannot reach that of Pt-based catalyst in terms of both reactivity and durability.

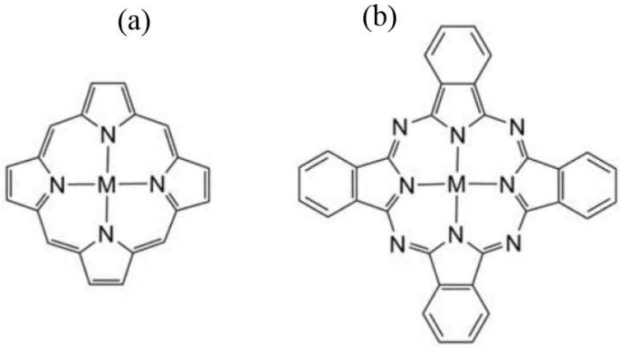

Figure 1-6 General structure of (a) metalloporphyrin and (b) metallopthalocyanine, where M is the central metal atom.

Nevertheless, studies on these complexes are useful to gain fundamental insight into trends of ORR activity. The advantage of molecular compounds is that the d-orbital configuration can easily be controlled and the molecules can be well characterized to develop structure-property relationships. While the choice of graphene as a support material is driven by anticipation that the extended conjugation can provide a strong interaction with FePc through the π-π stacking. Furthermore, the development of a straightforward, simple, and feasible synthetic route to produce low-cost and robust electrocatalysts with controlled structure and excellent stability is highly desirable.

1.7.3 Metal-free carbon-based electrocatalysts

Carbon nanomaterials are ideal candidates for catalyst supports and even metal-free catalysts due to their abundance, environmental acceptability, corrosion resistance, and unique surface and bulk properties. Activated carbon and glassy carbon have been long used as catalysts for specific chemical and electrochemical processes. Recently, new carbon nanomaterials of unique molecular structures and optoelectronic properties, including fullerenes, CNTs, graphene, and graphite nanoplatelets have been studied [20, 32, 77, 78]. These materials offer new prospects for the development of advanced carbon-based catalysts with much improved catalytic performance. The introduction of surface heteroatoms (e.g., nitrogen) into these carbon nanomaterials could further cause electron modulation to provide desirable electronic structures for many catalytic processes of practical significance. Consequently, metal-free heteroatom-doped carbon-based electrocatalysts demonstrated to be very tolerant of CO poisoning, which overcomes the inherent problems that Pt catalysts are facing. For example, the N-doped CNT electrode has been proved to be free from CO poisoning even after adding about 10 % CO with much higher electrocatalytic activity and better long-term operation stability than that of commercially available Pt-based electrodes in alkaline electrolytes [79].

1.8 Hydrogen evolution reaction

Hydrogen is highly considered to be the ultimate energy carrier of the future owing to its efficiency, clean combustion, and high gravimetric energy density (142 kJ g^{-1}) compared to methane (33 kJ g^{-1}). The use of hydrogen energy carrier would significantly mitigate the environmental concerns due to zero emission of carbonaceous species. Hydrogen can be used as fuel in FCs and is also a promising solution in the conversion of renewable energies into chemical fuels that can be stored and transported [47, 80]. To realize these economies of scale, the supply of hydrogen from a sustainable source is required. Likewise, the advantages of hydrogen FCs are meaningless without a viable source of producing hydrogen. While oxygen occurs naturally in the air; hydrogen must be supplied from the decomposition of other molecules. The conventional method of producing hydrogen such as steam reforming processes are both energy intensive and unfriendly to the environment (producing CO_2) [81]. On the other hand, photoelectrochemical and electrochemical hydrogen evolution are two possible approaches to realizing solar-to-hydrogen conversion. Photoelectrochemical (PEC) devices are promising as they have high solar-to-hydrogen efficiency [82]. However, for practical applications, PEC requires huge electrode area due to inherently low efficiency [83, 84]. Also, PEC naturally excludes all other renewable energies in the energy conversion process. Electrochemical HER is the most fundamental reaction in electrochemistry. Despite the lower solar-to-hydrogen efficiency than the direct photoelectrochemical route, the electrochemical HER is more attractive due to the higher flexibility and applicability [48, 83]. Combining grid-scale renewable energy harvesting infrastructures with electrochemical HER can efficiently convert the intermittent electricity obtained from renewable energies into more valuable H_2 and thereby enhancing the diversity of renewable energy utilization [85]. Figure 1-7 shows a sustainable pathway for the integration of renewable energy into electrochemical HER and circulation of hydrogen energy [48]. This process of hydrogen production is CO_2-free and requires only water and electricity [86]. Nevertheless, the best known HER electrocatalyst is Pt/C. Unfortunately, the use of Pt-based catalyst limits the practical application of this method for the production of hydrogen.

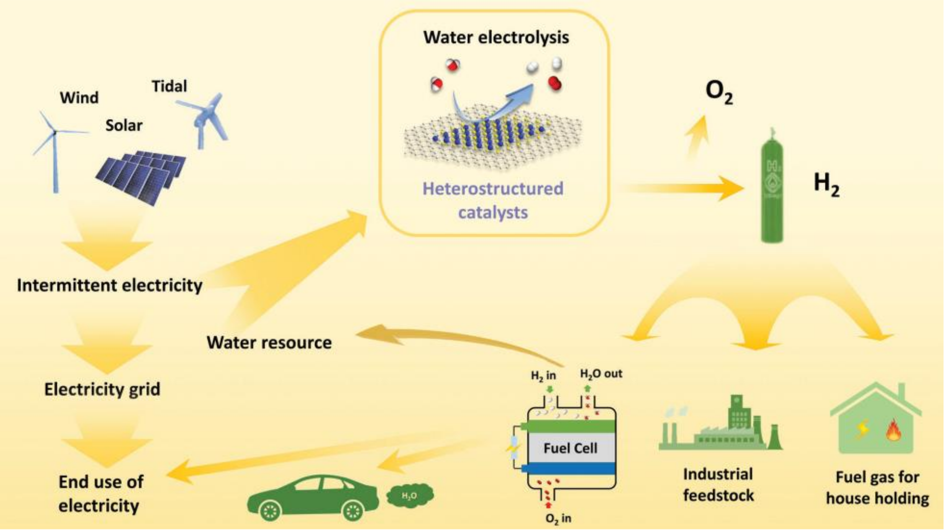

Figure 1-7 A sustainable pathway for the production and utilization of hydrogen energy [48].

1.8.1 Steam-methane gas reformation

The steam-methane gas reforming is the primary source of hydrogen production today. In this process, methane is reacted with high-temperature steam (700 °C – 1000 °C) under pressure in the presence of a catalyst to produce hydrogen, carbon monoxide, and a relatively small amount of carbon dioxide according to reformer general Equation 1-2. Steam reforming is an endothermic reaction, whereby heat supply is required to complete the reaction process [87]. Subsequently, the water-gas shift reaction proceeds (Equation 1-3), whereby the carbon monoxide reacts with steam in the presence of a catalyst to produce carbon dioxide and more hydrogen. In the final process carbon dioxide and other impurities are removed from the gas stream, leaving substantially pure hydrogen. Steam reforming can also be used to produce hydrogen from other fuels, such as ethanol, propane, or even gasoline [88].

$$CH_4(g) + H_2O(g) \underset{\Delta}{\rightarrow} CO + 3H_2 \qquad (1\text{-}2)$$

$$CO(g) + H_2O(g) \rightarrow CO_2 + H_2 + \text{heat} \qquad (1\text{-}3)$$

1.8.2 Photoelectrochemical hydrogen evolution

Photoelectrochemical hydrogen evolution from water splitting has been attracting significant attention recently due to its utilization of solar energy and hydrogen production [89]. In the early 1970s, Fujishima and Honda demonstrated the use of TiO_2 in the decomposition of water into H_2 and O_2 under PEC conditions [90, 91]. Under light circumstances, the reaction involved in the water splitting of water is given in Equation 1-4 and Equation 1-5.

$$\text{HER: } 4H^+ + 4e^- \rightarrow 2H_2(g) \qquad (1\text{-}4)$$

$$\text{OER: } 2H_2O(l) \rightarrow 4H^+ + O_2 + 4e^- \qquad (1\text{-}5)$$

Overall reaction: $2H_2O \rightarrow 2H_2 + O_2$ (g), $\Delta E° = -1.229$ (V vs. RHE), ($\Delta G° = 237.18$ kJ mol^{-1})

The negative sign in the electrodynamic potential implies that HER is an uphill process, and thus, additional energy must be supplied to complete the reaction. In PEC hydrogen evolution, a photocatalyst, which is a semiconductor, is irradiated by UV-visible light with energy greater or equivalent to the band gap of the semiconductor (Figure 1-8a). The light energy will be absorbed by the photocatalyst, which results in charge separation at the valence band and conduction band. The holes are produced at the valence band, and the photo-excited electrons jump into the conduction band. The holes trigger the oxidation of water at the surface of the conduction band while the photo-excited electrons at conduction band reduce the absorbed H^+ onto the photocatalyst surface to H_2. Generally, in the photoelectrochemical HER, semiconductors are utilized as a photocathode or photoanode depending on the type of favorable reaction [91, 92]. The semiconductor electrode should be in contact with an electrolyte, which contains a redox couple. In the PEC system, hydrogen and oxygen production reactions take place at two different electrodes [93]. In principle, catalysts are needed to increase the kinetics of photoelectrodes to match with the charge generation and separation. However, PEC hydrogen evolution is hindered by the sluggish surface dynamics that impede the improvement of their performance.

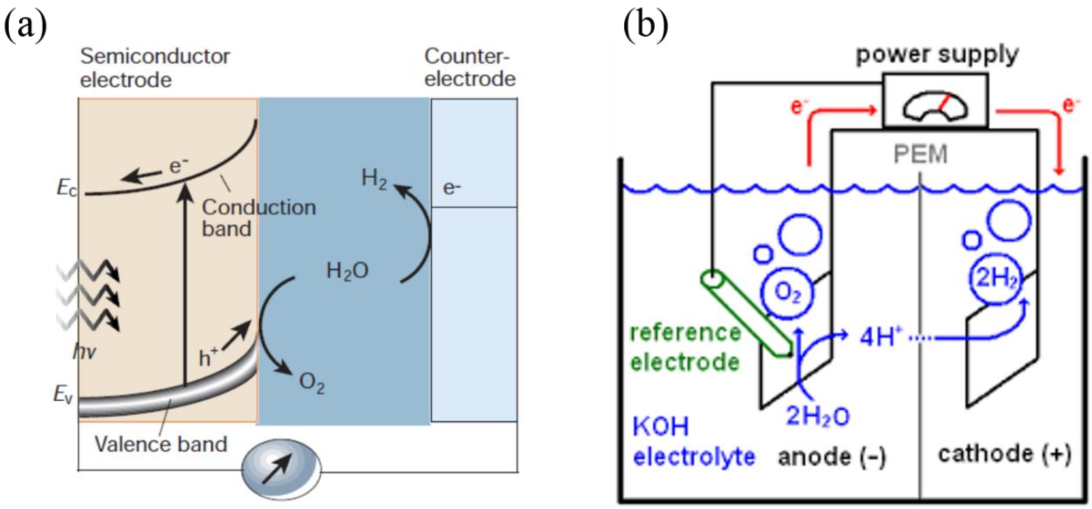

Figure 1-8 Schematic presentation of water electrolytic cells (a) photoelectrochemical based on n-type semiconductor [92], and (b) electrochemical process.

1.8.3 Electrochemical hydrogen evolution

Hydrogen production either by electrolytic or photocatalytic water splitting presents the most promising option. Currently, hydrogen is produced primarily from the steam reforming of fossil fuels [81, 83, 85]. It is particularly appealing to produce hydrogen from clean, renewable, and sustainable energy sources. The electrochemical hydrogen production process is CO_2-free and requires only water and electricity. As shown in Figure 1-8b, electrochemical oxygen evolution reaction (OER) takes place at the anode, and the HER occurs at the cathode. Naturally, the OER is a more complicated process involving $4e^-$ while HER subject of this study is a $2e^-$process, one of the simplest and well-studied electrochemical reaction [84]. The mechanism of HER is highly dependent on the pH value of the electrolyte. In an acidic solution, H_2 is generated from the reduction of either proton (H^+) while alkaline electrolyte is from the reduction of H_2O molecules. Both of these processes involve a series of elementary steps. HER in acidic media begins with the discharge step (Volmer step) where H^+ ions adsorb on the catalyst surface to form an adsorbed hydrogen atom (H_{ads}), (Equation 1-6).

$$\mathrm{H^+ + e^- \rightarrow H_{ads}} \qquad (1\text{-}6)$$

$$\mathrm{H_{ads} + H^+ + e^- \rightarrow H_2} \qquad (1\text{-}7)$$

$$\mathrm{H_{ads} + H_{ads} \rightarrow H_2} \qquad (1\text{-}8)$$

$$\text{Overall equation:} \qquad \mathrm{2H^+ + 2e^- \rightarrow H_2} \qquad (1\text{-}9)$$

The second step is called electrochemical desorption (Heyrovsky step) where the adsorbed H_{ads} combines with an H^+ and an electron to form an H_2 molecule, as described in Equation 1-7. Alternatively, H atoms adsorbed on the surface of the catalyst may combine to form H_2 molecule in the so-called chemical desorption step or Tafel step (Equation 1-8). The overall HER is represented in Equation 1-9, the standard electrode potential ($E°$) is used as the reference for evaluating the standard electrode potential of electrochemical reactions. Regardless of the electrochemical HER being most straightforward, the detailed explanation of the pathway on different materials is not direct. By plotting the current exchange densities for HER on various metals versus calculated corresponding hydrogen adsorption energy ($\Delta G_{H°}$) on distinct catalyst surface, Nørskov *et al*. constructed the volcano plot for the HER activity [94]. As shown in Figure

1-9, the results entirely reveal the origin of the superior HER activity of Pt group metals (Pt, Pd, Rh, Ir) and provide an intuitive description for the dependence of HER activity on hydrogen binding energy. The Pt-group minerals are located right on top of the volcano plot and have the optimal HER activities. Transition metals to the right of Pt group metals (Au, Ag, Cu) bonds to hydrogen too weakly to initiate the HER reaction, whereas to their right (Ni, Co, Mo, W) bonds to hydrogen too strongly to release the product. Pt is the best electrocatalyst for HER, primarily because the evolution reaction is thermo-neutral on Pt at the equilibrium potential. The volcano plot is useful in the development of HER electrocatalyst targeting materials which have ΔG_H closer to the thermoneutral ($\Delta G_H \sim 0$).

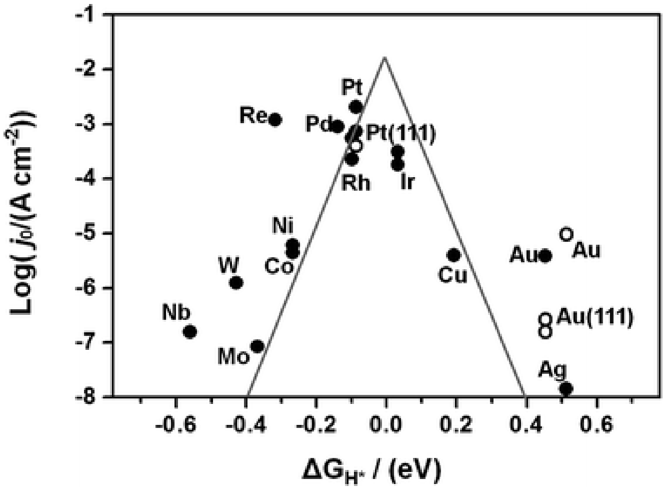

Figure 1-9 Volcano plot of exchange current density (j_o) as a function of DFT-calculated Gibbs free energy (ΔG_{H^*}) of adsorbed atomic hydrogen on pure metals [94].

The mechanism of the HER in alkaline media is very similar to that of acidic media, and the ΔG_{H° still works for describing the adsorption behavior of hydrogen on the surface of catalysts. But the catalytic activity towards HER in alkaline of most metals is inferior to that in acidic medium. HER in alkaline proceeds with the dissociation of H_2O molecules to provide protons. The steps involved in alkaline HER are presented by Equation 1-10 (Volmer step) and Equation 1-11 (Heyrovsky step), while the Tafel step (Equation 1-8) remains similar to that of acid solutions. Equation 1-12 depicts the overall HER reaction process in alkaline. The HER electrocatalysts are also grouped into three main classes. The first class is the precious metal-based electrocatalysts (PMCs). This class of catalysts, particularly Pt, are the most active HER catalysts. Unfortunately, their high cost and low abundance limit their large-scale application of water electrolyzers. As mitigation, several strategies have been put in place. The most common procedures are the development of nanostructures of PMCs or supporting the nanostructures of PMCs on low–cost substrates [95].

$$\mathrm{H_2O + e^- \rightarrow H_{ads} + OH^-} \qquad (1\text{-}10)$$

$$\mathrm{H_{ads} + H_2O + e^- \rightarrow OH^- + H_2} \qquad (1\text{-}11)$$

$$\mathrm{2H_2O + 2e^- \rightarrow 2OH^- + H_2} \qquad (1\text{-}12)$$

Another approach is to alloy the PMCs with other metals permitting much lower catalyst loading to be used [96]. The second class is NPMCs, which include metals, oxides, chalcogenides, carbides, nitrides, and phosphides or their combinations. Nevertheless, the materials developed so far exhibited significant HER activity but suffered from limited stability [1]. The final class of HER electrocatalysts is metal-free. These electrocatalysts constitute carbon-based materials doped with heteroatoms such as N, B, O, S, P or their combination. The presence of heteroatoms in carbon lattice is believed to cause a structural disorder that changes the local electronic properties leading to the promotion of electrocatalytic activities [97]. The most active HER metal-free catalyst reported so far is the N and P co-doped graphene with an overpotential of 420 mV to reach a current density of 10 mA cm^{-2} in 0.5 M H_2SO_4 [97]. Despite the improved promising performance, thus far the HER activity of metal-free electrocatalysts is too low and cannot compete with their metal containing counterparts.

1.9 Thesis objectives and organization

1.9.1 Thesis objectives

The general objective of this thesis is the development of low-cost, robust, and highly durable electrocatalysts for ORR and HER, with a controlled structure using straightforward, simple, and feasible synthesis approaches. Specifically, the objectives of the thesis are:

(i) To fabricate high-quality graphene by electrochemical exfoliation of graphite substrates and use as efficient metal-free electrocatalysts for the ORR.

(ii) To develop durable and high-performance NPMCs towards ORR based on supporting Iron II phthalocyanine on the fabricated graphene by employing a straightforward slow evaporation approach.

(iii) To fabricate a highly efficient and durable electrochemical hydrogen evolution electrocatalysts based on MoS_2 supported free-standing TiO_2-nanotubes by employing a straightforward slow evaporation approach.

1.9.2 Thesis organization

This thesis consists of 6 chapters (2 introductory chapters, 3 articles chapters, and one final chapter for the summary. The following is the outline of the structure of thesis:

Chapter 1 Introduction. In this Chapter, we give a brief description of the history and fundamental of Fuel cells, oxygen reduction reaction, hydrogen evolution reactions, and their electrocatalysts.

Chapter 2 Experimental. In this Chapter, we present the description of synthesis and characterization techniques used throughout this work.

Chapter 3 The use of graphene as a metal-free catalyst for oxygen reduction. In this Chapter, we present the results for the controlled synthesis of graphene via electrochemical route and its use as an efficient metal-free catalyst for oxygen reduction. We demonstrate the fabrication of large pieces of high-quality graphene via exfoliation of graphite plates and foils. The N-doped graphene exhibits high performance as metal-free catalysts for oxygen reduction.

Chapter 4 Iron (II) phthalocyanine/N-doped graphene as non-precious metal electrocatalysts for oxygen reduction. In this Chapter, the results for non-pyrolyzed Iron (II) phthalocyanine on N-doped graphene as a highly efficient non-precious catalyst for oxygen reduction. We discuss the direct and straightforward approach to fabricate iron (II) phthalocyanine/N-doped graphene as practical and durable oxygen reduction electrodes.

Chapter 5 TiO_2-nanotubes as potential support of MoS_2 an active material for electrochemical hydrogen evolution. We present results for the controlled fabrication of TiO_2-nanotubes on Ti substrate as a potential hydrogen evolution electrode. We describe an electrochemical method as a novel strategy to fabricate TiO_2 nanotubes with controlled morphology and the fabrication of the composite MoS_2/TiO_2-NTs electrode. Finally, the results of TiO_2 nanotubes as potential hydrogen evolution electrode presented.

Chapter 6 Conclusions and recommendations based on the analysis of the results and the proposition of supplementary studies.

Summary

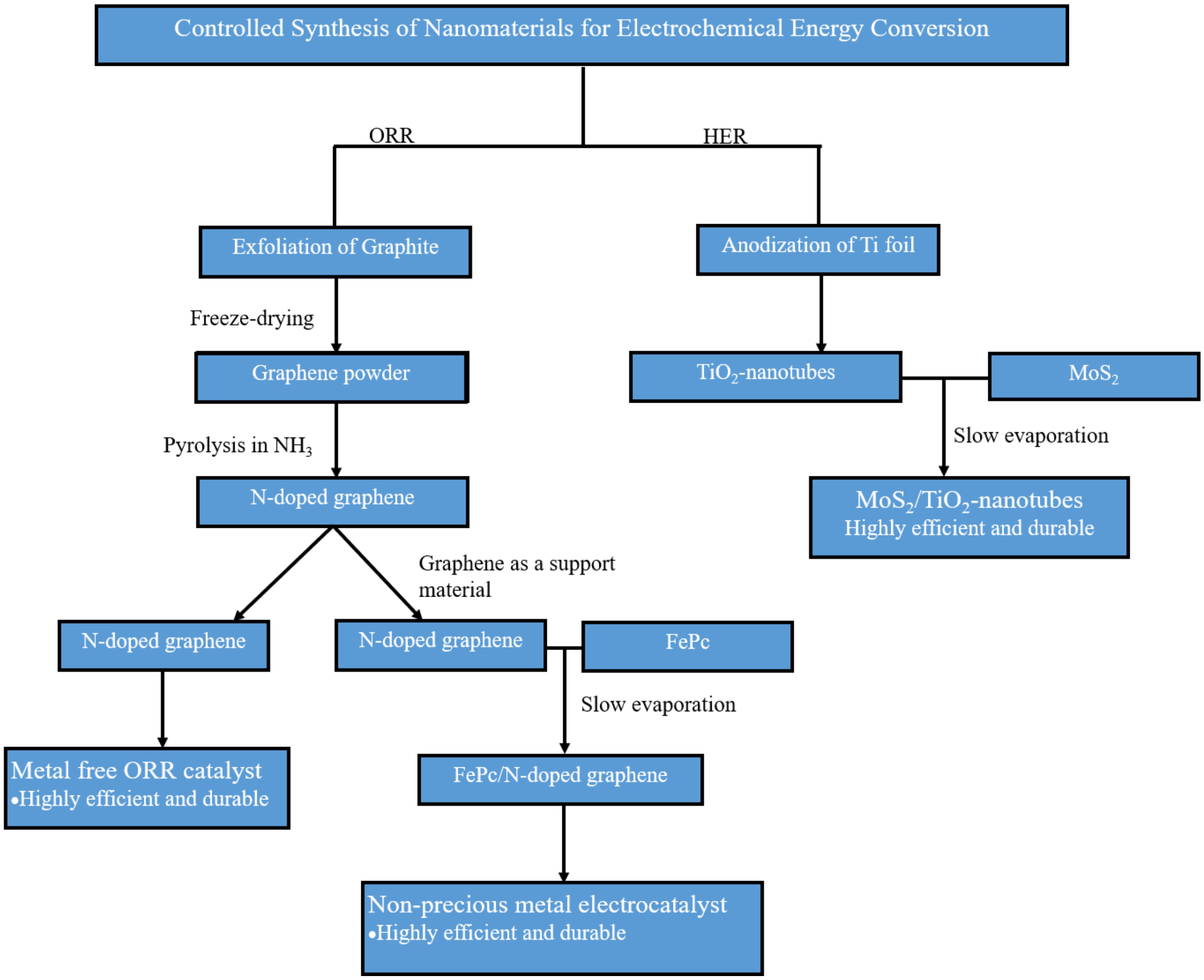

Figure 1-10 Conceptual flow chart of the thesis.

Chapter 2 Experimental Methods

In this chapter, the description of methods of fabrication and characterization techniques used in subsequent Chapters briefly presented. These are essential techniques used to study the structure, morphology, surface composition, and electrochemical properties of the prepared electrocatalysts materials investigated in this study.

2.1 Synthesis techniques

2.1.1 Electrochemical exfoliation of graphite

An electrochemical exfoliation of graphite can be performed using either a two-electrode cell or three-electrode cell. The cell set-up consists of graphite or Pt as cathode or counter electrode, graphite plate or foil (graphene precursor) as anode or working electrode, reference electrode (in the three-electrode system) and the electrolytes. Electrochemical exfoliation can be performed using either a conventional DC power supply or potentiostat. Before to begin the experiment, the graphite substrates are cleansed by polishing followed by thorough washing in water by sonication (using an ultrasonic cleaner, 40 kHz, 80 W) for 15 minutes then dried under nitrogen. In this work, we used the DC power supply (PSC-260, Circuit Test Electronics) and the two-electrode cell. The cell setup and the associated steps in the fabrication of graphene are illustrated in block diagram Figure 2-1 (part A). During exfoliation, the graphite is connected to the positive terminal of a DC power supply, and a Pt wire was employed at the negative terminal while immersed in an electrolyte solution. A bias potential of +2.5 V applied between the electrodes for wetting and activation of graphite. With this applied potential, initiation of intercalation of electrolyte ions and water molecules into the interlayer spacing of graphite begins [16].

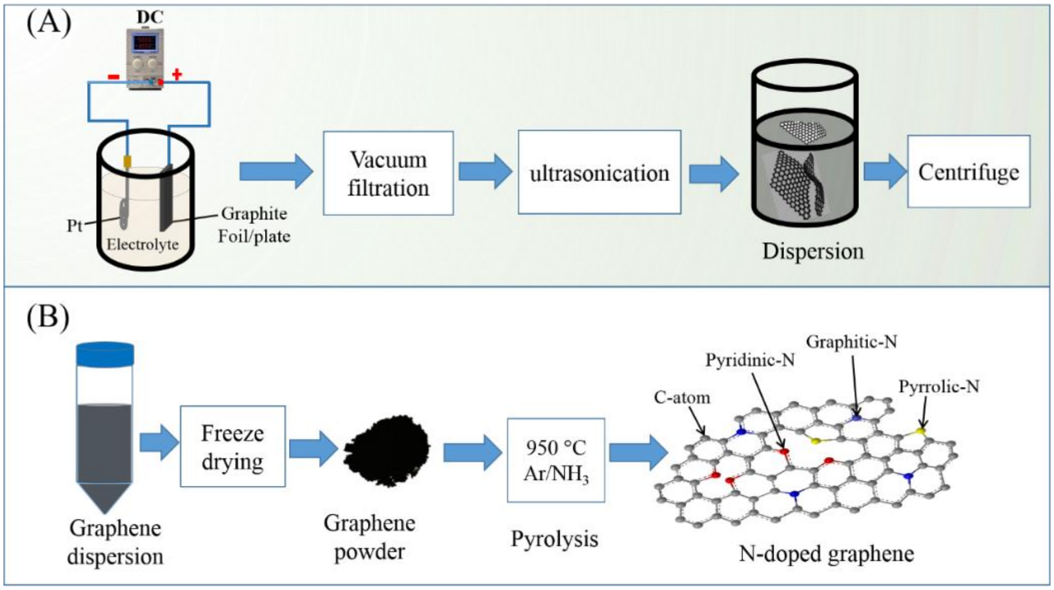

Figure 2-1 Schematic view of steps in preparation of graphene and FePc/N-graphene composite, (A) an electrochemical cell setup for exfoliation of graphite and subsequent procedures, (B) the steps to obtain N-graphene (N-GP).

In the final stage, the bias potential is ramped up to +10 V to achieve the oxidation of edges, intercalation, expansion, and exfoliation. The bias potential can also be reversed to −10 V for reduction of oxidized carbon and final exfoliation [16, 98, 99]. Afterward, the exfoliated graphitic produce collected by vacuum filtration and repeatedly washed with Milli-Q water and ethanol to remove the residual electrolyte. After that, the product obtained is dispersed in a solvent of interest (dimethylformamide, N-methyl-2-pyrrolidone) by ultra-sonication. The graphitic particles are separated by centrifuging the dispersion at 1000 rpm for 10 minutes. Similarly, the supernatant can further be centrifuged at a different speed to fractionate the graphene (GP) into various layered components, 2500 rpm (multi-layer), 5000 rpm (thin layer) and 14000 rpm (few layers). As shown in Figure 2-1 (part B), the graphene components then re-dispersed in deionized water by low power sonication for 15 minutes and then frozen at -80 °C. The graphene powder is obtained by freeze-drying. Finally, N-doping is achieved by heating the graphene powders at 950 °C under Argon/NH_3 atmosphere for 15 minutes to get the N-doped graphene (N-GP950).

2.1.2 Electrochemical fabrication of Titanium dioxide

Titanium dioxide nanotube (TiO_2-NT) membranes can be prepared by electrochemical anodization of Ti foil in fluoride ethylene glycol solution or aqueous solution. The anodization experiment is performed in a polytetrafluoroethylene (PTFE) cell with a two- or three-electrode system [100-102]. Graphite plate is used as a negative electrode. A positive bias potential is applied between the electrodes (Ti foil and graphite plate) placed 2 cm apart for a specified time using a DC power supply (PSC-260, Circuit Test Electronics).

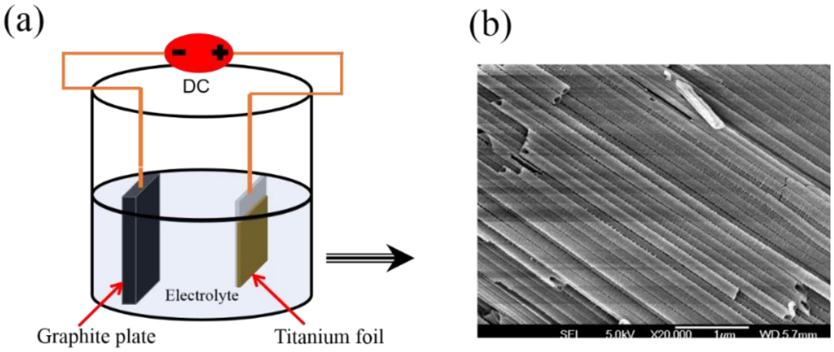

Figure 2-2 A scheme of fabrication of highly ordered TiO_2-nanotubes arrays by anodic oxidation of Ti substrate (a) anodization experimental setup, and (b) a typical SEM image of the as-anodized TiO_2-NTs.

The anodization experiment cell setup and a typical SEM image of the as-anodized TiO_2-NTs are shown in Figure 2-2. Before anodization, the substrates are polished by using 800 Grit fine silicon carbide sandpaper. Subsequently, the substrates are washed thoroughly by sequential ultrasonication (40 kHz, 80 W) in acetone, ethanol, and Milli Q water and dried under nitrogen gas. The as-anodized TiO_2-NTs then was used to support MoS_2 sheets.

2.1.3 Slow evaporation method

Slow evaporation method can start by dispersing the support materials in a suitable solvent. To the dispersion, an equal volume of the solution of supporting material added dropwise while stirring. The mass ratio of support material and supporting material is fixed. The resulting mixture is continuously stirred at room temperature for at least two hours. Subsequently, the reaction mixture is slowly heated (~65 °C) to evaporate 75% of the original solution. Afterward, the slurry is left to dry in an air-oven at 95 °C overnight, to yield the desired product.

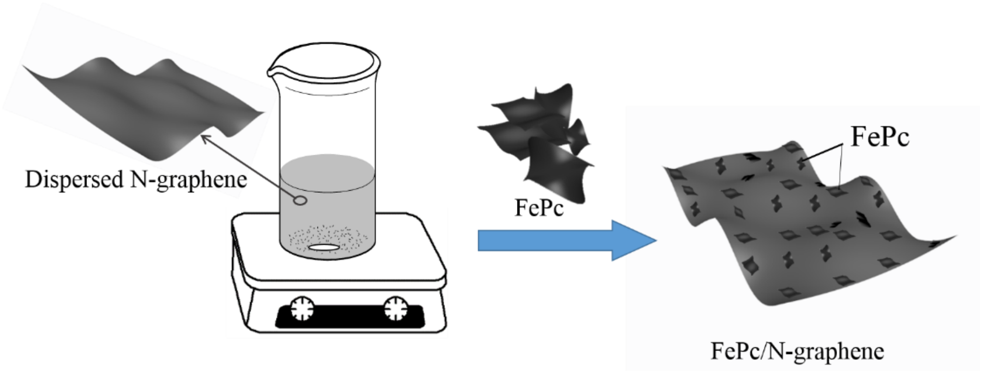

Figure 2-3 Schematic illustration of the immobilization of FePc on the N-doped graphene.

In this study, the direct, slow evaporation method was used to immobilize FePc on the graphene under atmospheric conditions. The preparation scheme of FePc/graphene is shown in Figure 2-3. The grafting of FePc in the N-graphene is facilitated by the π-π interaction and interfacial bonds between the Fe in the FePc and the residual oxygen groups in the N-doped graphene. Additionally, the hydrothermal method was used to prepare the composite of MoS_2 and TiO_2-nanotubes.

2.1.4 Solvothermal synthesis

Solvothermal synthesis involves solution-based chemical reactions carried out in a sealed, heated solution above ambient temperature and pressure. When a solvent is heated in a sealed vessel, the autogenous pressure is developed, which by far exceeds the ambient pressure. Thus, the solution is brought to temperatures well above their boiling points. The pressure within the sealed reaction vessel depends on other experimental factors, such as the percentage fill of the vessel and any dissolved salts [103, 104]. A typical solvothermal synthesis is commonly performed using Teflon-lined stainless autoclave, as shown in Figure 2-4.

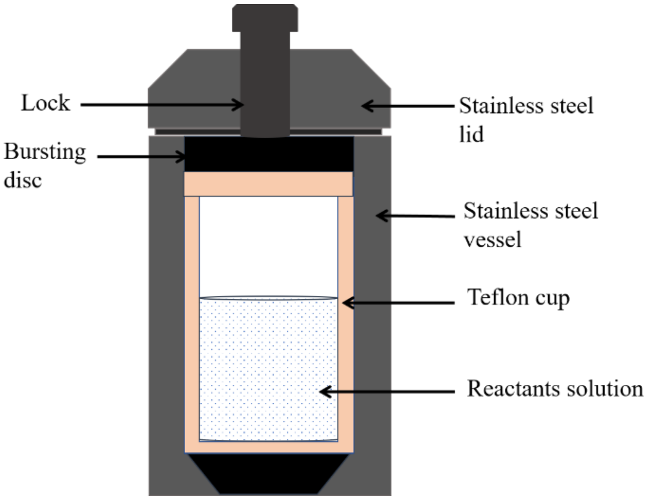

Figure 2-4 A schematic cross-section view of a Teflon-lined, stainless autoclave.

Precise control over solvothermal synthetic conditions is essential for controlled-growth of nanostructures. This method is widely applied to generate different kinds of nanomaterials [103, 105]. The controllable conditions in the hydrothermal reaction include the concentration, pH of the solution, time, pressure, and organic additives or templates, and temperature. In this study, the hydrothermal method was used to prepare the MoS_2 nanostructures.

2.2 Physical characterization methods

Various characterization techniques were employed to investigate different properties of prepared materials. The methods used in the present work include X-ray photoelectron spectroscopy (XPS), transmission electron microscopy (TEM), scanning electron microscopy (SEM), X-ray Diffraction (XRD), and UV-visible electronic absorption spectroscopy.

2.2.1 X-ray photoelectron spectroscopy

XPS is a potent tool for material science. XPS is based on the measurement of kinetic energy (KE) of photoelectrons generated when a sample is irradiated with X-rays of well-defined energy (hv), e.g., from monochromatic Al Kα rays. Figure 2-5a illustrates the photoelectrons generation. From the relationship (Equation 2-1), the binding energy (BE) can be determined [106].

$$BE = hv - (KE + \varphi) \qquad (2\text{-}1)$$

Where φ is the work function of the material. The binding energies are characteristic for different orbitals of the specific element. The peaks in the XPS spectrum are the identity of particular atoms. Thus, the surface composition of the sample can be analyzed. A chemical environment, such as bonding in molecules causes the binding energies to shift. Therefore, it is possible to determine the identity of surface species, chemical nature (electronic state) as well as quantification. XPS is usually conducted under ultra-high vacuum (UHV) conditions. The information obtained in XPS comes from the surface of the sample, with a sampling depth in the order of 5 nm [106]. Figure 2-5b shows the XPS spectrum of FePc/N-doped graphene composite where the electrons of various elements are labeled. In this work, the XPS has been used to determine the surface composition of all materials studied, type of nitrogen functionalities, e.g., pyridinic, pyrrolic, etc., in the N-doped graphene, FePc, and FePc/N-doped graphene, and electronic interaction in the FePc/N-graphene.

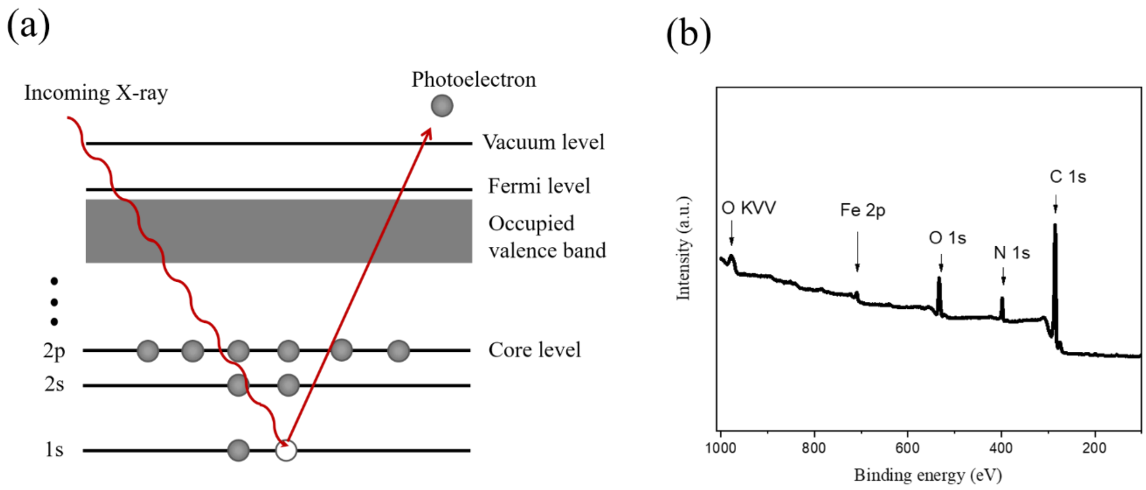

Figure 2-5 Principle of X-ray photoelectron spectroscopy (a) photoelectron generation caused by absorption of incoming light by a core electron, (b) a typical XPS survey spectrum of FePc/N-graphene.

2.2.2 Transmission electron microscopy

TEM is a compelling technique for structural and chemical characterization of materials. TEM can directly image atoms in a crystalline specimen at a resolution close to 0.1 nm, which is smaller than the interatomic distances [107]. TEM provides different types of diffraction patterns such as dots, regions, or circles which have originated from the irradiated area of the sample. Dotted, center-circled and diffuse-circled diffraction pattern indicate mono-crystalline, the polycrystalline and amorphous structure of the specimen, respectively. This type of characterization of materials is essential at a length scale from atoms to hundreds of nanometers. Thus, TEM provides information such as particle size, shape, interparticle interaction, crystallinity, number of layers, and morphology. The specimen should be thin enough to allow to transmit through the sample. The beam of electrons is focused through the specimen. Interaction between the beam and specimen generates scattered electrons according to the Bragg's law along with some unscattered electrons in the forward direction after the sample has been detected [108-110]. The scattered beams at small angles are focused by the objective lens to form a diffraction pattern at its back focal plane. The scattered beams are recombined to create an image in the image plane. The block diagram of a typical TEM shown in Figure 2-6. In the case of diffraction patterns, the whole illuminated area of sample generates electrons to protect the screen, a virtual image of the specimen produced by placing a small aperture in the image plane of the objective lens. The pattern obtained by placing this aperture is called selected area electron diffraction (SAED).

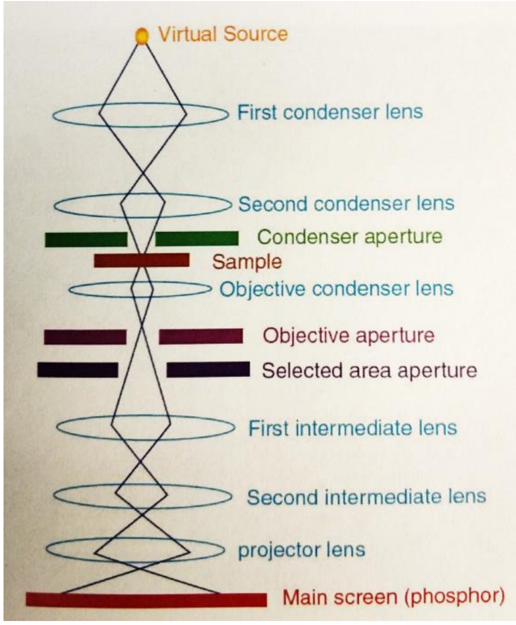

Figure 2-6 Block diagram of a typical transmission electron microscopy [109].

In this thesis, we used JEOL 2100F TEM at 200 KV [à l'école Polytechnique de Montréal] to obtain topological, morphological, compositional and crystallographic information about of the materials studied (the graphene, N-doped graphene, FePc, FePc/N-doped graphene, TiO_2-

nanotubes, and MoS_2/TiO_2-nanotubes). The TEM can be coupled with an analytical technique, energy dispersive X-ray spectroscopy (EDS) used for the elemental analysis. This technique relies on the interaction between the sample and electromagnetic radiation. The X-rays emitted from the sample during bombardment by an electron beam detected and analyzed to characterize the elemental composition of the analyzed volume.

2.2.3 Scanning electron microscopy

SEM is a powerful technique for imaging the surfaces of any material with a resolution down to 1 nm. In SEM, a focused electron beam scans over the surface of the sample in vacuum to extract structural and chemical information point-by-point from a region of interest in the example. The average beam diameter of the SEM is in the range of 5 nm to 2 µm, and the working (accelerating) voltage is in the range of 2 to 50 KV. SEM deals with basically three types of electrons: secondary electrons, backscattered electrons, and elemental X-ray. In SEM, secondary and backscattered electron signals are used for the visualization of the surface of a specimen. Secondary electrons, a result of inelastic collisions, are used to image the surface structure of a sample with the resolution of 10 nm or better. Nevertheless, backscattered electrons, a result of the elastic collision, help to resolve topographical contrast and atomic number contrast with a lateral resolution better than 1 micron. While secondary electron imaging infers energy of the emitted electrons below 50 eV, the backscattered electrons have a strength higher than 50 eV. SEM can only deal with conductive specimens and provides surface imaging. Also, it cannot detect the materials which have an atomic number smaller than that of carbon [108-110].

2.2.4 UV-visible electronic absorption spectroscopy

UV-visible electronic absorption spectroscopy (UV-vis) is one of the optical spectroscopic techniques widely used to study the optical properties of different materials. The basic operating principle of UV-vis spectroscopy based on the measurement of light absorption due to electronic transitions in a sample. In this technique, the wavelength of light required for the automatic transition originates from the UV and visible region of the electromagnetic radiation spectrum. The typical UV-vis consists of a light source, a monochromator, sample cell, and a detector. The light source which emits electromagnetic radiation in the UV region is a deuterium lamp while a tungsten lamp is used for wavelengths in the visible part of the spectrum. The monochromator is a diffraction grating; its role is to disperse the incident beam of light into its component wavelengths. Then the desired wavelength is focused on the sample cell. The light that passes through the sample cell reaches the detector, which records the intensity of transmitted light. The detector is either photomultiplier tubes, photodiodes, or a charge-coupled device [109].

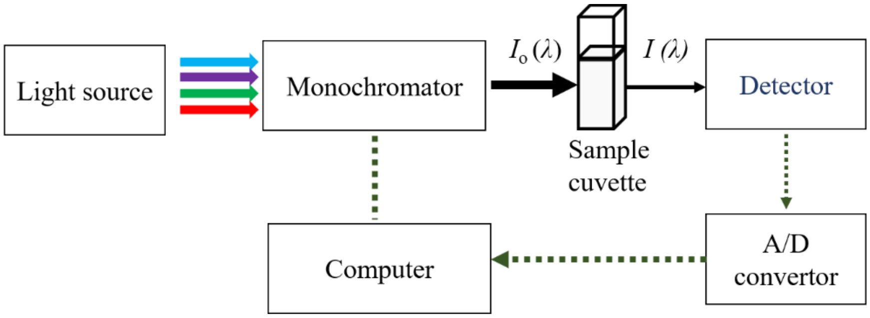

Figure 2-7 Block diagram of key components of a typical UV-vis spectrometer.

As illustrated in Figure 2-7, in a typical measurement, the intensity of light from a light source is measured by a detector, where no sample in the sample cell is taken as background/reference. If the sample absorbs light at any wavelength, the intensity of transmitted light will be reduced. The intensity of transmitted light is then plotted as a function of light wavelength producing the absorption spectrum of a sample. Furthermore, the more effectively a molecule absorbs light of a given wavelength, the greater the extent of light absorption. These absorptions are explained by empirical expression known as Beer-Lambert law, (Equation 2-2), where absorbance, A, is related to the incident light intensity, I_o, and transmitted intensity, I, molar concentration of the sample, c, length of the sample cell, l, in cm, absorption coefficient, α, and molar absorptivity, ε [109].

$$A = log\, I_o/I = \varepsilon cl = \alpha c \qquad (2\text{-}2)$$

Therefore, both I_o and I can be determined empirically, and if l and c are known, the absorption coefficient can also be determined. The absorption coefficient is dependent on the wavelength, and when plotted as a function of wavelength, λ, the spectrum of interest is obtained which represent fundamental electronic properties of the given sample. In most UV-vis spectrometers the wavelength range of 200 nm to 800 nm. The sample cell must be constructed of a material that is transparent to electromagnetic radiation used in the experiment and does not absorb radiation in this region of the spectrum. In this work, the UV-vis was used to determine the quality of the graphene exfoliated by electrochemical method and the electronic interaction in the FePc/N-graphene composite.

2.2.5 X-ray diffraction

The XRD method is a powerful technique for determining the crystal structure of crystalline materials [111]. A crystalline sample scatters incident X-rays according to Bragg's law (Equation 2-3):

$$n\lambda = 2d\sin\theta \qquad (2\text{-}3)$$

Where λ is the wavelength of the X-ray beam, θ is the incident angle, and d is the distance between crystal planes. The value of d is dependent on the Miller indices h, k, and l. The crystal phase of the materials can easily be identified by examining the diffraction pattern. While small angle scattering is useful for evaluation of the average interparticle distance, wide-angle is instrumental for refining the atomic structure of nanoclusters [111]. In this thesis, we have used a diffractometer named X-pert Philips (equipped with a Panalytical X'celerator detector), using graphite monochromatized Cu Kα radiation (λ = 1.54056 Å) to determine the crystal structure of the free-standing nanotubes membrane.

2.3 Electrochemical characterizations

In this subsection, electrochemical techniques employed to characterize and evaluate the electrochemical properties of the electrocatalysts introduced.

2.3.1 Rotating disk electrode

The rotating disk electrode (RDE) is a widely used system to evaluate the electrocatalytic activity of ORR catalysts for fuel cells. It allows for the screening of catalysts under controlled quasi fuel cell conditions, *i.e.*, constant reactant flux and steady state. Information that can be obtained includes kinetic parameters such as the rate regular of the reaction, and electron transfer number [112, 113]. The RDE is simple to construct with a variety of electrode materials. Its assembly consists of a disk of the electrode material (inert metals and glassy carbon) embedded into a rod of an insulating material such as Teflon or epoxy resin (Figure 2-8a). The assembly is often referred to as an electrode tip. The electrode tip is attached to a control motor directly by a flexible rotating brass shaft and is rotated at a particular frequency, f (revolutions per second). From the rotation frequency, a useful descriptor of rotation rates, the angular velocity, ω (s^{-1}) is determined ($\omega = 2\pi f$). Electrical connection is made to the electrode by means of a brush contact [112]. RDE creates a totally defined solution flow pattern in which the mass transport of the species is almost completely due to convection. Thus, RDE can be used to calculate parameters related to mass transport.

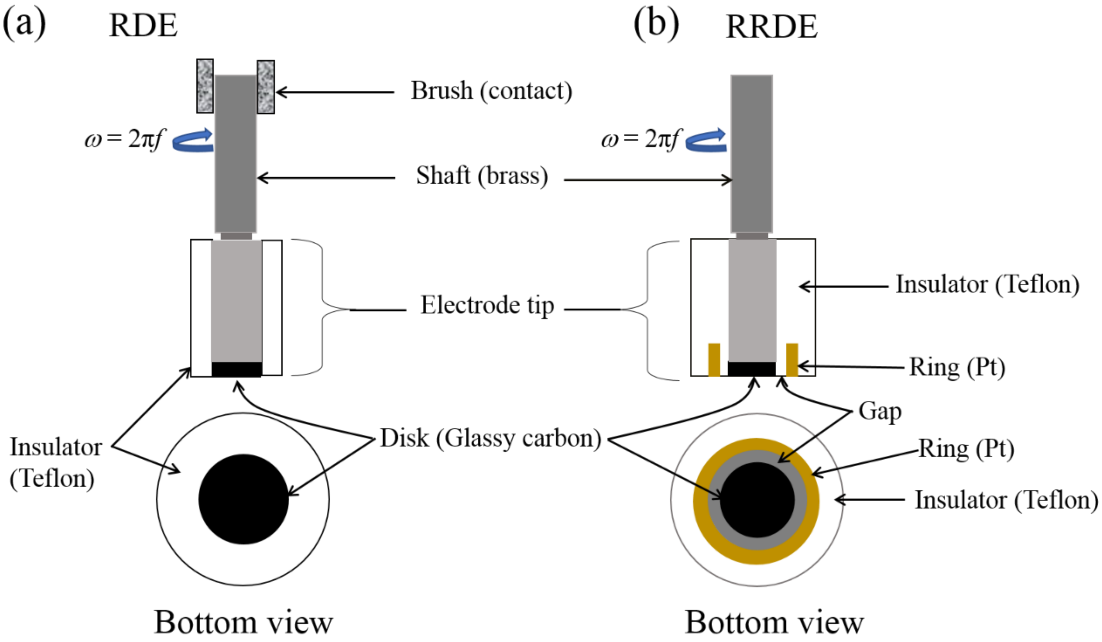

Figure 2-8 Schematic presentation of the working electrode, (a) rotating disk electrode and (b) rotating ring-disk electrode.

2.3.2 Rotating ring-disk electrode

Rotating ring-disk electrode (RRDE), a variant of the RDE which includes a glassy carbon disk, and second electrode a concentric ring electrode (Pt or Au) placed outside the disk and used to analyze the species generated on the disk (Figure 2-8b). The ring is electrically insulated from the disk so that their potentials can be controlled independently. By measuring the current at the ring electrode, information about what is occurring at the disk electrode surface can be obtained. For example, if the potential of the ring is held at the foot of the wave for the reduction of species, O, present at disk electrode surface to form a product R, which is swept over to the ring by the radial flow. At the ring, the product R will be oxidized back to species O (or be collected). The ring current is recorded from the oxidation of R, at the ring electrode. The ring current relates to disk current by a quantity N, called the collection efficiency. The collection efficiency is the fraction of the material from the disk, which subsequently flows past the ring electrode. It can be expressed as a fraction between 0.0 and 1.0 or as a percentage. The collection efficiency is empirically determined using a well-defined redox system. The most straightforward redox couple is ferrocyanide/ferricyanide and is commonly used as the basis for evaluation of the collection efficiency [113-115]. The RRDE is placed in an electrolyte of interest (i.e., 0.1 M KOH) containing a small concentration (10 mM) of potassium ferricyanide, $K_3Fe(CN)_6$. The experiment is performed at varying rotation frequency, between 500 to 2000 rpm. The ring electrode is held at a constant potential of 1.55 V. At this potential, oxidation of $[Fe(CN)_6]^{4-}$ produced at disk electrode proceeds under diffusion control, while the oxygen evolution reaction at Pt ring is negligible [114-117]. The collection efficiency is then determined from the ratio of limiting ring (i_R) and disk (i_D) currents (in units of mA). During oxygen reduction experiment, the HO_2^- species generated at the disk is detected at the ring electrode. The corresponding electron transfer number (ne^-) and the fraction of current due to HO_2^- is recorded by ring electrode (χHO_2^-) during ORR is calculated by Equations

1-3 and 1-4. The RRDE experiments are usually carried out with a bipotentiostat, which allows separate adjustment of disk and ring potentials. Several different types of tests are possible at the RRDE. The most common measurements are collection experiments, where the species generated from the disk is detected at the ring, and shielding experiments, in which the flow of bulk electroactive species to the ring is perturbed because of the disk reaction [113].

2.3.3 Electrochemical cell setup

The electrochemical measurements were carried out in a three-electrode cell system under either a dry nitrogen or oxygen atmosphere at ~22 °C. The three-electrode electrochemical cell setup and block diagram of RRDE apparatus for a bipotentiostat are shown in (Figure 2-9a-b).

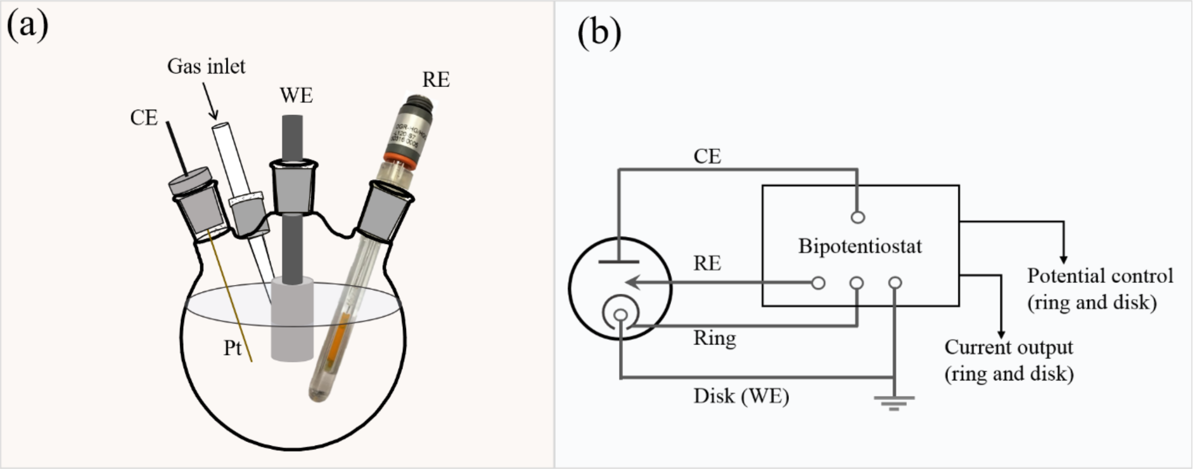

Figure 2-9 Three-electrode electrochemical cell system. (a) A cell setup, and (b) block diagram of RRDE apparatus for a bipotentiostat.

The electrodes used in this study were; the working electrode (WE): modified glassy carbon (GC), 5.61 mm, or 5 mm. Reference electrodes (RE) were saturated calomel electrode (SCE) for acidic electrolyte and Hg/HgO in the alkaline electrolyte. In all ORR experiments, the counter electrode

(CE) was Pt-wire and graphite rod for the HER. All the electrochemical measurements were conducted by using either a bipotentiostat, PINE Research Instrumentation (Model PGSTAT-72637) workstation or an Autolab electrochemical system (Model, PGSTAT-302, Ecochemie, Brinkman Instruments).

2.3.4 Linear sweep and cyclic voltammetry

Linear sweep and cyclic voltammetry methods have been widely employed for numerous necessary studies of electrochemical systems and analytical purposes. These techniques are especially powerful tools in the study of electrode reaction mechanisms and electrode surfaces. In linear sweep voltammetry, the potential is linearly swept concerning time (*t*) at a constant scan rate (ν) from an initial potential E_1 to a final potential E_2. Figure 2-10a shows excitation where the potential is swept from positive to negative with time while recording the variation of current (*i*) as a function of potential (*E*). If the potential swept in the cathodic direction with the initial potential well positive of the formal potential of an electrode ($E°$) for the reduction, only nonfaradaic currents would flow for a while. When the electrode potential reaches the vicinity of $E°$, the reduction process begins, and the current starts to flow.

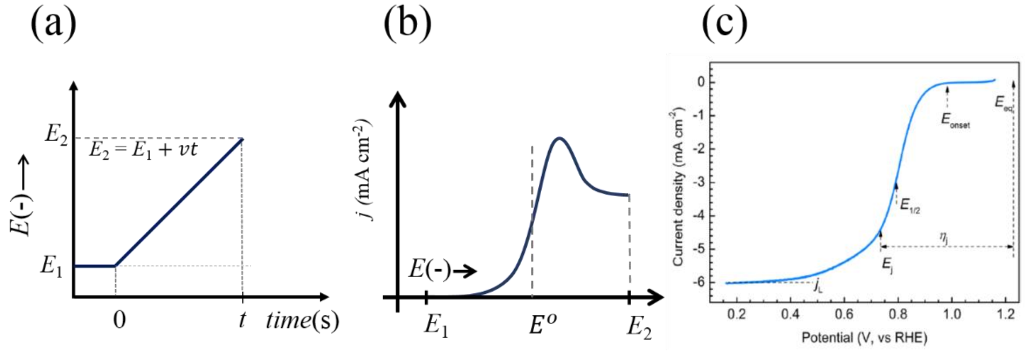

Figure 2-10 Line sweep voltammetry measurement. (a) Excitation of linear sweep voltammetry, (b) typical linear sweep voltammogram of reduction of electroactive species for stationary electrode [112]. (c) Characteristic ORR polarization curve of Pt/C recorded by RDE system with the electrode rotation rate of 2000 rpm [118].

As the potential is swept further to more negative, the surface concentration of the oxidized species decreases drastically; hence, the flux to the surface (and the current) increases. As the potential moves past $E°$, the surface concentration of oxidized species drops nearly to zero, mass transfer of oxidized species to the surface reaches a maximum rate, and then it declines as the depletion effect begins. Therefore, the resulting current-potential curve is peaked, as depicted in Figure 2-10b. A typical LSV of oxygen reduction for Pt/C recorded from RDE system with an electrode rotation rate of 2000 rpm is shown in Figure 2-10c. From the LSV some performance parameters of the reaction kinetics are identified: the onset potential (E_{onset}), half-wave potential ($E_{1/2}$), overpotential under a specific current density (η_{j}), and diffusion-limited current density (j_{L}). The diffusion-limited current density of the plateau (Figure 2-10c) is calculated from the Levich equation (Equation 2-6). This equation applies to the mass-transfer-limited conditions at the electrode surface and predicts that j_{L} is proportional to the square root of angular velocity (ω) in the unit of rad s^{-1} [118]. Where n, D_o, v, F and C_{O}^{*}s the total electrons transfer number, diffusion coefficient of the reactant, kinematic viscosity of the electrolyte, Faraday constant and concentration of the reactant in the bulk electrolyte, respectively.

$$j_L = 0.62nFAD_o^{2/3}\omega^{1/2}\nu^{-1/6}C_{\mathrm{O}}^{*} \qquad (2\text{-}6)$$

$$\frac{1}{j} = \frac{1}{j_k} + \frac{1}{j_L} = \frac{1}{j_k} + \frac{1}{0.62nFAD_o^{2/3}\omega^{1/2}\nu^{-1/6}C_O} \qquad (2\text{-}7)$$

The electrochemical and hydrodynamic properties of RDE/RRDE are correlated with the Koutecký-Levich (K-L) equation (Equation 2-7). Where, j is the measured current density, and j_{k} represents the current density in the kinetic controlled effects, when the mass transfer are efficient to keep the C_{O} at the electrode surface equal to the C_{O}^{*} value, regardless of the electrode reaction.

From Equation 2-7, the plot of j^{-1} vs $\omega^{-1/2}$ at a given value of η is predicted to be linear, and the intercept of the plot allows the determination of kinetic parameters. Also, the ne^- can be deduced from the slope of the linear plot.

The ORR mechanism of oxygen reduction can be quantitatively probed based on the forced convection methods on the RRDE/RDE. In the RRDE method, the ORR takes place on the disk electrode, and production of peroxide/hydroperoxyl (HO_2^-) can directly be measured by recording its oxidation current (Equation 2-8) on the ring disk. Figure 2-11 depicts the schematic presentation of the oxygen reduction reaction processes on a RRDE, where k_1, k_2, k_{-2}, k_3, k_4, and k_5 are the reaction rate constants. It follows that when $k_2 = 0$, direct $4e^-$ transfer occur in the O_2/OH^- redox couple. And when the $k_1 = k_3 = 0$, $2e^-$ transfer O_2/HO_2^- redox couple is the only process occurring at the electrode surface [119].

$$HO_2^- + OH^- \rightarrow O_2 + H_2O + 2e^- \qquad (2\text{-}8)$$

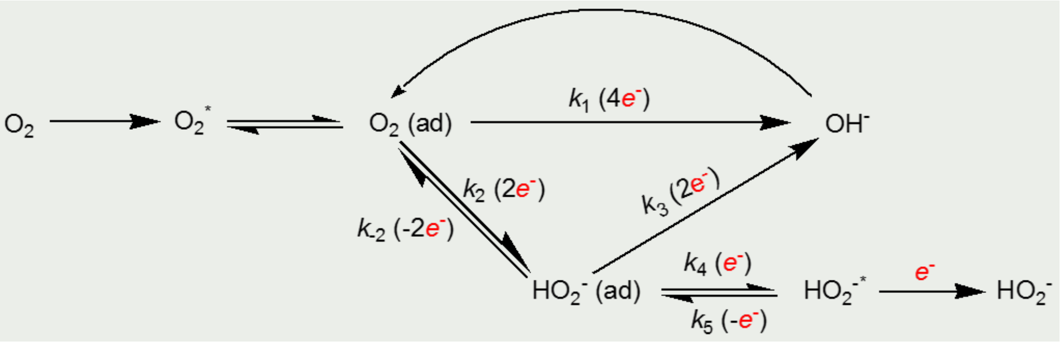

Figure 2-11 Schematic presentation of the oxygen reduction reaction processes on a rotating ring-disk electrode [119].

The total number of electrons (ne^-) transfer during the reduction of one oxygen molecule can be calculated by considering the disk current (i_D) and ring current (i_R) using Equation 2-9 where N is the collection efficiency of the RRDE, defined as the fraction of product from the disk to the ring. Similarly, the fraction of the HO_2^- ($\chi_{HO_2^-}$) is defined as the ratio of total moles of HO_2^- produced to O_2 reduced and is calculated by Equation 2-10. For RDE measurement, the electron transfer number can be calculated by a method based on the Koutecký-Levich theory, specifically using Equation 2-7, which describes the current density behavior on the RDE [112, 114].

$$ne^- = \frac{4i_D}{i_D + i_R/N} \tag{2-9}$$

$$\chi_{HO_2^-} = \frac{2i_R/N}{i_D + i_R/N} \tag{2-10}$$

On the other hand, cyclic voltammetry (CV) is a reversal technique of the LSV where the potential of an electrode in solution is linearly scanned from an initial potential possibility to the final potential and back to the initial potential making one cycle (see Figure 2-12a). The data are recorded as current density vs. potential, and represented in a waveform called a cyclic voltammogram, as shown in Figure 2-12b. A typical CV of Pt/C recorded in 0.1 M KOH solution saturated with nitrogen gas is shown in Figure 2-12c. The CV is a versatile technique, especially for initial electrochemical studies of new systems and in obtaining information about somewhat complicated electrode reactions. CV can probe information on redox active species within the catalyst, which can be correlated to the catalytic activity and ultimately giving information about the active site. If active redox species are present, a reduction and oxidation peak will be observed.

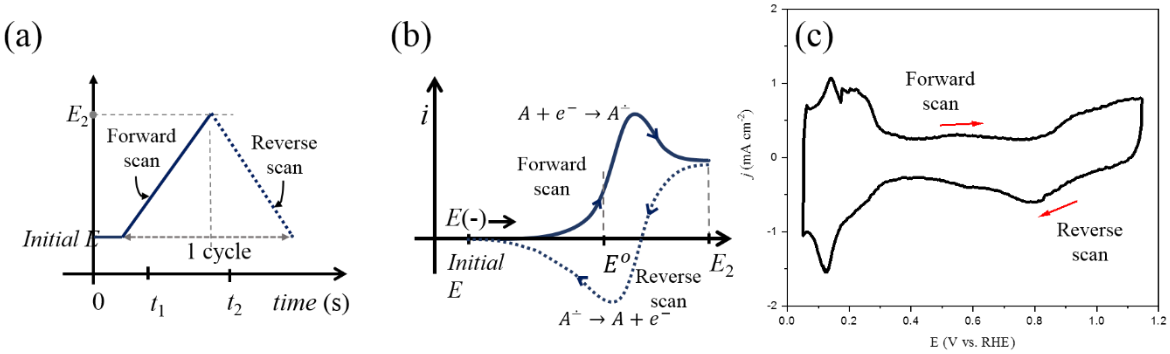

Figure 2-12 Cyclic voltammetry measurement. (a) Cyclic potential scan, (b) a resulting cyclic voltammogram of electroactive species for stationary electrode [113], (c) a typical cyclic voltammogram of Pt/C in 0.1 M KOH recorded at a scan rate of 50 mV s^{-1}.

Both techniques (LSV and CV) are used in this study to evaluate the activity and durability of the prepared material for the ORR. In practice, first, the background currents are recorded in the presence of inert atmosphere (N_2-saturated electrolyte). Under similar experimental conditions, ORR currents are recorded in the O_2-saturated electrolyte. Then the ORR currents (Faradaic currents) are obtained by subtraction of the background currents (measured under N_2) from the current measured under O_2. To condition the catalyst layer, the potential is cycled at various scan rates in the presence and absence of O_2 until no change is observed in the voltammogram. The initial potential cycling ensures that the surface is electrochemically clean, and the whole accessible catalyst surface area is adequately wet with electrolyte [120].

2.3.5 Accelerated durability test

The accelerated durability test (ADT) was conducted with a glassy carbon modified electrode. The electrode was cycled between 0.6 and 1.2 V for 5000 cycles in O_2-saturated 0.1 M KOH solution at room temperature, with scan rate 50 mV s^{-1}. Before and at the end of 5000 cycles, LSVs were recorded to track the degradation of the catalysts. The scan rate of 10 mV s^{-1} and the rotation of the electrode of 1600 rpm were used.

2.3.6 Chronoamperometry

Chronoamperometry (CA) has the simplest potential waveform, the potential step. During CA measurement, the potential is changed instantaneously from the initial possibility to the first step potential, and it is held at this value for the first step time. If the experiment end-up at this step, it is a single potential step experiment. However, if the potential is changed to the second step potential after the first step time, and which is then held at that value for the second step time it is a double potential step experiment [24, 112, 121]. CA is a time-dependent technique where a square-wave potential is applied to the working electrode. The current of the working electrode is measured as a function of time. The current at the working electrode fluctuates according to the diffusion of an analyte from the bulk solution toward the electrode surface. Therefore, CA can be used to measure the current-time dependence of the diffusion-controlled process occurring at a working electrode surface. In this work, CA experiments were carried out to examine the electrochemical activity and stability of the electrocatalysts.

2.4 Presentation of results

The results are presented into three independent chapters, each corresponding to a particular article. In chapter 3, controlled fabrication of large pieces high-quality graphene through the low-cost electrochemical method and their use as efficient metal-free ORR electrocatalysts were presented. Chapter 4 shows the results of the preparation of FePc/N-doped graphene as non-precious metal electrocatalysts for ORR using a simple, direct, and low-cost approach. Finally, chapter 5 is the extension of the application of the electrochemical method in controlled fabrication of TiO_2-nanotubes membrane using titanium as substrates and their potential application as an active electrode for hydrogen evolution.

Chapter 3 Graphene-Based Metal Free Electrocatalyst for Oxygen Reduction

The use of precious metal-based materials as the benchmark electrocatalysts to facilitate the oxygen reduction reaction (ORR) limit the mass application of fuel cells. The exploration of efficient, low cost and highly durable non-precious ORR electrocatalysts, to replace the rare and expensive Pt-based catalysts, is critical. In this work, we fabricate a few layers of high-quality graphene by a straightforward electrochemical approach using abundant and low-cost materials. Further, we investigate the use of the graphene as efficient and durable metal-free ORR electrocatalyst.

3.1 Introduction

The oxygen reduction reaction (ORR) is a fundamental process in energy conversion devices such as fuel cells [5] and energy storage technologies such as metal-air batteries [3, 122]. The ORR is a cathodic process which plays a critical role in the overall performance of a fuel cell. In aqueous solution, the ORR is a slow and highly irreversible process [118, 123, 124]. Due to the inherent nature of the sluggish kinetics of ORR, the demand for highly efficient electrocatalysts is indispensable to improve the performance of fuel cells.

Currently, platinum (Pt) based catalysts are the only commercially available efficient catalysts for fuel cells. However, the high cost and low abundance of Pt hinder the wide-spread commercialization of hydrogen fuel cells [63, 125, 126]. Besides, in normal test conditions, Pt-based catalysts suffer from susceptibility to methanol cross-over, carbon monoxide poisoning, carbon corrosion, and Pt particles agglomeration [16, 125, 127]. Considerable efforts have been directed towards 1) decreasing Pt content in the catalysts by developing either Pt-metal alloy or novel support materials and 2) replacing Pt-based catalysts by either non-precious metal [25, 26, 70, 128, 129] or metal free materials [21, 23, 79, 130]. In particular, the exploration of highly efficient and inexpensive metal-free electrocatalysts for the ORR is widely investigated [21, 78, 131]. Among various alternatives, graphene is an emerging and promising candidate for a metal-free catalyst to replace Pt, especially in alkaline media.

Graphene, a two-dimensional sheet of sp^2 carbon atoms covalently bonded into a honey comb lattice matrix, displays unique physicochemical properties, such as large surface area, high electronic conductivity, and excellent chemical stability [32, 132, 133]. These remarkable features may be useful for many potential applications such as electronic devices, transparent electrodes, catalysis, energy storage, and conversion [134-137]. Moreover, it has been shown that the catalytic activity of graphene can be increased significantly by doping it with heteroatoms such as N and S atoms [32, 133]. Accordingly, when graphene is doped with N-atoms, it is found to have excellent electrocatalytic activity towards ORR in alkaline media [138, 139].

The specific method used to prepare graphene is also crucial for ORR electrocatalysis, as it is closely related to the quality, yield, and efficiency of the final product, as well as its production cost. Therefore, methods that preserve the inherent properties of graphene, while avoiding the use of any hazardous chemical/condition, are highly desired [98, 140, 141]. However, in the most traditional Hummer’s method for the preparation of graphene, strong mineral acids and oxidizing agents are used, causing several manufacturing challenges which are not easy to address [16, 142]. On the other hand, for ORR applications, catalysts with high surface area, excellent electronic conductivity, and balanced, functional groups are highly desired. Although perfect reduced graphene oxide (r-GO) inherently has a high surface area and excellent conductivity, its hydrophobic nature causes challenges such as electrode wettability, thereby decreasing the ORR performance [143].

On the other hand, the highly hydrophilic graphene oxide shows poor conductivity, which is unfavorable for ORR. Therefore, a method that could lead to high-quality graphene with well-balanced catalytic properties is highly desirable. In this context, electrochemical exfoliation is a promising method for the preparation of graphene for ORR electrocatalysis. The electrochemical approach potentially has many advantages over traditional chemical methods, including its being simple, easily scalable, and cost-effective, and most importantly allowing the tuning of the level of oxidation [16, 99]. Graphene exfoliated using electrochemical methods are of high quality, with a few defects. In this work, taking advantage of the electrochemical exfoliation method, we use two types of raw materials, i.e., graphite plate and graphite foil, to prepare high-quality graphene under different reaction conditions. Systematic studies revealed that N-doping was successfully achieved with pyridinic nitrogen dominance. The ORR activity of the catalysts varied significantly with the exfoliating and post-exfoliation conditions. The optimal N-doped graphene exhibits comparable ORR performance to commercial Pt/C catalysts. Our work suggests that the low cost and environmentally friendly electrochemical method is a potentially viable approach to prepare graphene with excellent ORR activity.

3.2 Experimental

3.2.1 Materials.

Graphite plate (99%) and foils (0.5 mm, 99.8%) were purchased from Alfa Aesar, Fischer Scientific. Ammonium sulfate ($(NH_4)_2SO_4$, 99 %)), Polyvinylpyrrolidone (average molecular weight 40,000) (99%), 2,2,6,6-Tetramethyl-1-piperidinyloxy, (TEMPO) (98%), Pt on Vulcan

(20%, XC-72R; E-TEK), potassium hydroxide (KOH) and reagent alcohol, were purchased from Sigma-Aldrich. All chemicals were of analytical grade and used without further purification.

3.2.2 Electrochemical exfoliation of graphite

The exfoliation of graphene (GP) was carried out using a DC power supply in a two-electrode cell as reported elsewhere with slight modification [16, 140, 141]. In a typical synthesis, graphite substrates (graphite foils and plates) served as a positive electrode, and Pt wire acted as a negative electrode in an electrochemical cell filled with $(NH_4)_2SO_4$ (0.1 M) aqueous solution. A constant biased potential of ±10 V was applied between the two electrodes. The exfoliation of graphene was achieved at room temperature (~22 °C) and in some cases carried out at different temperatures (22, 40, 60, and 80 °C) in a heated oil bath. The duration of the exfoliation process depended on the graphite source, the concentration of the electrolyte, and the applied bias potential. To gain insights on the quality of the exfoliated graphene, different doses of an organic reagent, TEMPO was added to some recipes. Figure 3-1 display the scheme of exfoliation of the graphite substrate. The as-exfoliated product was collected and thoroughly washed with deionized water and reagent alcohol by vacuum filtration, then dispersed in water by sonication for 15 minutes. The graphitic particles which are not wholly exfoliated were separated from graphene by centrifuging the dispersion at 1000 rpm for 10 minutes. The fine suspension in the upper part of the centrifuge tube was fractionated into components with different graphene layers by controlling the centrifugation speed from 2500 rpm (to get multi-layers), 5000 rpm (to get thin layers) to 14000 rpm (to obtain very thin layers). The graphene powders were obtained by freeze-drying. While, the graphene powder samples collected from graphite plates denoted as GP, those from graphite foils denoted as GPf. The obtained graphene was screened for oxygen reduction reaction in alkaline solution. The optimized samples were functionalized with nitrogen atoms by heating the graphene powders at 950 °C in argon for 60 minutes and then in ammonia (NH_3) for 15 minutes to obtain nitrogen-doped graphene.

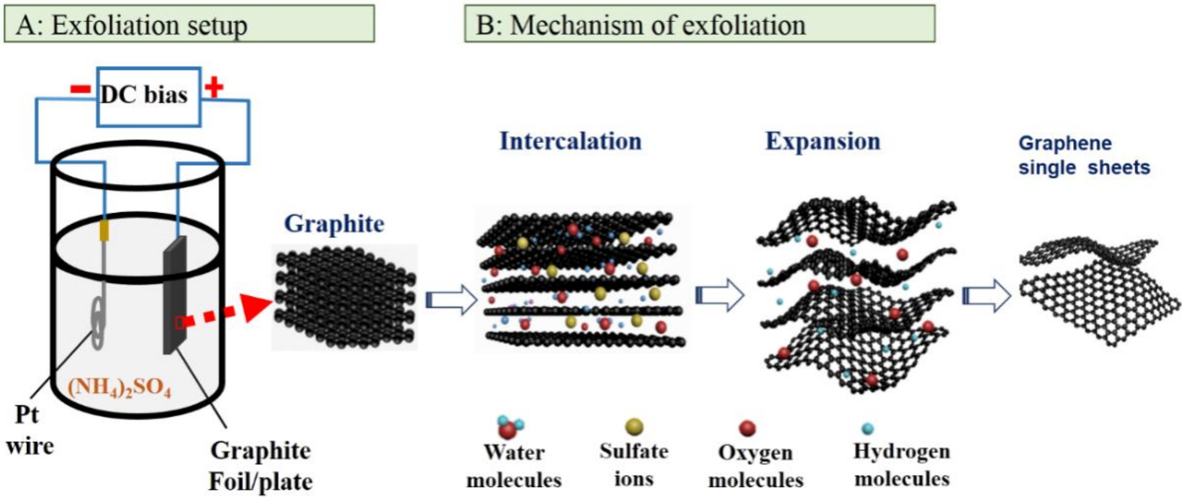

Figure 3-1 Schematic illustration of the setup for the electrochemical exfoliation production of graphene, and the exfoliation mechanism in aqueous $(NH_4)_2SO_4$ solution.

3.3 Characterization of graphene

3.3.1 Physical characterization

The structural morphologies and composition of the catalysts were characterized using transmission electron microscopy (TEM, JEOL JEM-2100F operated at 200 kV), field emission scanning electron microscopy (FE-SEM) and X-ray photoelectron spectroscopy (XPS) using a VG (Escalab220i - XL) equipped with Al K_α line as an excitation source. The electronic structure was investigated using a UV-vis absorption spectrophotometer (thermos scientific Nanodrop 2000c).

3.3.2 Electrochemical characterization

The graphene ink was prepared by dispersing 10 mg of the catalyst to the solution of ethanol (350 μl) and Nafion ionomer (95 μl, 5wt %), followed by two cycles of 15 minutes sonication and agitation in a vortex shaker. This ink, then casted on the disc part of the rotating ring disc electrode (RRDE, 5.61 mm diameter glassy carbon disk and Pt ring) or the 5.0 mm diameter glassy carbon rotating disc electrode (RDE), with a catalyst loading of 0.8 mg cm^{-2}. For comparison, 20 wt% Pt/C catalyst (E-ETK) was prepared through the same procedure with a loading amount of 100 μg/cm^2 (20 μg_{Pt}/cm^2). All electrochemical measurements were carried out in a three-electrode cell at room temperature using the Autolab electrochemical system (Model, PGSTAT-302, Ecochemie, Brinkman Instruments). In all experiments, Pt wire and mercury/mercury oxide (Hg/HgO) was used as the counter electrode (CE) and a reference electrode (RE), respectively. The ORR activity of the graphene catalysts was evaluated in O_2 saturated 0.1 M KOH solution with scan rates of 50 mV s^{-1} and 10 mV s^{-1} for cyclic Voltammetry (CV) and linear sweep voltammograms (LSVs), respectively, recorded in the range of 0 – 1.2 V. To record LSVs, the electrode was rotated at 1600 rpm. The potentials in this work are normalized to the reversible hydrogen electrode (RHE). The peroxide yield (H_2O_2%) and the electron transfer number (n) were calculated using a ring, disk currents (I_r, I_d) and the estimated collection efficiency (N = 0.37) using Equation 2-4 and Equation 2-5. To investigate the stability of the catalysts accelerated degradation testing (ADT) were performed in the oxygen-saturated 0.1 M KOH between 0.6 and 1.0 V vs. RHE at 100 mV s^{-1}. The LSV tests were carried in the oxygen-saturated electrolyte at the beginning and end of each ADT to evaluate the effect of the cycles on catalytic activity.

3.4 Results and discussion

3.4.1 The electrochemical exfoliation of graphite

Figure 3-1 illustrates a process of an electrochemical exfoliation of graphite which is widely accepted, to begin with, the oxidation of graphite edges and grain boundaries, followed by intercalation of water molecules and electrolyte ions into interlayers of graphite when a bias potential is applied [16, 98, 99, 140, 141]. The electrolysis of the intercalated species in the interlayers of graphite produces some gaseous products which cause the expansion of graphitic layers and consequently separation into particles with loosely attached layers or individual sheets of graphene [98, 99]. However, the mechanism of the exfoliation steps could be slightly different depending on the type of graphite raw material. For example, as shown in Figure 3-2, during the exfoliation of graphite foils to GPf, we observed only the expansion of graphite foil using a static bias potential of -10 V for five minutes. For both processes, expansion, and exfoliation were seen when the bias potential was +10 V for a similar duration. This observation can be accounted for by the degree of compaction of the two kind of graphite substrates and the mechanism of exfoliation. The graphite plate is made of fine grain, with high strength and density graphite as well as a high degree of compaction, it is very hard compared to the soft nature of the graphite foils.

In the mechanism of graphite exfoliation, there are three suggested key processes; (i) oxidation of the edge sites and grain boundaries, (ii) intercalation of ions within the graphitic layers, and (iii) expansion and separation [16, 99]. Generally, in the optimized conditions of exfoliation of graphite foils, we applied a bias potential of +2.5 V for wetting, then ramped up to +10 V for the oxidation of edges, intercalation, and exfoliation. Afterward, -10 V is applied for the reduction of oxidized groups [16]. Due to the soft nature of the graphite foil, during the wetting process (by application of +2.5 V), some of the electrolytes ions and water molecules easily intercalate into the layers of graphite foils. Since the graphite edges are not oxidized, when a bias potential is changed to -10 V, the reduced gaseous products of the electrolysis only causes the expansion of the graphite foil, but the force is not enough to create the separation of the graphene sheet. However, when a bias potential of +10 V is applied after wetting, all three key processes happen in sequence, i.e., the exfoliation is initiated by oxidation of graphite edges, followed by the intercalation, expansion (electrolysis of gaseous products) and separation to graphene. On the other hand, the alternation of bias potential -10/+10 V was necessary to achieve the exfoliation of graphite sheets using a graphite plate as a precursor. The difference in the mechanism of exfoliation is probably caused by the different compact degree and level of the order of the graphite used.

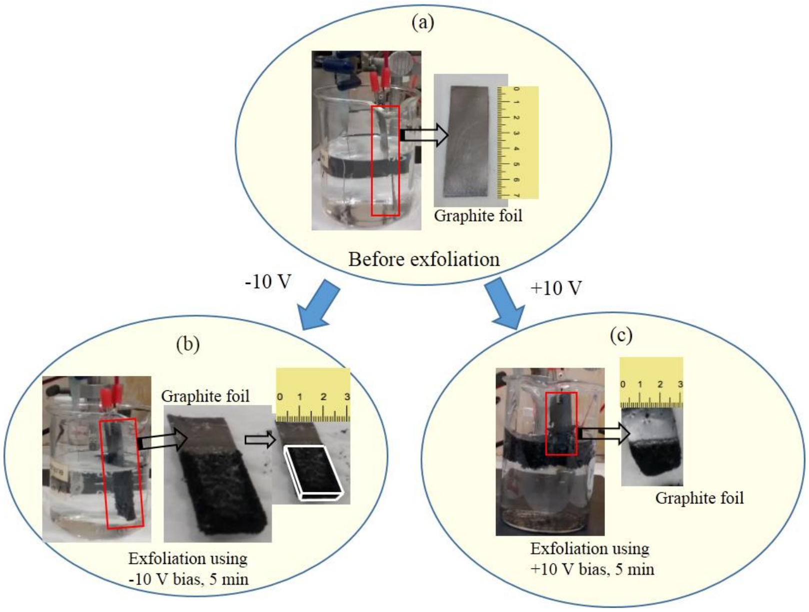

Figure 3-2 Digital image of the experimental setup and foil substrates before and after the electrochemical exfoliation experiment in 1.0 M $(NH_4)_2SO_4$ solution. (a) Before an exfoliation begins, (b) after exfoliation using bias of -10 V and (c) after exfoliation of a graphite foil using +10 V bias potential. Complete exfoliation of graphite foils was observed only when the positive static biased potential applied or alternation to the bias potentials (±10 V).

3.4.2 The structural morphology of graphene samples

TEM and SEM used to investigate the morphologies of as-synthesized graphene samples. Figure 3-3 shows representative TEM images of graphene exfoliated from a graphite foil (Figure 3-3a-c) and graphite plate (Figure 3-3d-f). The graphene sheets from both graphite sources appear to be large, uniform, and very thin. To identify the layer thickness of the samples, we performed high-resolution TEM (HRTEM). Figure 3-3b,e displays typical HRTEM images showing the folded edges of graphene sheets reveal that the graphene is only a few layers. To obtain information about the crystal structure of the as-exfoliated graphene samples, we performed selected area electron diffraction (SAED) analysis. Figure 3-3c,f depict the SAED pattern images which indicate a clear single crystalline lattice structure with a characteristic hexagonal diffraction pattern of few layers graphene obtained from both graphite sources [98, 144]. However, there are some slight differences when using different graphite precursors. For example, very uniform, large piece and ultrathin (1-2 layers) graphene sheets are obtained when the graphite foil is used, while small-sized pieces with less-uniform thickness graphene sheets are obtained when the graphite plate is used (as shown in Figure 3-3a, d). The degree of crystallinity is higher in the graphene that is exfoliated from graphite foil (GPf) than the graphite plate (GP). This could be attributed to the longer exfoliation time when the graphite plate is used, compared to graphite foils. The exfoliation process, using a graphite plate as precursor took about one hour or longer to obtain a significant amount of graphene, while it only takes 3-5 minutes to complete the process when using graphite foils. The long exfoliation time of graphite plate imparts the as-exfoliated GP to a more prolonged oxidizing environment, resulting in the formation of relatively small pieces with a large number of oxidized functional groups.

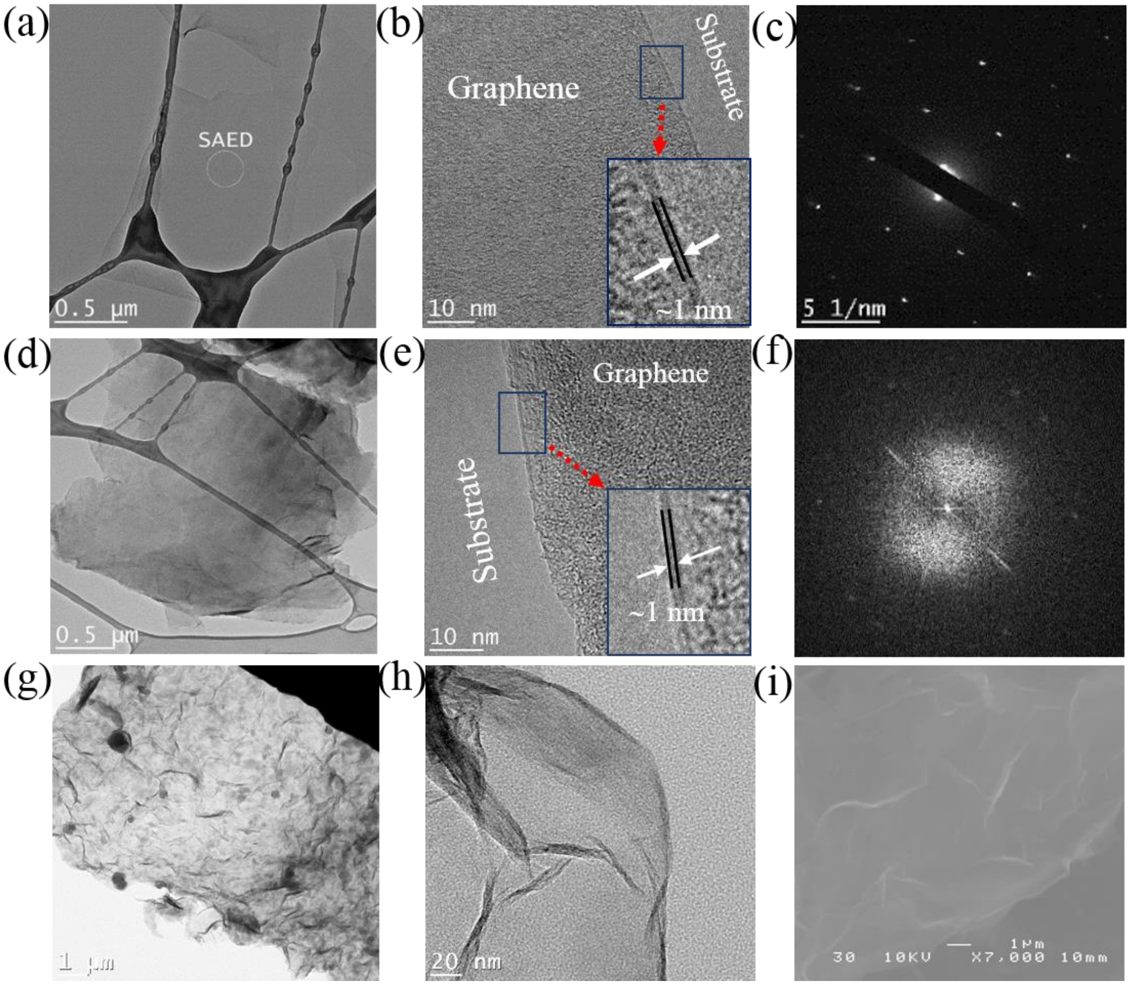

Figure 3-3 TEM images and selected area electron diffraction (SAED) of typical graphene samples exfoliated from graphite foils and plates. (a-c) Graphene of graphite foil (GPf). (d-f) Graphene of graphite plate (GP). (g,h) TEM images of N-doped graphene. (i) SEM images of GP at low magnification. Few-layers characterize the graphene from both graphite substrate, uniform, have a well-defined crystalline structure, and large sized.

The selected area electron diffraction (SAED) features with less well-defined diffraction spots (Figure 3-3f), confirms the poor crystalline structure of the GP [145]. Figure 3-3g-h display the TEM images of graphene samples after NH_3 pyrolysis (N-GP950). It is evident that the N-GP950 retains all features of parent graphene that is large, uniform as well as a few layers. Figure 3-3i depict the SEM image of as-exfoliated GP, further confirming that the surface of graphene to be thin and uniform.

3.4.3 The degree of oxidation in graphene

The degree of oxidation in graphene occurred during the exfoliation process was investigated by UV-vis absorption spectroscopy (Uv-vis). The analysis of electronic absorption gives useful information about the extent of oxidation during the exfoliation process. Figure 3-4 display the UV-vis absorption spectra of the graphene samples exfoliated in an electrolyte containing a different dosage of organic reducing agent, TEMPO. The absorption peak of the as-exfoliated graphene in an electrolyte containing no TEMPO dosage is observed at about 257 nm. The peaks, then gradually redshifted to 262, 266, and 270 nm as the amount of TEMPO in the electrolyte increased from 0.32, 0.64, to 0.96 mmol, respectively.

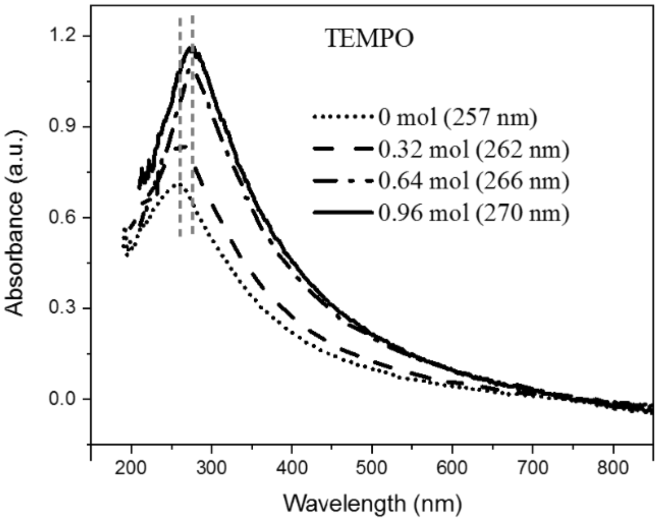

Figure 3-4 UV-vis absorption spectra are showing absorption peaks of the graphene samples prepared in 0.1 M $(NH_4)_2SO_4$ electrolyte containing different doses of organic reducing agent 2,2,6,6-Tetramethylpiperidine-1-oxyl (TEMPO). The reducing agent was added to reduce part of the functional groups introduced during exfoliation.

These results are in good agreement with the absorption peak maximum of reduced graphene oxide, which is around 271 nm, and that of the graphene oxide occurs at ca. 231 nm [140, 146]. Furthermore, these results show the as-exfoliated graphene contains less oxidized carbon atoms.

The observed shifts in the absorption peak can be attributed to the restoration of C-C sp^2 hybridization within the graphene lattice structure. The absorption in this region (270 nm) arises from the excitation π-plasmon resonance in the graphene structure [146-148]. Therefore, the occurrence of the absorption peak at ca. 257-270 nm for the as-exfoliated graphene further confirms the production of high-quality graphene with a controllable degree of oxidation employing electrochemical exfoliation methods.

3.4.4 The surface chemical composition of graphene

To investigate the surface chemical composition of the graphene samples, we conducted X-ray photoelectron spectroscopy (XPS) analysis. Figure 3-5 displays the XPS spectra of as-exfoliated graphene (GP) and nitrogen doped graphene (N-GP950). The survey spectra are shown in Figure 3-5a, suggests that the as-exfoliated graphene contains two peaks, sharp and prominent C 1s peak at binding energy (BE) of 284.6 eV and relatively small O 1s peak at about 532 eV. The surface contents of O and C in the GP measured by XPS is 5 at% and 95 at%, respectively. The calculated ratio of C/O to be 19. This observation suggests the as-exfoliated graphene have fewer oxygen-containing functional groups. The high ratio of C/O implies that the as-exfoliated graphene has a high degree of sp^2 carbon [16, 147, 149]. On the other hand, the survey spectrum of the N-GP indicates the presence of N 1s peak in addition to C 1sand O 1s peaks, suggesting the successful doping of N atoms into the GP during pyrolysis in NH_3. The surface concentration of C 1s, N 1s, and O 1s in the N-GP950 as estimated is 96.7 at%, 2.0 at% and 1.5 at%, respectively. The surface concentration of O in graphene found to decrease by 3.5 at% after pyrolysis. This decrease is attributed to the decomposition of carboxyl functional groups during pyrolysis as well as replacement of oxygen by nitrogen bonded to carbon. The plots in Figure 3-5b show deconvolution of C 1s peak into a component main at binding energy (BE) of 284.6 eV for C=C, and minor peaks for C-O and C=O at BE of 285.5 eV and 286.7 eV, respectively in the as-exfoliated GP. The appearance of the C 1s peak with the main component at 284.6 eV for C=C, minor peaks at 285.5 eV for C-O and 286.7 eV for C=O is a signature of the low level of oxidized species in the as-exfoliated graphene lattice structure [16, 150]. These components of C 1s are consistent with previously reported electrochemical exfoliated graphene [16, 150].

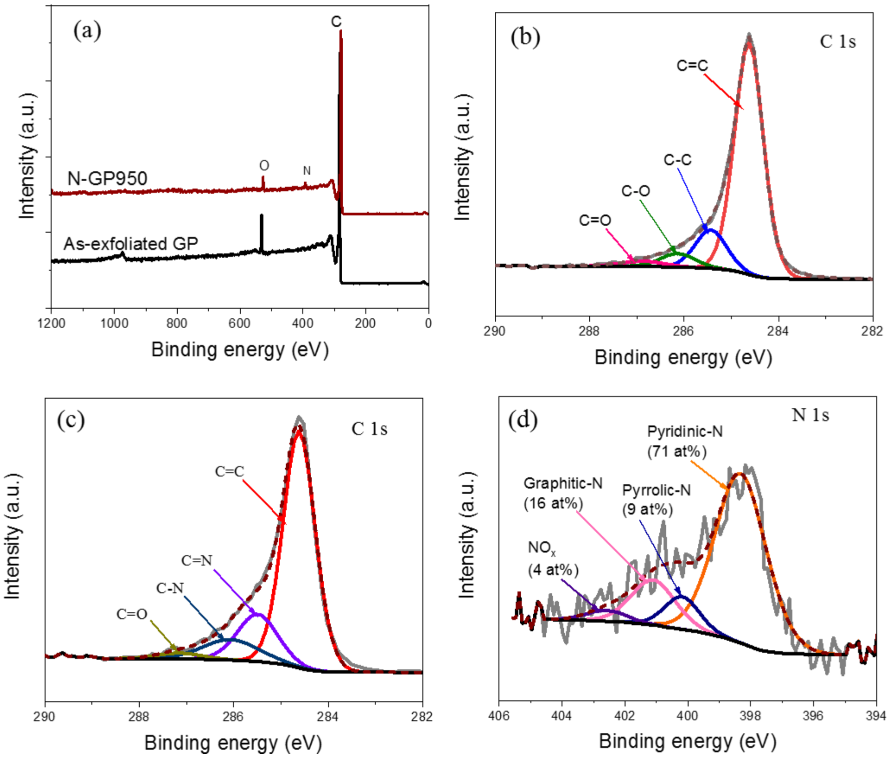

Figure 3-5 XPS spectra of graphene exfoliated from a graphite plate (GP) (a) survey of as-exfoliated GP and N-doped graphene (N-GP950) and high-resolution C 1s spectrum (b) as-exfoliated GP and (c) N-GP950, and (d) high-resolution N 1s spectrum of the N-GP950.

Similarly, Figure 3-5c display C 1s peak of N-GP950 deconvoluted into four components, corresponding to C=C (284.6 eV), C=N (285.5 eV), C-N (286 eV), and C=O (287 eV), respectively. It is well established that the charge distribution in the C atoms in the N-doped carbon matrix can be influenced by the neighboring N dopants, which serve as a potential active center for ORR [151]. Besides, Figure 3-5d shows the deconvolution of the N 1s peak into four components corresponding to different N atom configurations. These components are assigned to pyridinic-N (398.3 eV, 71 at %), pyrrolic-N (400.2 eV, 9 at %), graphitic-N (401 eV, 16 at %), and oxidized-N (402.7 eV, 4 at %). Furthermore, the prepared N-doped graphene contains the abundant composition of pyridinic-N, which contributes to one π electron to the π system of graphene. This phenomenon is believed to be able to enhance the ORR activity of the N-doped graphene [136, 152, 153]. The XPS results are consistent with TEM analysis and Uv-vis measurement that the as-exfoliated graphene is of high quality. Particularly, the N-doping and the abundance of pyridinic-N argued to provide active sites for improving ORR electrocatalytic performance of carbon materials [152, 153].

3.4.5 The electrochemical properties of graphene

The as-exfoliated graphene and the N-doped graphene was used as electrocatalysts for ORR. Firstly, we investigated the influence of the graphite sources on ORR performance of graphene. The LSV experiments were performed to evaluate the ORR activity of the as-exfoliated graphene from graphite foil (GPf) and plate precursors (GP). The ORR activity of the electrocatalysts was evaluated based on the exhibition of the highest possible positive value of the onset potential, half-wave potential ($E_{1/2}$) or current density at 0.80 V vs. RHE. Figure 3-6 shows the typical ORR polarization curves; the corresponding calculated electrons transfer number and percentage peroxide produced. The GP exhibited superior ORR activity than the GPf. GP displayed better onset potential (0.82 V vs. RHE), the half-wave potential (0.75 V) and current density at 0.80 V (0.34 mA cm^{-2}) in comparison to 0.78 V, 0.67 V and 0.04 mA cm^{-2} respectively, of the GPf.

Furthermore, the as-exfoliated GP displayed better ORR performance in 0.1 M KOH solution than the graphene prepared by other methods, e.g., three-dimensional (3D) graphene [154, 155], nanosheets by grinding high purity graphite in ionic liquid [132, 156], edge-functionalized graphene by ball milling [143], and reduced graphene oxide by Hummer's method [157, 158].

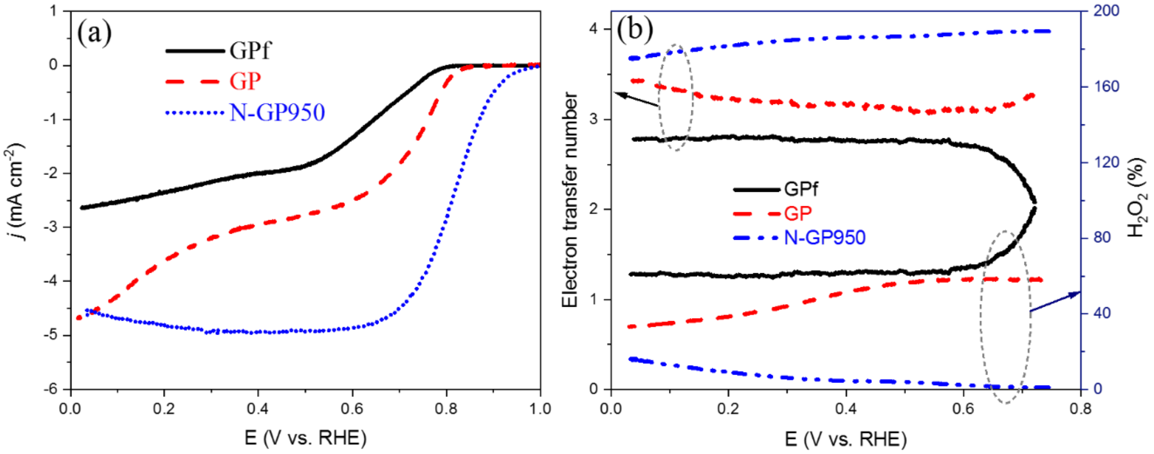

Figure 3-6 ORR polarization curves of (a) as-exfoliated graphene from graphite foil (GPf, black line) and graphite plate (GP, red line), and N-doped graphene (N-GP950, blue line), (b) The calculated electron transfer number, and peroxide production in the three catalysts. The measurements were carried out in N_2, or O_2 saturated 0.1 M KOH, scan rate: 10 mV/s at 1600 rpm. Showing the electrocatalytic activities towards ORR.

Detailed comparison of ORR performance is given in Table 3-1. The improved ORR performance of GP is ascribed to the presence of numerous functionalized edges available for the adsorption and dissociation of O_2 in addition to the efficient electron transfer between the electrode and the structural crystalline of its basal plane [151, 159, 160]. The abundance of the edges of the former possibly originates from the exfoliation process. The duration of the exfoliation process for the graphite plate was long (one to a few hours), compared to the graphite foil (3-5 min). The extended period of the exfoliation process subjects the edges of graphene to further oxidation, consequently leading to the formation of more functional groups along the edges.

Table 3-1 The ORR performance of recent metal-free electrocatalysts. The electrochemical evaluation was carried out in O_2-saturated 0.1 M KOH, scan rate: 10 mV s^{-1} and disk rotation rate: 1600 rpm.

Materials	**Onset potential (V vs. RHE)**	**Half-wave potential (V vs. RHE)**	**j_L (mA/cm^2)**	**Reference(s) in the main document**
GP	0.82	N/A	N/A	This work
N-GP950	0.94	0.82	4.9	
3D Graphene in nickel foam	0.71	N/A	N/A	[154]
N-doped 3D graphene	0.82	0.70	3.9	[155]
Nanosheets graphene by grinding graphite	0.80	0.72	3.9	[132]
Ball milled graphene	0.78	0.70	2.2	[156]
Ball milled graphene	0.80	N/A	N/A	[143]
rGO				[157]
As-prepared	0.78	N/A	N/A	
N-doped	0.78	0.71	3.9	
rGO				[158]
As-prepared	0.74	N/A	N/A	
N-doped	0.94	0.82	3.9	

The functionalized edges of graphene render the hydrophilic nature of the modified electrode, facilitating the diffusion of oxygen, thereby providing more active centers [143, 160, 161]. Furthermore, a blue curve in Figure 3-6a-b depicts the pyrolysis further enhances the ORR activity of the GPin the presence of NH_3 at 950 °C (N-GP950). The high-temperature pyrolysis in NH_3 introduces N-atoms into the graphene lattice matrix, which in turn causes the change of the charge distribution and electronic properties of the adjacent carbon atoms, hence increasing the probability of adsorption of oxygen molecules [136, 151]. The increased ORR activity of the N-GP950 is evidenced by the more positive shifts of both half-wave (0.83 V vs. RHE) and onset (0.96 V) potentials, as well as the current density at 0.80 V (3.0 mA cm^{-2}). The enhanced activity is also revealed by the increase of the electron transfer number (above 3.5) and the relatively low production of hydrogen peroxide, H_2O_2, (below 15%) in the potential range of 0.20 - 0.70 V, as shown in Figure 3-6b. Therefore, it is apparent that graphite precursors and pyrolysis of graphene samples in NH_3 significantly influence the ORR activity of the exfoliated catalysts.

Secondly, we investigated the influence of temperature of electrolyte during exfoliation on the ORR activity of the graphene samples. Figure 3-7 displays the influence of temperature of the electrolyte during exfoliation on amount of exfoliation produce and the ORR performance of the graphene. Figure 3-7a shows digital photos of the exfoliation products in the electrolytes (upper) and their associated graphite substrates (lower) after 5 minutes of exfoliation, at different electrolyte temperatures. The exfoliation speed/efficiency is observed to decrease when the temperature increases. For example, at room temperature (~22 °C), the most substantial amount of graphene was produced (upper image in Figure 3-7a). The high production of graphene is consistent with the enormous consumption of the graphite substrate at ~22 °C while the least consumption occurs at 80 °C (lower image in Figure 3-7a). After exfoliation at various temperatures, the as-synthesized GP samples were heat-treated in an argon atmosphere at 1050 °C for 1 hour and then in NH_3 at 950 ºC for 15 minutes, to obtain N-doped graphene (N-GP950). Figure 3-7b-d, depict the ORR performance of these N-doped graphene exfoliated at different electrolyte temperatures. The ORR performance of these graphene samples decreased with the increasing temperature of the electrolyte. Among all the graphene samples exfoliated at different temperatures, the sample exfoliated at 22 ºC exhibited the best ORR activity in terms of highest half-wave (0.82 V) and onset (0.94 V) potentials, electron transfer number (above 3.8), and current density (3.0 mA/cm^2) at 0.80 V, as well as the lowest peroxide yield (below 11%). The performance parameters of all N-doped graphene samples exfoliated at different are summarised in Table 3-2. The high density of the defects on the graphene obtained at a lower temperature may be responsible for its better ORR activity [162] These results are consistent with Hossain and Wang observation that that graphene exfoliated at higher electrolyte solution by the electrochemical method has low defect density [162].

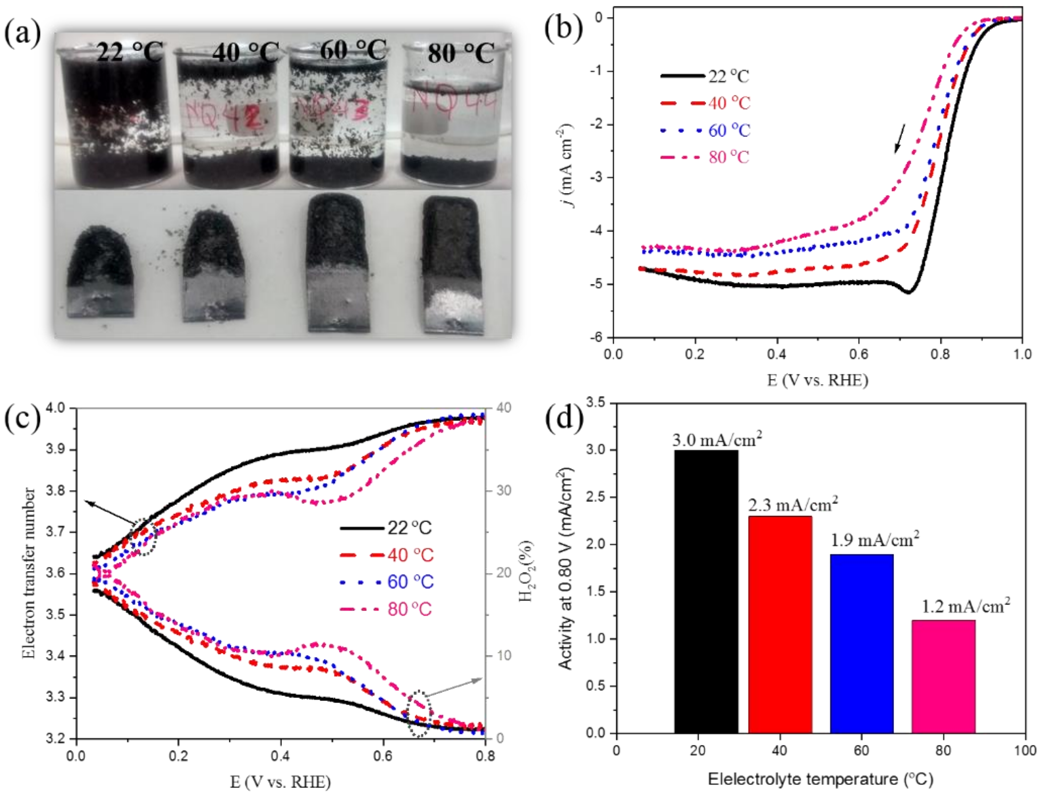

Figure 3-7 Influence of exfoliation electrolyte temperature on the ORR activity of graphene. (a) Digital images of as-exfoliated graphene products (in the beakers) and their corresponding graphite substrates after 5 minutes of exfoliation at 22, 40, 60 and 80 ºC, respectively. (b) ORR polarization curves ranging from 0 - 1.0 V of the graphene exfoliated at different electrolyte temperature, followed by pyrolysis in Ar at 1050 °C for 1 hour and NH_3 at 950 ºC for 15 minutes. The corresponding calculated (c) electron transfer number and (d) peroxide produced for the catalysts. Electrolytes: 0.1 M KOH, scan rate: 10 mV/s and rotation: 1600 rpm.

Table 3-2 The ORR performance of N-doped graphene exfoliated from graphite plate at different temperatures. The electrochemical evaluation was carried out in O_2-saturated 0.1 M KOH, scan rate: 10 mV s^{-1} and disk rotation rate: 1600 rpm.

Temperature of the exfoliation electrolyte (°C)	**Onset potential (V)**	**Half-wave potential (V)**	**Current density at 0.80 V (mA/cm^2)**	**Limiting current density (mA cm^{-2})**	**Electron transfer number at 0.30 V**	**Peroxide produced at 0.30 V (%)**
22	0.94	0.82	3.0	5.0	3.85	7
40	0.90	0.80	2.3	4.7	3.80	10
60	0.90	0.80	1.9	4.3	3.77	11
80	0.87	0.77	1.2	4.2	3.77	11

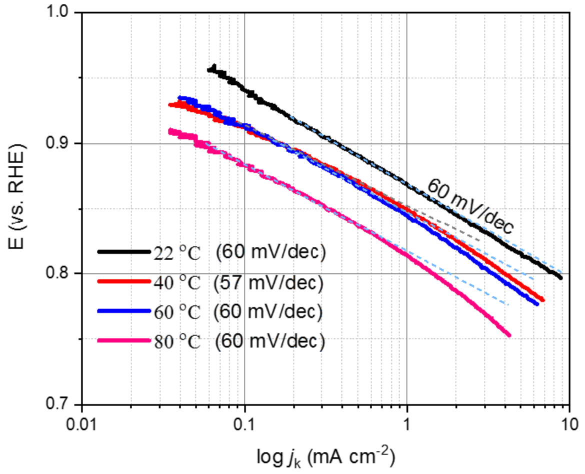

Figure 3-8 Tafel plots for ORR of N-doped graphene samples exfoliated at four different electrolyte temperatures; 22, 40, 60 and 80 ºC, respectively.

However, Figure 3-8 shows the graphene samples exfoliated at different temperatures display similar ORR kinetics as evidenced by their close Tafel slopes at the lower overpotential region. We believe that the presence of a suitable number of defects in the graphene edges could improve the hydrophilicity of the graphene, which, in turn, facilitates the adsorption of O-atoms in neighboring C-atoms while maintaining excellent electronic conductivity.

Thirdly, we studied the influence of various experimental parameters on the ORR performance of graphene samples. The influence of the number of layers of graphene, the temperature of pyrolysis in NH_3, duration of sonication of dispersion, and the concentration of exfoliation electrolyte solution on the ORR activity of the graphene samples, are demonstrated in LSVs presented in Figure 3-9. Before the ORR performance test, all the GP samples underwent pyrolysis at 950 °C in an argon atmosphere for one hour and NH_3 for 15 minutes, except for two examples (at 750 °C and 1050 °C, respectively) in Figure 3-9b, forming N-GP950 samples. Figure 3-9a shows that the ORR activity of the catalysts follows the following order: few layers N-GP950 > thin layers N-GP950 > multilayers N-GP950. The enhanced activity of few layers N-GP950 originates from the abundance of edges sites (capable of promoting the adsorption of O_2 molecules) and efficient electron transfer between the electrode's surface and the edges [132].

To study the effect of the pyrolysis temperature in NH_3, the few-layer GP was used as reference material and annealed in NH_3 for 15 min at 750 °C, 950 °C and 1050 °C, respectively. As shown in Figure 3-9b, the current density at 0.80 (V vs. RHE) is 0.5 mA cm^{-2}, 3.0 mA cm^{-2} and 1.9 mA cm^{-2} for the sample pyrolyzed at 750, 950 and 1050 °C, respectively. Particularly, there is a significant increase in specific current density for the sample pyrolyzed at 950 °C. The specific current density at 0.8 V is 3.0 mA cm^{-2}, which is about five times higher than that of sample pyrolyzed at 750 °C. This increase of specific current density indicates the enhancement of ORR activity for the graphene sample pyrolyzed at 950 ºC.

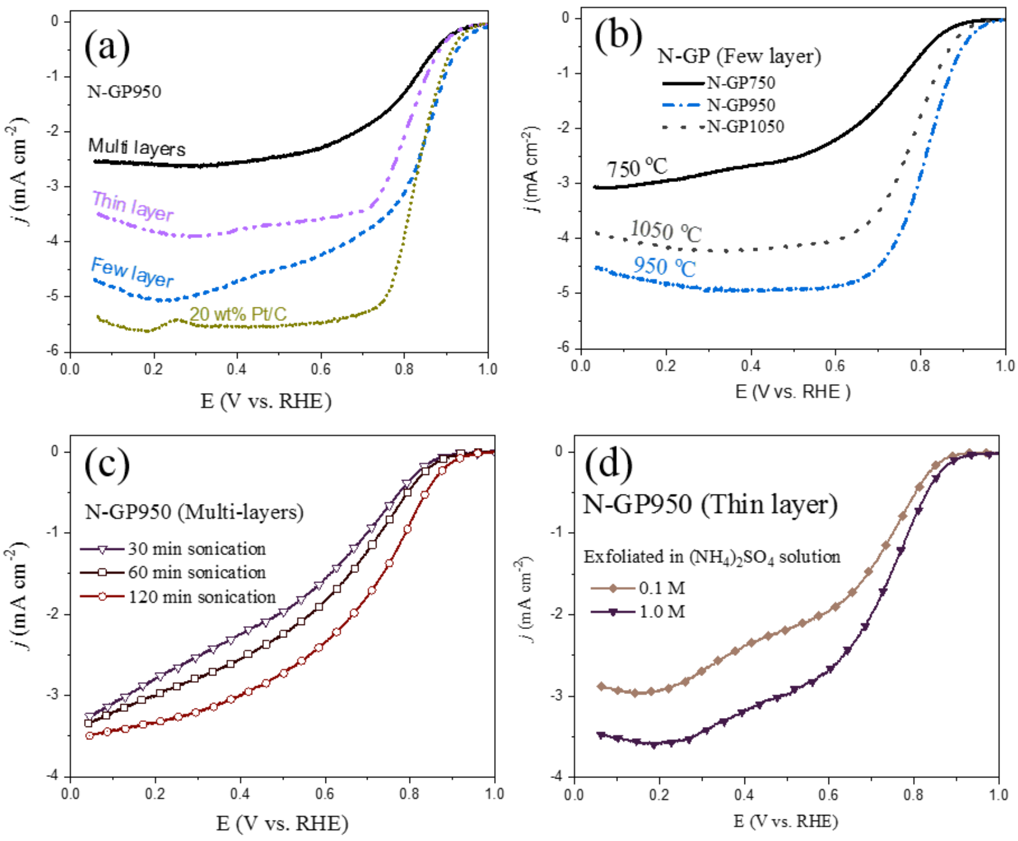

Figure 3-9 The ORR polarization curves of N-GP catalysts. (a) With different layers, (b) after different temperatures of pyrolysis in NH3, (c) sonication for a different duration. (d) Exfoliated in 0.1 M and 1.0 M (NH4)2SO4 electrolytes. All LSVs measurements were carried out in 0.1 M KOH media, scan rate: 10 mV/s, rotation speed: 1600 rpm.

This enhancement in ORR activity can be attributed to the increased N-doping in the graphene lattice at higher NH_3pyrolysis temperature, hence providing more active sites [79]. However, we noticed a decrease in current density at1050 °C. The drift in ORR activity of N-GP1050 ºC can be attributed to the possible loss of pyridinic nitrogen as well as total nitrogen content occurred at a higher temperature of pyrolysis [163, 164]. Also, at such elevated temperature, there is a high probability that the graphene loses most of the oxygen functional groups, and the surface became highly hydrophobic. Further, we investigated the influence of the length of sonication time as sonication is an essential step in the post-exfoliation treatment of the exfoliated products. Figure 3-9c show a significant enhancement of the ORR activity of the catalysts when the sonication period is prolonged from 5 minutes to 120 minutes. The enhancement in the activity is attributed to the introduction of more defects (active sites) in the graphene structure as the sonication time was extended. Also, the concentration of exfoliation electrolyte also displayed a significant influence in the ORR activity of the N-GP950 samples. As shown in Figure 3-9d, the N-GP950 derived from graphene exfoliated at 1.0 M $(NH_4)_2SO_4$ exhibited superior ORR activities than the one at 0.1 M $(NH_4)_2SO_4$. We anticipate that at high concentration of the electrolyte, the oxidation process of graphite edges is fast and the graphene produced is, accordingly, have more edge defects which in turn acts as the active sites for the ORR.

Finally, to investigate the stability of the N-GP950 and 20% Pt/C catalysts towards ORR, ADT was performed by continuous potential cycling between 0.6 and 1.0 V in O_2-saturated 0.1 M KOH, for 5000 potential cycles with a scan rate of 200 mV s^{-1}. As shown in Figure 3-10, the N-GP950 displayed exceptional durability. After 5000 consecutive CV cycles, the N-GP950 catalysts showed almost superimposed LSVs before and after the ADT cycling. In contrast, the half-wave potential of the 20 wt% Pt/C electrode significantly reduced by 30 mV after 5000 potential cycles under identical conditions. This observation suggests that N-GP950 is more stable than the commercial Pt/C for ORR in alkaline media, which can be attributed to the strong covalent bonds between the active sites and the graphitic lattice, as well as the high corrosion resistance of graphene.

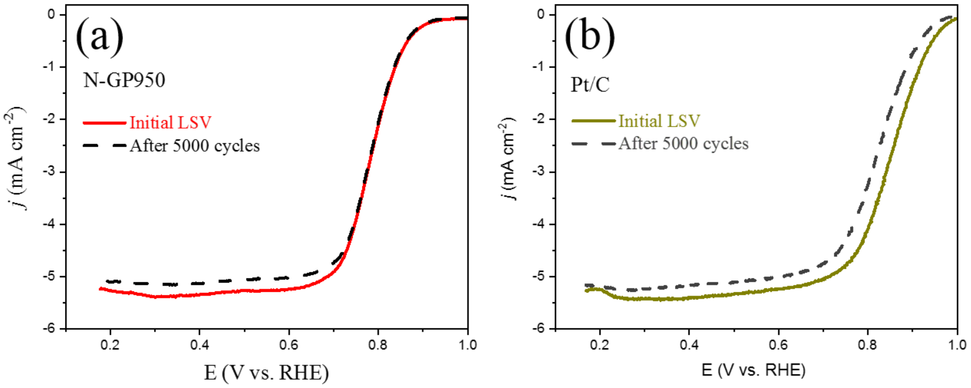

Figure 3-10 Long-term performance of the catalysts (before and after ADT test, 5000 cycles). LSVs (a) few layer N-GP950 and (b) 20% Pt/C recorded at 10 mV s-1 and1600 rpm in O_2-saturated 0.1 M KOH at room temperature. Showing the stability of electrocatalysts toward ORR.

3.5 Conclusions and perspectives

High-quality graphene with a controllable number of layers was successfully fabricated by a simple and inexpensive electrochemical method, using a low-cost graphite foil and plates as precursors in an aqueous electrolyte. In general, both graphite precursors generated thin and highly uniform graphene. We found that the ORR activity of graphene exfoliated from the graphite plate was higher than the graphene obtained from the graphite foil. Further, as-synthesized graphene samples were converted into N-doped graphene (N-GP950) after NH_3 pyrolysis, which exhibits a highly enhanced ORR performance compared to pristine graphene, due to N-doping. Moreover, the N-GP950 exhibited comparable ORR activity and better stability than the state-of-the-art commercial Pt/C catalyst. Also, we found that the ORR activity of exfoliated graphene is influenced by the exfoliation and post-exfoliation parameters such as the temperature of the exfoliation electrolyte, the number of layers of graphene, pyrolysis temperature and concentration of the electrolyte. Therefore, it is possible to fine-tune the ORR activity of the graphene and N-GP950 by manipulating the experimental parameters. Thus, we believe the N-GP950 which can be prepared by a cost-effective method using low-cost precursors is a potential candidate of ORR catalyst in an alkaline fuel cell. Similarly, by taking advantages of physical and electrochemical properties demonstrated, the N-GP950 can be utilized as an effective support material of metal-based ORR electrocatalysts to enhance their performance.

Chapter 4 Graphene-based Metal-Macrocycle Electrocatalyst for Oxygen Reduction

Electrocatalysts for oxygen reduction are a critical component that may dramatically promote the widespread application of fuel cells and metal-air batteries. For decades, the metal macrocycle iron (II) phthalocyanine (FePc) investigated as a precursor to prepare the ORR electrocatalysts. To date, however, the use of FePc has been limited by its low electrocatalytic activity and insufficient durability when not embedded in carbon support via high-temperature pyrolysis. Inspired by the high-quality and high surface area as well as the high ORR performance, we employed the N-doped graphene as the support of FePc, forming FePc/N-doped graphene composites as a high-performance non-precious metal oxygen reduction electrocatalyst. We use a low-cost, straightforward and safe strategy of fabrication at ambient temperature.

4.1 Introduction

Driven by the increasing demand for clean energy and concerns over climate change, significant research efforts worldwide actively exploring new materials and approach towards sustainable and efficient energy conversion, saving, and storage technologies. Fuel cells (FCs) and metal-air batteries are considered promising because they can offer high power density, high energy-conversion efficiency, and are environmentally benign [2, 3, 8, 165]. However, the overall performance of FCs and metal-air batteries is mainly dependent on the sluggish cathodic oxygen reduction reaction (ORR) [1, 7, 25, 165]. Highly active ORR electrocatalysts are essential for the widespread commercialization of FCs. Platinum (Pt)-based materials have been the most widely used ORR electrocatalysts for decades [125-127]. For example, in the early 1960s, alkaline FCs with Pt/C as an electrocatalyst for the ORR was developed in the Apollo lunar mission [10, 11, 53]. Nevertheless, the high cost and limited supply of Pt hamper the large-scale commercial application of FCs. Also, Pt-based materials suffer from time-dependent activity [12, 13] and CO poisoning effects [14, 15, 70]. Therefore, replacing Pt-based ORR electrocatalysts with high-performance non-precious metal catalysts (NPMCs) is highly desirable [63, 70].

Transition-metal-based materials have been the focal point of NPMCs investigations due to their partially filled d-orbitals [166-168]. Various types of NPMCs have been widely studied such as metal chalcogenides [169-171], metal oxides [172, 173], pyrolyzed metal/nitrogen/carbon (M/N/C, M = Fe, Co, Ni) compounds [174, 175], and metal macrocycles (M-N_4-macrocycles) [34, 176, 177]. The ideal strategy to enhance the catalytic performance of these NPMCs involves a high-temperature pyrolysis process, which results in the formation of complex structural composition and potential safety issues [34, 178]. Among these candidates, metal macrocycles are the only ones possible to prepare as ORR catalyst with relatively high performance without the high-temperature pyrolysis process [34, 168]. Among other metal macrocycles, iron (II) phthalocyanine (FePc), with iron atoms coordinated to four nitrogen atoms (Fe-N_4) and aromatic rings, is considered as a potential alternative ORR catalyst [35, 179]. Despite the possibility of potential multiple adsorption sites of oxygen, the catalytic properties of FePc are severely hindered due to its poor conductivity and aggregation [180, 181]. Two strategies have been employed to address these challenges, namely: (i) attaching electrons donating group to the FePc structure as a supplementary electron source to prevent issues arising from the slow electron transfer [180, 181], and (ii) supporting the FePc on a variety of carbon materials, such as carbon black [182, 183], carbon nanotubes [34], and reduced graphene oxide [35, 176]. In the latter case, graphene-supported FePc showed promising ORR activity, mostly benefiting from the excellent conductivity and π-π interaction between FePc and graphene, which is believed to play a critical role in the distribution of catalytic sites and eventually prevent aggregation of the FePc molecules [35]. However, most of these reported graphene supports are prepared using Hummers' method, which suffers from poor quality and environmental and safety issues due to its use of hazardous and explosive chemicals. Thus, improving the ORR performance of the M-N_4 macrocycles by designing new support materials in a simple and cost-effective approach still represents an interesting opportunity.

Recently, we prepared large and high-quality graphene thin sheets by electrochemical exfoliation of graphite [51]. This method of preparation of graphene is very appealing because it is low-cost, fast, scalable, and environmentally friendly. In this study, we report a direct approach to prepare FePc/N-GP950 composite by immobilization of FePc on nitrogen-doped electrochemically exfoliated graphene (N-GP950) sheets as efficient, durable ORR electrocatalysts. In virtue of the unique structural morphology and composition of our N-GP950, the as-prepared FePc/N-GP950 catalyst displayed excellent ORR activity, with excellent onset potential (0.97 V vs. RHE), a half-wave potential (0.89 V vs. RHE), and activity at 0.8 V (5.0 mA cm^{-2}). Also, the FePc/N-GP950 exhibited remarkable long-term stability with no apparent loss of activity after accelerated durability test (ADT) up to 5000 cycles of potential between 0.6 and 1.0 (V vs. RHE). These values are among the best for unpyrolysed metal macrocycles-based catalysts. Our results suggest that graphene fabricated using a low cost and environmentally friendly, electrochemical method may act as support for FePc, yielding excellent ORR performance.

4.2 Experimental

4.2.1 Chemicals and materials

Graphite plate (99%) was purchased from Alfa Aesar, Fischer Scientific. Commercially available solvents and reagents were used without further purification. Ammonium sulfate ($(NH_4)_2SO_4$, 99 %), platinum on Vulcan (20 wt% Pt/C, XC-72R; E-TEK), potassium hydroxide (KOH), and iron II phthalocyanine (FePc) were purchased from Sigma-Aldrich. All aqueous solutions were prepared with deionized water from a Millipore system (>18 MΩ cm).

4.2.2 Preparation of graphene and N-doped graphene

Graphene was prepared by electrochemical exfoliation of graphite. The detailed synthesis procedure of graphene by modification of the previous method of electrochemical exfoliation of graphite is reported in Chapter 3. Graphene exfoliation was carried out in a two-electrode cell using a DC power supply. Figure 4-1 (part A) shows the exfoliation experimental cell-setup consisting of a graphite plate (5 mm, 6 cm^2) serving as an anode, platinum (Pt) wire acting as a cathode and an aqueous solution of $(NH_4)_2SO_4$ (1.0 M, 80 ml) as an electrolyte. A constant biased potential of ±10 V was applied between the two electrodes placed approximately two centimeters apart. The exfoliation of graphite was achieved at room temperature (~22 °C) [98, 99, 184, 185]. Subsequently, the as-exfoliated product was collected and thoroughly washed with deionized water and reagent alcohol by vacuum filtration. The product was then dispersed in deionized water by low power sonication for 15 minutes. Consequently, the dispersion was centrifuged at 5000 rpm for 10 minutes. The supernatant was freeze-dried to obtain powder designated as-exfoliated graphene (GP). Nitrogen atom doping was achieved by heating the graphene powders at 950 °C in argon for 60 minutes and in ammonia (NH_3) for 15 minutes (N-GP950). Subsequently, the N-GP950 was used as a support material of FePc.

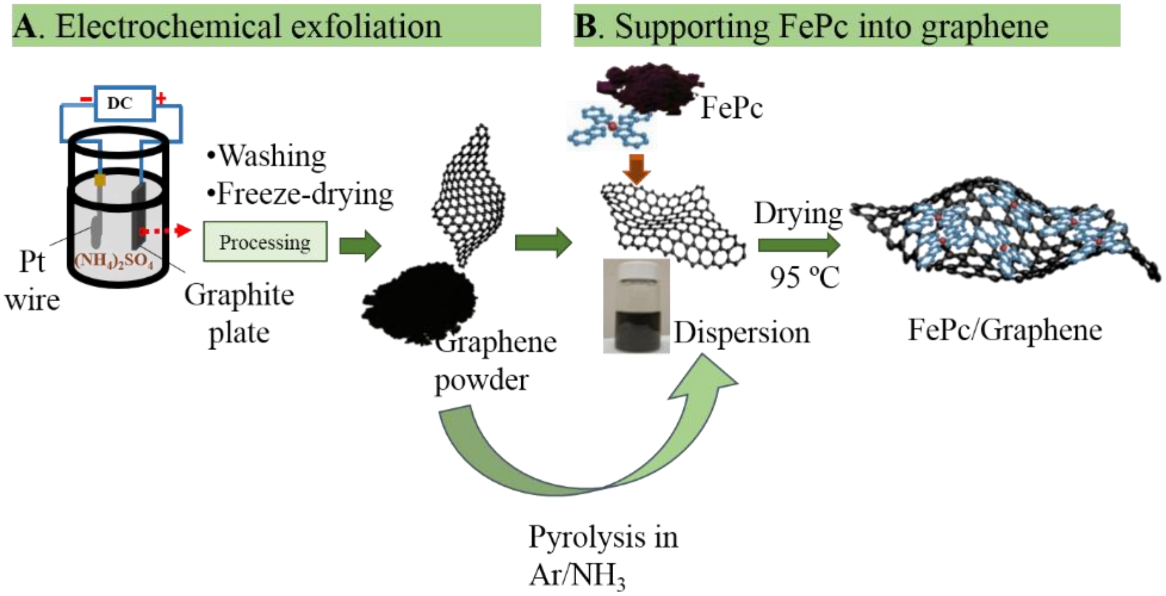

Figure 4-1 Schematic view of preparation of FePc/N-GP950 catalyst. The setup of electrochemical exfoliation of graphite (part A) and immobilization of iron (II) phthalocyanine (FePc) into the graphene and nitrogen-doped graphene (part B).

4.2.3 Preparation of iron (II) phthalocyanine/N-doped graphene

The iron (II) phthalocyanine/ N-doped graphene (FePc/N-GP950) catalyst was fabricated by immobilization of FePc onto the as-prepared N-GP950 via a slow evaporation method. In a typical experiment, 100 mg N-GP950 was dispersed in ethanol (150 ml) by sonication for 15 minutes. To this dispersion, an equal volume of an ethanol-water solution of FePc (50 mg, 50 ml) was added. The mixture was continuously stirred at room temperature for two hours. Subsequently, the reaction mixture was slowly heated (~65 °C) to evaporate 75% of the original solution. The obtained slurry was then transferred to an air-oven and left at 95 °C overnight, to yield the FePc/N-GP950 catalyst. The schematic illustration of the preparation of the FePc/N-GP950 and analogs is shown in Figure 4-1 (part B). The contents of the FePc in the FePc/N-GP950 catalysts varied by employing different weight ratios of FePc to N-GP950, such as 1:0, 1:1, 1:2, and 1:5, for the FePc alone, 50 wt% FePc (FePc-50/N-GP950), 33 wt% FePc (FePc-33/N-GP950) and 16 wt% FePc (FePc-16/N-GP950).

4.3 Characterization of FePc/N-doped graphene

4.3.1 Physical characterization

The surface properties and electronic structure of the catalysts were evaluated by X-ray photoelectron spectroscopy (XPS) using a VG (Escalab220i - XL) equipped with Al K_α line excitation source. The positions of the spectral lines were accurately determined using the C 1s peak (BE = 284.6 eV) as a reference. The UV−Vis absorption spectra of samples were measured using a UV-Vis absorption spectrophotometer (thermos scientific Nanodrop 2000c). The structural morphologies and composition of the catalysts were characterized using transmission electron microscopy (TEM, JEOL JEM-2100F operated at 200 kV).

4.3.2 Electrochemical characterization

All electrochemical tests were conducted in a three-electrode cell at room temperature (~22 °C) using a bipotentiostat, PINE Research Instrumentation (Model PGSTAT-72637) workstation with Rotating Ring-Disk Electrode apparatus (RRDE, Pine Instruments). All measurements were carried out in a single compartment glass cell. A Platinum wire and mercury/mercury oxide (Hg/HgO) were used as a counter electrode (CE) and a reference electrode (RE), respectively. Before the test, the electrolytes were saturated with high purity N_2 or O_2 gas for at least 30 min.

The ORR activity of the prepared catalysts was evaluated in 0.1 M KOH solution using the scan rates of 50 mV s^{-1} for cyclic voltammetry (CV) and 10 mV s^{-1} linear sweep voltammograms (LSVs), respectively. The as-prepared catalyst (10 mg) was dispersed in a solution of ethanol (350 μl) and Nafion ionomer (95 μl, 5 wt %). The suspension was homogenized in two cycles of 15 minutes by low power ultrasonication and agitation to obtain an ink-like dispersion. This catalyst ink was then coated on the disc part of the rotating ring disc electrode (RRDE, 5.61 mm diameter glassy carbon disk and Pt ring), Pine Instruments. The catalyst loading was 0.8 mg cm^{-2}. Similarly, for comparison purposes, 20 wt% Pt/C (E-ETK) was prepared using the same procedure with a loading of 0.1 mg/cm^2 (20 μg_{Pt}/cm^2). In the analysis, the electron transfer number (ne^-) and peroxide yield (H_2O_2%) and were calculated using Equation 2-4 and Equation 2-5. All potentials in this work were corrected and reported relative to the reversible hydrogen electrode (RHE). The accelerated durability test (ADT) was performed in the oxygen-saturated 0.1 M KOH electrolytes by cycling potential for 5000 cycles between 0.6 and 1.0 V vs. RHE (stare case) using the scan rate of 100 mV s^{-1}. The LSVs were recorded before and at the end of the ADT test. Chronoamperometric responses (percentage of current retained against operation time) of the FePc-33/N-GP and 20 wt% Pt/C were also recorded in O_2-saturated 0.1 M KOH the potential was held at 0.8 V, and electrode rotation speed of 1600 rpm.

4.4 Results and discussion

4.4.1 Preparation of FePc/N-doped graphene

Oxygen reduction catalysts were prepared from immobilization of different proportion of FePc on the surface of graphene (N-GP950). The π-π assembling interaction between FePc and the N-GP950 leads to the significantly homogeneous distribution of the immobilized FePc. This method (Figure 4-1-part B) avoids high-temperature pyrolysis that could be detrimental to the intrinsic properties of FePc [186-188]. For comparison purposes, we also immobilized the FePc on the GP950 (as-exfoliated graphene pyrolyzed only in argon at 950 °C) and as-exfoliated graphene (GP) and on the N-doped reduced graphene oxide (N-rGO) prepared using Hummer's method.

4.4.2 Surface and structural morphology of FePc/N-doped graphene

EM was used to characterize the surface morphology of the as-exfoliated graphene (GP), N-GP950, FePc, and FePc/N-GP950 composites. Figure 4-2 and Figure 4-3 display the TEM images of the GP, N-GP950, FePc, and FePc/N-GP950 composite. In general, the N-GP950 retained most features of the parent as-exfoliated GP and is characterized by a very smooth surface with a crumply structure (Figure 4-2c-d, 4-3a). On the other hand, Figure 4-3b displays the TEM image of FePc indicating aggregates of cuboidal-like particles with an average size of 165 nm. TEM images of FePc/N-GP composites, Figure 4-3c-e, show the dispersion of FePc nanostructures across the entire surface of N-GP950. In comparison with the individual N-GP, the TEM images of FePc/N-GP950 show cuboidal-like nanostructures of FePc with the size range of 30–45 nm, seamlessly stacked on the surface of N-GP950. The appearance of relatively small sized nanostructures of FePc on the FePc/N-GP950 surface as compared to unsupported FePc can reflect the absence of aggregation as well as the presence of strong π-π interactions pulls the structure of FePc inward hence decreasing the radius of the phthalocyanine ring (Fe-N_4 structure) [35, 187].

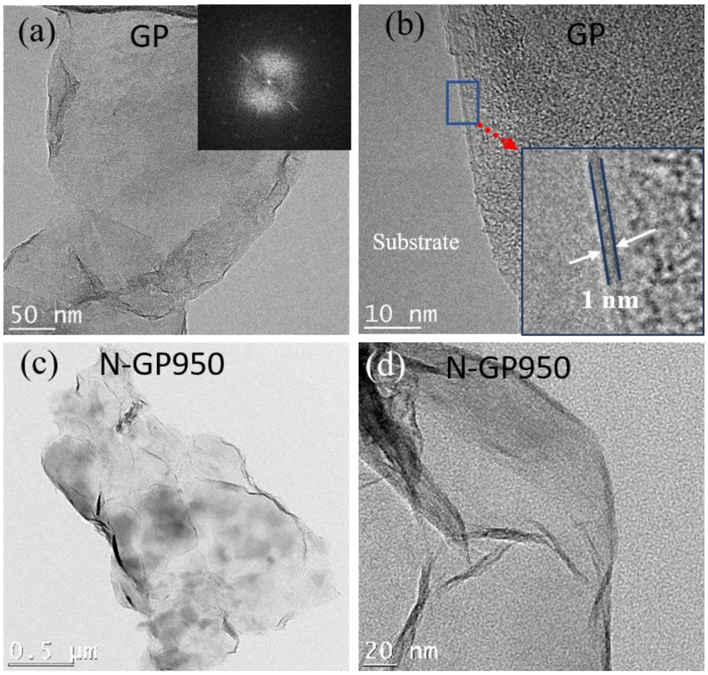

Figure 4-2 TEM images of (a, b) as-exfoliated graphene (GP) and (c, d) N-doped graphene (N-GP950). The as-exfoliated graphene and N-GP950 are very thin and have a uniform morphology with a well-defined crystalline structure.

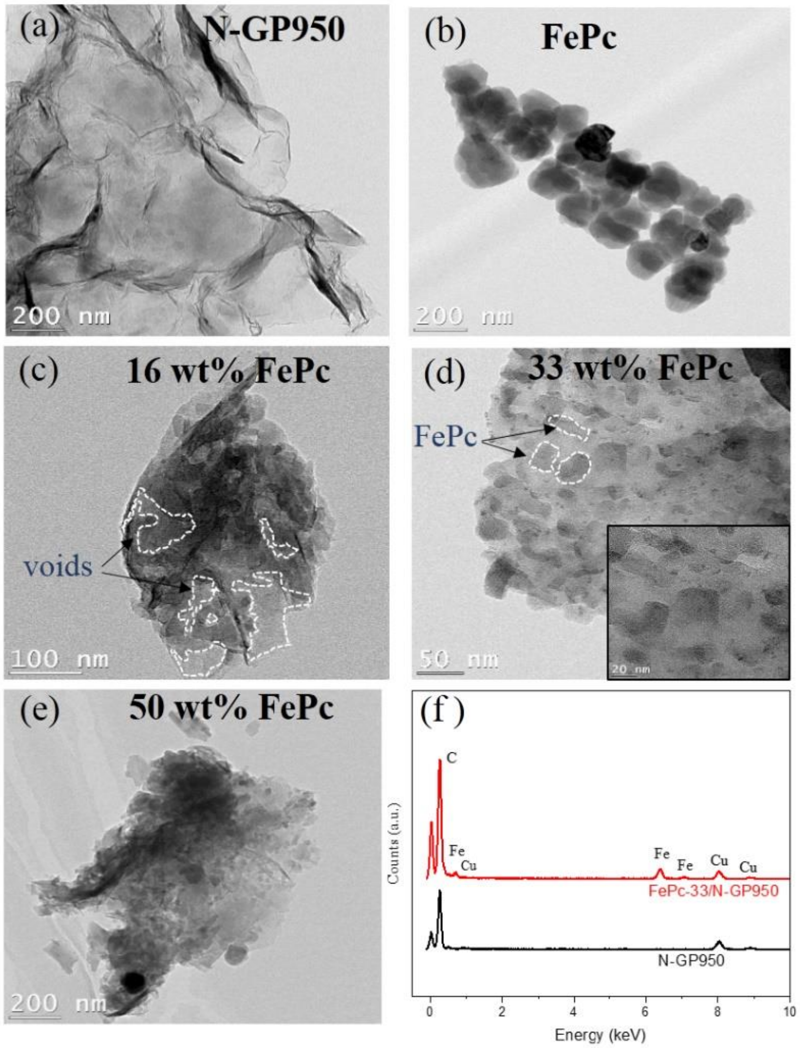

Figure 4-3 TEM images of (a) N-doped graphene (N-GP950), (b) the aggregation of FePc of size ca. 165 nm, (c) FePc-16/N-GP950, (d) FePc-33/N-GP950, (e) FePc-50/N-GP950, and (f) energy dispersive spectroscopy of the N-GP950 and FePc-33/N-GP950. The FePc successfully loaded and homogeneously distributed on the surface of N-GP950.

Nevertheless, Figure 4-3c depicts TEM image of the FePc-16/N-GP950 with 16 wt% FePc showing a partial distribution of FePc nanoclusters with many void regions of the N-GP950. Figure 4-3c-e show when the level of the FePc supported on N-GP950 increased, from 16 wt% to 50 wt%, the dispersion and uniform distribution of the FePc nanostructures gradually improved. We speculate that the increased electronic interaction between FePc and N-GP950 plays a crucial role in the dispersion of FePc at higher loadings. The uniform dispersion and distribution of FePc on the N-GP950 achieved when the level of FePc reached 33 wt% in the FePc-33/N-GP950 (Figure 4-3d). However, as indicated in Figure 4-3e when the level of FePc was 50 wt% as in the case of FePc-50/N-GP950, the FePc nanostructures became congested on the surface of N-GP950. The piling of the FePc on the surface of N-GP can compromise the accessibility of the active sites [176]. Figure 4-3f shows the energy dispersive spectroscopy (EDS) spectra of N-GP950 and FePc-33/N-GP950. The appearance of Fe signals in the EDS spectrum of FePc-33/N-GP950 is consistent with the presence of FePc on the surface of N-GP950.

4.4.3 The surface chemical composition of FePc/N-doped graphene

The surface chemical composition of the FePc, N-GP950, and FePc-33/N-GP950 catalysts was probed by X-ray photoelectron spectroscopy (XPS). Figure 4-4 displays the XPS survey spectra, high-resolution spectra of the three catalysts for the Fe 2p, N 1s, and C 1s peaks and the nominal composition of N-species in the N-GP950, FePc and FePc-33/N-GP950 catalysts. The presence of Fe peak in the survey spectrum of FePc-33/N-GP950 (Figure 4-4a), further confirms the successful immobilization of FePc on N-GP950. The elemental composition of N-GP950 is dominated by C (~97 at %) whereas the concentrations of O (1.5 at %) and N (1.7 at %) are relatively low. After loading the 33 wt% FePc onto the N-GP950, we observed a significant increase in the surface concentration of N (7 at %), which may arise from the addition of FePc. The similarity in atomic compositions between FePc and FePc-33/N-GP950 (33 wt% FePc) suggests the retention of the inherent properties of individual FePc [181]. Figure 4-4b depicts the Fe 2p core level spectra obtained for FePc and FePc-33/N-GP950. Both spectra have two peaks that correspond to the lower binding energy (Fe 2p3/2) and higher binding energy (Fe 2p1/2) asymmetric bands arising from spin-orbital splitting [189, 190]. The relative intensity ratio of these two bands is approximately 2:1. The two peaks are located at 709.9 and 723.1 eV for FePc, and 712.5 and 725.7 eV for the FePc-33/N-GP950. The standard Fe 2p3/2 and Fe 2p1/2 peaks for metallic Fe and its oxidized forms are located at 706.7/719.8, 709.2/722.8, and 711.2/724.8 eV binding energies [190, 191]. After the immobilization of the FePc on N-GP950, we observed the shift of Fe 2p peak from 709.9/723.1 eV (FePc) to higher binding energy of 712.5/725.7 eV (FePc-33/N-GP). This positive chemical shift of Fe 2p peak in FePc/N-GP950 spectrum is caused by the modification of the electronic environment attributed to electron transfer behavior from FePc to N-GP950. Furthermore, the curve fitting shows two species of iron (Fe^{2+} and Fe^{3+}) are present in both FePc and FePc-33/N-GP950 [192, 193]. The high-resolution N 1s XPS spectra of N-GP950, FePc, and FePc-33/N-GP950 indicate several binding configurations, as shown in Figure 4-4c. Specifically, the spectrum of N-GP950 shows that the peaks of N functionalities are assigned to pyridinic-N (I, 398.4 eV), pyrrolic-N (II, 400.2 eV), graphitic-N (III, 401.1 eV) and oxidized-N (IV, 402.7 eV) [174, 194]. The N 1s peaks of the FePc located at 398.5, 400.2 and 401.1 eV. However, the N 1s peaks of FePc-33/N-GP950 shifted to the higher binding energy. These results suggested that N-atoms are also involved in either chemical bonding or intermolecular interactions between FePc and N-GP950 [190, 191, 193-195]. The abundance of pyridinic-N in the FePc-33/N-GP950 composite is shown in Figure 4-4d. Previous studies reported that the iron coordinated with pyridinic-N (in the $M-N_4$ system) acts as a kernel of activity centers that facilitate the ORR [196, 197]. Figure 4-4e, display the deconvolution of the C 1s peak into four regions of species in N-GP950: C=C (284.6 eV), C=N (285.5 eV), C-N (286 eV), and a shoulder of O-C=O (287 eV). The C 1s components of FePc and FePc-33/N-GP950 occur with a broad peak area in slight shifting binding energy between 282 to 290 eV. The identified components are C=C (284.6 eV), C=N

(286.4 eV), C-N (287.8 eV), and O-C=O (290 eV). We anticipate that the shift of the binding energy may be due to the adsorption of FePc on N-GP950 sheets [194].

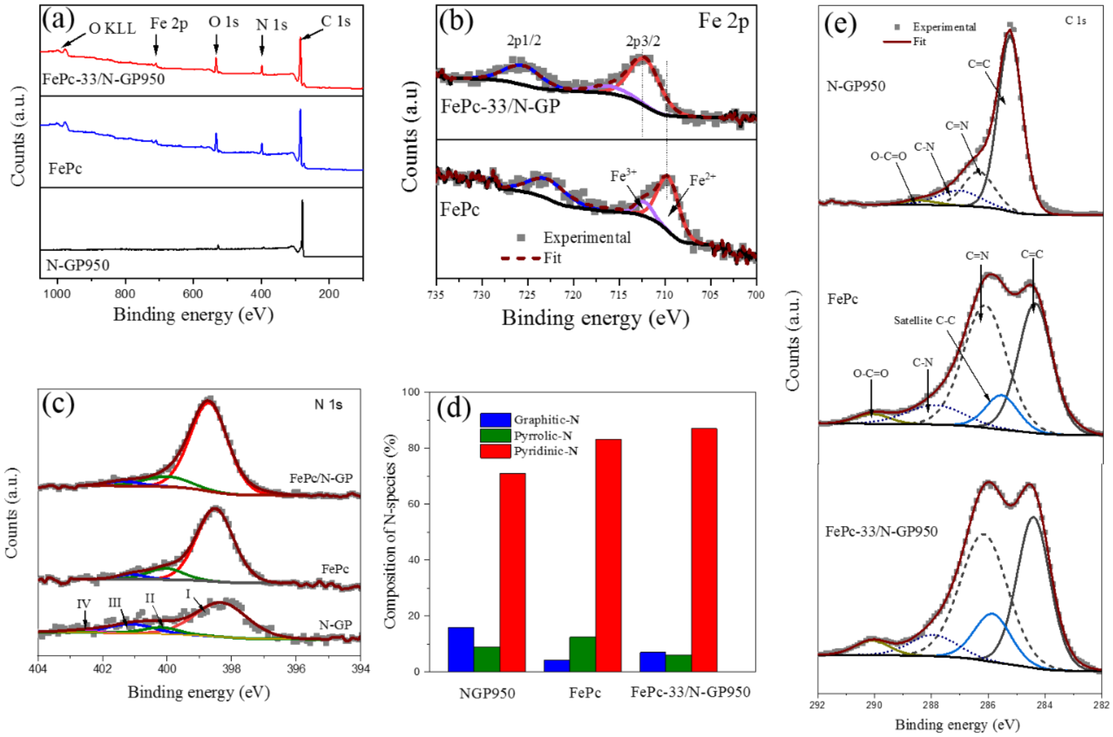

Figure 4-4 XPS analysis to elucidate the electronic properties of N-doped graphene (N-GP950), FePc, and FePc-33/N-GP950. (a) Survey spectra. High-resolution spectra of (b) Fe 2p and (c) N 1s, and (d) the nominal composition of N-species in the catalysts. (e) A high-resolution C 1s spectra of the N-GP950, FePc, and FePc-33/N-GP950, indicating various forms of carbons.

4.4.4 Electrochemical performance of FePc/N-doped graphene

The cyclic voltammetry (CV) results in Figure 4-5 performed initially, to investigate the ORR activities of FePc, N-GP950, and FePc-33/N-GP950 catalysts in 0.1 M KOH solution. Figure 4-5a displays the CV curves characteristic of cathodic peaks of oxygen reduction in the O_2-saturated electrolyte while no apparent oxygen reduction peaks were observed in the N_2-saturated electrolyte. The oxygen reduction peak potential of FePc-33/N-GP950 shifts positively for ca. 150 mV (Vs.

RHE) compared to the ORR peak potentials of individual FePc and N-GP950 catalysts. Additionally, the ORR peak position of FePc-33/N-GP is 30 mV more positive than that of commercial Pt/C, indicating an enhancement of ORR catalytic activity. The remarkable ORR activity exhibited by the FePc-33/N-GP is ascribed to the synergistic effect between FePc and N-GP950 [164, 184, 194].

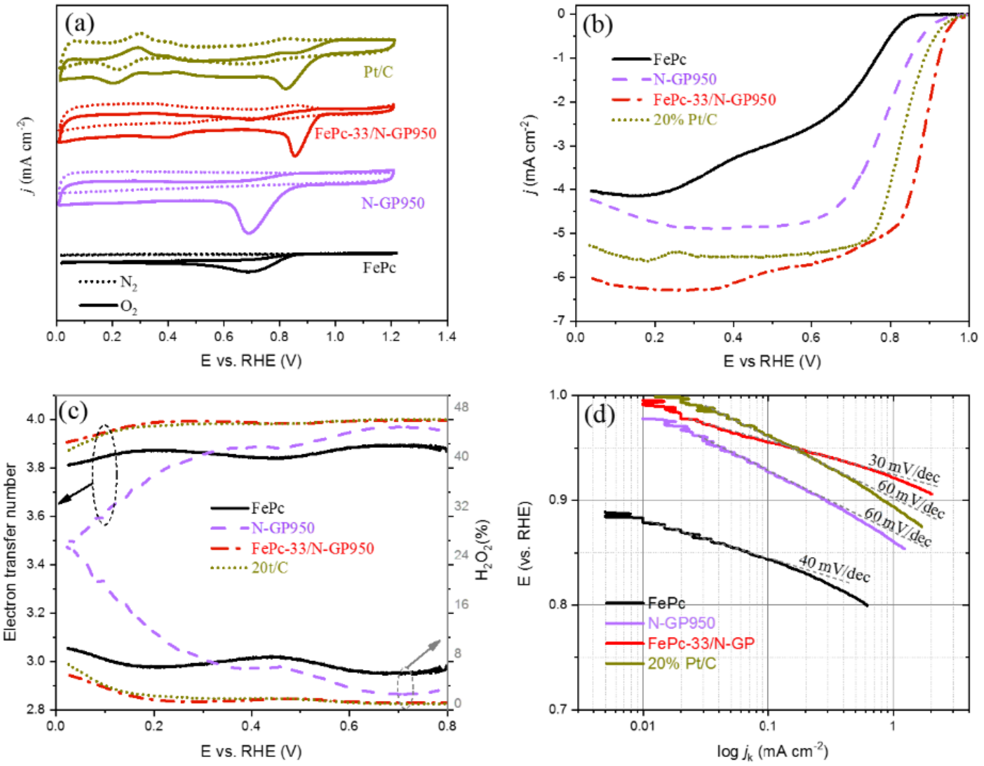

Figure 4-5 Electrochemical performance of FePc, N-GP950, FePc-33/N-GP950, and 20% Pt/C catalysts. (a) CV curves of the catalysts in N2 (dot lines) and O2 (solid lines) recorded using a scan rate of 50 mV s-1, (b) ORR polarization curves of the catalysts, (c) corresponding electron transfer number and H_2O_2 yield, and (d) the Tafel plots of the catalysts. The RRDE measurements recorded with scan rate: 10 mV s^{-1}, and the disk rotation rate of 1600 rpm.

Table 4-1 The ORR performance of N-doped graphene and recent FePc-based electrocatalysts. The electrochemical evaluation was carried out in O_2-saturated 0.1 M KOH, scan rate: 10 mV s^{-1} and disk rotation rate: 1600 rpm.

Catalysts		**Property**				**Ref**
		E_{onset} (V vs. RHE)	$E_{1/2}$ (V vs. RHE)	$j_{@0.8V}$ (mA cm^{-2})	j_L (mA cm^{-2})	
FePc on electrochemical exfoliated graphene	FePc-33/N-GP950	0.97	0.89	5.0	6.3	This study
	FePc	0.84	0.70	0.5	4.0	
	N-GP950	0.92	0.82	2.1	5.0	
	N-rGO	0.89	0.80	2.0	4.5	
	FePc-33/N-rGO	0.93	0.84	3.0	5.0	
	20 wt% Pt/C	0.95	0.84	4.0	5.5	
FePc on partly reduced graphene	FePc/rG	0.98	0.88	4.5	5.5	[35]
	Pt/C	0.97	0.85	3.8	5.1	
FePc on electrochemical reduced graphene	FePc/ERGO	0.95	0.85	2.6	4.5	[176]◊
	Pt/C	0.90	0.78	1.3	4.1	
Fe-SPc on carbon black	Fe-SPc/KJ300	0.91	0.87	2.7	3.0	[180]♠
FePc on mesoporous carbon	FePc/OMC	0.95	0.89	2.7	2.9	[198]
	FePc/MCV	0.94	0.86	1.5	2.1	
	FePc/RGO	0.89	0.83	1.2	1.7	
	Pt/OMC	0.88	0.81	2.2	3.5	
FePc on SBA-15 Silica as hard templating	FePc/SBA-15	0.98	0.87	4.0	4.5	[199]
	Pt/C	0.95	0.93	3.2	4.5	
FePc on SBA-15 silica as hard template	FePc/SBA-15	0.98	0.87	4.0	4.5	[200]
	Pt/C	1.00	0.89	3.8	4.2	
FePc on carbide derived carbon	FePc/CDC (50:50)	0.96	0.85	-	-	[201]♥
	Pt/C	0.91	0.81	-	-	
FePc on graphitized carbon black	Pc-FePc/Mn-GCB	0.96	0.90	4.7	5.1	[202]
	FePc/C	0.93	0.85	4.0	4.3	
	Pt/C	0.93	0.83	3.7	5.0	
FePc supported on CNTs	FePc/MWCNTs	0.91	0.86	2.5	5.0	[203]
	Pt/C	1.0	0.88	3.0	3.1	

◊The value reported against SCE reference electrode and calculated using equation.

$$E \text{ vs. RHE} = E_{Hg/HgO} + E^{o}_{Hg/HgO} + 0.059 \times pH.$$

♠The test was conducted in 0.1 M NaOH.

♥The ORR current values were not normalized with the geometrical surface area.

To gain further insight into the ORR activity of the FePc/N-GP catalysts, we performed linear sweep voltammetry (LSV) experiments on a RRDE in O_2-saturated 0.1 M KOH. Commercial 20 wt% Pt/C was also studied as a control. The ORR activity of the catalysts was evaluated by the exhibition of the highest possible positive value of the onset potential, a half-wave potential ($E_{1/2}$), limiting current densities, or current density at 0.80 V vs. RHE. Figure 4-5b-d shows the ORR polarization curves, the corresponding calculated electrons transfer number and percentage peroxide produced, and the Tafel plots of the FePc, N-GP950, FePc-950/N-GP950, and Pt/C catalysts. The FePc-33/N-GP950 catalyst exhibits enhancement of ORR activity in all measured parameters. The onset potential (0.97 V vs. RHE), the half-wave potential (0.89 V vs. RHE), limiting current (6.3 mA cm^{-2}) and the current density at 0.80 V (5.0 mA cm^{-2}) are shown in Table 4-1. These results demonstrate the superior catalytic activity of FePc-33/N-GP950 catalyst among the best ORR performing metal macrocycles [35, 176, 180, 198-203]. The excellent ORR performance of FePc-33/N-GP950 is attributed to: i) the high dispersion of FePc on the surface of N-GP950 (Figure 4-3d), which in turn increases accessible active sites while preventing agglomeration of FePc, ii) the synergistic effect between FePc and N-GP950 [34, 35] and iii) the abundance of pyridinic N [193, 196] as evidenced by XPS measurements (Figure 4-4d). The introduction of electron rich FePc into thin, large and well uniform N-GP950 sheets (TEM images, Figure 4-2 and Figure 4-3a) cause changes in charge distribution and electronic properties of the neighboring atoms in the graphene matrix, thus increasing the possibility of the adsorption of oxygen molecules [35, 176]. The electronic interaction is also evidenced by the shift of binding energies of N 1s species seen in Figure 4-4c. The excellent ORR activity of the FePc-33/N-GP950 further revealed by the calculated electron transfer number and H_2O_2% produced, as shown in Figure 4-5c. The FePc-33/N-GP950 predominantly exhibited a 4*e*- pathway with the calculated electron transfer number 3.99 which is consistent with a scanty production of hydrogen peroxide,

H_2O_2, (below 2.5%) in the potential range of 0.20 – 0.80 V. Figure 4-5d shows that the FePc-33/N-GP exhibits a much lower Tafel slope (~30 mV per decade) at low overpotential than the corresponding individual components and Pt/C, indicating faster ORR reaction rates [197]. Tafel slope in the smaller overpotential area is related to the first electron transfer in the rate-limiting step.

We also studied the influence of percentage loading of FePc in the composite on the ORR performance. Figure 4-6a-b shows ORR results for the catalysts different loading percentage of FePc, 16, 33, 50 wt% and 100 wt% for the FePc-16/N-GP950, FePc-33/N-GP950, FePc-50/N-GP950 and FePc alone, respectively. We find a significant enhancement of the ORR activity when the loading percentage of FePc in the composite increases. The highest ORR activity achieved when the percentage loading of FePc in the composites reached 33 wt% in the FePc-33/N-GP950, due to high dispersion and homogeneous distribution of the FePc [193]. However, when the weight ratio reached 50%, the ORR activity slightly decreased. We anticipate that the composition of 50 wt% FePc compromises the electronic conductivity of the composite due to the agglomeration of FePc particles [34, 35]. A further increase of the level of FePc beyond 50 wt% may cause the entire surface of N-GP sheet to be covered by FePc agglomerates, rendering poor conductivity and consequently, reduction of the ORR activity. Consistently, TEM image (Figure 4-3e) indicates overcrowded FePc nanostructures in the composite of FePc-50/N-GP950, with 50 wt% of FePc. Therefore, we established that 33 wt% FePc to be the optimal composition of FePc in the preparation of FePc/graphene composite to achieve maximum ORR performance. For easy comparison, the ORR parameters obtained from Figure 4-6a are listed in Table 4-2.

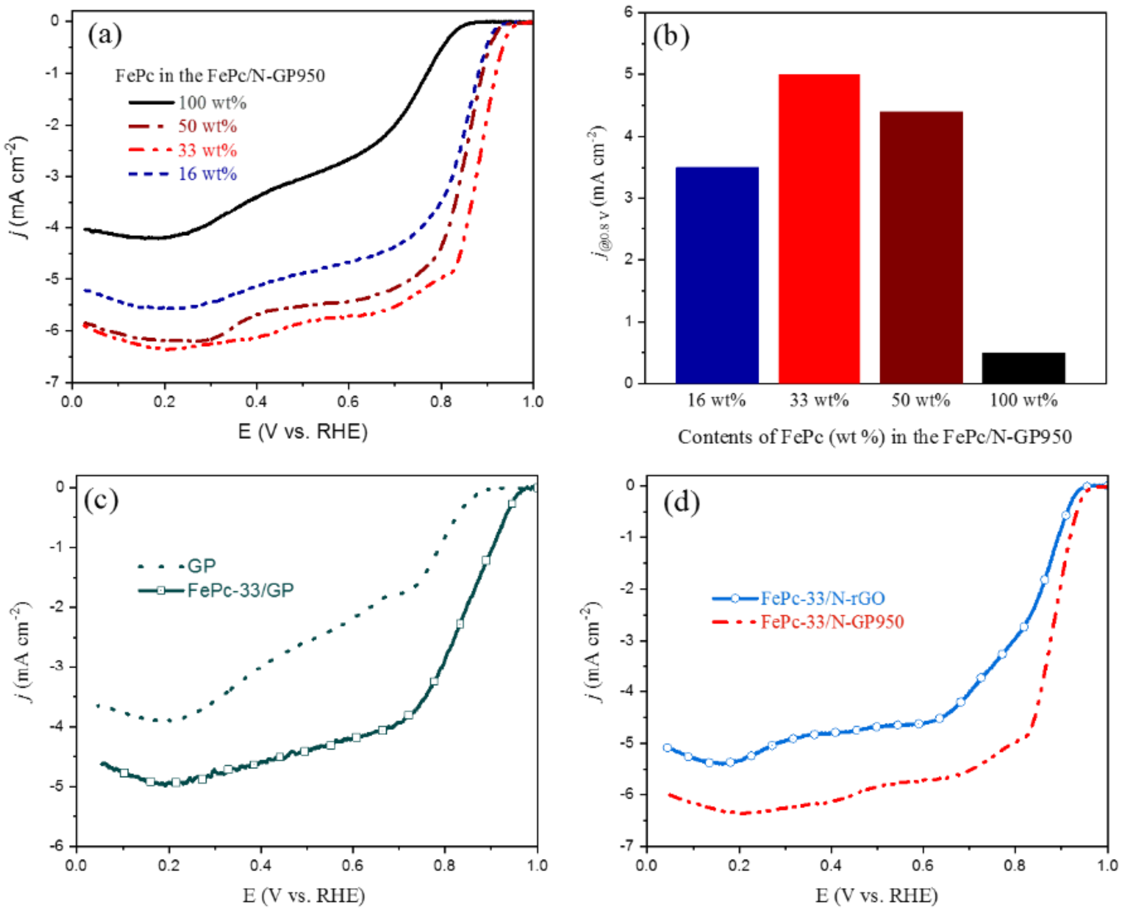

Figure 4-6 ORR performance of prepared catalysts. The LSVs of catalysts (a) FePc-33/N-GP950 catalysts prepared with different FePc loading 16, 33, 50, and 100 wt%, (b) correlation between content of FePc (wt %) and ORR activity at 0.8 V, (c) the LSVs of as-exfoliated GP and a composite of 33 wt% FePc and as-exfoliated GP (FePc-33/GP), and (d) composite of 33 wt% FePc, and N-doped Hummer's method exfoliated graphene (FePc-33/N-rGO) and the FePc-33/N-GP950. Electrolyte: 0.1 M KOH, scan rate: 10 mV s^{-1}, RRDE rotation: 1600 rpm.

Table 4-2 The correlation of ORR performance and the percentage of FePc loading in the FePc/N-GP950. The electrochemical evaluation was carried out in O_2-saturated 0.1 M KOH, scan rate: 10 mV s^{-1} and disk rotation rate: 1600 rpm.

FePc in the composite (%)	Activity at 0.8 V (mA cm^{-2})	Limiting Current (mA cm^{-2})	Onset potential (V vs. RHE)	Half-wave potential (V vs. RHE)
16	3.5	5.3	0.93	0.84
33	5.0	6.3	0.97	0.89
50	4.4	6.0	0.93	0.84
100	0.5	4.0	0.84	0.70

Comparatively, we also immobilized the FePc on three different samples of graphene; GP(as-exfoliated graphene), GP950 (GP which underwent one cycle of pyrolysis in an argon atmosphere at 950 ºC for 1 h) and on the N-rGO (graphene prepared by Hummer's method pyrolyzed at 950 °C in argon for 1 h and NH_3 atmosphere for 15 min). The as-prepared GP exhibited significant ORR activity. The ORR activity of the GP is further enhanced after immobilization of 33 wt% FePc to produce a FePc-33/GP composite (Figure4-6c). Interestingly, the catalytic performance of FePc-33/GP, specifically its onset of ORR polarization potential, is equivalent to our best catalyst, FePc-33/N-GP950. Accordingly, the development of FePc-33/GP with great ORR activity can be desirable in electrocatalysis because its synthesis did not involve high-temperature pyrolysis at any stage. To gain an in-depth understanding of the influence of support materials, we compared the ORR activity of FePc-33/N-rGO and our best catalyst, FePc-33/N-GP950. From Figure 4-6d, the ORR performance of the FePc-33/N-rGO is lower than that of FePc-33/N-GP950 in which the drift of the onset and half-wave potentials is about~20 and ~50 (mV vs. RHE) respectively. Likewise, the FePc-33/N-rGO exhibited lower limiting current density (5.0 mA cm^{-2}) and current density at 0.8 V (3.0 mA cm^{-2}) than the FePc-33/N-G950, 6.1 and 5.5 mA cm^{-2} respectively.

We also found that there is a significant difference in ORR activity between the individual support materials, the N-rGO, and the N-GP950. The N-GP950 displayed better ORR performance than the N-rGO, as shown in Figure 4-7a (also in Table 4-1). The difference in ORR performance is attributed to the variation of the quality of graphene produced by the two methods. The electrochemically exfoliated graphene (N-GP950), having high quality, uniform morphology, thin and large piece provided excellent support, conductivity, and stabilization of FePc compared to its counterpart (N-rGO) prepared by Hummers method. We infer that the morphology and quality of graphene obtained by electrochemical exfoliation of graphite play a central role in the superior performance demonstrated by the FePc-33/N-GP950. Similarly, we found an enhancement of ORR activity when the 33 wt% FePc was supported on the GP950, as shown in Figure 4-7b. Our experiments attest that graphene obtained by electrochemical exfoliation of graphite is an excellent support material for the FePc electrocatalyst.

We have also supported the ligand alone, the phthalocyanine (H_2Pc) on the N-GP950 to probe the role of the Fe atom as a coordinating center in the ORR activity of the FePc-33/N-GP950 composite. Despite the H_2Pc molecule being rich in pyridinic-N, the H_2Pc-33/N-GP950 exhibited a low ORR activity as seen in Figure 4-7c, indicating that the activity of FePc-33/N-GP950 is mainly dependent on the central iron atom in the Fe-N_4 system. Also, it is worth to mention that the N-GP950 was obtained by pyrolysis of graphene under optimized conditions (i.e., at 950 °C in Ar for 1 hour and 950 °C in NH_3 for 15 minutes. The ORR performance of the graphene samples pyrolyzed in NH_3 at 750, 950, and 1050 °C are presented (Figure 3-9) and discussed in Chapter 3. In which the graphene pyrolyzed at 950 °C (N-GP950) exhibited the highest limiting current density (4.9 mA cm^{-2}), the current density at 0.8 V (3.0 mA cm^{-2}) and lowest overpotential.

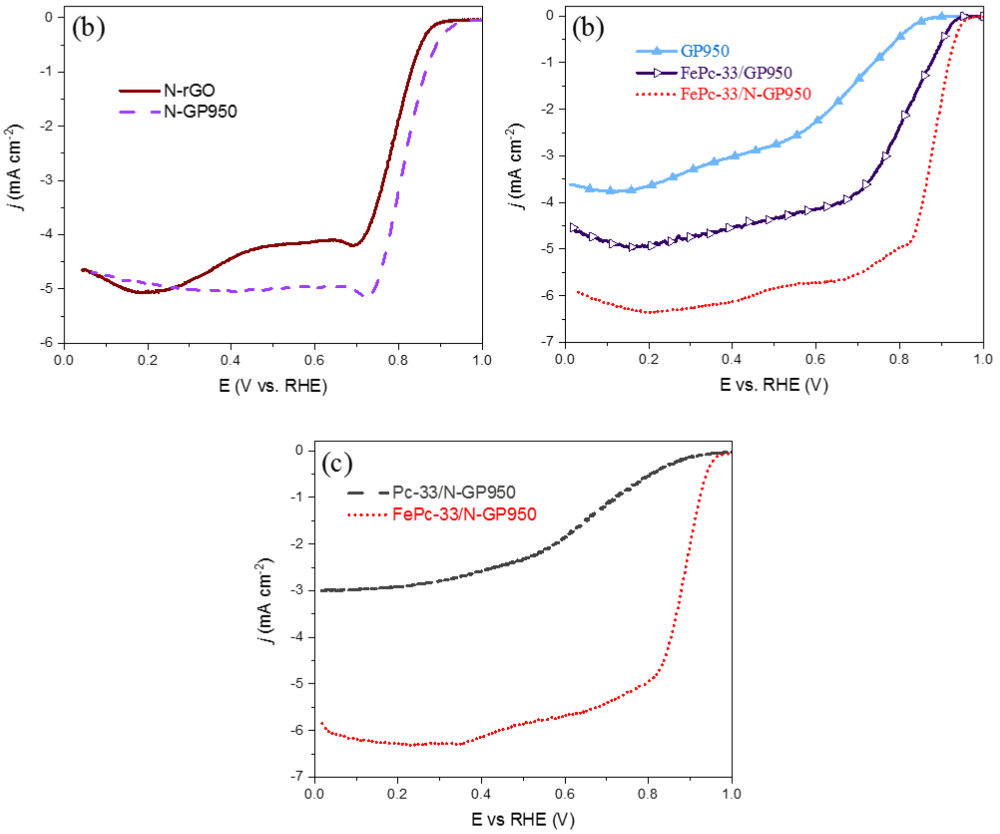

Figure 4-7 The linear sweep voltammograms of N-GP950, N-rGO, FePc-33/GP950, and Pc-33/N-GP950. (a) N-rGO and N-GP950, (b) GP950, FePc-33/GP950 and FePc-33/N-GP950, and (c) 33 wt% phthalocyanine (Pc-33)/N-GP950 and FePc-33/N-GP950. The LSVs recorded using 10 mV s^{-1} and working electrode rotation of 1600 rpm in the O_2-saturated 0.1 M KOH at room temperature. The Pc-33/N-GP950 displayed the lowest activity towards ORR, indicating the Fe in FePc plays a key role in the ORR process.

Furthermore, in Figure 4-8, we compared the ORR activity of our best composite catalyst, FePc-33/N-GP950 as a non-pyrolyzed and its pyrolyzed derivatives. The FePc-33/N-GP950 composite underwent pyrolysis in Ar atmosphere at 450, 750, and 950 °C for 1 hour. Compared to pyrolyzed FePc-33/N-GP950, the ORR performance of non-pyrolyzed FePc-33/N-GP950 is superior in all parameters. Also, we noted that the increase of pyrolysis temperature is associated with a significant loss of ORR activity of FePc-33/N-GP950. This loss of activity is attributed to the decomposition of the grafted FePc covering the N-GP950 surface [204].

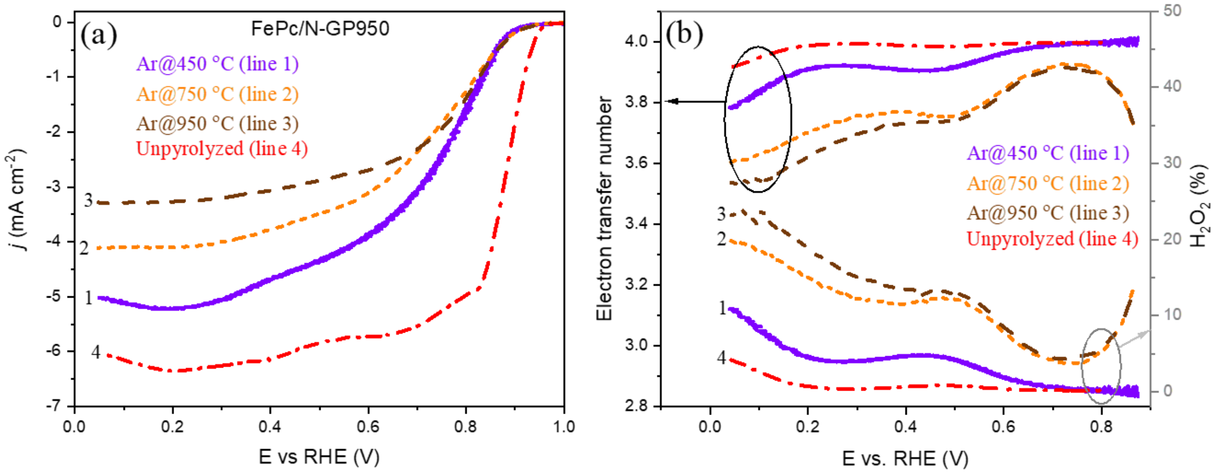

Figure 4-8 ORR electrochemical performance of the pyrolyzed FePc-33/N-GP950 (a) the LSVs (b) the corresponding electron transfer number, and H_2O_2 yield. Electrolyte: 0.1 KOH, the scan rate of 10 mV s^{-1}, the electrode rotation speed of 1600 rpm. The activity of the FePc-33/N-GP950 significantly lost after pyrolysis in argon.

In addition to the catalytic activity, long-term durability is another major challenge in electrocatalysis in general, and in fuel cells in particular. Therefore, ADT was used to examine the cycle stability of FePc-33/N-GP950 electrocatalyst. In Figure 4-9, the FePc-33/N-GP950 displayed excellent stability. After 5000 potential cycles, the FePc-33/N-GP950 electrode showed no substantial change either in the LSVs (Figure 4-9a) or CVs (Figure 4-9c) before and after 5000 continuous potential cycles. The excellent durability implies that there is no or little loss of the activity centers of the FePc-33/N-GP950 electrodes during long-term cycling of potential. The ORR durability results of FePc-33/N-GP950 is the best for unpyrolysed metal macrocycles/graphene catalysts so far. In contrast, the LSVs of Pt/C (Figure 4-9b), shows a significant drift of half-wave potential by about 30 mV after 5000 potential cycles under similar test conditions.

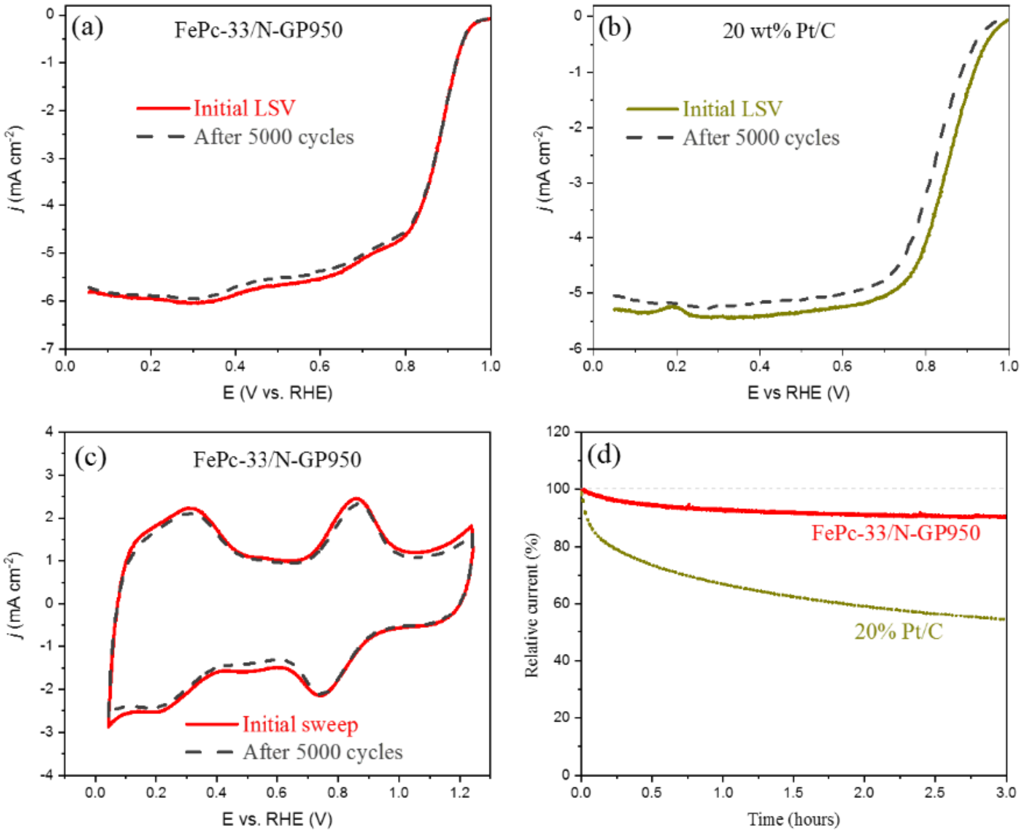

Figure 4-9 LSVs recorded before and after 5000 cycles ADT test between 0.6 to 1.0 V using scan rate 10 mV s^{-1} and working electrode rotation of 1600 rpm in O_2-saturated 0.1 M KOH for (a) FePc-33/N-GP950 and (b) 20% Pt/C, (c) CV curves of FePc-33/N-GP950 before and after ADT test recorded in N_2-saturated 0.1 M KOH. (d) Chronoamperometric responses (at 0.8 V vs. RHE) of FePc-33/N-GP950 and 20 wt% Pt/C catalysts in O_2-saturated 0.1 M KOH.

We also tested the stability of FePc-33/N-GP950 by chronoamperometry while holding the potential at 0.8 V (vs. RHE) in the O_2-saturated 0.1 M KOH with a rotation speed of 1600 rpm. The FePc-33/N-GP950 retained ca. 90% of the initial current after continuous measurement for three hours, whereas the commercial Pt/C retained only ca. 55% of the initial current in a similar condition (Figure 4-9d). The excellent durability exhibited by the FePc-33/N-GP950 electrode is attributed to the strong π-π interaction between the FePc and the N-GP950, improved dispersion of FePc on N-GP950 sheets and the intrinsic high corrosion resistance property of the support material, is of great importance for applications in catalysis [35].

Lastly, the graphene obtained by electrochemical exfoliation of graphite has several attributes as support that may have contributed to the improved ORR performance of the FePc/graphene composites. In addition to its unique 2D structure, the graphene (GP) we prepared by this method is thin, uniform, large sheet with relatively few functional groups [51, 98]. The large size and uniform morphology of the GP enabled homogeneous distribution of the FePc on the entire sheet providing numerous open and accessible activity centers. These attributes facilitate ORR kinetics by ensuring easy diffusion of the reactants and products to and from the catalytic centers [35, 179, 205, 206]. Similarly, the high quality of graphene offers an excellent conductivity property, which is highly desirable for charge transfer processes during the ORR. Also, the π-π interaction between the FePc and the N-GP950 is argued to provide stabilization of active sites and hence improve the stability of the FePc-33/N-GP950 [35].

4.5 Conclusions and perspectives

We prepared, high-performance NPMCs for ORR by immobilization of FePc onto nitrogen-doped electrochemical exfoliated graphene (N-GP950) by a simple, cost-effective and environmentally friendly method. Our best composite catalyst, FePc-33/N-GP950, demonstrated exceptionally high ORR activity and long-term durability in alkaline media with better performance than the commercial Pt/C. FePc-33/N-GP950 has the best ORR activity among the unpyrolysed metal macrocycles catalysts. We believe that the strong π-π electronic interaction between the FePc and high-quality N-doped graphene was instrumental in achieving the high ORR performance as deduced from XPS results. The N-doped electrochemical exfoliated graphene (N-GP950) demonstrated to be an excellent support material to improve the ORR performance of FePc. Therefore, this work provides an effective approach for the development of future NPMCs for practical applications in alkaline fuel cells. The findings open up new avenues for energy conversion technologies based on low-cost, scalable, nonprecious metal catalysts.

Chapter 5 Fabrication of MoS_2/TiO_2-Nanotubes for Hydrogen Evolution

Hydrogen is produced from water splitting via electrochemical method represents one of the most promising clean and renewable chemical energy carriers. Precious metals are widely investigated as the catalysts for hydrogen evolution reaction owing to their low overpotential and fast kinetics. However, to overcome the barriers of high-cost and limited resources of precious metals, considerable efforts have been made to discover viable alternatives electrocatalysts. In this work we combine promising catalytic activity of the MoS_2 and excellent charge transfer and chemical stability of the TiO_2-nanotubes, to fabricate a MoS_2/TiO_2-nanotubes as an efficient hydrogen evolution electrocatalyst. The new electrocatalyst exhibit high electrocatalytic activity with exceptional durability in an acidic media.

5.1 Introduction

Hydrogen, a potential energy carrier source that would significantly mitigate the environmental concerns due to zero-emission of carbonaceous species when combusted. Hydrogen can be used as fuel in fuel cells and also a promising solution in the conversion of renewable energies into chemical fuels that can be stored and transported [48, 207, 208]. However, a clean, low-cost, and scalable production of hydrogen is still challenging. Of the attractive and promising approaches to produce hydrogen, electrochemical hydrogen evolution reaction (HER) emerges as the best choice due to its flexibility and broad applicability. Besides the HER demands not only efficient and durable but also low-cost electrocatalysts [209, 210]. While, to date, the most performing HER electrocatalysts are still Pt-based materials, their prohibitive costs hamper the large-scale exploitation of production of hydrogen [209-211].

Recently, numerous efforts directed toward the development of low-cost and high-performance electrocatalysts for HER as replacement of expensive Pt-based materials. Various exciting earth-abundant transition metal-based compounds have been developed and stand out as promising HER electrocatalysts, including, metal selenides, phosphides, carbides, sulfides, and their composites [212-216]. Despite the volume of work, most of these materials have inferior performance compared to state-of-art Pt-based electrocatalysts. Besides, the majority of the catalysts are fabricated using complicated multistep techniques, which add up to the cost of the final products and present scaling challenges. In a recent exploration of alternative HER catalysts, layered nanostructures of transition metal dichalcogenides, including molybdenum disulfide (MoS_2) are developed with promising activity [217, 218]. However, none of them showed excellent HER performance comparable to the noble metals, mainly due to the low density of reactive active sites or poor electrical conductivity of the catalyst. Thus, the development of new MoS_2 structures with exposed edges sites on a chemically stable and one-dimensional support material is highly desirable to boost the HER catalytic performance.

Titania (TiO_2) materials are critical for several clean energy applications, including conversion and storage technologies [219-221]. In particular, TiO_2 is considered as a promising photoanode material for the UV-light-driven hydrogen evolution due to its high activity, excellent chemical stability, non-toxicity, and low-cost [100, 222, 223]. Material scientists, partly inspired by these properties, made remarkable progress over the past decades in the synthesis of high-quality TiO_2 nanostructures. Notably, the fabrication of one-dimensional (1D) TiO_2 materials like nanowires, nanorods, nanofibers, or nanotubes attracted significant interests because of their compelling properties [100, 101, 224]. Propitiously, the 1D TiO_2 structures combine the increased surface area and unidirectional electron conducting properties [100-102, 225, 226]. Compared to other 1D TiO_2

geometries, nanotubes, allow great control of the chemical and physical properties crucial to optimize the catalytic performance [227-231]. In recent years, numerous methods to fabricate TiO_2 nanotubes (TiO_2-NTs) have been developed, including template [232], hydrothermal [233, 234], sol-gel [235], as well as electrochemical anodization [236-238]. Among these methods, anodization is highly attractive, owing to its low-cost, straightforward, and allow the control of tubes morphology [16, 101]. The electrocatalytic activity of TiO_2 NTs is primarily influenced by their structural parameters [101]. Therefore, employing a cost-effective method, which can generate TiO_2-NTs with a controlled morphology is necessary for further exploration of potential electrochemical applications.

In this work, we fabricated highly organized free-standing TiO_2-NTs arrays membrane via the anodization of titanium foils, in an organic electrolyte containing fluoride ion. Subsequently, we assembled MoS_2-supported free-standing TiO_2-NTs (MoS_2/TiO_2-NTs) by merely immobilizing the grown hydrothermal MoS_2 on the surface of the anodic grown TiO_2-NTs by using a slow evaporation approach. The hybrid catalyst, MoS_2/TiO_2-NTs exhibits efficient HER electrocatalytic activity with exceptional durability in acidic media owing to the synergetic effect arising from the interaction between the dispersed MoS_2 and the TiO_2-NTs support. Our results demonstrate that TiO_2-NTs are an excellent support material for MoS_2 as HER electrocatalyst. This study provides a straightforward approach to fabricate efficient electrocatalyst for the production of hydrogen from water based on low-cost and abundant materials

5.2 Experimental

5.2.1 Chemicals and Materials

Titanium foil (99.7%, 0.5 mm, Sigma-Aldrich), graphite plate and rod (Alfa Aesar), ethanol, methanol, isopropanol, acetone, ethylene glycol (EG, 99.8%), ammonium fluoride (98%), sulfuric acid (99.9), hydrofluoric acid (HCl, 37%), potassium hydroxide (KOH, 85%), ammonium heptamolybdate tetrahydrate ($H_{24}Mo_7O_{24}.4H_2O$, 99%), thiourea (NH_2CSNH_2, 99%), and hydrazine ($N_2H_4.H_2O$, 98%). All chemicals purchased from Sigma Aldrich used as received.

5.2.2 Preparation TiO_2-nanotubes

The TiO_2-NT membranes were prepared by anodization of Ti foil in EG electrolyte, containing 0.3 wt% NH_4F, and two wt% Milli Q water using 60 V for a specified time. In all the anodization experiments Ti foil used as a working electrode (20 mm × 15 mm× 0.5 mm), graphite plate (20 mm × 20 mm× 3 mm) as a counter electrode and a direct current power supply (PSC-260, Circuit Test Electronics). The anodization carried in a polytetrafluoroethylene (PTFE) cell with two electrodes system. Before anodization, the foils were ultrasonically cleaned sequentially in acetone, ethanol, and Milli Q water. Initially, the Ti foil was anodized for 1 hour, and the resulting oxide layer was removed by ultrasonication in 0.1 M HCl to obtain highly self-ordered dimples-like imprinted Ti foil. The textured Ti foil subsequently underwent second anodization to form self-organized TiO_2-NTs membrane arrays. Then, the as-anodized TiO_2-NTs ultrasonically cleaned in ethanol for 15 s, using an ultrasonic cleaner (40 kHz, 80 W), and then left to dry at room temperature or in the oven at 75 °C. Drying of the as-anodized Ti foil in an oven resulted in detachment of the formed TiO_2-NT membranes. Two methods are used to induce crystallinity of the as-anodized TiO_2-NTs. In the first method, the as-anodized free-standing TiO_2-NTs were annealed at 450 °C in the air muffle furnace for 2 hours, with heating and cooling rates set at 10 °C/min. In the second method, the as-anodized Ti foil was exposed to hot water steam, for about 30 min.

5.2.3 Preparation of MoS_2 layers

The MoS_2 was synthesized by hydrolysis of aqueous ammonium heptamolybdate tetrahydrate ($(NH_4)_6Mo_7O_{24}.4H_2O$) in the presence of thiourea and hydrazine using a hydrothermal method. In a typical synthesis, 52 mg of thiourea and 1 ml of hydrazine was added to an aqueous solution of $(NH_4)_6Mo_7O_{24}.4H_2O$ (114 mg, 50 ml). The mixture was transferred into a 100 ml Teflon vessel which was then placed and sealed in a stainless-steel cup and kept at 200 °C for 10 hours. After cooling the black precipitate was collected by centrifugation, washed with deionized water and ethanol. Subsequently, the black precipitates of MoS_2 were dispersed in the Milli-Q water and finally freeze-dried. Then, the dry MoS_2 layers were used in the subsequent stage and for characterization.

5.2.4 Preparation of MoS_2-supported free-standing TiO_2-NTs

The MoS_2-supported free-standing TiO_2-NTs were prepared by a slow evaporation method. The mole ratio of MoS_2 to TiO_2-nanotube was kept at 1:3.7. Briefly, the as-prepared free-standing TiO_2-NTs (60 mg) were dispersed in 100 ml ethanol by sonication for 15 minutes. To this mixture, 32 mg of the as-prepared MoS_2 particles were added and the resulting suspension sonicated for about 10 min in ice water. Then the solvent was evaporated at 65 °C, and the slurry dried in an oven at 95 °C. The dried powder underwent annealing in argon at 480 °C for 2 hours to obtain the MoS_2/TiO_2-NTs catalyst.

5.2.5 Preparation of hydrogen evolution electrodes

The modified glass carbon WE electrodes were prepared by initially dispersing 10 mg catalyst in 350 µl of water/ethanol (5:3 v/v) with 5 wt% Nafion (95 μl), with the Nafion-to-catalyst ratio of 0.4. The mixture was homogenized by alternating circles of 15 minutes of sonicating and shaking for 1 hour, to obtain an ink-like suspension. Then 5 µl of the catalyst ink was deposited onto a GC electrode (geometric surface area 0.2475 cm^2). The loading of the catalysts was 0.450 mg cm^{-2}. The carbon fibre paper (CP) electrode was prepared by depositing the catalyst ink prepared above onto a carbon fibre (10 mm × 0.5 mm) with a catalyst loading of 0.450 mg cm^{-2}.

5.3 Characterization TiO_2 NTs and MoS_2/TiO_2-NTs

5.3.1 Physical characterization

The morphologies of TiO_2 NTs and MoS_2/TiO_2-NTs were investigated by using a scanning electron microscope (SEM, Lyra3 SEM-FIB by Tescan) and a transmission electron microscope (TEM, JEOL 2100F). All the geometrical properties were measured from SEM and TEM images (Image J software) in the average of 10 measurements. The crystallographic properties of the materials analyzed by X-ray diffraction (XRD) were performed with an X'pert Philips (equipped with a Panalytical X'celerator detector), using graphite monochromatized Cu Kα radiation ($\lambda = 1.54056$ Å). The chemical states and surface composition of the TiO_2 NTs was characterized by X-ray photoelectron spectroscopy (XPS, VG Escalab220i - XL).

5.3.2 Electrochemical characterization

The electrochemical tests were performed using a standard three-electrode cell setup with 0.5 M H_2SO_4 and 1.0 M KOH solution as the electrolyte. All electrochemical measurements were performed using a rotating disk electrode (RDE, PINE Research Instrumentation) with a bipotentiostat (Pine, Model PGSTAT-72637) workstation at room temperature. In all measurements, we used a saturated calomel electrode (SCE) and graphite rod as the reference and counter electrodes, respectively. The reference electrode calibrated to the reversible hydrogen electrode (RHE) potentials in a high purity H_2 saturated electrolyte with a Pt wire as the working electrode. The measurement carried in H_2SO_4 solution (0.5 M) and KOH solution (0.1 M). Before use, the GC electrodes in RDE are polished using aqueous alumina suspension on felt polishing pads. Initially, several CV cycles were performed on all the WE electrodes to get rid of possible contaminants. The polarization curves recorded by scanning the potential from 0 to -0.7 (V vs. RHE) with a scan rate of 10 mV s^{-1}. Durability test of the catalyst conducted by recording HER polarization curves before and after 5000, potential cycles between -0.4 and +0.2 (V vs. RHE) at a scan rate of 100 mV s^{-1}. Electrolyte: 0.5 M H_2SO_4. All potentials in this study refer to a reversible hydrogen electrode (RHE).

5.4 Results and discussion

5.4.1 Electrochemical anodization of titanium

The general procedure of anodization of the Ti substrate is illustrated in Figure 5-1a, in which the Ti foil serves as the anode and graphite plate as a cathode. The mechanism of the formation of TiO_2-NTs, by anodization of Ti foil, begins with field assisted oxidation of Ti foil surface in contact with electrolyte, and subsequently forming the TiO_2 layer (Equation 5-1 and 5-2) Simultaneously, the occurrence of selective chemical dissolution of formed TiO_2, by the action of F ions (Equation 5-3), etches out the cell boundaries leading to the formation of individual TiO_2 NTs [100-102].

$$Ti \rightarrow Ti^{4+} + 4e^{-} \qquad (5\text{-}1)$$

$$Ti + 2\,H_2O \rightarrow TiO_2 + 4H^{+} + 4e^{-} \qquad (5\text{-}2)$$

$$TiO_2 + 6F^{-} + 4H^{+} \rightarrow [TiF_6]^{2-} + 2H_2O \qquad (5\text{-}3)$$

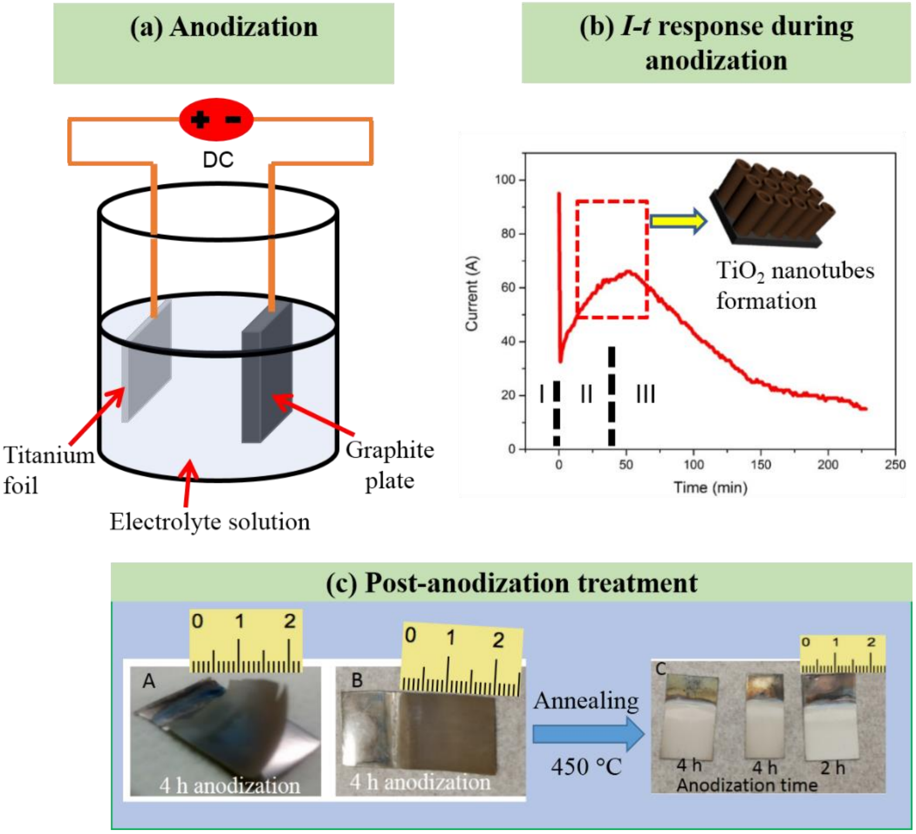
(a) Anodization

(b) *I-t* response during anodization

(c) Post-anodization treatment

Figure 5-1 A scheme of fabrication of highly ordered TiO_2 nanotubes arrays (a) anodization experimental setup, (b) *I-t* response during anodization process, and (c) the appearance of anodized Ti substrate after drying and annealing.

The growth of nanotubes depends on the presence of fluoride species, and the balance between the formation of the TiO_2 layer and dissolution of the fluoride rich layer at the bottom and around the tube. Monitoring the current-time response, during the anodization process, produced a characteristic current-time profile. The typical current-time (*I-t*) profile during the growth of nanotubes is depicted in Figure 5-1b, characterized by three zones of growth. In zone I, a rapid current decay was observed due to the oxidation Ti substrate and formation of a compact layer of TiO_2. In zone II, the current increases, owing to the dissolution of formed TiO_2 layer, induced by F^- ions, resulting in the initial formation of the nanotubes. Finally, in zone III, as nanotubes continue to grow, the current continues to increase until it reaches a limit and begins to drop again until a steady-state situation is established between the formation of oxide at the metal/oxide interface and the dissolution [236-238].

Photographic images of the dry TiO_2-NTs are given in Figure 5-1c. It is apparent that the as-anodized TiO_2-NTs is brown and easily detached itself from the Ti substrate after drying in an oven at 70 °C (image A) to obtain a free-standing membrane. The existence of fluoride rich layer, at the interfacial layer between the Ti substrate and nanotubes, is believed to weaken the interfacial adhesion [229, 239]. However, when the as-anodized Ti substrate dried in air at room temperature (~22 ºC), followed by drying in an oven at 85 °C for overnight, the membrane remains firmly attached to the Ti substrate (Figure 5-1c, image B). Interestingly, the TiO_2-NTs membrane remained firmly attached to the Ti substrate, even after annealing in air at 450 °C for 2 hours (Figure 5-1c, image C). All of these observations indicated that the slow drying process reduced the stress of the oxide film at the interface. Besides, the strong adhesion of anodic TiO_2-NTs arrays to the underlying Ti foil is highly advantageous in some promising applications where the use of binders in electrode material may compromise the performance.

5.4.2 The structural morphology of TiO_2-nanotubes

Figure 5-2 display the morphology of free-standing TiO_2-NTs arrays. The TiO_2-NTs membrane obtained by drying the as-anodized sample in an oven at 75 °C detached itself from the Ti foil. The free-standing TiO_2 NTs are smooth, round in shape and have an open mouth and closed bottom.

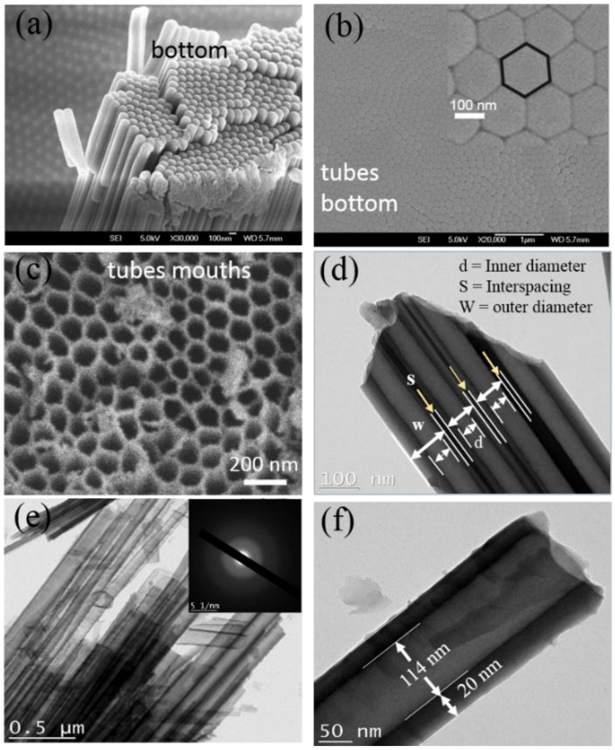

Figure 5-2 Structural morphology of as-anodized TiO_2-NTs, (a) SEM images of a longitudinal section of free-standing TiO_2-NTs with a closed bottom up, (b) a top view of bottom morphology of the nanotubes, (c) top view morphology. TEM images (d) interspacing between the individual nanotubes, anodized under ice bath, (e) cross-section and its selected area electron diffraction (SAED) pattern as an inset, and (f) high-resolution image of the nanotube prepared at room temperature.

Figure 5-2a-b display the SEM images of longitudinal aerial section and bottom view of the TiO_2-NTs, and its corresponding inset indicates that nanotubes are self-organized in a hexagonal packing with each of the nanotube surrounded by 6 nearest neighbors. While the top views of the nanotubes layer reveal locally ordered nanotubes openings (Figure 5-2c) with an average inner diameter of about 95 nm. Further, an organized interspacing between the nanotubes visible in Figure 5-2d with an average spacing of about 12 nm (for the nanotubes grown under ice bath electrolyte temperature). These interspacing between the nanotubes are formed as a consequence of the chemical dissolution of the fluoride rich layer due to its susceptibility to high-water solubility [238-240]. Predominantly, the as-anodized nanotubes array (Figure 5-2e-f) are mainly characterized by uniform tube diameter and wall thickness along the whole length. For example, the mean tube diameters for the anodization temperatures of 0, 22 and, 50 ºC, are 54±1.2, 96±1.1 and 114±1.4 nm, respectively. On the other hand, the tube wall thickness is observed to be 50±1.4, 24±1.1, and 20±1 nm, respectively. Conversely, the reported TiO_2 nanotubes grown in organic electrolytes had a small inner diameter at the bottom and wide at the top [102, 240]. The average wall thickness and the inner diameter of the nanotubes are 20 and 114 nm (anodized at room temperature) respectively. Furthermore, the inserted selected area electron diffraction (SAED) in Figure 5-2e, shows a diffused rings pattern, which confirms the amorphous nature of the as-anodized TiO_2-NTs.

Also, it is worth noting that when ethanol was added to the electrolyte, no growth of nanotubes on the Ti foil was observed. Instead, we observed the electropolishing of the Ti foil. We believe that the presence of ethanol in the electrolyte solution prevented the formation of TiO_2 layer (chemical reaction Equation 2). For a reason, that ethanol in the electrolyte reacts with the dissolved Ti ions to form a soluble $Ti(OEt)_4$, which in turn limits the formation of the TiO_2 layer.

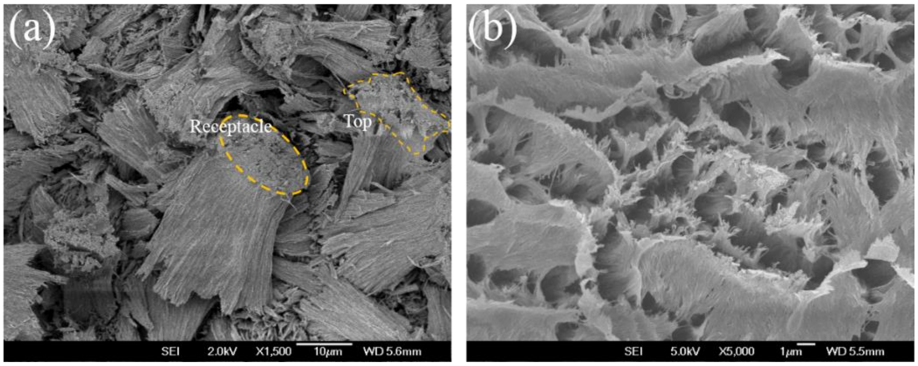

Figure 5-3 SEM images of TiO_2 nanostructures formed during anodization of electropolished Ti substrate in EG containing 0.3 wt% NH4F and 2 wt% deionized water with 20% V/V ethanol, (a) cross-section view of spindle bundles, and (b) top view.

Surprisingly, anodization of the electropolished Ti, yielded bundles of spindles, with grass-like top morphologies (nano-grass) as shown in Figure 5-3. Contrary to the previous reports on the formation of TiO_2 bundle layers during short anodization period, the bundles of spindles described in this study were obtained after a long period of anodization as well as persisted after 3 seconds of ultrasonic cleaning [102, 241, 242]. In an aqueous electrolyte, the formation of TiO_2 grass-like morphologies is associated to the rapid rate of etching of the tube at their top especially after long-duration of anodization experiments causing the development of needle- or grass-like morphologies [242-246].

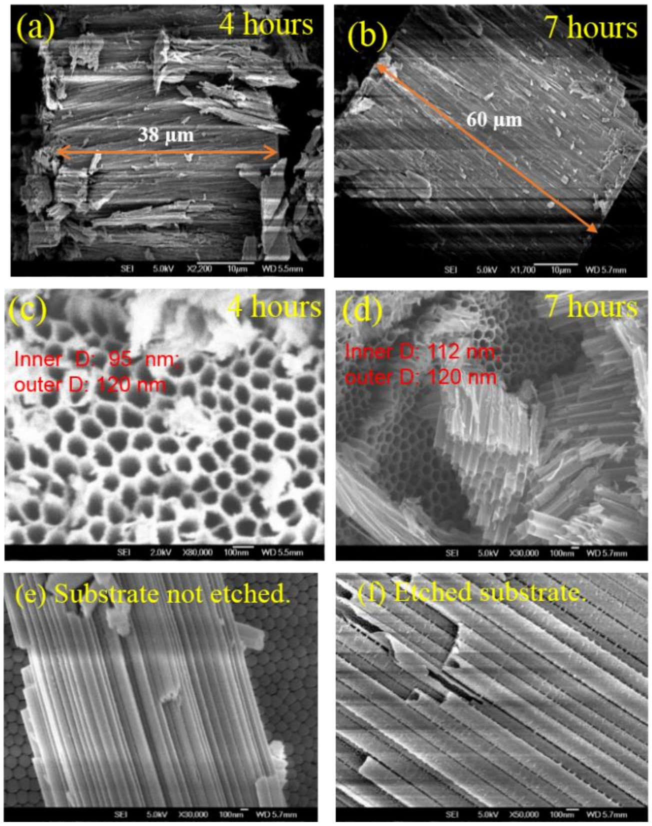

Figure 5-4 SEM images of TiO_2-nanotubes, showing the evolution of morphologies with different anodization conditions. (a-d) effect of length of anodization period, and (e-f) effect of the substrate etching on the nanotube surface textures.

Besides, manipulation of the anodization conditions plays a crucial role in the evolution and control of morphologies of the TiO_2 nanotubes. As shown in Figure 5-4, it is possible to obtain nanotubes with different length, diameter, and the wall thickness by controlling anodization time. For example, longer nanotubes were obtained by extending the anodization period. The nanotubes fabricated after 7 hours, have an average length of about 60 µm, while approximately 38 µm long nanotubes were obtained after 4 hours shown in Figure 5-4a-b. Figure 5-4c-d, reveal the inner and outer diameters of nanotubes are 95, 120 nm and 112, 120 nm for the duration of anodization of 4 and 7 hours respectively. These results indicate that the extended anodization period has a significant effect on the length, inner nanotubes diameter as well as wall thickness at a particular bias potential. Besides, the estimated wall thickness of the nanotubes decreased with the anodization period from 25 nm (4 hours) to 8 nm (7 hours), as measured from Figure 5-4c-d, due to the extended dissolution of the TiO_2 in the inner wall of the nanotubes. Additionally, surface morphology of the nanotubes is affected by the pre-anodization treatment of the substrate. When the Ti foil was etched with 1 wt% HF before anodization, there was the formation of nanotubes with ripples, resulting in a rough tube outer wall surface. On the other hand, a smooth-walled outer surface of nanotubes was observed from the substrate without etching (Figure 5-4e-f). The reasons for the rippled wall surface remain unclear. To conclude, desirable morphologies of nanotubes can be fabricated by controlling pre-anodization and anodization conditions.

Further, to understand the influence of electrolyte temperature during anodization on the morphologies of the nanotubes, we carried out anodization of Ti substrate, under ice bath (~0 ºC) and silicon oil bath, at 22 and 50 ºC. From TEM images in Figure 5-5, the nanotubes prepared under ice bath comparatively have the thickest wall (~50 nm) and inner tube diameter (54 nm). While, at 22 and 50 ºC, the tube wall thickness, inner diameters of the fabricated nanotubes are 24, 94 nm, and 20, 114 nm, respectively. Also, the wall thickness of the TiO_2-nanotubes decreased when the anodization was carried out at 22 and 50 °C, respectively, while the tube diameters increased. This observation can be attributed to the formation mechanism of the TiO_2-NTs [241, 246]; in which both the main chemical reactions for the formation of nanotubes in the electrolyte containing fluoride, namely the formation and dissolution of TiO_2 (Equation 5-2 and 5-3) are temperature dependent [241].

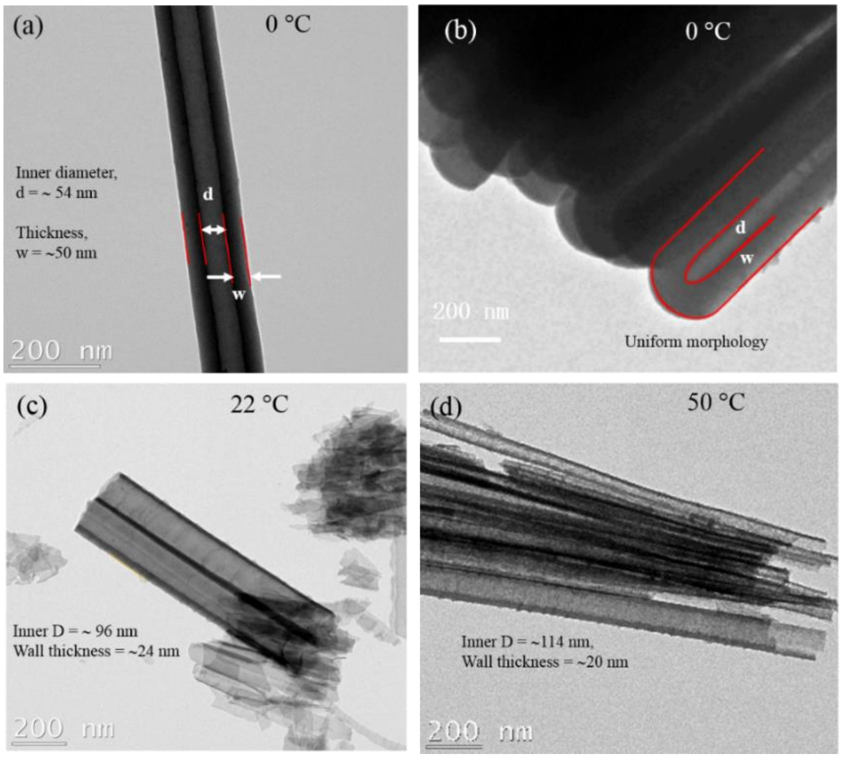

Figure 5-5 TEM images of the TiO_2-NTs prepared by anodization of Ti substrate, in EG containing 0.3% NH_4F and 2 wt% water, for 7 hours at (a-b) 0 °C, (c) 22 °C, and (d) 50 °C.

At low temperature, the mobility of ions in the viscous EG electrolyte is limited, which in turn leads to the slow rate of etching and dissolution of formed TiO_2 layer, leading to a wider tube wall thickness. However, at high temperature, the rates of etching and dissolution of TiO_2 were higher than that in the ice bath, consequently resulting in thinner tube walls and wider diameters. It is therefore rational to ascribe that etching by fluoride ions as well as dissolution of the oxide will be slow at low temperatures, thus accounting for the thick wall and thin diameters and vice versa [236, 246]. The findings show that the electrolyte temperature gives excellent control over the morphology of nanotubes, namely; the tube wall thickness, tube diameter, and uniformity of the tubular layer.

Structurally, the as-anodized TiO_2-NTs are highly amorphous (Figure 5-2e) but transforms into crystalline phase after annealing or subjecting the sample in the hot water steam as shown in Figure 5-6a-c. From the TEM image and its corresponding SAED patterns (Figure 5-6b), we can see that that the amorphous structure of the as-anodized TiO_2-NTs is completely transformed into crystalline diffraction rings after annealing. Further, SAED analysis revealed that the calculated d-spacing corresponding to the diffraction ring patterns is congruent with the anatase phase of TiO_2 nanocrystals (JCPDS, 21-1272) [247]. The diffraction ring patterns are indexed to (101), (004), (200), and (211) in their respective SAED patterns shown in Figure 5-6b. Likewise, the high-resolution TEM (HR-TEM) image given in Figure 5-6c indicates that the individual crystalline nanotube comprises of well-defined lattice planes, with d-spacing of 3.5 Å, which corresponds to the (101) plane of the anatase phase of TiO_2 [247, 248]. The crystalline nature of the nanotubes was confirmed by the XRD analysis (Figure 5-6d) for the as-anodized TiO_2-NTs sample, annealed at 450 ºC for 2 hours (red line), and the other samples were subjected to hot water steam for 30 (black line) and 60 minutes (blue line). In both cases, the TiO_2-NT samples demonstrated high crystallinity with all peaks of XRD patterns, indexed to anatase TiO_2 phase (JCPDS: 21-1272) [247]. Notably, the XRD results are consistent with TEM analysis. Another exciting feature is that we found only a pure phase composition of TiO_2 membranes in the XRD spectra for both samples from the two crystallization approaches. However, the samples subjected to hot steam at 30 minutes and 60 minutes show the variation of intensity of the main anatase reflection peak at $2\theta \sim 25$ and 50 °C. The results suggest that the degree of crystallinity of the TiO_2-NTs membrane improved with a duration of exposure to hot water steam. To conclude, the XRD results indicate the possibility of inducing pure phase crystallinity of the TiO_2 NTs, at low temperature. Crystallization of TiO_2-NTs at low temperature provides a cost-effective and straightforward approach to fabricate crystalline TiO_2-nanotubes.

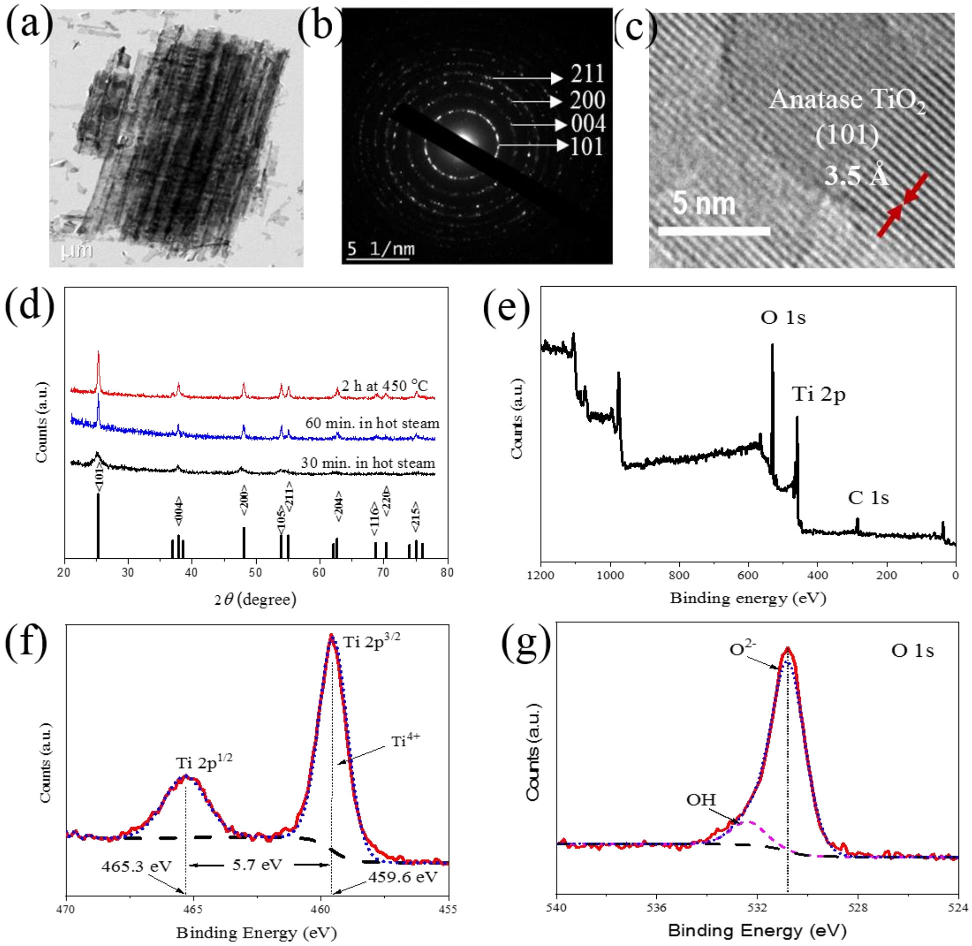

Figure 5-6 The structure of the annealed TiO$_2$-NTs. (a) The TEM image of annealed at 450 °C for 2 hours, (b) selected area electron diffraction (SAED), (c) HRTEM image of anatase phase TiO$_2$-NTs. (d XRD spectra of crystalline TiO$_2$-NTs array obtained by subjecting the as-anodized sample in hot water steam, and annealed at 450 °C for 2 hours in an air oven, with their corresponding characteristic powder diffraction pattern, for anatase TiO$_2$ JCPDS: 21-1272. The XPS spectra of the annealed TiO$_2$-NTs, (e) Survey spectrum, (f) high-resolution Ti 2p, and (g) high-resolution O 1s.

5.4.3 Surface elemental composition of TiO$_2$-nanotubes

XPS measurements performed to identify the surface elemental composition and their chemical states for the TiO$_2$-NTs, as shown in Figure 5-6e-g. The binding energy (BE) position calibrated using the C 1s peak at 284.6 eV. The XPS survey spectrum, Figure 5-6e, confirms the presence of individual elements along with adventitious carbon. The as-anodized TiO$_2$ nanotubes surface contain the Ti 2p, and O 1s peaks. The high resolution of Ti 2p (Figure 5-6f), indicates the spin-orbital splitting photoelectrons into Ti 2p1/2 and Ti 2p3/2, located at binding energies of 465.3 and 459.6 eV, respectively, characteristic of the Ti^{4+} formal oxidation state of TiO_2. The peak separation of 5.7 eV between the Ti 2p1/2 and Ti 2p3/2 signals is in excellent agreement with the reported literature values [249-251]. The O 1s signal for the TiO_2 nanotubes (Figure 5-6g), at a binding energy of 531 eV, is assigned to lattice oxygen species and a shoulder located towards higher binding energies associated to adsorbed -OH species on the surface. All the peaks in XPS spectra are in good agreement with the reported values elsewhere [247, 248, 252-255].

5.4.4 Synthesis of MoS_2-supported free-standing TiO_2-nanotubes

The scheme of preparation and morphology and structure of the composite are shown in Figure 5-7. The steps of fabrication of the composite schemed in Figure 5-7a. The TEM image Figure 5-7b displays individual layers of MoS_2 amassed like a flower. Figure 5-7c depict the morphology of MoS_2/TiO_2-NTs in which the layered MoS_2 highly disperse on the entire surface of the TiO_2-NTs. Meanwhile, the HRTEM image of MoS_2/TiO_2 sample, Figure 5-7d, clearly show that the layered MoS_2 tightly embedded in the TiO_2-NTs. The close assembly of components shows that the slow-evaporation approach achieves strong interaction between MoS_2 and free-standing TiO_2-NTs. Notably, two different lattice fringes can be observed, d = 3.5 Å corresponding to the lattice spacing of anatase TiO_2 (101) planes, and d = 6.2 Å, which matches with the (002) plane of the 2H-MoS_2 crystal [256]. The TEM images show the formation of a unique heterostructure of MoS_2/TiO_2-NTs, which play a crucial role in the improvement of HER performance arising from catalytic synergetic effect between MoS_2 and TiO_2 [257, 258].

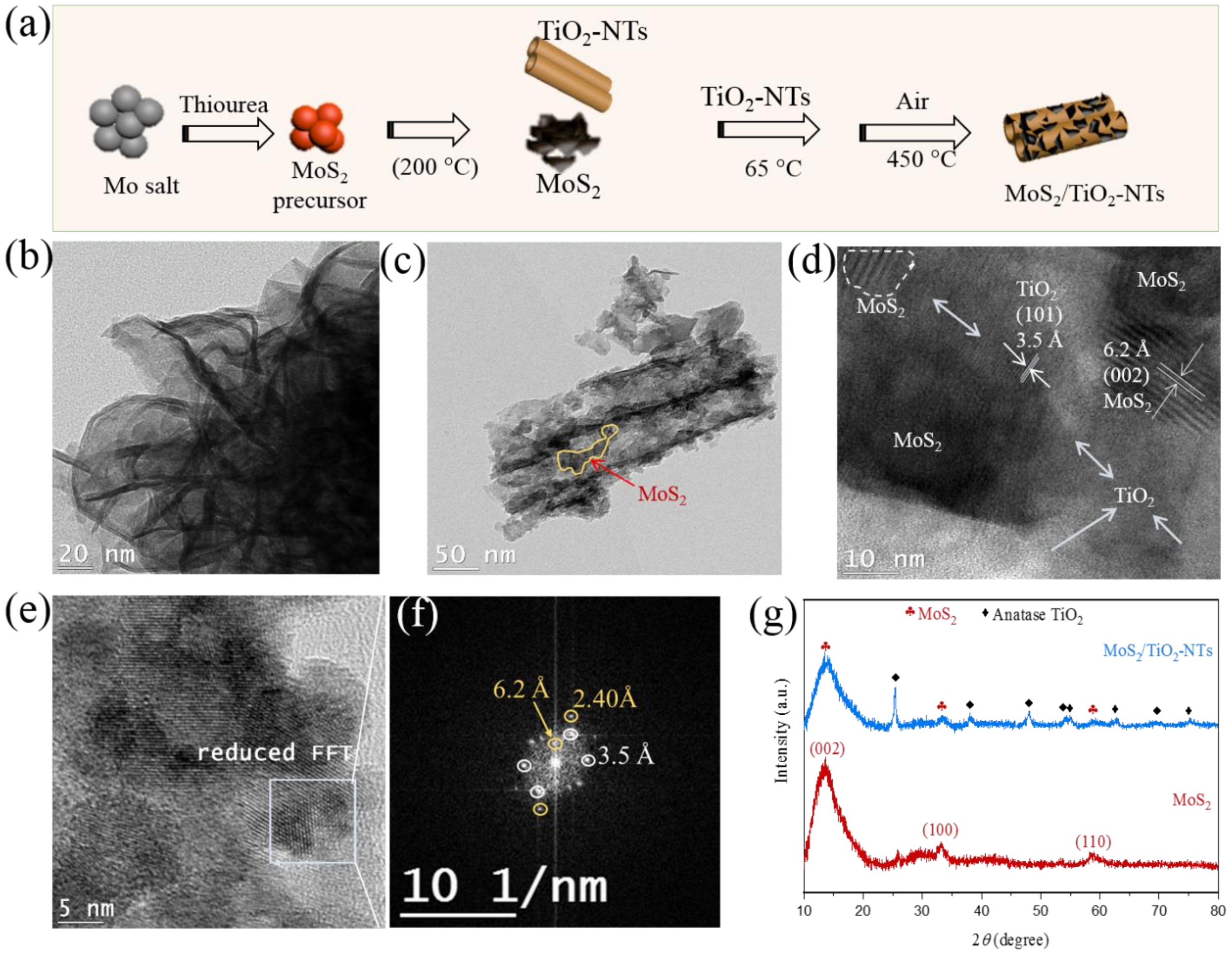

Figure 5-7 Fabrication scheme, structure, and chemical composition of the MoS_2 and $MosS_2/TiO_2$-NTs catalysts. (a) Scheme of fabrication of MoS_2/TiO_2-NTs. TEM images of (b) MoS_2, (c) MoS_2/TiO_2-NTs, (d) High resolution TEM of MoS_2/TiO_2-NTs. (e) High-resolution TEM of MoS_2/TiO_2-NTs with a marked area of reduced fast Fourier transform (FFT), (f) FFT image MoS_2/TiO_2-NTs showing the diffraction spots from anatase MoS_2 and TiO_2-NTs, (g) The XRD pattern of MoS_2 and MoS_2/TiO_2-NTs.

The HRTEM images of MoS_2/TiO_2-NTs (Figure 5-7e) further confirm the seamless grafting of layered MoS_2 to the TiO_2-NTs surface along with the exposed edges. Figure 5-7f depicts the fast Fourier transform (FFT) patterns of the selected area (marked by white frame in the HRTEM image Figure 5-7e) showing the lattice spacing corresponding to the MoS_2 and TiO_2-NTs, which are in good agreement with the hexagonal MoS_2 and anatase TiO_2 [256, 258]. Energy dispersive X-ray spectroscopy (EDS) employed to investigate the elemental composition and homogeneity of MoS_2/TiO_2-NTs. Figure 5-8a shows the presence of all possible elements of the composite Ti, Mo, O, and S, in the spectrum measured from identified areas of the HRTEM (Figure 5-8b). This observation shows that the MoS_2 layers homogeneously disperse entirely on the surface of TiO_2-NTs, with sufficient contact between the two components and the absence of adventitious contamination detected within the sensitivity of EDS.

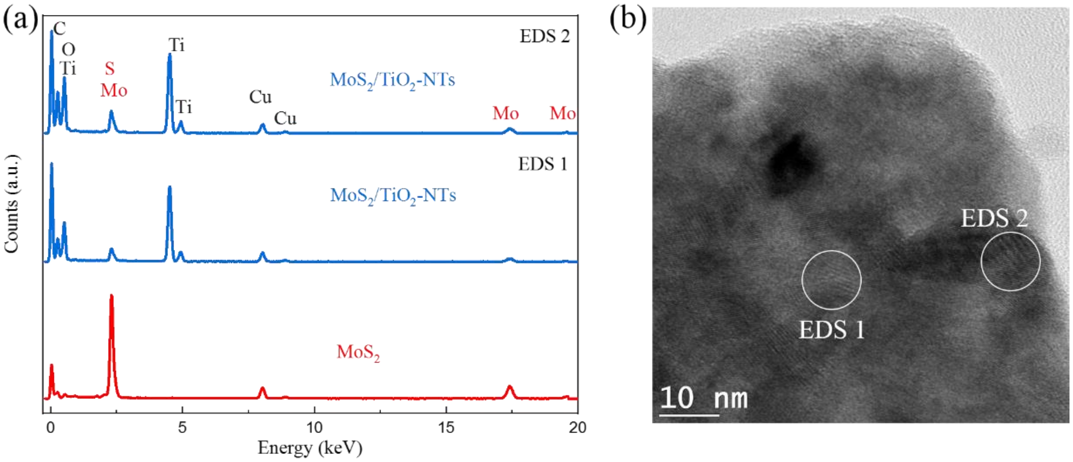

Figure 5-8 Morphology and elemental composition of catalysts. (a) The electron diffraction spectra of the MoS_2 and MoS_2/TiO_2-NTs showing the elemental composition. (b) High-resolution TEM of MoS_2/TiO_2-NTs indicating respective areas of the energy dispersive X-ray. No adventitious impurity detected from the sample.

5.4.5 Hydrogen evolution reaction electrocatalytic activities

The electrocatalytic HER activities of the catalysts were investigated in 0.5 M H_2SO_4 solution using a standard three-electrode setup. Figure 5-9a shows the polarization curves of GC modified electrodes of TiO_2-NTs, MoS_2, and MoS_2/TiO_2-NTs, respectively. The individual TiO_2 and MoS_2 electrodes display limited HER activity. By contrast, the HER activity of MoS_2/TiO_2-NTs composite material significantly enhanced compared with TiO_2-NTs and MoS_2. Specifically, the

MoS_2/TiO_2-NTs composite exhibited small HER onset potential of ~100 mV, while the HER onset potential for the individual MoS_2 and TiO_2-NTs are 260 mV and 350 mV, respectively. The onset potential of MoS_2/TiO_2-NTs is of several folds higher than that of different components. The improved HER performance of the composite (MoS_2/TiO_2-NTs) ascribed to the synergetic effect due to the chemical and electronic interactions between the TiO_2-NTs and MoS_2. Besides, the MoS_2/TiO_2-NTs requires a low overpotential of about 170 mV to steadily deliver cathodic current densities of 10 mA cm^{-2}, offering a promising HER activity amongst the TiO_2-based precious-free electrocatalysts [214, 256-260].

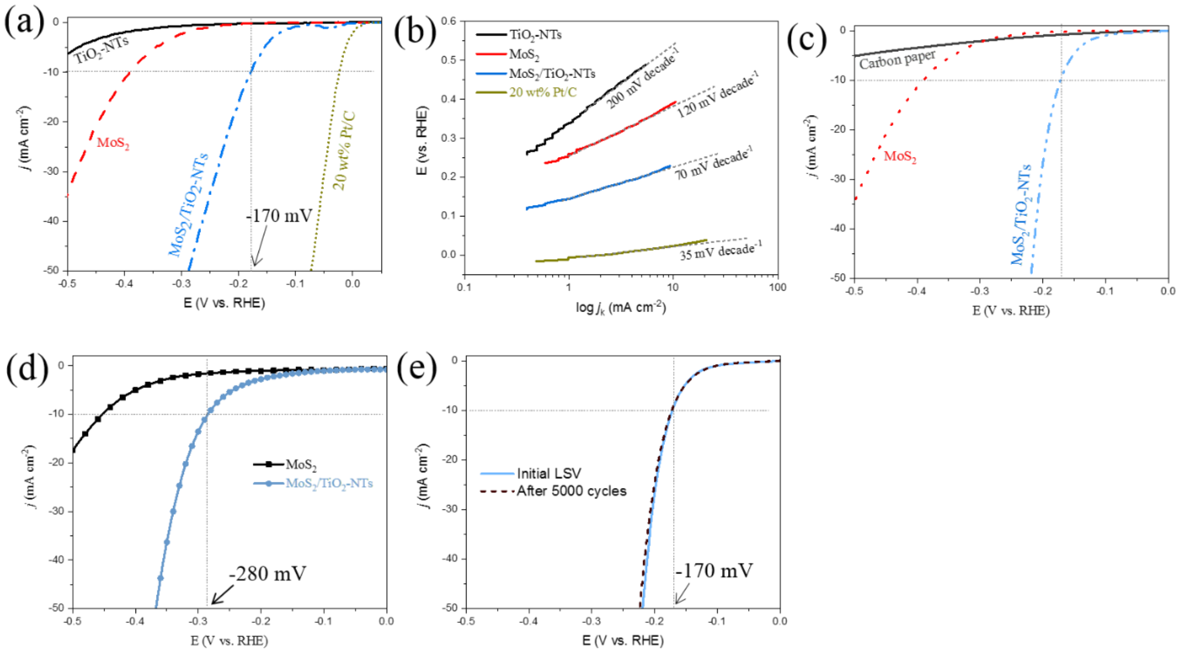

Figure 5-9 The hydrogen evolution reaction activity of TiO_2-NTs, MoS_2, MoS_2/TiO_2-NTs, and 20 wt% Pt/C (a) The polarisation curves obtained with catalysts, and (b) corresponding Tafel plot recorded on glassy carbon with catalysts loading 0.8 mg cm^{-2} at a scan rate of 10 mV s^{-1} in the 0.5 M H_2SO_4. (c) The polarisation curves recorded on carbon fiber paper (CP) with a similar scan rate and loading for the MoS_2/TiO_2-NTs. (d) The polarisation curves of MoS_2 and MoS_2/TiO_2-NTs on CP recorded in a 1.0 M KOH solution with a similar scan rate. (e) The polarisation curves of MoS_2/TiO_2-NTs composite on CP recorded before and after durability test. Negligible HER current lost after 5000 potential cycles between -0.4 and +0.2 (V vs. RHE) at 100 mV s^{-1}.

Tafel slope is another important parameter of merit for the HER catalysis, from which information about the kinetics attained. The Tafel slopes are obtained by fitting the linear region of the Tafel plots (Figure 5-9b) to Tafel equation (Equation 5-4) where η is the overpotential, j is the current density and b is the Tafel slope. In an acidic electrolyte, Tafel slopes are 35, 70, 120, and 200 mV decade^{-1} for 20 wt% Pt/C, MoS_2/TiO_2-NTs, MoS_2, and TiO_2-NTs, respectively.

$$(\eta_{(V\ vs.RHE)} = a + b log j) \qquad (5\text{-}4)$$

Besides, the overall equation for HER in acidic media (Equation 5-5) may involve up to three elementary steps for reduction of the hydronium (H_3O^+) ions: namely Volmer (Equation 5-6), Heyrovsky (Equation 5-7), and Tafel (Equation 5-8) reactions [40, 261, 262].

$$2H_3O^+ + 2e^- \rightleftharpoons H_2 + 2H_2O, \qquad (5\text{-}5)$$

$$H_3O^+ + e^- \rightleftharpoons H_{ads} + H_2O, \qquad (5\text{-}6)$$

$$H_3O^+ + H_{ads} + e^- \rightleftharpoons H_2 + H_2O, \qquad (5\text{-}7)$$

$$H_{ads} + H_{ads} \rightleftharpoons H_2, \qquad (5\text{-}8)$$

Accordingly, the Tafel slope, regarded as an intrinsic property of electrocatalysts determined from the rate determining step, allows identification of the possible mechanism of HER. The accepted HER kinetics model consists of three elementary steps, namely, Volmer, Heyrovsky and Tafel. Each of these steps can be considered as the rate-determining step. The corresponding Tafel slopes for the Volmer, Heyrovsky and Tafel steps are about 120, 40, or 30 mV decade^{-1}, respectively [40, 261, 263]. The Tafel slope of the MoS_2/TiO_2-NTs was as low as 70 mV decade^{-1} (Figure 5-9b), indicating HER electrocatalysis mechanism is dominated by Volmer-Heyrovsky steps [259-262, 264]. In particular, the Tafel slope of MoS_2/TiO_2-NTs was significantly far lower than that of individual TiO_2-NTs (200 mV decade^{-1}) and MoS_2 (120 mV decade^{-1}) indicating superior HER performance. Also, we deposited the MoS_2 and MoS_2/TiO_2-NTs catalysts on the carbon fiber paper (CP) with a loading similar to GC (0.8 mg cm^{-2}) and tested their HER performance in acid solutions. Figure 5-9c markedly, shows the MoS_2/TiO_2-NTs composite exhibiting low overpotential for achieving 10 mA cm^{-2} current density in acidic solution. The HER performance of the composite (MoS_2/TiO_2-NTs) is higher than the individual CP and MoS_2. The enhancement of the HER performance of MoS_2/TiO_2-NTs can be attributed to the synergetic effect and high dispersion of MoS_2 on the surface of the TiO_2-NTs with widely exposing MoS_2 edges (Fig. 5d). The high dispersion prevents the agglomeration of MoS_2 layers [8,55]. Further, the composite also exhibits relatively low HER overpotential in the alkaline environment (Fig. 5-9d). Another essential criterion for an excellent electrocatalyst is high stability. Finally, we performed a durability test of the MoS_2/TiO_2-NTs composite electrocatalyst on CP in acidic medium via cyclic voltammetry. Figure 5-9e reveals after 5000 potential cycles the electrocatalyst maintains the potential (170 mV) at a fixed current density of 10 mA cm^{-2}. This test indicates that in addition to the efficient HER activity, the composite electrode exhibits excellent durability. The superb durability of MoS_2/TiO_2-NTs electrode is attributed to the homogeneous dispersion of the MoS_2 layers and the chemical stability of the TiO_2-NTs support. These results confirm the long-term sustainability of our MoS_2/TiO_2-NTs as HER electrocatalyst.

5.5 Conclusions and perspective

We fabricated highly ordered free-standing TiO_2-NT membranes, with one end open after drying the as-anodized Ti foil in the oven, at 70 °C for 2 h. The TiO_2-NTs membranes firmly adhered to the Ti foil after drying the as-anodized foils, in the air (~22 °C) followed by baking at 85 °C overnight. The manipulation of anodization conditions played a vital role in controlling the morphologies of the prepared TiO_2-NTs. We successfully fabricated MoS_2/TiO_2-NTs by a slow evaporation approach. The TiO_2-NTs provided excellent support of the MoS_2 layers. TEM revealed the MoS_2 layers in MoS_2/TiO_2-NTs uniformly distributed over the entire surface of the TiO_2-NTs. The new MoS_2/TiO_2-NTs catalyst exhibited high HER performance. The overpotential obtained at 10 mA cm^{-2} acidic and alkaline environment is 170 and 290 mV, respectively. Moreover, the MoS_2/TiO_2-NTs showed small Tafel slope of 70 mV $decade^{-1}$ in acidic media and the MoS_2/TiO_2-NTs exhibit excellent durability after 5000 potential cycles between -0.4 and +0.2 (V vs. RHE). These results offer useful insights into the evolution of morphologies of TiO_2 nanotubes by adjusting the anodization conditions. Also, we anticipate the controlled morphologies is critical in improving the performance of TiO_2-NTs based materials in a wide range of energy conversion technologies. We demonstrated straightforward approach of fabrication of MoS_2/TiO_2 with significantly improved HER performance, representing a significant advance for the practical and massive exploitation of the electrochemical hydrogen production.

Chapter 6 Conclusions and recommendations

6.1 Conclusions

The general objective of this thesis was to develop durable, cost-effective, and high-performance electrocatalysts for ORR and HER. Both ORR and HER are essential reactions in electrochemical energy conversion devices, including fuel cells, metal-air batteries, and water electrolyzers. Consequently, in this thesis, highly efficient electrocatalysts with controlled morphologies have been synthesized using materials that are abundant and low-cost, as well as employing a direct, straightforward, and environmentally friendly approach. The enabling parameters for controlled fabrication of materials, physical characterization, and performance properties have been discussed. The hypotheses were that: (i) electrocatalyst materials with controlled morphologies can be fabricated by a simple and environmentally friendly electrochemical approach using low-cost materials; (ii) high-quality electrochemically exfoliated graphene is an efficient metal-free electrocatalyst for ORR; (iii) high-quality graphene can provide excellent support of FePc, a potential active material for ORR as NPMCs; (iv) a free-standing TiO_2-nanotubes membrane array with a controlled morphology is a potential electrochemical HER electrode; and v) the TiO_2-nanotubes can provide excellent support MoS_2 nanosheets for efficient HER electrode. Therefore, based on these hypotheses, the following conclusions have been drawn:

In chapter three, we demonstrated the successful fabrication of large sheets (3 μm) of high-quality graphene with a controllable number of layers by using a simple electrochemical method and low-cost graphite as precursors. The graphene samples were rigorously characterized physicochemical and electrochemically to determine their structure, ORR activity, and structure-activity relationship. The production of high-quality graphene was confirmed with the TEM, XPS, and UV-Vis measurements. Graphene sheets generated from both graphite precursors were large, very thin, highly uniform, and exhibited high activity towards ORR. The ORR activity of graphene exfoliated from the graphite plate was better than the graphene obtained from the graphite foils. An enhanced ORR performance was observed after the N-doping of the graphene. The N-doped graphene (N-GP950) exhibited comparable ORR activity to, and better stability than, the state-of-the-art commercial Pt/C catalyst in alkaline media. Various conditions, during exfoliation and post-exfoliation, influenced the ORR activity of the graphene samples, providing an opportunity to fine-tune their performance. Therefore, the N-GP950, which can be prepared from low-cost precursors using a direct, cost-effective method, is a potential candidate for an ORR catalyst in an alkaline fuel cell.

In chapter four, we used the large, high-quality N-GP950 as support for FePc in the fabrication of a highly efficient, non-precious metal electrocatalyst for ORR. The slow evaporation fabrication approach to make the composite (FePc/N-GP950) was not only direct and straightforward but also cost-effective and environmentally friendly. The optimized composite catalyst, FePc-33/N-GP950, demonstrated exceptionally high ORR activity and long-term durability in alkaline media with better performance than the commercial Pt/C. The FePc-33/N-GP950 was also shown to have the best ORR activity among the unpyrolysed metal macrocycle catalysts. The XPS and UV-Vis analysis revealed the existence of the electronic interaction between the FePc and N-GP950. We believe that these strong π-π electronic interactions between the FePc and N-GP950 are instrumental in achieving high ORR performance. The N-GP950 was demonstrated to be an excellent support material to improve the ORR performance of FePc. Therefore, this work provides an effective approach for the development of future NPMCs for practical applications in alkaline fuel cells. These findings open up new avenues for energy conversion technologies based on low-cost, scalable, non-precious metal catalysts.

In chapter five, we fabricated highly ordered free-standing TiO_2-NT membranes, with one end open after drying the as-anodized Ti foil in the oven at 70 °C for 2 hours. Interestingly, when the as-anodized Ti foils were dried in air (~22 °C), followed by baking at 85 °C overnight, the TiO_2-NT membrane was firmly adhering to the substrates. The influence of electrolyte temperature, anodization period, and pre-anodization treatment of the substrates on the morphology of nanotubes was investigated. TEM and SEM analysis revealed that the manipulation of anodization condition plays a vital role in the evolution of the morphologies of the as-anodized TiO_2-NTs. The property tests indicated that the fabricated TiO_2-NTs exhibited apparent activity towards electrochemical HER. As support material, the TiO_2-nanotubes provided a uniform dispersion of the MoS_2 layers over the entire surface. The fabricated MoS_2/TiO_2-NTs exhibited enhanced HER activity with an onset overpotential of 100 mV and a small Tafel slope of 70 mV decade^{-1} in a lower potential region. Also, the MoS_2/TiO_2-NTs delivered cathodic current densities of 10 mA cm^{-2} at a low overpotential (170 mV) which remained stable after 5000 potential cycles. These results offered useful insights about the evolution of morphologies of TiO_2 nanotubes by adjusting anodization conditions, and their possible use as HER electrodes. Also, we anticipate that controlled morphologies can be critical in improving the performance of TiO_2-NT based materials in a wide range of energy conversion technologies. In conclusion, the electrochemical water splitting driven by sustainable energies plays an indispensable role in making hydrogen fuel cell reach low- or zero-emissions.

6.2 Recommendations

Facile and straightforward fabrication approaches of graphene, FePc/N-doped graphene, TiO_2-NTs and MoS_2/TiO_2-NTs with controlled morphologies using environmentally friendly and abundant resources, in addition to the high performance of the catalysts, provide an enormous opportunity for low-cost and practical applications for fuel cells and water electrolyzers. However, the research on these materials as alternative electrocatalysts to precious metal-based ones is still not conclusive, and there is enormous scope to explore their properties further.

N-doped graphene, as a metal-free catalyst, displayed high activity with performance comparable to state-of-the-art commercial Pt/C. However, further investigations are needed to comprehend the structural-performance relationship of these materials and expand application horizons. Specifically, we highlight the rigorous examination of structural-performance relationships by employing spectroscopy techniques (TEM, XPS) before and after performance tests. This study will lead to identifying structural morphology, and electronic changes which occurred during electrochemical measurements, hence leading to a better understanding of the nature of the active site in this class of metal-free electrocatalyst. This study, in turn, can offer a valuable and rational way to fabricate metal-free electrocatalysts with predictable performance.

Furthermore, porosity and high conductivity play a critical role in controlling the kinetics of the electrochemical reactions. Thus, it is complementary to this study to design and fabricate a new class of metal-free catalysts by combining graphene and carbon-based materials in building hybrid materials with improved porosity and high conductivity and hence facilitating efficient mass transport and charge transfer. Also, in chapter 3, Figure 3-5b displays the graphene exfoliated from the graphite foil (GPf) generated a high amount of hydrogen peroxide (ca. 60%) in the potential range of 0.20 - 0.70 (V vs. RHE). The ORR results indicate that the GPf has high selectivity towards the production of peroxide. Therefore, in expanding the horizon of application of the graphene, it would be of great interest to investigate the potency of GPf in the studies of electrochemical production of hydrogen peroxide.

Moreover, although the high ORR performance of FePc-33/N-GP950 as NPMCs in the alkaline solution presented new insights, few points were highlighted for further investigations to complement this work. In chapter 4, the FePc-33/N-GP950 showed a significant loss of ORR activity after high-temperature pyrolysis in an NH_3 atmosphere. Firstly, we suggest research on the effect of temperature of pyrolysis in NH_3 on the structural morphology of the catalyst. This investigation will provide a further understanding of structural changes of the Fe-N_4 moieties after pyrolysis that led to a decrease in the activity. Secondly, as the optimized FePc-33/N-GP950 exhibited inferior performance in the acidic electrolyte with onset potential 0.83 (V vs. RHE), further investigation on the origin of the inferior ORR activity by conducting XPS and TEM measurements will complement these results. Thirdly, we want to take advantage of the diazonium reaction, to graft the FePc on the surface of graphene. In this approach, the FePc is expected to covalently bond with the nitrogen atom in pyridine linked to graphene. Thus, the Fe centre in the composite catalyst will have a coordination number of five, mimicking cytochrome c oxidase in biological systems. It would be highly interesting to explore chemical interactions between FePc and graphene and to give a comparative study to the observed physical interactions in the current study. Considering covalent bonds are strong, we expect to obtain a much more stable structure, boosting the stability of the electrocatalyst composite.

Finally, in the investigation of TiO_2-nanotubes and TiO_2/MoS_2 composites for electrocatalytic HER, further studies are imperative to unravel structural-performance relationships. We need to carry out the more additional characterization of the TiO_2-nanotubes and TiO_2/MoS_2 composite by employing various spectroscopy techniques, both before and after performance property testing. This set of experiments will provide useful information about the structure, morphology, and electronic changes occurring during electrochemical measurements. Also, since the catalytic activity is greatly affected by the morphology and construction, it is appealing to support the MoS_2-layers with nanotubes of selected morphologies and carry out systematic studies. It is clear from the results in the previous sections that the MoS_2/TiO_2-NTs achieved low HER overpotential. However, critical advancements are required to raise their efficiency to a satisfactory level. In-depth research on these issues will improve the HER performance of the MoS_2-supported TiO_2-NTs and bring an understanding of these materials.

References

[1]. Y. Huang, M. Zeng, Q. Gong, Y. Li, Electrocatalytic Processes in Energy Technologies. In: D. Wang, G. Cao (Eds.). Nanomaterials for Energy Conversion and Storage, World Scientific, London, 2018, pp. 291-341.

[2]. O.Z. Sharaf, M.F. Orhan, An overview of fuel cell technology: Fundamentals and Applications, *Renewable Sustainable Energy Rev*., 32 (2014) 810-853.

[3]. M. Winter, R.J. Brodd, What Are Batteries, Fuel Cells, and Supercapacitors?, *Chem. Rev*., 104 (2004) 4245-4270.

[4]. M.A.J. Cropper, S. Geiger, D.M. Jollie, Fuel Cells: A Survey of Current Developments, *J. Power Sources*, 131 (2004) 57-61.

[5]. C. Song, J. Zhang, Electrocatalytic Oxygen Reduction Reaction., in: J. Zhang (Ed.) PEM Fuel Cell Electrocatalysts and Catalyst Layers: Fundamentals and Applications, Springer, London: London, 2008, pp. 89-134.

[6]. Y. Bing, H. Liu, L. Zhang, D. Ghosh, J. Zhang, Nanostructured Pt-Alloy Electrocatalysts for PEM Fuel Cell Oxygen Reduction Reaction, *Chem. Soc. Rev*., 39 (2010) 2184-2202.

[7]. K.C. Neyerlin, W. Gu, J. Jorne, H.A. Gasteiger, Study of the Exchange Current Density for the Hydrogen Oxidation and Evolution Reactions, *J. Electrochem. Soc*., 154 (2007) B631-B635.

[8]. A. Rabis, P. Rodriguez, T.J. Schmidt, Electrocatalysis for Polymer Electrolyte Fuel Cells: Recent Achievements and Future Challenges, *ACS Catal*., 2 (2012) 864-890.

[9]. J. Durst, A. Siebel, C. Simon, F. Hasché, J. Herranz, H.A. Gasteiger, New Insights into the Electrochemical Hydrogen Oxidation and Evolution Reaction Mechanism, *Energy Environ. Sci*., 7 (2014) 2255-2260.

[10]. The National Museum of American History, Smithsonian Institution (2009), https://americanhistory.si.edu/fuelcells/alk/alkmain.htm

[11]. M.L. Perry, T.F. Fuller, A Historical Perspective of Fuel Cell Technology in the 20th Century, *J. Electrochem. Soc.*, 149 (2002) S59-S67.

[12]. R. Borup, J. Meyers, B. Pivovar, Y.S. Kim, R. Mukundan, N. Garland, D. Myers, M. Wilson, F. Garzon, D. Wood, P. Zelenay, K. More, K. Stroh, T. Zawodzinski, J. Boncella, J.E. McGrath, M. Inaba, K. Miyatake, M. Hori, K. Ota, Z. Ogumi, S. Miyata, A. Nishikata,

Z. Siroma, Y. Uchimoto, K. Yasuda, K.-i. Kimijima, N. Iwashita, Scientific Aspects of Polymer Electrolyte Fuel Cell Durability and Degradation, *Chem. Rev.*, 107 (2007) 3904-3951.

[13]. Y. Shao, G. Yin, Y. Gao, Understanding and approaches for the durability issues of Pt-based catalysts for PEM fuel cell, *J. Power Sources*, 171 (2007) 558-566.

[14]. Q. Li, R. He, J.-A. Gao, J.O. Jensen, N.J. Bjerrum, The CO Poisoning Effect in PEMFCs Operational at Temperatures up to 200 °C, *J. Electrochem. Soc.*, 150 (2003) A1599-A1605.

[15]. J.J. Baschuk, X. Li, Carbon monoxide poisoning of proton exchange membrane fuel cells, *Int. J. Energy Res.*, 25 (2001) 695-713.

[16]. S. Sun, G. Zhang, D. Geng, Y. Chen, R. Li, M. Cai, X. Sun, A Highly Durable Platinum Nanocatalyst for Proton Exchange Membrane Fuel Cells: Multiarmed Starlike Nanowire Single Crystal, *Angew. Chem., Int. Ed.*, 50 (2011) 422-426.

[17]. H.R. Colón-Mercado, B.N. Popov, Stability of platinum-based alloy cathode catalysts in PEM fuel cells, *J. Power Sources*, 155 (2006) 253-263.

[18]. S. Sharma, B.G. Pollet, Support materials for PEMFC and DMFC electrocatalysts-A review, *J. Power Sources*, 208 (2012) 96-119.

[19]. A.S. Aricò, P. Bruce, B. Scrosati, J.-M. Tarascon, W. van Schalkwijk, Nanostructured materials for advanced energy conversion and storage devices, *Nat. Mater.*, 4 (2005) 366.

[20]. A.S. Aricò, P. Bruce, B. Scrosati, J.-M. Tarascon, W.V. Schalkwijk, A.S. Aricò, P. Bruce, B. Scrosati, J.-M. Tarascon, W.V. Schalkwijk, Nanostructured materials for advanced energy conversion and storage devices. In: V. Dusastre (Ed.) Materials for Sustainable Energy, World Scientific, London, 2010, pp. 148-159.

[21]. L. Dai, Y. Xue, L. Qu, H.-J. Choi, J.-B. Baek, Metal-Free Catalysts for Oxygen Reduction Reaction, *Chem. Rev.*, 115 (2015) 4823-4892.

[22]. X. Liu, L. Dai, Carbon-based metal-free catalysts, *Nat. Rev. Mater.*, 1 (2016) 16064.

[23]. J. Zhang, Z. Xia, L. Dai, Carbon-based electrocatalysts for advanced energy conversion and storage, *Sci. Adv.*, 1 (2015).

[24]. R. Bashyam, P. Zelenay, A class of non-precious metal composite catalysts for fuel cells, Materials for Sustainable Energy, World Scientific, London, 2010, pp. 247-250.

[25]. M. Lefèvre, E. Proietti, F. Jaouen, J.-P. Dodelet, Iron-Based Catalysts with Improved Oxygen Reduction Activity in Polymer Electrolyte Fuel Cells, *Science*, 324 (2009) 71-74.E.

Proietti, F. Jaouen, M. Lefèvre, N. Larouche, J. Tian, J. Herranz, J.-P. Dodelet, Iron-based cathode catalyst with enhanced power density in polymer electrolyte membrane fuel cells, *Nat. Commun.*, 2 (2011) 416.

[26]. E. Proietti, F. Jaouen, M. Lefèvre, N. Larouche, J. Tian, J. Herranz, J.-P. Dodelet, Iron-based cathode catalyst with enhanced power density in polymer electrolyte membrane fuel cells, *Nat. Commun.*, 2 (2011) 416.

[27]. T. Palaniselvam, V. Kashyap, S.N. Bhange, J.-B. Baek, S. Kurungot, Nanoporous Graphene Enriched with Fe/Co-N Active Sites as a Promising Oxygen Reduction Electrocatalyst for Anion Exchange Membrane Fuel Cells, *Adv. Funct. Mater.*, 26 (2016) 2150-2162.

[28]. R. Jasinski, A New Fuel Cell Cathode Catalyst, *Nature*, 201 (1964) 1212-1213.

[29]. J. Shui, M. Wang, F. Du, L. Dai, N-doped carbon nanomaterials are durable catalysts for oxygen reduction reaction in acidic fuel cells, *Sci. Adv.*, 1 (2015) e1400129.

[30]. M. Shen, C. Wei, K. Ai, L. Lu, Transition metal-nitrogen-carbon nanostructured catalysts for the oxygen reduction reaction: From mechanistic insights to structural optimization, *Nano Res.*, 10 (2017) 1449-1470.

[31]. L. Yang, J. Shui, L. Du, Y. Shao, J. Liu, L. Dai, Z. Hu, Carbon-Based Metal-Free ORR Electrocatalysts for Fuel Cells: Past, Present, and Future, *Adv. Mater.*, 31 (2019) 1804799.

[32]. L. Qu, Y. Liu, J.-B. Baek, L. Dai, Nitrogen-Doped Graphene as Efficient Metal-Free Electrocatalyst for Oxygen Reduction in Fuel Cells, *ACS Nano*, 4 (2010) 1321-1326.

[33]. X. Mao, G. Kour, C. Yan, Z. Zhu, A. Du, Single Transition Metal Atom-Doped Graphene Supported on a Nickel Substrate: Enhanced Oxygen Reduction Reactions Modulated by Electron Coupling, *J. Phys. Chem. C*, 123 (2019) 3703-3710.

[34]. R. Cao, R. Thapa, H. Kim, X. Xu, M. Gyu Kim, Q. Li, N. Park, M. Liu, J. Cho, Promotion of oxygen reduction by a bio-inspired tethered iron phthalocyanine carbon nanotube-based catalyst, *Nat. Commun*, 4 (2013) 2076.

[35]. Y. Jiang, Y. Lu, X. Lv, D. Han, Q. Zhang, L. Niu, W. Chen, Enhanced Catalytic Performance of Pt-Free Iron Phthalocyanine by Graphene Support for Efficient Oxygen Reduction Reaction, *ACS Catal*, 3 (2013) 1263-1271.

[36]. L. Schlapbach, A. Züttel, Hydrogen-storage materials for mobile applications, *Nature*, 414 (2001) 353-358.

[37]. S.Z. Baykara, Hydrogen: A brief overview on its sources, production and environmental impact, *Int. J. Hydrogen Energy*, 43 (2018) 10605-10614.

[38]. N. Armaroli, V. Balzani, The Hydrogen Issue, *ChemSusChem*, 4 (2011) 21-36.

[39]. J. Zhang, T. Wang, P. Liu, Z. Liao, S. Liu, X. Zhuang, M. Chen, E. Zschech, X. Feng, Efficient hydrogen production on MoNi4 electrocatalysts with fast water dissociation kinetics, *Nat. Commun*, 8 (2017) 15437.

[40]. J.M. Jakšić, M.V. Vojnović, N.V. Krstajić, Kinetic analysis of hydrogen evolution at Ni–Mo alloy electrodes, *Electrochim. Acta*, 45 (2000) 4151-4158.

[41]. Z.W. Seh, J. Kibsgaard, C.F. Dickens, I. Chorkendorff, J.K. Nørskov, T.F. Jaramillo, Combining theory and experiment in electrocatalysis: Insights into materials design, *Science*, 355 (2017) eaad4998.

[42]. J.D. Benck, T.R. Hellstern, J. Kibsgaard, P. Chakthranont, T.F. Jaramillo, Catalyzing the Hydrogen Evolution Reaction (HER) with Molybdenum Sulfide Nanomaterials, *ACS Catal*, 4 (2014) 3957-3971.

[43]. B. Hinnemann, P.G. Moses, J. Bonde, K.P. Jørgensen, J.H. Nielsen, S. Horch, I. Chorkendorff, J.K. Nørskov, Biomimetic Hydrogen Evolution: MoS_2 Nanoparticles as Catalyst for Hydrogen Evolution, *J. Am. Chemi. Soc.*, 127 (2005) 5308-5309.

[44]. H. Wang, D. Kong, P. Johanes, J.J. Cha, G. Zheng, K. Yan, N. Liu, Y. Cui, $MoSe_2$ and WSe_2 Nanofilms with Vertically Aligned Molecular Layers on Curved and Rough Surfaces, *Nano Lett.*, 13 (2013) 3426-3433.

[45]. X. Fan, Y. Liu, Z. Peng, Z. Zhang, H. Zhou, X. Zhang, B.I. Yakobson, W.A. Goddard, X. Guo, R.H. Hauge, J.M. Tour, Atomic H-Induced Mo_2C Hybrid as an Active and Stable Bifunctional Electrocatalyst, *ACS Nano*, 11 (2017) 384-394.

[46]. S.T. Hunt, T. Nimmanwudipong, Y. Román-Leshkov, Engineering Non-sintered, Metal-Terminated Tungsten Carbide Nanoparticles for Catalysis, *Angew. Chem., Int. Ed*, 53 (2014) 5131-5136.

[47]. E.J. Popczun, J.R. McKone, C.G. Read, A.J. Biacchi, A.M. Wiltrout, N.S. Lewis, R.E. Schaak, Nanostructured Nickel Phosphide as an Electrocatalyst for the Hydrogen Evolution Reaction, *J. Am. Chemi. Soc.*, 135 (2013) 9267-9270.

[48]. G. Zhao, K. Rui, S.X. Dou, W. Sun, Heterostructures for Electrochemical Hydrogen Evolution Reaction: A Review, *Adv. Funct. Mater*, 28 (2018) 1803291.

[49]. C. Ray, T. Pal, Recent advances of metal-metal oxide nanocomposites and their tailored nanostructures in numerous catalytic applications, *J. Mater. Chem. A*, 5 (2017) 9465-9487.

[50]. W.T. Hong, M. Risch, K.A. Stoerzinger, A. Grimaud, J. Suntivich, Y. Shao-Horn, Toward the rational design of non-precious transition metal oxides for oxygen electrocatalysis, *Energy Environ. Sci.*, 8 (2015) 1404-1427.

[51]. N. Komba, Q. Wei, G. Zhang, F. Rosei, S. Sun, Controlled synthesis of graphene via electrochemical route and its use as efficient metal-free catalyst for oxygen reduction, *Appl. Catal., B*, 243 (2019) 373-380.

[52]. Fuel cell today, Johnson Matthey Plc, 2018, http://www.fuelcelltoday.com/history.

[53]. J.M. Andujar, F. Segura, Fuel cells: History and updating. A walk along two centuries, *Renew. Sust. Energ. Rev.*, 13 (2009) 2309-2322.

[54]. L. Mond, C. Langer, J.W. Strutt, V. A new form of gas battery, *Proc. Royal Soc. Lond.*, 46 (1890) 296-304.

[55]. X.-Z. Yuan, H. Wang, *PEM fuel cell fundamentals*. In: J. Zhang (Ed.). PEM fuel cell electrocatalysts and catalyst layers: Fundamentals and applications, Springer London, London, 2008, pp. 1-87.

[56]. S. Sun, Development of Novel Nanomaterials for High-performance and Low-cost Fuel Cell Applications. Ph.D. Thesis, The University of Western Ontario, London, Ontario, Canada, 2011, pp. 1-44.

[57]. L. Carrette, K.A. Friedrich, U. Stimming, Fuel Cells-Fundamentals and Applications, *Fuel Cells*, 1 (2001) 5-39.

[58]. T.J. Omasta, X. Peng, H.A. Miller, F. Vizza, L. Wang, J.R. Varcoe, D.R. Dekel, W.E. Mustain, Beyond 1.0 W cm-2performance without platinum: The Beginning of a new era in anion exchange membrane fuel cells, *J. Electrochem. Soc.*, 165 (2018) J3039-J3044.

[59]. S. Gottesfeld, D.R. Dekel, M. Page, C. Bae, Y. Yan, P. Zelenay, Y.S. Kim, Anion exchange membrane fuel cells: Current status and remaining challenges, *J. Power Sources*, 375 (2018) 170-184.

[60]. D.R. Dekel, Review of cell performance in anion exchange membrane fuel cells, *J. Power Sources*, 375 (2018) 158-169.S. Kabir, K. Lemire, K. Artyushkova, A. Roy, M. Odgaard, D. Schlueter, A. Oshchepkov, A. Bonnefont, E. Savinova, D.C. Sabarirajan, P. Mandal, E.J. Crumlin, I.V. Zenyuk, P. Atanassov, A. Serov, Platinum group metal-free NiMo hydrogen

oxidation catalysts: high performance and durability in alkaline exchange membrane fuel cells, *J. Mater. Chem. A*, 5 (2017) 24433-24443.

[61]. S. Kabir, K. Lemire, K. Artyushkova, A. Roy, M. Odgaard, D. Schlueter, A. Oshchepkov, A. Bonnefont, E. Savinova, D.C. Sabarirajan, P. Mandal, E.J. Crumlin, I.V. Zenyuk, P. Atanassov, A. Serov, Platinum group metal-free NiMo hydrogen oxidation catalysts: high performance and durability in alkaline exchange membrane fuel cells, *J. Mater. Chem*. A, 5 (2017) 24433-24443.

[62]. H. Lv, D. Li, D. Strmcnik, A.P. Paulikas, N.M. Markovic, V.R. Stamenkovic, Recent advances in the design of tailored nanomaterials for efficient oxygen reduction reaction, *Nano Energy*, 29 (2016) 149-165.

[63]. Y. Nie, L. Li, Z. Wei, Recent advancements in Pt and Pt-free catalysts for oxygen reduction reaction, *Chem. Soc. Rev*., 44 (2015) 2168-2201.

[64]. J.K. Nørskov, J. Rossmeisl, A. Logadottir, L. Lindqvist, J.R. Kitchin, T. Bligaard, H. Jónsson, Origin of the Overpotential for Oxygen Reduction at a Fuel-Cell Cathode, *J. Phys. Chem. B*, 108 (2004) 17886-17892.

[65]. M. Nesselberger, S. Ashton, J.C. Meier, I. Katsounaros, K.J.J. Mayrhofer, M. Arenz, The Particle Size Effect on the Oxygen Reduction Reaction Activity of Pt Catalysts: Influence of Electrolyte and Relation to Single Crystal Models, *J. Am. Chemi. Soc.*, 133 (2011) 17428-17433.

[66]. L. Wang, A. Holewinski, C. Wang, Prospects of Platinum-Based Nanostructures for the Electrocatalytic Reduction of Oxygen, *ACS Catal*, 8 (2018) 9388-9398.

[67]. J.-P. Dodelet, Oxygen Reduction in PEM Fuel Cell Conditions: Heat-Treated Non-Precious Metal-N4 Macrocycles and Beyond. In: J.H Zagal, F. Bedioui, J-P Dodele (Eds.). N4-Macrocyclic Metal Complexes, Springer, New York, NY, 2006, pp. 83-147.

[68]. S.M. Adam, G.B. Wijeratne, P.J. Rogler, D.E. Diaz, D.A. Quist, J.J. Liu, K.D. Karlin, Synthetic Fe/Cu Complexes: Toward Understanding Heme-Copper Oxidase Structure and Function, *Chem. Rev*., 118 (2018) 10840-11022.

[69]. E. Yeager, Electrocatalysts for O_2 reduction, *Electrochim. Acta*, 29 (1984) 1527-1537.

[70]. M. Shao, Q. Chang, J.-P. Dodelet, R. Chenitz, Recent Advances in Electrocatalysts for Oxygen Reduction Reaction, *Chem. Rev.*, 116 (2016) 3594-3657.

[71]. Y.-S. Chao, D.-S. Tsai, A.-P. Wu, L.-W. Tseng, Y.-S. Huang, Cobalt selenide electrocatalyst supported by nitrogen-doped carbon and its stable activity toward oxygen reduction reaction, *Int. J. Hydrogen Energy*, 38 (2013) 5655-5664.

[72]. N.A. Vante, H. Tributsch, Energy conversion catalysis using semiconducting transition metal cluster compounds, *Nature*, 323 (1986) 431-432.

[73]. M. Chisaka, A. Ishihara, N. Uehara, M. Matsumoto, H. Imai, K. Ota, Nano-TaOxNy particles synthesized from oxy-tantalum phthalocyanine: how to prepare precursors to enhance the oxygen reduction reaction activity after ammonia pyrolysis?, *J. Mater. Chem. A*, 3 (2015) 16414-16418.

[74]. A. Ishihara, M. Chisaka, Y. Ohgi, K. Matsuzawa, S. Mitsushima, K. Ota, Synthesis of nano-TaOx oxygen reduction reaction catalysts on multi-walled carbon nanotubes connected via a decomposition of oxy-tantalum phthalocyanine, *Phys. Chem. Chem. Phys.*, 17 (2015) 7643-7647.

[75]. L. Yang, N. Larouche, R. Chenitz, G. Zhang, M. Lefèvre, J.-P. Dodelet, Activity, Performance, and Durability for the Reduction of Oxygen in PEM Fuel Cells, of Fe/N/C Electrocatalysts Obtained from the Pyrolysis of Metal-Organic-Framework and Iron Porphyrin Precursors, *Electrochim. Acta*, 159 (2015) 184-197.

[76]. G. Wu, K.L. More, C.M. Johnston, P. Zelenay, High-Performance Electrocatalysts for Oxygen Reduction Derived from Polyaniline, Iron, and Cobalt, *Science*, 332 (2011) 443-447.

[77]. S. Yang, X. Feng, X. Wang, K. Müllen, Graphene-Based Carbon Nitride Nanosheets as Efficient Metal-Free Electrocatalysts for Oxygen Reduction Reactions, *Angew. Chem., Int. Ed*, 50 (2011) 5339-5343.

[78]. C. Hu, L. Dai, Carbon-Based Metal-Free Catalysts for Electrocatalysis Beyond the ORR, *Angew. Chem., Int. Ed*, 55 (2016) 11736-11758.

[79]. K. Gong, F. Du, Z. Xia, M. Durstock, L. Dai, Nitrogen-Doped Carbon Nanotube Arrays with High Electrocatalytic Activity for Oxygen Reduction, *Science*, (2009) 760-764.

[80]. J. Turner, G. Sverdrup, M.K. Mann, P.-C. Maness, B. Kroposki, M. Ghirardi, R.J. Evans, D. Blake, Renewable hydrogen production, International Journal of Energy Research, 32 (2008) 379-407.

[81]. A. Haryanto, S. Fernando, N. Murali, S. Adhikari, Current Status of Hydrogen Production Techniques by Steam Reforming of Ethanol, *Energy & Fuels*, 19 (2005) 2098-2106.

[82]. Y. Tachibana, L. Vayssieres, J.R. Durrant, Artificial photosynthesis for solar water-splitting, *Nat. Photonics*, 6 (2012) 511.

[83]. S. Chu, A. Majumdar, Opportunities and challenges for a sustainable energy future, *Nature*, 488 (2012) 294.

[84]. M. Carmo, D.L. Fritz, J. Mergel, D. Stolten, A comprehensive review on PEM water electrolysis, *Int. J. Hydrogen Energy*, 38 (2013) 4901-4934.

[85]. G.W. Crabtree, M.S. Dresselhaus, M.V. Buchanan, The Hydrogen Economy, *Phys. Today*, 57 (2004) 39-44.

[86]. W. Kreuter, H. Hofmann, Electrolysis: The important energy transformer in a world of sustainable energy, *Int. J. Hydrogen Energy*, 23 (1998) 661-666.

[87]. P. Nikolaidis, A. Poullikkas, A comparative overview of hydrogen production processes, , *Renewable & Sustainable Energy Rev.*, 67 (2017) 597-611.

[88]. V. Subramani, P. Sharma, L. Zhang, K. Liu, Catalytic Steam Reforming Technology for the Production of Hydrogen and Syngas. In: K. Liu, C. Song, V. Subramani (Eds.). Hydrogen and Syngas Production and Purification Technologies, Wiley-AIChE, 2009, pp. 14-126.

[89]. X. Chen, S. Shen, L. Guo, S.S. Mao, Semiconductor-based Photocatalytic Hydrogen Generation, *Chem. Rev*., 110 (2010) 6503-6570.

[90]. A. Fujishima, K. Honda, Electrochemical photolysis of water at a semiconductor electrode, *Nature*, 238 (1972) 37.

[91]. M. Grätzel, Photoelectrochemical cells, *Nature*, 414 (2001) 338.

[92]. N. Cox, D.A. Pantazis, F. Neese, W. Lubitz, Artificial photosynthesis: understanding water splitting in nature, *Interface Focus*, 5 (2015) 20150009.

[93]. H. Ahmad, S.K. Kamarudin, L.J. Minggu, M. Kassim, Hydrogen from photo-catalytic water splitting process: A review, *Renewable & Sustainable Energy Rev.*, 43 (2015) 599-610.

[94]. J.K. Nørskov, T. Bligaard, A. Logadottir, J.R. Kitchin, J.G. Chen, S. Pandelov, U. Stimming, Trends in the exchange current for hydrogen evolution, *J. Electrochem. Soc.*, 152 (2005) J23-J26.

[95]. D.V. Esposito, J.G. Chen, Monolayer platinum supported on tungsten carbides as low-cost electrocatalysts: opportunities and limitations, *Energy Environ. Sci*., 4 (2011) 3900-3912.

[96]. D.V. Esposito, S.T. Hunt, A.L. Stottlemyer, K.D. Dobson, B.E. McCandless, R.W. Birkmire, J.G. Chen, Low-cost hydrogen-evolution catalysts based on monolayer platinum on tungsten monocarbide substrates, *Angew. Chem., Int. Ed* 49 (2010) 9859-9862.

[97]. Y. Zheng, Y. Jiao, L.H. Li, T. Xing, Y. Chen, M. Jaroniec, S.Z. Qiao, Toward design of synergistically active carbon-based catalysts for electrocatalytic hydrogen evolution, *ACS Nano*, 8 (2014) 5290-5296.

[98]. C.-Y. Su, A.-Y. Lu, Y. Xu, F.-R. Chen, A.N. Khlobystov, L.-J. Li, High-Quality Thin Graphene Films from Fast Electrochemical Exfoliation, *ACS Nano*, 5 (2011) 2332-2339.

[99]. K. Parvez, Z.-S. Wu, R. Li, X. Liu, R. Graf, X. Feng, K. Müllen, Exfoliation of Graphite into Graphene in Aqueous Solutions of Inorganic Salts, *J. Am. Chemi. Soc.*, 136 (2014) 6083-6091.

[100]. S. Yang, S. Brüller, Z.-S. Wu, Z. Liu, K. Parvez, R. Dong, F. Richard, P. Samorì, X. Feng, K. Müllen, Organic Radical-Assisted Electrochemical Exfoliation for the Scalable Production of High-Quality Graphene, *J. Am. Chemi. Soc.*, 137 (2015) 13927-13932.

[101]. K. Lee, A. Mazare, P. Schmuki, One-Dimensional Titanium Dioxide Nanomaterials: Nanotubes, *Chem. Rev*., 114 (2014) 9385-9454.

[102]. P. Roy, S. Berger, P. Schmuki, TiO_2 Nanotubes: Synthesis and Applications, *Angew. Chem., Int. Ed*, 50 (2011) 2904-2939.

[103]. X. Chen, S.S. Mao, Titanium Dioxide Nanomaterials: Synthesis, Properties, Modifications, and Applications, *Chem. Rev*., 107 (2007) 2891-2959.

[104]. R.I. Walton, Subcritical solvothermal synthesis of condensed inorganic materials, *Chem. Soc. Rev*., 31 (2002) 230-238.

[105]. J.H. Han, M. Kwak, Y. Kim, J. Cheon, Recent Advances in the Solution-Based Preparation of Two-Dimensional Layered Transition Metal Chalcogenide Nanostructures, *Chem. Rev*., 118 (2018) 6151-6188.

[106]. A. Mansouri, N. Semagina, Colloidal Synthesis Protocol of Shape- and Dimensionally-Controlled Transition-Metal Chalcogenides and Their Hydrodesulfurization Activities, *ACS Appl. Nano Mater*., 1 (2018) 4408-4412.

[107]. H. Konno, X-ray Photoelectron Spectroscopy. In: M. Inagaki, F. Kang (Eds.) Materials Science and Engineering of Carbon, Butterworth-Heinemann, 2016, pp. 153-171.

[108]. P.M.A. Sherwood, Paul van der Heide, X-ray photoelectron spectroscopy: An introduction to principles and practices, *Anal. Bioanal. Chem.*, 405 (2013) 2415-2416.

[109]. C.B. Carter, D.B. Williams, Transmission Electron Microscopy: Diffraction, Imaging, and Spectrometry, Springer, Cham, 2016.

[110]. J.Z. Zhang, Optical Properties and Spectroscopy of Nanomaterials, World Scientific, Santa Cruz, USA, 2009.

[111]. D.B. Williams, C.B. Carter, Transmission electron microscopy: A textbook for materials science, Second ed., Springer, New York, 2009.

[112]. A.J. Blake, W. Clegg, Crystal structure analysis : principles and practice, Oxford University Press, Oxford, 2009.

[113]. Allen J. Bard, Larry R. Faulkner, Electrochemical Methods: Fundamentals and Applications, New York: Wiley, 2001, 2nd ed, 2002.

[114]. G. Zhang, Q. Wei, X. Yang, A.C. Tavares, S. Sun, RRDE experiments on noble-metal and noble-metal-free catalysts: Impact of loading on the activity and selectivity of oxygen reduction reaction in alkaline solution, *Appl. Catal., B*, 206 (2017) 115-126.

[115]. R. Zhou, Y. Zheng, M. Jaroniec, S.-Z. Qiao, Determination of the Electron Transfer Number for the Oxygen Reduction Reaction: From Theory to Experiment, ACS Catalysis, 6 (2016) 4720-4728.

[116]. W.J. Albery, S. Bruckenstein, Ring-disc electrodes. First-order kinetic collection efficiencies at the ring electrode, *Trans. Faraday Soc.*, 62 (1966) 1946-1954.

[117]. U.A. Paulus, T.J. Schmidt, H.A. Gasteiger, R.J. Behm, Oxygen reduction on a high-surface area Pt/Vulcan carbon catalyst: a thin-film rotating ring-disk electrode study, *J. Electroanal. Chem.*, 495 (2001) 134-145.

[118]. L. Zhang, H. Li, J. Zhang, Kinetics of oxygen reduction reaction on three different Pt surfaces of Pt/C catalyst analyzed by rotating ring-disk electrode in acidic solution, *J. Power Sources*, 255 (2014) 242-250.

[119]. X. Ge, A. Sumboja, D. Wuu, T. An, B. Li, F.W.T. Goh, T.S.A. Hor, Y. Zong, Z. Liu, Oxygen Reduction in Alkaline Media: From Mechanisms to Recent Advances of Catalysts, *ACS Catal*, 5 (2015) 4643-4667.

[120]. M.I. Awad, T. Ohsaka, An electrocatalytic oxygen reduction by copper nanoparticles-modified Au(100)-rich polycrystalline gold electrode in 0.5 M KOH, *J. Power Sources*, 226 (2013) 306-312.

[121]. D. Pletcher, R. Greff, R. Peat, L.M. Peter, J. Robinson, Potential sweep techniques and cyclic voltammetry. In: D. Pletcher, R. Greff, R. Peat, L.M. Peter, J. Robinson (Eds.). Instrumental Methods in Electrochemistry, Woodhead Publishing, 2010, pp. 178-228.

[122]. Klans Jüttner, *Technical Scale of Electrochemistry*, Encyclopedia of Electrochemistry, Wiley-VCH Verlag GmbH & Co Weinheim, Germany, 2007.

[123]. Q. Wei, Y. Fu, G. Zhang, S. Sun, Rational design of carbon-based oxygen electrocatalysts for zinc-air batteries, *Curr. Opin. Electrochem.*, 4 (2017) 45-59.

[124]. J. Healy, C. Hayden, T. Xie, K. Olson, R. Waldo, M. Brundage, H. Gasteiger, J. Abbott, Aspects of the Chemical Degradation of PFSA Ionomers used in PEM Fuel Cells, *Fuel Cells*, 5 (2005) 302-308.

[125]. Q. Ly, B.V. Merinov, H. Xiao, W.A. Goddard, T.H. Yu, The Oxygen Reduction Reaction on Graphene from Quantum Mechanics: Comparing Armchair and Zigzag Carbon Edges, *J. Phys. Chem. C*, 121 (2017) 24408-24417.

[126]. S. Sun, F. Jaouen, J.-P. Dodelet, Controlled Growth of Pt Nanowires on Carbon Nanospheres and Their Enhanced Performance as Electrocatalysts in PEM Fuel Cells, *Adv. Mater.*, 20 (2008) 3900-3904.

[127]. J. Wu, H. Yang, Platinum-Based Oxygen Reduction Electrocatalysts, *Acc. Chem. Res.*, 46 (2013) 1848-1857.

[128]. Z. Liu, X. Lin, J.Y. Lee, W. Zhang, M. Han, L.M. Gan, Preparation and Characterization of Platinum-Based Electrocatalysts on Multiwalled Carbon Nanotubes for Proton Exchange Membrane Fuel Cells, *Langmuir*, 18 (2002) 4054-4060.

[129]. X. Cui, S. Yang, X. Yan, J. Leng, S. Shuang, P.M. Ajayan, Z. Zhang, Pyridinic-Nitrogen-Dominated Graphene Aerogels with Fe–N–C Coordination for Highly Efficient Oxygen Reduction Reaction, *Adv. Funct. Mater*, 26 (2016) 5708-5717.

[130]. Q. Wei, G. Zhang, X. Yang, R. Chenitz, D. Banham, L. Yang, S. Ye, S. Knights, S. Sun, 3D Porous Fe/N/C Spherical Nanostructures As High-Performance Electrocatalysts for Oxygen Reduction in Both Alkaline and Acidic Media, *ACS Appl. Mater. Interfaces*, 9 (2017) 36944-36954.

[131]. J.-C. Li, P.-X. Hou, C. Liu, Heteroatom-Doped Carbon Nanotube and Graphene-Based Electrocatalysts for Oxygen Reduction Reaction, *Small*, 13 (2017) 1702002.

[132]. Y. Zheng, Y. Jiao, M. Jaroniec, Y. Jin, S.Z. Qiao, Nanostructured Metal-Free Electrochemical Catalysts for Highly Efficient Oxygen Reduction, *Small*, 8 (2012) 3550-3566.

[133]. J. Benson, Q. Xu, P. Wang, Y. Shen, L. Sun, T. Wang, M. Li, P. Papakonstantinou, Tuning the Catalytic Activity of Graphene Nanosheets for Oxygen Reduction Reaction via Size and Thickness Reduction, *ACS Appl. Mater. Interfaces*, 6 (2014) 19726-19736.

[134]. X. Zhou, J. Qiao, L. Yang, J. Zhang, A Review of Graphene-Based Nanostructural Materials for Both Catalyst Supports and Metal-Free Catalysts in PEM Fuel Cell Oxygen Reduction Reactions, *Adv. Energy Mater.*, 4 (2014) 1301523.

[135]. X. Tong, Q.L. Wei, X.X. Zhan, G.X. Zhang, S.H. Sun, The New Graphene Family Materials: Synthesis and Applications in Oxygen Reduction Reaction, *Catalysts*, 7 (2017) 1.

[136]. E.P. Randviir, D.A.C. Brownson, C.E. Banks, A decade of graphene research: production, applications and outlook, *Mater. Today*, 17 (2014) 426-432.

[137]. J. Wu, L. Ma, R.M. Yadav, Y. Yang, X. Zhang, R. Vajtai, J. Lou, P.M. Ajayan, Nitrogen-Doped Graphene with Pyridinic Dominance as a Highly Active and Stable Electrocatalyst for Oxygen Reduction, *ACS Appl. Mater. Interfaces*, 7 (2015) 14763-14769.

[138]. Z. Lin, G. Waller, Y. Liu, M. Liu, C.-P. Wong, Facile Synthesis of Nitrogen-Doped Graphene via Pyrolysis of Graphene Oxide and Urea, and its Electrocatalytic Activity toward the Oxygen-Reduction Reaction, *Adv. Energy Mater.*, 2 (2012) 884-888.

[139]. Q. Wei, X. Tong, G. Zhang, J. Qiao, Q. Gong, S. Sun, Nitrogen-Doped Carbon Nanotube and Graphene Materials for Oxygen Reduction Reactions, *Catalysts*, 5 (2015) 1574-1602.

[140]. S. Wang, L. Zhang, Z. Xia, A. Roy, D.W. Chang, J.-B. Baek, L. Dai, BCN Graphene as Efficient Metal-Free Electrocatalyst for the Oxygen Reduction Reaction, *Angew. Chem., Int. Ed*, 51 (2012) 4209-4212.

[141]. K. Parvez, R. Li, S.R. Puniredd, Y. Hernandez, F. Hinkel, S. Wang, X. Feng, K. Müllen, Electrochemically Exfoliated Graphene as Solution-Processable, Highly Conductive Electrodes for Organic Electronics, *ACS Nano*, 7 (2013) 3598-3606.

[142]. J.M. Munuera, J.I. Paredes, M. Enterría, A. Pagán, S. Villar-Rodil, M.F.R. Pereira, J.I. Martins, J.L. Figueiredo, J.L. Cenis, A. Martínez-Alonso, J.M.D. Tascón, Electrochemical Exfoliation of Graphite in Aqueous Sodium Halide Electrolytes toward Low Oxygen Content Graphene for Energy and Environmental Applications, *ACS Appl. Mater. Interfaces*, 9 (2017) 24085-24099.

[143]. N. Liu, F. Luo, H. Wu, Y. Liu, C. Zhang, J. Chen, One-Step Ionic-Liquid-Assisted Electrochemical Synthesis of Ionic-Liquid-Functionalized Graphene Sheets Directly from Graphite, *Adv. Funct. Mater*, 18 (2008) 1518-1525.

[144]. I.-Y. Jeon, H.-J. Choi, S.-M. Jung, J.-M. Seo, M.-J. Kim, L. Dai, J.-B. Baek, Large-Scale Production of Edge-Selectively Functionalized Graphene Nanoplatelets via Ball Milling and Their Use as Metal-Free Electrocatalysts for Oxygen Reduction Reaction, *J. Am. Chemi. Soc.*, 135 (2013) 1386-1393.

[145]. A.M. Abdelkader, I.A. Kinloch, R.A.W. Dryfe, Continuous Electrochemical Exfoliation of Micrometer-Sized Graphene Using Synergistic Ion Intercalations and Organic Solvents, *ACS Appl. Mater. Interfaces*, 6 (2014) 1632-1639.

[146]. G. Wang, J. Yang, J. Park, X. Gou, B. Wang, H. Liu, J. Yao, Facile Synthesis and Characterization of Graphene Nanosheets, *J. Phys. Chem. C*, 112 (2008) 8192-8195.

[147]. D. Li, M.B. Müller, S. Gilje, R.B. Kaner, G.G. Wallace, Processable aqueous dispersions of graphene nanosheets, *Nat. Nanotechnol.*, 3 (2008) 101.

[148]. A. Ganguly, S. Sharma, P. Papakonstantinou, J. Hamilton, Probing the Thermal Deoxygenation of Graphene Oxide Using High-Resolution In Situ X-ray-Based Spectroscopies, *J. Phys. Chem. C*, 115 (2011) 17009-17019.

[149]. S. Saxena, T.A. Tyson, S. Shukla, E. Negusse, H. Chen, J. Bai, Investigation of structural and electronic properties of graphene oxide, *Appl. Phys. Lett.*, 99 (2011) 013104.

[150]. S. Yang, M.R. Lohe, K. Müllen, X. Feng, New-Generation Graphene from Electrochemical Approaches: Production and Applications, *Adv. Mater.*, 28 (2016) 6213-6221.

[151]. J.M. Munuera, J.I. Paredes, S. Villar-Rodil, M. Ayán-Varela, A. Pagán, S.D. Aznar-Cervantes, J.L. Cenis, A. Martínez-Alonso, J.M.D. Tascón, High quality, low oxygen content and biocompatible graphene nanosheets obtained by anodic exfoliation of different graphite types, *Carbon*, 94 (2015) 729-739.

[152]. I.S. Flyagina, K.J. Hughes, D.C. Mielczarek, D.B. Ingham, M. Pourkashanian, Identifying the Catalytic Active Sites in Heteroatom-Doped Graphene for the Oxygen Reduction Reaction, *Fuel Cells*, 16 (2016) 568-576.

[153]. H.B. Yang, J. Miao, S.-F. Hung, J. Chen, H.B. Tao, X. Wang, L. Zhang, R. Chen, J. Gao, H.M. Chen, L. Dai, B. Liu, Identification of catalytic sites for oxygen reduction and oxygen evolution in N-doped graphene materials: Development of highly efficient metal-free bifunctional electrocatalyst, *Sci. Adv.*, 2 (2016) e1501122.

[154]. T. Xing, Y. Zheng, L.H. Li, B.C.C. Cowie, D. Gunzelmann, S.Z. Qiao, S. Huang, Y. Chen, Observation of Active Sites for Oxygen Reduction Reaction on Nitrogen-Doped Multilayer Graphene, *ACS Nano*, 8 (2014) 6856-6862.

[155]. L. Wang, Z. Sofer, A. Ambrosi, P. Šimek, M. Pumera, 3D-graphene for electrocatalysis of oxygen reduction reaction: Increasing number of layers increases the catalytic effect, *Electrochem. Commun.,* 46 (2014) 148-151.

[156]. Z. Lin, G.H. Waller, Y. Liu, M. Liu, C.-p. Wong, 3D Nitrogen-doped graphene prepared by pyrolysis of graphene oxide with polypyrrole for electrocatalysis of oxygen reduction reaction, *Nano Energy*, 2 (2013) 241-248.

[157]. D. Deng, L. Yu, X. Pan, S. Wang, X. Chen, P. Hu, L. Sun, X. Bao, Size effect of graphene on electrocatalytic activation of oxygen, *Chem. Commun*., 47 (2011) 10016-10018.

[158]. S.K. Bikkarolla, P. Cumpson, P. Joseph, P. Papakonstantinou, Oxygen reduction reaction by electrochemically reduced graphene oxide, *Faraday Discuss*., 173 (2014) 415-428.

[159]. K. Parvez, S. Yang, Y. Hernandez, A. Winter, A. Turchanin, X. Feng, K. Müllen, Nitrogen-Doped Graphene and Its Iron-Based Composite As Efficient Electrocatalysts for Oxygen Reduction Reaction, *ACS Nano*, 6 (2012) 9541-9550.

[160]. W. Yuan, Y. Zhou, Y. Li, C. Li, H. Peng, J. Zhang, Z. Liu, L. Dai, G. Shi, The edge- and basal-plane-specific electrochemistry of a single-layer graphene sheet, *Sci. Rep.*, 3 (2013) 2248-2248.

[161]. T. Ikeda, Z. Hou, G.-L. Chai, K. Terakura, Possible Oxygen Reduction Reactions for Graphene Edges from First Principles, *J. Phys. Chem. C*, 118 (2014) 17616-17625.

[162]. Z. Xu, X. Fan, H. Li, H. Fu, W.M. Lau, X. Zhao, Edges of graphene and carbon nanotubes with high catalytic performance for the oxygen reduction reaction, *Phys. Chem. Chem. Phys*., 19 (2017) 21003-21011.

[163]. S.T. Hossain, R. Wang, Electrochemical Exfoliation of Graphite: Effect of Temperature and Hydrogen Peroxide Addition, *Electrochim. Acta*, 216 (2016) 253-260.

[164]. T.-F. Hung, M.-H. Tu, C.-W. Tsai, C.-J. Chen, R.-S. Liu, W.-R. Liu, M.-Y. Lo, Influence of pyrolysis temperature on oxygen reduction reaction activity of carbon-incorporating iron nitride/nitrogen-doped graphene nanosheets catalyst, *Int. J. Hydrogen Energy*, 38 (2013) 3956-3962.

[165]. Chi Chen, Yu-jiao Lai, Zhi-you Zhou, Xin-sheng Zhang, Shi-gang Sun, Thermo-stability and active site structure of Fe/N/C electrocatalyst for oxygen reduction reaction, *J. Electrochem.*, 23 (2017) 400-408.

[166]. M.K. Debe, Electrocatalyst approaches and challenges for automotive fuel cells, *Nature*, 486 (2012) 43.

[167]. K. Liu, Y. Lei, G. Wang, Correlation between oxygen adsorption energy and electronic structure of transition metal macrocyclic complexes, *J. Chem. Phys*., 139 (2013) 204306.

[168]. W. Xia, A. Mahmood, Z. Liang, R. Zou, S. Guo, Earth-Abundant Nanomaterials for Oxygen Reduction, *Angew. Chem., Int. Ed*, 55 (2016) 2650-2676.

[169]. Y. Liu, X. Yue, K. Li, J. Qiao, D.P. Wilkinson, J. Zhang, PEM fuel cell electrocatalysts based on transition metal macrocyclic compounds, *Coord. Chem. Rev*., 315 (2016) 153-177.

[170]. K. Lee, N. Alonso-Vante, J. Zhang, Transition Metal Chalcogenides for Oxygen Reduction Electrocatalysts in PEM Fuel Cells. In: Z. Chen, J.P. Dodelet, J. Zhang (Eds.) Non-Noble Metal Fuel Cell Catalysts, Wiley-VCH, Weinheim, 2014, pp. 157-182.

[171]. R. Othman, A.L. Dicks, Z. Zhu, Non precious metal catalysts for the PEM fuel cell cathode, *Int. J. Hydrogen Energy*, 37 (2012) 357-372.

[172]. Y. Feng, A. Gago, L. Timperman, N. Alonso-Vante, Chalcogenide metal centers for oxygen reduction reaction: Activity and tolerance, *Electrochim. Acta*, 56 (2011) 1009-1022.

[173]. F. Cheng, Y. Su, J. Liang, Z. Tao, J. Chen, MnO2-Based Nanostructures as Catalysts for Electrochemical Oxygen Reduction in Alkaline Media, *Chem. Mater.*, 22 (2010) 898-905.

[174]. Y. Wang, J. Li, Z. Wei, Transition-metal-oxide-based catalysts for the oxygen reduction reaction, *J. Mater. Chem. A*, 6 (2018) 8194-8209.

[175]. Q. Wei, X. Yang, G. Zhang, D. Wang, L. Zuin, D. Banham, L. Yang, S. Ye, Y. Wang, M. Mohamedi, S. Sun, An active and robust Si-Fe/N/C catalyst derived from waste reed for oxygen reduction, *Appl. Catal., B*, 237 (2018) 85-93.

[176]. F. Jaouen, E. Proietti, M. Lefèvre, R. Chenitz, J.-P. Dodelet, G. Wu, H.T. Chung, C.M. Johnston, P. Zelenay, Recent advances in non-precious metal catalysis for oxygen-reduction reaction in polymer electrolyte fuel cells, *Energy Environ. Sci.*, 4 (2011) 114-130.

[177]. D. Liu, Y.-T. Long, Superior Catalytic Activity of Electrochemically Reduced Graphene Oxide Supported Iron Phthalocyanines toward Oxygen Reduction Reaction, *ACS Appl. Mater. Interfaces*, 7 (2015) 24063-24068.

[178]. R. Chen, H. Li, D. Chu, G. Wang, Unraveling Oxygen Reduction Reaction Mechanisms on Carbon-Supported Fe-Phthalocyanine and Co-Phthalocyanine Catalysts in Alkaline Solutions, *J. Phys. Chem. C*, 113 (2009) 20689-20697.

[179]. G. Lalande, G. Faubert, R. Côté, D. Guay, J.P. Dodelet, L.T. Weng, P. Bertrand, Catalytic activity and stability of heat-treated iron phthalocyanines for the electroreduction of oxygen in polymer electrolyte fuel cells, *J. Power Sources*, 61 (1996) 227-237.

[180]. D.Y. Chung, M.J. Kim, N. Kang, J.M. Yoo, H. Shin, O.-H. Kim, Y.-E. Sung, Low-Temperature and Gram-Scale Synthesis of Two-Dimensional Fe-N-C Carbon Sheets for Robust Electrochemical Oxygen Reduction Reaction, *Chem. Mater.*, 29 (2017) 2890-2898.

[181]. W. Li, A. Yu, D.C. Higgins, B.G. Llanos, Z. Chen, Biologically Inspired Highly Durable Iron Phthalocyanine Catalysts for Oxygen Reduction Reaction in Polymer Electrolyte Membrane Fuel Cells, *J. Am. Chemi. Soc.*, 132 (2010) 17056-17058.

[182]. Y. Liu, Y.-Y. Wu, G.-J. Lv, T. Pu, X.-Q. He, L.-L. Cui, Iron(II) phthalocyanine covalently functionalized graphene as a highly efficient non-precious-metal catalyst for the oxygen reduction reaction in alkaline media, *Electrochim. Acta*, 112 (2013) 269-278.

[183]. H.A. Miller, M. Bellini, W. Oberhauser, X. Deng, H. Chen, Q. He, M. Passaponti, M. Innocenti, R. Yang, F. Sun, Z. Jiang, F. Vizza, Heat treated carbon supported iron(ii)phthalocyanine oxygen reduction catalysts: elucidation of the structure-activity relationship using X-ray absorption spectroscopy, *Phys. Chem. Chem. Phys.*, 18 (2016) 33142-33151.

[184]. R.F. Parton, P.E. Neys, P.A. Jacobs, R.C. Sosa, P.G. Rouxhet, Iron–Phthalocyanine Immobilized on Activated Carbon Black: A Selective Catalyst for Alkane Oxidation, *J. Cat.*, 164 (1996) 341-346.

[185]. T. Kuila, P. Khanra, N.H. Kim, J.K. Lim, J.H. Lee, Effects of sodium hydroxide on the yield and electrochemical performance of sulfonated poly(ether-ether-ketone) functionalized graphene, *J. Mater. Chem. A*, 1 (2013) 9294-9302.

[186]. F. Lou, M.E.M. Buan, N. Muthuswamy, J.C. Walmsley, M. Rønning, D. Chen, One-step electrochemical synthesis of tunable nitrogen-doped graphene, *J. Mater. Chem. A*, 4 (2016) 1233-1243.

[187]. S. Gupta, D. Tryk, I. Bae, W. Aldred, E. Yeager, Heat-treated polyacrylonitrile-based catalysts for oxygen electroreduction, *J. Appl. Electrochem.*, 19 (1989) 19-27.

[188]. F. Jaouen, A.M. Serventi, M. Lefèvre, J.-P. Dodelet, P. Bertrand, Non-Noble Electrocatalysts for O2 Reduction: How Does Heat Treatment Affect Their Activity and Structure? Part II. Structural Changes Observed by Electron Microscopy, Raman, and Mass Spectroscopy, *J. Phys. Chem. C*, 111 (2007) 5971-5976.

[189]. U.I. Kramm, I. Herrmann-Geppert, P. Bogdanoff, S. Fiechter, Effect of an Ammonia Treatment on Structure, Composition, and Oxygen Reduction Reaction Activity of Fe-N-C Catalysts, *J. Phys. Chem. C*, 115 (2011) 23417-23427.

[190]. H. Yin, C. Zhang, F. Liu, Y. Hou, Doped Graphene: Hybrid of Iron Nitride and Nitrogen-Doped Graphene Aerogel as Synergistic Catalyst for Oxygen Reduction Reaction (Adv. Funct. Mater. 20/2014), *Adv. Funct. Mater*, 24 (2014) 2929-2929.

[191]. T. Li, Y. Peng, K. Li, R. Zhang, L. Zheng, D. Xia, X. Zuo, Enhanced activity and stability of binuclear iron (III) phthalocyanine on graphene nanosheets for electrocatalytic oxygen reduction in acid, *J. Power Sources*, 293 (2015) 511-518.

[192]. G. Bhargava, I. Gouzman, C.M. Chun, T.A. Ramanarayanan, S.L. Bernasek, Characterization of the "native" surface thin film on pure polycrystalline iron: A high resolution XPS and TEM study, *Appl. Surf. Sci.*, 253 (2007) 4322-4329.

[193]. C. Chen, Y.-j. Lai, Z.-y. Zhou, X.-s. Zhang, S.-g. Sun, Thermo-stability and active site structure of Fe/N/C electrocatalyst for oxygen reduction reaction, *J. Electrochem.*, 23 (2017) 400-408.

[194]. S. Wang, F. Li, Y. Wang, D. Qiao, C. Sun, J. Liu, A Superior Oxygen Reduction Reaction Electrocatalyst Based on Reduced Graphene Oxide and Iron(II) Phthalocyanine-Supported Sub-2 nm Platinum Nanoparticles, *ACS Appl. Nano Mater.*, 1 (2018) 711-721.

[195]. H. Yin, C. Zhang, F. Liu, Y. Hou, Hybrid of Iron Nitride and Nitrogen-Doped Graphene Aerogel as Synergistic Catalyst for Oxygen Reduction Reaction, *Adv. Funct. Mater*, 24 (2014) 2930-2937.

[196]. L. Cui, G. Lv, Z. Dou, X. He, Fabrication of iron phthalocyanine/graphene micro/nanocomposite by solvothermally assisted π–π assembling method and its application for oxygen reduction reaction, *Electrochim. Acta*, 106 (2013) 272-278.

[197]. D. Guo, R. Shibuya, C. Akiba, S. Saji, T. Kondo, J. Nakamura, Active sites of nitrogen-doped carbon materials for oxygen reduction reaction clarified using model catalysts, *Science*, 351 (2016) 361-365.

[198]. C. Zhang, R. Hao, H. Yin, F. Liu, Y. Hou, Iron phthalocyanine and nitrogen-doped graphene composite as a novel non-precious catalyst for the oxygen reduction reaction, *Nanoscale*, 4 (2012) 7326-7329.

[199]. A. Morozan, S. Campidelli, A. Filoramo, B. Jousselme, S. Palacin, Catalytic activity of cobalt and iron phthalocyanines or porphyrins supported on different carbon nanotubes towards oxygen reduction reaction, *Carbon*, 49 (2011) 4839-4847.

[200]. L. Osmieri, R. Escudero-Cid, A.H.A. Monteverde Videla, P. Ocón, S. Specchia, Application of a non-noble Fe-N-C catalyst for oxygen reduction reaction in an alkaline direct ethanol fuel cell, *Renew. Energy*, 115 (2018) 226-237.

[201]. L. Osmieri, A.H.A. Monteverde Videla, M. Armandi, S. Specchia, Influence of different transition metals on the properties of Me-N-C (Me = Fe, Co, Cu, Zn) catalysts synthesized using SBA-15 as tubular nano-silica reactor for oxygen reduction reaction, *Int. J. Hydrogen Energy*, 41 (2016) 22570-22588.

[202]. R. Praats, I. Kruusenberg, M. Käärik, U. Joost, J. Aruväli, P. Paiste, R. Saar, P. Rauwel, M. Kook, J. Leis, J.H. Zagal, K. Tammeveski, Electroreduction of oxygen in alkaline solution on iron phthalocyanine modified carbide-derived carbons, *Electrochim. Acta*, 299 (2019) 999-1010.

[203]. Z. Zhang, M. Dou, J. Ji, F. Wang, Phthalocyanine tethered iron phthalocyanine on graphitized carbon black as superior electrocatalyst for oxygen reduction reaction, *Nano Energy*, 34 (2017) 338-343.

[204]. Morozan, S. Campidelli, A. Filoramo, B. Jousselme, S. Palacin, Catalytic activity of cobalt and iron phthalocyanines or porphyrins supported on different carbon nanotubes towards oxygen reduction reaction, Carbon, 49 (2011) 4839-4847.

[205]. M.P. Karthikayini, T. Thirupathi, G. Wang, V.K. Ramani, R.K. Raman, Highly Active and Durable Non-Precious Metal Catalyst for the Oxygen Reduction Reaction in Acidic Medium, *J. Electrochem. Soc.*, 163 (2016) F539-F547.

[206]. Z. Zhang, S. Yang, M. Dou, J. Ji, F. Wang, One-step preparation of N-doped graphitic layer-encased cobalt/iron carbide nanoparticles derived from cross-linked polyphthalocyanines as highly active electrocatalysts towards the oxygen reduction reaction, *Catal. Sci. Technol*., 7 (2017) 1529-1536.

[207]. Y. Liang, H. Wang, J. Zhou, Y. Li, J. Wang, T. Regier, H. Dai, Covalent Hybrid of Spinel Manganese–Cobalt Oxide and Graphene as Advanced Oxygen Reduction Electrocatalysts, *J. Am. Chemi. Soc.*, 134 (2012) 3517-3523.

[208]. C.C.L. McCrory, S. Jung, J.C. Peters, T.F. Jaramillo, Benchmarking Heterogeneous Electrocatalysts for the Oxygen Evolution Reaction, *J. Am. Chemi. Soc.*, 135 (2013) 16977-16987.

[209]. C.C.L. McCrory, S. Jung, I.M. Ferrer, S.M. Chatman, J.C. Peters, T.F. Jaramillo, Benchmarking Hydrogen Evolving Reaction and Oxygen Evolving Reaction Electrocatalysts for Solar Water Splitting Devices, *J. Am. Chemi. Soc.*, 137 (2015) 4347-4357.

[210]. Y.P. Zhu, C. Guo, Y. Zheng, S.-Z. Qiao, Surface and Interface Engineering of Noble-Metal-Free Electrocatalysts for Efficient Energy Conversion Processes, *Acc. Chem. Res.*, 50 (2017) 915-923.

[211]. G. Rajeshkhanna, S. Kandula, K.R. Shrestha, N.H. Kim, J.H. Lee, A New Class of Zn1-xFex–Oxyselenide and Zn1- xFex–LDH Nanostructured Material with Remarkable Bifunctional Oxygen and Hydrogen Evolution Electrocatalytic Activities for Overall Water Splitting, *Small*, 14 (2018) 1803638.

[212]. X. Li, X. Hao, A. Abudula, G. Guan, Nanostructured catalysts for electrochemical water splitting: current state and prospects, *J. Mater. Chem. A*, 4 (2016) 11973-12000.

[213]. C.G. Morales-Guio, L.-A. Stern, X. Hu, Nanostructured hydrotreating catalysts for electrochemical hydrogen evolution, *Chem. Soc. Rev.*, 43 (2014) 6555-6569.

[214]. M.S. Faber, S. Jin, Earth-abundant inorganic electrocatalysts and their nanostructures for energy conversion applications, *Energy Environ. Sci.*, 7 (2014) 3519-3542.

[215]. A. Tahira, Z.H. Ibupoto, R. Mazzaro, S. You, V. Morandi, M.M. Natile, M. Vagin, A. Vomiero, Advanced Electrocatalysts for Hydrogen Evolution Reaction Based on Core–Shell MoS_2/TiO_2 Nanostructures in Acidic and Alkaline Media, *ACS Appl. Energy Mater.*, 2 (2019) 2053-2062.

[216]. S. Yuan, Z. Pu, H. Zhou, J. Yu, I.S. Amiinu, J. Zhu, Q. Liang, J. Yang, D. He, Z. Hu, G. Van Tendeloo, S. Mu, A universal synthesis strategy for single atom dispersed cobalt/metal clusters heterostructure boosting hydrogen evolution catalysis at all pH values, *Nano Energy*, 59 (2019) 472-480.

[217]. Z. Pu, Q. Liu, C. Tang, A.M. Asiri, X. Sun, Ni_2P nanoparticle films supported on a Ti plate as an efficient hydrogen evolution cathode, *Nanoscale*, 6 (2014) 11031-11034.

[218]. M.-R. Gao, Y.-F. Xu, J. Jiang, S.-H. Yu, Nanostructured metal chalcogenides: synthesis, modification, and applications in energy conversion and storage devices, *Chem. Soc. Rev.*, 42 (2013) 2986-3017.

[219]. J. Zhu, Z.-C. Wang, H. Dai, Q. Wang, R. Yang, H. Yu, M. Liao, J. Zhang, W. Chen, Z. Wei, N. Li, L. Du, D. Shi, W. Wang, L. Zhang, Y. Jiang, G. Zhang, Boundary activated hydrogen evolution reaction on monolayer MoS_2, *Nat. Commun*, 10 (2019) 1348.

[220]. Y. Sun, G. Wang, K. Yan, TiO_2 nanotubes for hydrogen generation by photocatalytic water splitting in a two-compartment photoelectrochemical cell, *Int. J. Hydrogen Energy*, 36 (2011) 15502-15508.

[221]. Q. Cai, M. Paulose, O.K. Varghese, C.A. Grimes, The Effect of Electrolyte Composition on the Fabrication of Self-Organized Titanium Oxide Nanotube Arrays by Anodic Oxidation, *J. Mater. Res.*, 20 (2005) 230-236.

[222]. Y. Xia, P. Yang, Y. Sun, Y. Wu, B. Mayers, B. Gates, Y. Yin, F. Kim, H. Yan, One-Dimensional Nanostructures: Synthesis, Characterization, and Applications, *Adv. Mater.*, 15 (2003) 353-389.

[223]. M. Ge, C. Cao, J. Huang, S. Li, Z. Chen, K.-Q. Zhang, S.S. Al-Deyab, Y. Lai, A review of one-dimensional TiO_2 nanostructured materials for environmental and energy applications, *J. Mater. Chem. A,* 4 (2016) 6772-6801.

[224]. M. Kulkarni, A. Mazare, E. Gongadze, P. Š, V. Kralj-Iglič, I. Milošev, P. Schmuki, A. Iglič, M. Mozetič, Titanium nanostructures for biomedical applications, *Nanotechnol*., 26 (2015) 062002.

[225]. T. Jin, Q. Han, Y. Wang, L. Jiao, 1D Nanomaterials: Design, Synthesis, and Applications in Sodium–Ion Batteries, *Small,* 14 (2018) 1703086.

[226]. X. Wang, Z. Li, J. Shi, Y. Yu, One-Dimensional Titanium Dioxide Nanomaterials: Nanowires, Nanorods, and Nanobelts, *Chem. Rev*., 114 (2014) 9346-9384.

[227]. C.-C. Chen, H.-W. Chung, C.-H. Chen, H.-P. Lu, C.-M. Lan, S.-F. Chen, L. Luo, C.-S. Hung, E.W.-G. Diau, Fabrication and Characterization of Anodic Titanium Oxide Nanotube Arrays of Controlled Length for Highly Efficient Dye-Sensitized Solar Cells, *J. Phys. Chem. C*, 112 (2008) 19151-19157.

[228]. M. Altomare, M. Pozzi, M. Allieta, L.G. Bettini, E. Selli, H2 and O2 photocatalytic production on TiO_2 nanotube arrays: Effect of the anodization time on structural features and photoactivity, *Appl. Catal., B*, 136-137 (2013) 81-88.

[229]. M. Chang, Y. Song, H. Zhang, Y. Sheng, K. Zheng, X. Zhou, H. Zou, Hydrothermal assisted sol-gel synthesis and multisite luminescent properties of anatase TiO_2:Eu^{3+} nanorods, *RSC Adv*., 5 (2015) 59314-59319.

[230]. P. Hoyer, Formation of a Titanium Dioxide Nanotube Array, *Langmuir*, 12 (1996) 1411-1413.

[231]. H.-H. Ou, S.-L. Lo, Review of titania nanotubes synthesized via the hydrothermal treatment: Fabrication, modification, and application, *Sep. Purif. Technol*., 58 (2007) 179-191.

[232]. D. Zhou, Z. Chen, T. Gao, F. Niu, L. Qin, Y. Huang, Hydrogen Generation from Water Splitting on TiO_2 Nanotube-Array-Based Photocatalysts, *Energy Technol*., 3 (2015) 888-895.

[233]. M.B. Zhang, Y.; Wada, K. J., Sol-gel template preparation of TiO_2 nanotubes and nanorods, *J. Mater. Sci. Lett*., 20, (2001,) 167-170.

[234]. G.K. Mor, K. Shankar, M. Paulose, O.K. Varghese, C.A. Grimes, Use of Highly-Ordered TiO_2 Nanotube Arrays in Dye-Sensitized Solar Cells, *Nano Lett*., 6 (2006) 215-218.

[235]. O.K. Varghese, M. Paulose, C.A. Grimes, Long vertically aligned titania nanotubes on transparent conducting oxide for highly efficient solar cells, *Nat. Nanotechnol.*, 4 (2009) 592.

[236]. D. Gong, C.A. Grimes, O.K. Varghese, W. Hu, R.S. Singh, Z. Chen, E.C. Dickey, Titanium oxide nanotube arrays prepared by anodic oxidation, *J. Mater. Res.,* 16 (2001) 3331-3334.D. Yu, X. Zhu, Z. Xu, X. Zhong, Q. Gui, Y. Song, S. Zhang, X. Chen, D. Li, Facile Method to Enhance the Adhesion of TiO_2 Nanotube Arrays to Ti Substrate, *ACS Appl. Mater. Interfaces*, 6 (2014) 8001-8005.

[237]. D. Yu, X. Zhu, Z. Xu, X. Zhong, Q. Gui, Y. Song, S. Zhang, X. Chen, D. Li, Facile Method to Enhance the Adhesion of TiO_2 Nanotube Arrays to Ti Substrate, *ACS Appl. Mater. Interfaces*, 6 (2014) 8001-8005.

[238]. D. Regonini, C.R. Bowen, A. Jaroenworaluck, R. Stevens, A review of growth mechanism, structure and crystallinity of anodized TiO_2 nanotubes, *Mater. Sci. Eng. R Rep*., 74 (2013) 377-406.

[239]. K. Zhu, T.B. Vinzant, N.R. Neale, A.J. Frank, Removing Structural Disorder from Oriented TiO_2 Nanotube Arrays: Reducing the Dimensionality of Transport and Recombination in Dye-Sensitized Solar Cells, *Nano Lett*., 7 (2007) 3739-3746.

[240]. D. Kim, A. Ghicov, P. Schmuki, TiO_2 Nanotube arrays: Elimination of disordered top layers (“nanograss”) for improved photoconversion efficiency in dye-sensitized solar cells, *Electrochem. Commun.,* 10 (2008) 1835-1838.

[241]. X. Zhou, N.T. Nguyen, S. Özkan, P. Schmuki, Anodic TiO_2 nanotube layers: Why does self-organized growth occur: A mini-review, *Electrochem. Commun.,* 46 (2014) 157-162.

[242]. B. Chen, J. Hou, K. Lu, Formation Mechanism of TiO_2 Nanotubes and Their Applications in Photoelectrochemical Water Splitting and Supercapacitors, *Langmuir*, 29 (2013) 5911-5919.

[243]. A. Valota, D.J. LeClere, P. Skeldon, M. Curioni, T. Hashimoto, S. Berger, J. Kunze, P. Schmuki, G.E. Thompson, Influence of water content on nanotubular anodic titania formed in fluoride/glycerol electrolytes, *Electrochim. Acta*, 54 (2009) 4321-4327.

[244]. S.P. Albu, A. Ghicov, S. Aldabergenova, P. Drechsel, D. LeClere, G.E. Thompson, J.M. Macak, P. Schmuki, Formation of Double-Walled TiO_2 Nanotubes and Robust Anatase Membranes, *Adv. Mater*., 20 (2008) 4135-4139.

[245]. W. Li, R. Liang, A. Hu, Z. Huang, Y.N. Zhou, Generation of oxygen vacancies in visible light-activated one-dimensional iodine TiO_2 photocatalysts, *RSC Adv*., 4 (2014) 36959-36966.

[246]. S.K. Das, M.K. Bhunia, A. Bhaumik, Self-assembled TiO_2 nanoparticles: mesoporosity, optical and catalytic properties, *Dalton Trans*., 39 (2010) 4382-4390.

[247]. L. Zhu, Q. Lu, L. Lv, Y. Wang, Y. Hu, Z. Deng, Z. Lou, Y. Hou, F. Teng, Ligand-free rutile and anatase TiO_2 nanocrystals as electron extraction layers for high performance inverted polymer solar cells, *RSC Adv.*, 7 (2017) 20084-20092.

[248]. M. Chandra, K. Bhunia, D. Pradhan, Controlled Synthesis of CuS/TiO_2 Heterostructured Nanocomposites for Enhanced Photocatalytic Hydrogen Generation through Water Splitting, *Inorga. Chem*., 57 (2018) 4524-4533.

[249]. N. Roy, Y. Sohn, K.T. Leung, D. Pradhan, Engineered Electronic States of Transition Metal Doped TiO_2 Nanocrystals for Low Overpotential Oxygen Evolution Reaction, *J. Phys. Chem. C*, 118 (2014) 29499-29506.

[250]. J.M. Macák, H. Tsuchiya, P. Schmuki, High-Aspect-Ratio TiO_2 Nanotubes by Anodization of Titanium, *Angew. Chem., Int. Ed*, 44 (2005) 2100-2102.

[251]. G.K. Mor, K. Shankar, M. Paulose, O.K. Varghese, C.A. Grimes, Enhanced Photocleavage of Water Using Titania Nanotube Arrays, *Nano Lett*., 5 (2005) 191-195.

[252]. G.K. Mor, O.K. Varghese, M. Paulose, N. Mukherjee, C.A. Grimes, Fabrication of tapered, conical-shaped titania nanotubes, *J. Mater. Res*., 18 (2003) 2588-2593.

[253]. S. Karthik, K.M. Gopal, E.P. Haripriya, Y. Sorachon, P. Maggie, K.V. Oomman, A.G. Craig, Highly-ordered TiO_2 nanotube arrays up to 220 μm in length: use in water photoelectrolysis and dye-sensitized solar cells, *Nanotechnology*, 18 (2007) 065707.

[254]. Y. Shen, X. Ren, X. Qi, J. Zhou, Z. Huang, J. Zhong, MoS_2 Nanosheet Loaded with TiO_2 Nanoparticles: An Efficient Electrocatalyst for Hydrogen Evolution Reaction, *J. Electrochem. Soc.*, 163 (2016) H1087-H1090.

[255]. B. Ma, P.-Y. Guan, Q.-Y. Li, M. Zhang, S.-Q. Zang, MOF-Derived Flower-like MoS_2@TiO_2 Nanohybrids with Enhanced Activity for Hydrogen Evolution, *ACS Appl. Mater. Interfaces*, 8 (2016) 26794-26800.

[256]. W. Zhou, Z. Yin, Y. Du, X. Huang, Z. Zeng, Z. Fan, H. Liu, J. Wang, H. Zhang, Synthesis of Few-Layer MoS_2 Nanosheet-Coated TiO_2 Nanobelt Heterostructures for Enhanced Photocatalytic Activities, *Small*, 9 (2013) 140-147.

[257]. J. Tao, S. Chen, L. Guan, G. Chen, C. Yu, L. Chen, X. Cheng, H. Zhang, X. Xie, Well-patterned Au nanodots on MoS_2/TiO_2 hybrids for enhanced hydrogen evolution activity, *Electrochim. Acta*, 283 (2018) 419-427.

[258]. J. Liang, C. Wang, P. Zhao, Y. Wang, L. Ma, G. Zhu, Y. Hu, Z. Lu, Z. Xu, Y. Ma, T. Chen, Z. Tie, J. Liu, Z. Jin, Interface Engineering of Anchored Ultrathin TiO_2/MoS_2 Heterolayers for Highly-Efficient Electrochemical Hydrogen Production, *ACS Appl. Mater. Interfaces*, 10 (2018) 6084-6089.

[259]. Y. Zheng, Y. Jiao, M. Jaroniec, S.Z. Qiao, Advancing the Electrochemistry of the Hydrogen-Evolution Reaction through Combining Experiment and Theory, *Angew. Chem., Int. Ed*, 54 (2015) 52-65.

[260]. T. Shinagawa, A.T. Garcia-Esparza, K. Takanabe, Insight on Tafel slopes from a microkinetic analysis of aqueous electrocatalysis for energy conversion, *Sci. Rep.*, 5 (2015) 13801-13801.

[261]. H. He, J. Lin, W. Fu, X. Wang, H. Wang, Q. Zeng, Q. Gu, Y. Li, C. Yan, B.K. Tay, C. Xue, X. Hu, S.T. Pantelides, W. Zhou, Z. Liu, MoS_2/TiO_2 Edge-On Heterostructure for Efficient Photocatalytic Hydrogen Evolution, *Adv. Energy Mater.*, 6 (2016) 1600464.

[262]. Y. Li, H. Wang, L. Xie, Y. Liang, G. Hong, H. Dai, MoS_2 Nanoparticles Grown on Graphene: An Advanced Catalyst for the Hydrogen Evolution Reaction, *J. Am. Chemi. Soc.*, 133 (2011) 7296-7299.

Appendix A Synopsis

L’Introduction

L’impact des activités humaines sur l’environnement est profondément enraciné dans les technologies de production d’énergie dominées par la combustion. Notre dépendance à l'énergie issue de la combustion des combustibles fossiles soulève de nombreuses préoccupations environnementales et mondiales, et constitue une menace pour la sécurité énergétique et d'autres vulnérabilités [1,2]. En tenant compte de la consommation et de la demande d’énergies croissantes sans cesse, l'exploration d'une nouvelle source de conversion d'énergie propre et durable à la place des sources d'énergie basées sur la combustion suscite un intérêt considérable. Parmi les options envisageables à l'étude pour la conversion et le stockage d'énergie propre et durable, l'électrochimique qui représente l'une des plus prometteuses et passionnantes méthodes. Les processus électrochimiques dans des dispositifs tels que les piles à combustible (PC) et les batteries constituent un mécanisme efficace et propre pour la conversion et le stockage de l'énergie. Les PC attirent particulièrement l'attention dans les domaines du développement durable et de la sécurité énergétique en raison de leur compatibilité avec les ressources d'énergie renouvelable telles que l'hydrogène et les alcools inférieurs. Les avantages des PC comme futur groupe électrogène comprend un rendement élevé, une densité d'énergie importante, un fonctionnement silencieux, une modularité inhérente à la pile et des émissions nulles ou faibles [3]. En conséquence, les PC sont attrayants pour une utilisation dans diverses applications couvrant les petites alimentations fixe et de secours, l’électronique portable, le transport à l'échelle du réseau [1,2,4].

Dans les PC, la réaction d’oxydation de l’hydrogène (HOR) se produit à la surface d’un catalyseur afin de produire des électrons et des protons. Les électrons sont transférés à la cathode par un circuit externe où ils provoquent une réaction de l'oxygène et de l’hydrogène pour produire de l’eau. Cette réaction cathodique est appelée réaction de réduction de l'oxygène (ORR). Le processus ORR dont les équations de réaction sont résumées dans le tableau 1-1 ci-dessous a une cinétique lente et hautement irréversible car elle implique un mécanisme de transfert complexe à 4 électrons et protons. Par conséquent, des électrocatalyseurs de l'ORR très efficaces sont nécessaires pour faire fonctionner le PC [5-7]. Les matériaux à base de platine (Pt) sont largement utilisés comme électrocatalyseurs pour l'ORR depuis des décennies. Néanmoins, le coût élevé et l'approvisionnement limité en Pt empêchent l'application commerciale à grande échelle des PC. De plus, les matériaux à base de platine souffrent d'une activité dépendant du temps [7-10]

, d'un empoisonnement au monoxyde de carbone (CO) [11-13] et d'une mauvaise sélectivité pour la réduction de l'oxygène. Par conséquent, des efforts considérables ont été consacrés au: (i) développement de matériaux à base de Pt hautement actifs et durables, présentant une teneur réduite en Pt, à travers la modification des nanostructures de Pt à surface spécifique élevée, utilisant des alliages de Pt et des métaux à faible coût [14-16] ou de nouveaux matériaux de support pour platine [17-19]; et (ii) le remplacement des catalyseurs à base de platine par des catalyseurs haute performance et bon marché sans métaux [20] et des catalyseurs à base de métaux non précieux (NPMCs) [21-29].

Tableau 1-1. Potentiels thermodynamiques des réactions de réduction de l'oxygène [5]

Solution aqueuse	Reactions ORR	E° (V vs. RHE)
Acide	$O_2 + 4H^+ + 4e^- \rightarrow 2H_2O$	1.229
	$O_2 + 2H^+ + 2e^- \rightarrow H_2O_2$	0.70
	$H_2O_2 + 2H^+ + 2e^- \rightarrow 2H_2O$	1.76
Alcalin	$O_2 + 2H_2O + 4e^- \rightarrow 4OH^-$	0.401
	$O_2 + H_2O + 2e^- \rightarrow HO_2^- + OH^-$	-0.065
	$HO_2^- + H_2O + 2e^- \rightarrow 3OH^-$	0.867

À la recherche de nouveaux matériaux électrocatalytiques, le graphène est une classe émergente de matériaux qui a beaucoup attiré l’attention comme l’électrocatalyse pour l’ORR en tant que catalyseur sans métal, électrocatalyseurs à métaux non précieux (NPMCs) ou matériau de support en raison de leurs propriétés physicochimiques uniques, grande surface, haute conductivité électronique et excellente stabilité chimique. Néanmoins, les méthodes de fabrication à grande échelle de graphène de haute qualité sont limitées. Mais la méthode électrochimique est attrayante car elle est écologique, directe, simple et évolutive, elle évite également la contamination fortuite de graphène par des atomes métalliques. De plus, cette méthode permet de contrôler le degré d'oxydation, permettant ainsi un réglage des groupes fonctionnels de surface tout en conservant la majorité des propriétés intrinsèques du graphène. En tant que tel, le candidat le plus polyvalent est le graphène [30-34].

D'autre part, la réalisation d'une utilisation significative des PC et de l'énergie repose sur la fourniture d'hydrogène ou d'autres combustibles issus de technologies de conversion des énergies renouvelables. À l'heure actuelle, la principale source de production d'hydrogène est le reformage à la vapeur de combustibles fossiles, qui consomme beaucoup d'énergie et produit des gaz à effet de serre [34-37]. Il reste difficile de produire de l'hydrogène de manière durable, à une échelle économique. Parmi les autres procédés de production d'hydrogène, le fractionnement électrochimique de l'eau par réaction de dégagement d'hydrogène (RDH) constitue l'option la plus prometteuse. Le processus RDH est une voie simple et propre pour produire de l'H_2. Néanmoins, un catalyseur haute performance pour le RDH est nécessaire pour surmonter le potentiel excessif de réduction de la quantité d'eau et par conséquent pour améliorer l'efficacité de ce processus électrochimique important. Actuellement, les catalyseurs à base de platine et de métaux précieux sont les plus efficaces [36]. Il est hautement souhaitable de rechercher des électrocatalyseurs alternatifs à partir d'éléments riches en terres pour remplacer le groupe des métaux rares et précieux. Plusieurs classes de matériaux à base de métaux de transition ont été largement étudiées comme électrodes RDH possibles. Les électrodes RDH les plus prometteuses sont les alliages ($MoNi_4$) [38,39], les chalcogénures (MoS_2, CoS_2, $CoSe_2$) [40-42], les carbures (WC, Mo_2C, Ni_2C) [43-44], les phosphures (Ni_2P, CoP) [45] et des oxydes ($SrTiO_3$, WO_3, Fe_2O_3, ZnO) [46,49]. Parmi eux, les chalcogénides ont démontré une activité RDH prometteuse. Cependant, les étapes compliquées de la synthèse représentent un défi pour la mise à l'échelle en plus d'une stabilité médiocre à long terme. Des recherches approfondies sur des approches simples pour obtenir des électrodes RDH à faible coût et durables sont hautement souhaitables. Par conséquent, dans cette étude, nous développons une approche simple pour fabriquer un électrocatalyseur RDH hautement efficace et durable en combinant des propriétés, une activité catalytique prometteuse du MoS_2 et une stabilité chimique du TiO_2-NTs.

Objectifs

L’objectif général de cette thèse est d’étudier l’approche peu coûteuse, évolutive et simple de la fabrication d’électrocatalyseurs durables et efficaces à base d’éléments abondants pour les applications pile à combustible, réaction de réduction de l’oxygène et électrolyseur d’eau, réaction de dégagement d’hydrogène. Les objectifs spécifiques de cette étude sont:

i. Préparer un graphène de grande taille et de haute qualité par exfoliation électrochimique de feuilles de graphite et affiner le graphène pour améliorer leurs performances de l’ORR sous la forme d'électrocatalyseurs sans métal;

ii. Développer des NPMC durables et à haute performance pour l’ORR sur la base de la phtalocyanine de fer II supportée par le graphène en utilisant une approche peu coûteuse et simple; et

iii. Fabriquer un électrocatalyseur électrochimique à dégagement d'hydrogène hautement efficace et durable, à base de nanotubes de TiO_2 autoportants sur support MoS_2.

Résultats

Dans la première partie de la thèse, nous rapportons la fabrication d'électrocatalyseurs sans métaux à base de graphène pour une réaction de réduction de l'oxygène (ORR), une étape cruciale dans le fonctionnement des piles à combustible. Nous avons fabriqué de grandes échantillons de graphène (GP) de haute qualité avec un nombre contrôlable de couches par une méthode électrochimique simple, économique et respectueuse de l'environnement, en utilisant une feuille de graphite à faible coût et des plaques comme précurseurs dans les solutions aqueuses sans ions métalliques (électrolyte). L'analyse par spectroscopie photoélectronique aux rayons X (XPS) a confirmé l'absence d'impuretés métalliques fortuites dans les échantillons de graphène tels qu'ils ont été exfoliés, que ce soit en feuille de graphite (GPf) ou en plaque (GP). Les échantillons GPf et GP ont été évalués pour l'ORR. Les échantillons GP ont démontré une activité ORR supérieure à celle des échantillons GPf. Par la suite, les échantillons optimisés tels que exfoliés (GP) ont été convertis en graphène dopé avec l'azote N (N-GP) après pyrolyse de NH_3, ce qui présente une performance ORR très améliorée par rapport au graphène exfoliée, en raison du dopage N.

À partir de l'étude de la morphologie et de la structure par microscopie électronique à transmission (TEM) et haute résolution TEM (HRTEM) (Figure 1a-e), les échantillons de graphène provenant des deux sources de graphite (GPf et GP) semblent être des pièces plus grandes, uniformes et très mince, environ deux à quelques couches, comme observé en comptant les bords repliés des images HRTEM. Les diagrammes correspondants de diffraction électronique en zone sélectionnée (SAED) du graphène (Figure 1b,e) indiquaient la structure de réseau monocristallin avec un diagramme de diffraction hexagonal caractéristique qui montre que peu de couches et du graphène de haute qualité sont obtenus à partir des deux sources de graphite [27,29]. Grâce à nos études systématiques, nous soulignons que: les grandes pièces de peu de couches et le graphène de haute qualité peuvent être facilement fabriqués par une méthode électrochimique simple, rapide, économique et respectueuse de l'environnement. L'activité ORR du graphène exfolié est fortement influencée par les paramètres d'exfoliation et de post-exfoliation tels que la température de l'électrolyte d'exfoliation, le nombre de couches de graphène, la température de pyrolyse et la concentration de l'électrolyte et du précurseur de graphite. La Figure 1f indique que la morphologie des échantillons de graphène a conservé sa morphologie après pyrolyse dans une atmosphère d'ammoniac à 950 °C.

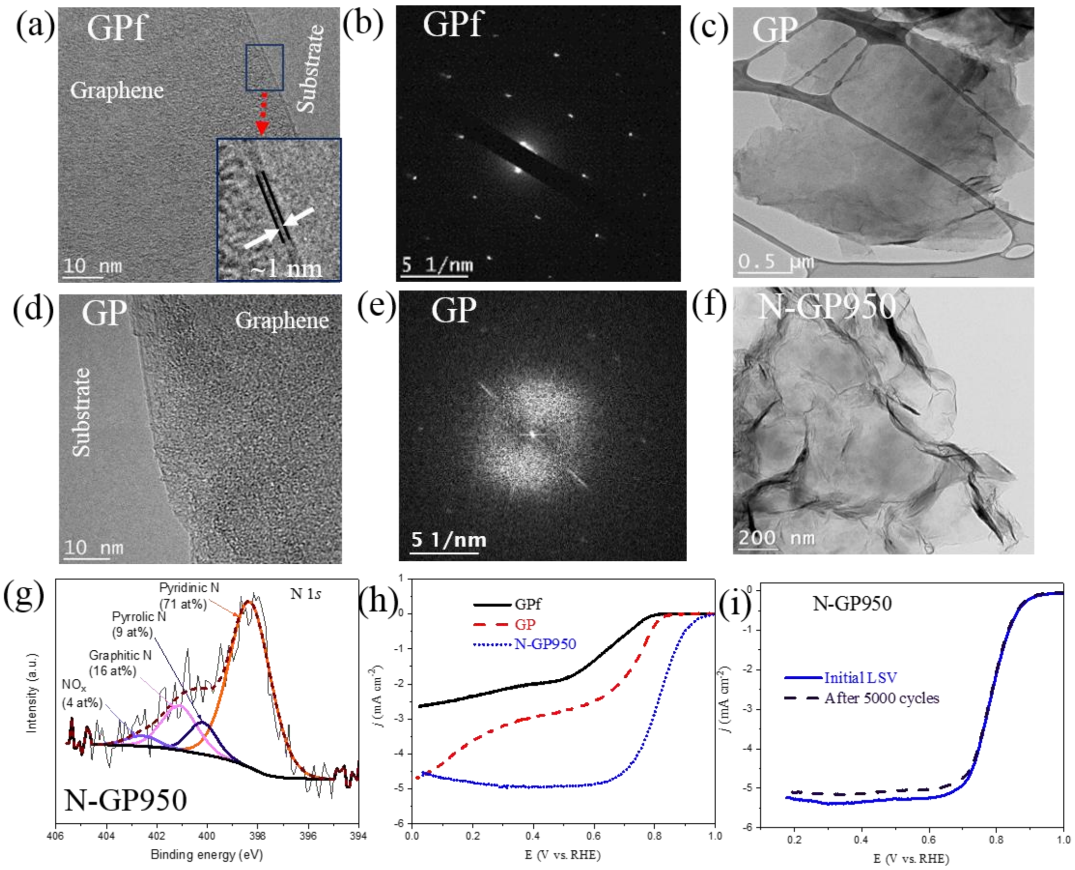

Figure 1 Images de microscopie électronique à transmission et diffraction électronique à zone sélectionnée (SAED) d'échantillons de graphène exfoliés, (a-b) Graphène en feuille de graphite (GPf); (c-e) graphène de plaque de graphite (GP), (f) N-GP950. (g) Haute résolution des N-GP950 XPS N 1s. (h) Courbes de polarisation ORR des échantillons de graphène, et (i) courbe de polarisation ORR avant et après l'essai de durabilité. Les mesures ont été effectuées en KOH 0.1 M saturé en N_2 ou en O_2 saturé, vitesse de balayage: 10 mV s^{-1} à 1600 tr/min.

Le graphène exfolié à partir de plaques de graphite, GP, a démontré une activité ORR supérieure à celle du graphène exfolié à partir de la feuille de graphite, GPf, (Figure 1h); l'activité ORR du GP s'est encore accrue de 10 fois après la pyrolyse dans du NH_3 à 950 °C pendant 15 minutes (Figure 1h, courbe bleue). En outre, la Figure 1i montre les courbes de polarisation du N-GP950 avant et après l'essai de durabilité accéléré. La N-GP a montré une excellente durabilité après 5000 cycles potentiels d'activité ORR alcaline comparable et une meilleure stabilité que le catalyseur Pt/C commercial à la pointe de la technologie. Par conséquent, il est possible d'affiner l'activité ORR du graphène et du N-GP en manipulant les paramètres expérimentaux. Ainsi, nous pensons que le N-GP préparé par une méthode rentable utilisant des précurseurs à faible coût est un candidat potentiel du catalyseur ORR dans une pile à combustible alcaline.

Les résultats présentés dans ce chapitre sont basés sur l'article suivant :

N. Komba, Q. Wei, G. Zhang, F. Rosei, S. Sun, Synthèse contrôlée du graphène par voie électrochimique et son utilisation comme catalyseur efficace sans métal pour la réduction de l'oxygène. *Applied Catalysis* B*: Environmental* 2019, 243, 373-380.

Deuxièmement, nous rapportons une approche rentable et directe pour fabriquer une nouvelle classe de CMNP en immobilisant la phtalocyanine de fer (FePc) dans une surface de graphène exfolié électrochimique dopé à l'azote (N-GP950). L'approche de fabrication du FePc/N-GP950 est une méthode simple, directe, économique et respectueuse de l'environnement. A partir de l'image TEM, les Figures 2a-c, l'échantillon optimisé (FePc-33/N-GP950) illustrent une dispersion élevée de FePc à la surface du N-GP950. Nous pensons que la forte interaction électronique entre FePc et N-GP950 joue un rôle clé dans la dispersion de FePc. Le déplacement des énergies de liaison des espèces N 1s observé à la Figure 2d est attribué à une interaction électronique accrue entre FePc et le N-GP950 [48-49]. D'après la Figure 2f-i, notre échantillon optimisé, FePc-33/N-GP950, a démontré une activité ORR exceptionnellement élevée et une durabilité à long terme dans des supports alcalins offrant de meilleures performances que le Pt/C du commerce.

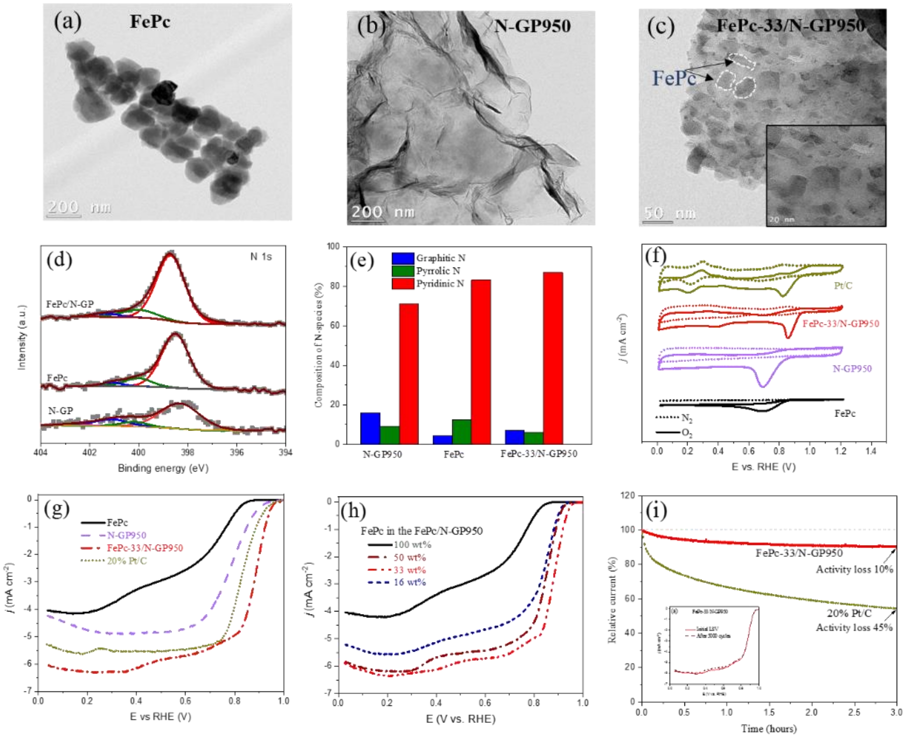

Figure 2 Images TEM de (a) l'agrégation de FePc de taille environ 165 nm, (b) graphène dopé au N (N-GP950), (c) FePc-33/N-GP950, (d) spectres XPS à haute résolution de N 1s pour les trois échantillons, (e) composition nominale de N-espèces dans les échantillons. Performances électrochimiques des catalyseurs FePc, N-GP950, FePc-33/N-GP950 et 20% Pt/C: (f) Courbes CV des catalyseurs en N$_2$ (lignes de points) et O2 (lignes pleines) enregistrées à l'aide d'une vitesse de balayage de 50 mV s^{-1}, (g) les LSVs de FePc, N-GP950, FePc-33/N-GP950 et 20% Pt/C, (h) Les LSVs de FePc/N-GP950 avec différentes charges de FePc 16 33, 50 et 100% en poids. Les mesures RRDE enregistrées dans 0.1 M KOH, vitesse de balayage: 10 mV s^{-1} et la vitesse de rotation du disque de 1600 tr/min. (i) Réponses chrono-ampérométriques (à 0,8 V vs. RHE) de catalyseurs FePc-33/N-GP950 et à 20% en poids de Pt/C dans du KOH 0.1 M saturé en O$_2$ et l'insert correspond aux LSV enregistrés avant et après 5000 cycles de test ADT entre 0.6 et 1.0 V, vitesse de balayage 10 mV s^{-1}, rotation du disque de 1600 tr/min dans du KOH 0.1 M saturé en O$_2$.

Le FePc-33/N-GP950 présente la meilleure activité ORR parmi les catalyseurs de macrocycles métalliques non pyrolysés [34,176,180, 198-203]. En plus de l'abondance de pyridinique-N (Figure 2e), nous pensons que la forte interaction électronique π-π entre le FePc et le graphène dopé au N de haute qualité a été déterminante pour l'obtention de la haute performance ORR déduite des résultats XPS [34,176]. Les points saillants de cette étude sont les suivants: une approche simple, directe et respectueuse de l’environnement a été mise au point pour la fabrication de FePc/N-graphène avec une dispersion élevée de FePc; le graphène exfolié électrochimique dopé au N (N-GP950) est un excellent matériau de support pour améliorer les performances de FePc en termes de ORR; plus important encore, le composite optimisé FePc/N-GP présentait une excellente activité ORR et une durabilité à long terme. La performance ORR du FePc/N-NGP est comparable à 20% en poids de Pt/C avec une bien meilleure stabilité; et une forte interaction π-π entre FePc et le graphène dopé au N est essentielle pour la performance ORR élevée du composite FePc/N-GP950.

Les résultats présentés dans ce chapitre sont basés sur l'article suivant :

Komba, N., Zhang, G., Wei, Q., Prakash, J., Chenitz, R., Rosei, F., Sun, S., Iron (II), Phtalocyanine/graphène dopé au N: un non hautement efficace Catalyseur de métaux précieux pour la réduction de l'oxygène. *International Journal of Hydrogen Energy*, 44 (2019) 18103-18114.

Dans le dernier article, nous décrivons la fabrication de membranes de TiO_2-NTs autonomes très ordonnées, dont une extrémité est ouverte après séchage de la feuille de Ti anodisée au four, à 70 °C pendant 2 h. L'influence de la température de l'électrolyte, de la période d'anodisation et des substrats de pré-anodisation a été étudiée. La configuration expérimentale d'anodisation est illustrée à la Figure 3a. La manipulation des conditions d'anodisation a joué un rôle clé dans l'évolution des morphologies des TiO_2-NTs. Comme le montre la Figure 3b-c, les membranes de TiO_2-NTs autonomes telles qu'elles ont été fabriquées ont été fortement ordonnées dans un garnissage hexagonal, chacun des nanotubes étant entouré de 6 voisins les plus proches. Les diamètres intérieur et extérieur des nanotubes sont de 95, 120 nm et 112, 120 nm pour une durée d'anodisation de 4 et 7 heures respectivement. Les TiO_2-NTs autonomes ont ensuite été utilisés pour prendre en charge MoS_2. Les couches de MoS_2 dans MoS_2/TiO_2-NTs sont uniformément réparties sur toute la surfac des TiO_2-NTs. Des tests de propriétés ont montré que les TiO_2-NTs tels que fabriqués peuvent constituer un excellent support pour les couches de MoS_2 en tant que catalyseurs HER.

Les différentes étapes de fabrication du composé sont représentées en Figure 3d. L'image TEM (Figure 3e) montrent une morphologie des MoS_2/TiO_2-NTs dans laquelle les couches de MoS_2 sont fortement dispersées sur toute l'étendue des surfaces de nanotubes de TiO_2. Les nanotubes de MoS_2/TiO_2 préparés présentent une activité HER améliorée (Figure 3f-g) avec une de potentiel d'activation (ou de démarrage ou seuil) de 150 mV et une faible pente de Tafel (70 mV par décade). L'activité HER des MoS_2/TiO_2-NTs est significativement améliorée en comparaison (ou comparée) à celle du MoS_2 pris seul ou à celle des nanotubes de TiO_2. Ce qui indique que les nanotubes de TiO_2 constituent un excellent support pour les couches de MoS_2. L'amélioration des performances HER du de l'assemblage (nanotubes de MoS_2/TiO_2) sont attribués à l'effet combiné des interactions chimique et électronique entre les nanotubes d eTiO_2 et le MoS_2 [215].

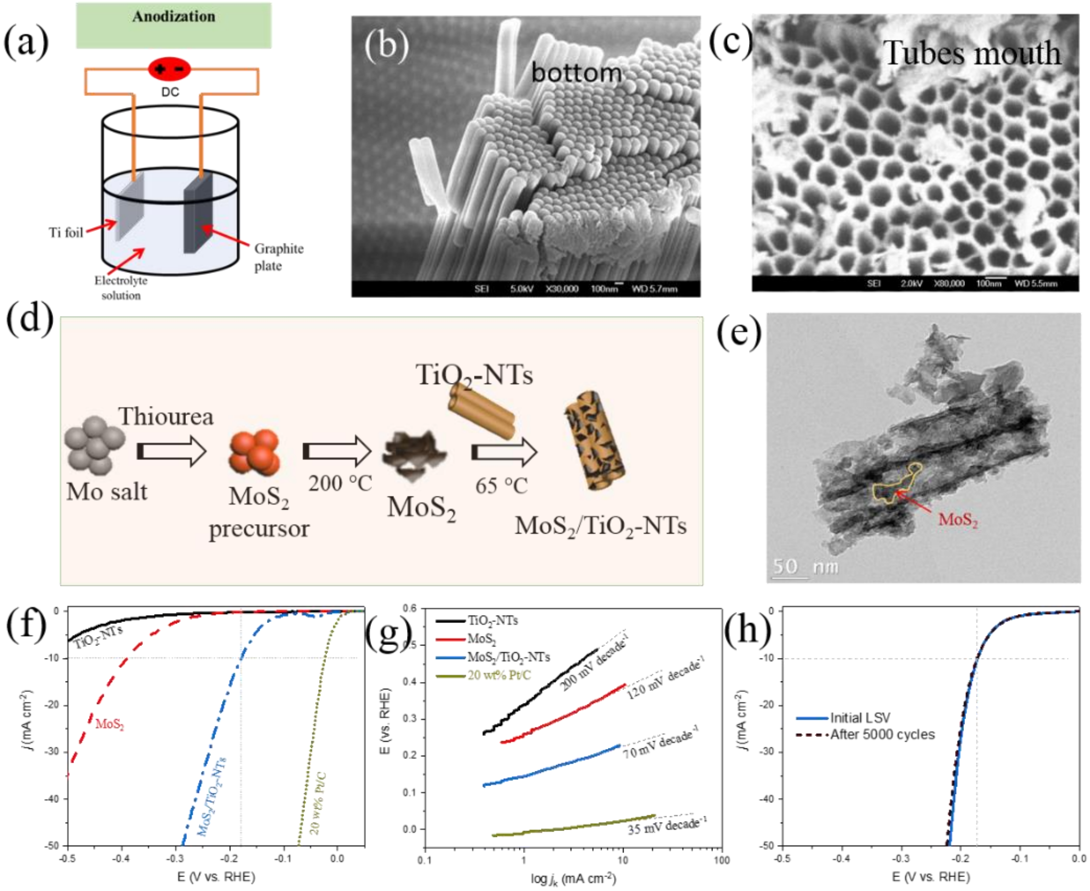

Figure 3 Fabrication de réseaux de nanotubes de TiO_2 hautement ordonnés (a) dans un dispositif expérimental d'anodisation. Images au MEB de TiO_2-NTs sous forme anodisée, (b) coupe longitudinale de TiO_2-NTs en pose libre avec un fond fermé, (c) morphologie vue de dessus. (d) Schéma de fabrication de MoS_2/TiO_2-NTs, (e) image TEM des MoS_2/TiO_2-NTs, (f) courbe de polarisation HER de TiO_2-NTs, MoS_2, MoS_2/TiO_2-NTs et 20% en poids de Pt/C à une vitesse de balayage: 10 mV s^{-1}. (g) Les parcelles de Tafel correspondantes. (h) Test de durabilité du catalyseur composite MoS_2/TiO_2-NTs réalisé sur du papier en fibres de carbone. Le courant HER négligeable a perdu après 5000 cycles potentiels entre -0.4 et 0.2 (V vs. RHE) à une vitesse de balayage de 100 mV s^{-1}. L'electrolyte: 0.5 M H_2SO_4.

Par ailleurs, les MoS_2/TiO_2-NTs nécessitent un faible surpotentiel d'environ 170 mV pour délivrer régulièrement un courant cathodique d'une densité de 10 mA cm^{-2}, offrant une activité HER prometteuse parmi électrocatalyseurs à base de TiO_2-NTs [254-258]. De plus, les MoS_2/TiO_2-NTs présentent une excellente durabilité avec un changement négligeable du surpotentiel à des densités de courant cathodique de 10 mA cm^{-2} après 5000 cycles de potentiel (Figure 3h).

En général, nous démontrons une stratégie simple pour produire un électrocatalyseur avec une activité HER supérieure à celle observée en milieu acide. La méthode de production peu couteuse et évolutive des électrocatalyseurs (MoS_2/TiO_2-NTs) est prometteuse pour une implémentation pratique de cette technologie à grand échelle. De plus, ces résultats offrent de nouvelles informations utiles pour l'évolution des morphologies des TiO_2-NTs en ajustant les conditions d'anodisation. Nous prévoyons également que les morphologies contrôlées sont essentielles pour améliorer les performances des matériaux à base de TiO_2-NTs dans une large gamme de technologies de conversion d'énergie.

Les résultats présentés dans ce chapitre sont basés sur l'article suivant :

N. Komba, G. Zhang, Z. Pu, M. Wu, Rosei, S. Sun, MoS_2 supportés par des nanotubes de TiO_2 autonomes pour une réaction de dégagement d'hydrogène efficace. *Manuscrit* en préparation.